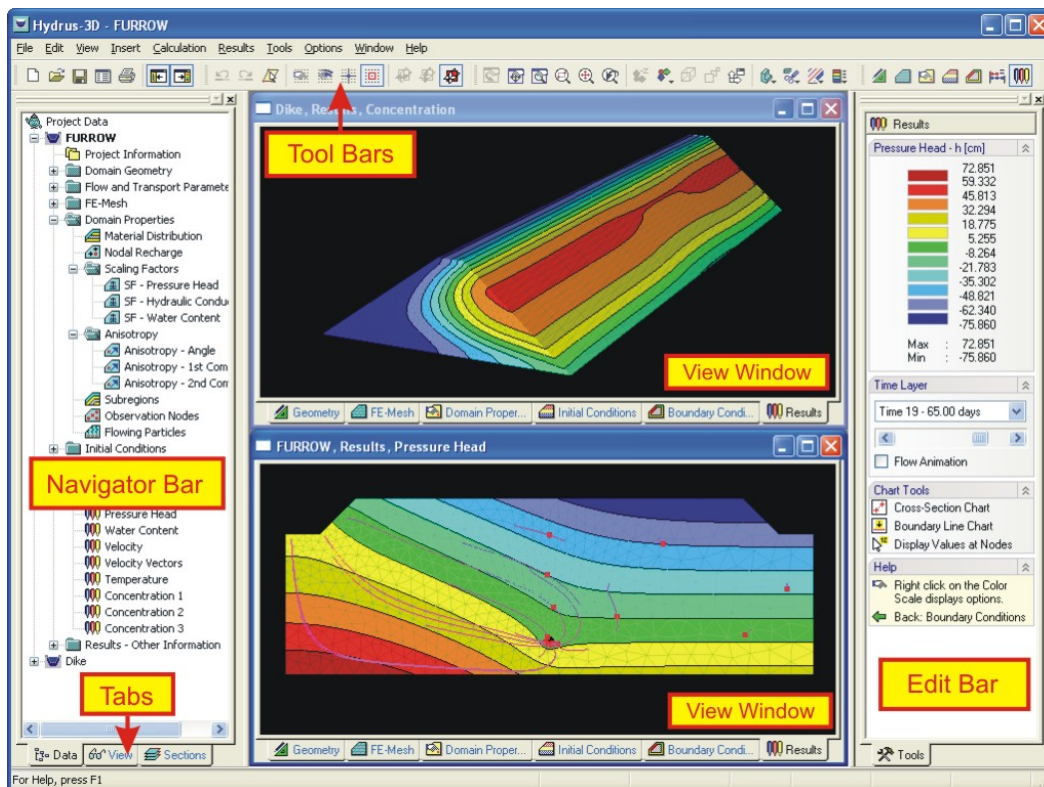


Soil Water
and
The Japanese Society of Irrigation, Drainage and Reclamation Engineering
Soil Physics HYDRUS Group

The Third HYDRUS Workshop

June 28, 2008

Tokyo, Japan



Proceedings

edited by

Hirotaka Saito, Masaru Sakai, Nobuo Toride, and Jirka Šimůnek

The texts of various papers in this volume were set individually by the authors or under their supervision and were not subject to additional editorial work.

ISBN978-4-9901192-5-6

The Third HYDRUS Workshop

Content

1. Saito, H., M. Sakai, N. Toride, and J. Šimůnek, Preface	1
2. Šimůnek, J., M. Šejna, H. Saito, and M.Th. van Genuchten, New Features and Developments in HYDRUS Software Packages	3
3. Watanabe, K., Water and heat flow in a directionally frozen silty soil	15
4. Watanabe, H., J. Tournebize, K. Takagi, and T. Nishimura, Simulation of fate and transport of pretilachlor in a rice paddy by PCPF-SWMS model	23
5. Fujimaki, H., Determination of irrigation amounts using a numerical model	33
6. Zeng, Y., L. Wan, Z. Su, and H. Saito, The study of diurnal soil water dynamics in coarse sand with modified HYDRUS1D code	39
7. Sakai, M., J. Šimůnek, and H. Saito, Surface boundary conditions from meteorological data using HYDRUS-1D	53
8. Nakamura, K., S. Watanabe and Y. Hirono, Applications and problems of numerical modeling of Nitrogen transport in agricultural soils using HYDRUS	58
9. Chamindu, D.T.K.K., K. Kawamoto, H. Saito, T. Komatsu and P. Moldrup, Transport and retention of colloid-sized materials in saturated porous media: Experimental and numerical analysis	70
10. Urakawa, R., H. Toda, K. Haibara, and D.S. Choi, Effects of NO ₃ ⁻ adsorption characteristics by subsoil on long-term NO ₃ ⁻ leaching from the forest watershed	79
11. Kato, C., T. Nishimura, T. Miyazaki, and M. Kato, Fluctuation of salt content profile of the field in Northwest China under repetitious border irrigation	85
12. Inosako, K., S. Kozaki, M. Inoue, and K. Takuma, Analysis of water movement in a wick sampler using HYDRUS-2D code	91
13. Yasutaka, T., and K. Nakamura, Risk assessment of soil and groundwater contamination using HYDRUS-1D	97
14. Inoue, M., K. Inosako, and K. C. Uzoma, Determination of soil hydraulic properties of undisturbed core sample using continuous suction outflow method	103
15. Andry, H., M. Inoue, T. Yamamoto, K. Uzoma, and H. Fujiyama, Inverse Estimation of Clay Soil Unsaturated Hydraulic Conductivity Treated with Organic Material by Multistep Outflow Method	107
16. Inaba, K., H. Tosaka, and M. Yoshioka, Integrated modeling of watershed hydrologic fluid and heat flows	112
17. Sakai, M., and N. Toride, Estimating hydraulic property for a dune sand and a volcanic ash soil using evaporation method	120

18. Chen, D., N. Toride , and D. Antonov, Calcium hydroxide leaching through a well-buffered volcanic-ash soil with pH dependent charges 126
19. Karunarithna, A.K., K. Kawamoto, P. Moldrup, L. W. de Jonge, and T. Komatsu, Development of a Predictive Expression for Soil Water Repellency Curve Based on Soil Organic Carbon Content 131
20. Nishimura, T., Y. Sato, and M. Kato, Water and salt behavior in Maize field under repeating boarder irrigation at Gansu province, China 137
21. Hirono, Y., S. Nakamura, and M. Ohta, Modelling of water and nitrogen transport in tea fields 143
22. Saito, T., H. Yasuda, H. Fujimaki, Simulation of soil water movement in a water harvesting system with sand ditches 148

Preface

The first two HYDRUS workshops were held in Europe; in 2005 in Utrecht, the Netherlands, and in 2008 in Prague, the Czech Republic. Each workshop attracted more than 40 scientists from all over the world. About 20 contributions were presented at each workshop and assembled in the workshop proceedings (Torkzaban and Hassanizadeh, 2005; Šimůnek and Kodešová, 2008).

Since the first workshop the community of HYDRUS users has been continuously growing not only in the US and Europe, but also in Asia. HYDRUS codes have been downloaded over two thousand times in the past year alone and HYDRUS web pages are visited on average by about seven hundred individual visitors daily. Hundreds of research papers, in which HYDRUS codes have been used, have appeared in the peer-reviewed literature. Also two major releases of new versions of HYDRUS software packages have occurred. While the HYDRUS (2D/3D) software package was released in 2006 as a complete rewrite of HYDRUS-2D and its extensions for two- and three-dimensional geometries, version 4.0 of HYDRUS-1D was released in 2008. To give HYDRUS community in Asia an opportunity to meet and share their experience with HYDRUS codes and to learn about new features and developments in HYDRUS codes, **The Third HYDRUS Workshop** was organized by Soil Water (the official HYDRUS distributor in Japan) on June 28, 2008 at University of Tokyo, following a HYDRUS short course that was held during two previous days at Tokyo University of Agriculture and Technology.

The purpose of the workshop was to bring together the users and developers of the HYDRUS software packages, to present the latest innovations in the model applications, and to discuss capabilities and limitations of HYDRUS. Over 60 scientists, graduate students, and practitioners from a number of Asian countries participated at this workshop. These proceedings contain the collection of papers presented at the workshop. This collective work includes contributions by users of the HYDRUS software packages ranging from the very fundamental to the most compelling and important applications. It also includes contributions by non-HYDRUS users, such as the user of GETFLOWS, an integrated numerical simulator. As evident from recent developments in coupling HYDRUS with other software packages (e.g., PHREEQC, UNSATCHEM, CW2D, and MODFLOW), we believe that frequent communications between HYDRUS and non-HYDRUS users are now essential for further improvements and progress in HYDRUS modeling.

The editors:

Hiroataka Saito

Masaru Sakai

Nobuo Toride

Jirka Šimůnek

Please refer to papers from these proceedings as follows:

Šimůnek, J., M. Šejna, H. Saito and M. Th. van Genuchten, New features and developments in HYDRUS software packages. In: H. Saito, M. Sakai, N. Toride and J. Šimůnek (eds.), Proc. of The Third HYDRUS Workshop, June 28, 2008, Tokyo University of Agriculture and Technology, Tokyo, Japan, ISBN 978-4-9901192-5-6, pp. 3-14, 2008.

New Features and Developments in HYDRUS Software Packages

J. Šimůnek

Department of Environmental Sciences, University of California Riverside, Riverside, CA 92521, USA

M. Šejna

PC-Progress, s.r.o., Anglicka 28, Prague 120 00, Czech Republic

H. Saito

Department of Ecoregion Science, Tokyo University of Agriculture & Technology, Fuchu, Tokyo 183-8509 Japan

M. Th. van Genuchten

U.S. Salinity Laboratory, USDA, ARS, Riverside, CA 92507, USA

ABSTRACT: While the first HYDRUS workshop was held in 2005 at the Utrecht University in Utrecht, the Netherlands, the second HYDRUS workshop was organized in 2008 at the Czech University of Life Sciences, Prague, the Czech Republic. Two major developments related to HYDRUS software packages have occurred since the first workshop. The main development undoubtedly was the replacement of HYDRUS-2D with **HYDRUS (2D/3D)** in 2006. The HYDRUS (2D/3D) software package is an extension and replacement of HYDRUS-2D and SWMS_3D. This software package is a complete rewrite of HYDRUS-2D and its extensions for two- and three-dimensional geometries. The second major development was the release of the new version (4.0) of **HYDRUS-1D** in 2008. This version allows consideration of coupled movement of water, vapor, and energy, and offers extended options for simulating nonequilibrium or preferential water flow using dual-porosity and dual-permeability approaches, and solute nonequilibrium transport. In addition to many new features, GUIs of HYDRUS-1D and HYDRUS (2D/3D) support also the biogeochemical flow and transport model HP1 and the constructed wetland module CW2D, respectively. Both software packages represent major upgrades of previous versions, with many new processes considered and with significantly improved graphical user interfaces and more detailed online helps. Additionally, HYDRUS-1D was significantly simplified and incorporated as the HYDRUS package into the groundwater flow model MODFLOW.

1 INTRODUCTION

While the first HYDRUS workshop was held on October 19, 2005 at the Department of Earth Sciences of the Utrecht University in Utrecht, the Netherlands, the second HYDRUS workshop was organized on March 28, 2008 at the Faculty of Agrobiological Sciences, Food and Natural Resources of the Czech University of Life Sciences, Prague, the Czech Republic. 22 and 18 contributions were presented at these workshops, respectively, and assembled in the workshop proceedings (Torkzaban and Hassanizadeh, 2005; Šimůnek and Kodesova, 2008). Since the first HYDRUS workshop, two major releases of new versions of HYDRUS software packages has occurred. While the HYDRUS (2D/3D) (Šimůnek et al., 2006; Šejna and Šimůnek, 2007) software package was released in 2006 as a complete rewrite of HYDRUS-2D (Šimůnek et al., 1999) and its extensions for two- and three-dimensional geometries, version 4.0 of HYDRUS-1D (Šimůnek et al., 2008a) was released in 2008. In the text below we summarize new features that were implemented in both software packages. We also briefly discuss other modeling developments related to HYDRUS family of models.

2 HYDRUS (2D/3D)

The HYDRUS (2D/3D) software package (Šimůnek et al., 2006; Šejna and Šimůnek, 2007) (Figure 1) is an extension and replacement of HYDRUS-2D (version 2.0) (Šimůnek et al., 1999) and SWMS_3D (Šimůnek et al., 1995). This software package is a complete rewrite of HYDRUS-2D and its extensions for two- and three-dimensional geometries.

2.1 *New features and processes in computational modules*

In addition to features and processes available in HYDRUS-2D and SWMS_3D, the new computational modules of HYDRUS (2D/3D) consider (a) water flow and solute transport in a dual-porosity system, thus allowing for preferential flow in fractures or macropores while storing water in the matrix (Šimůnek et al., 2003), (b) root water uptake with compensation, (c) the spatial root distribution functions of Vrugt et al. (2001ab), (d) the soil hydraulic property models of Kosugi (1996) and Durner (1994), (e) the transport of viruses, colloids, and/or bacteria using an attachment/detachment model, filtration theory, and blocking functions (e.g., Bradford et al., 2002), (f) a constructed wetland module (only in 2D) (Langergraber and Šimůnek, 2005, 2006), (g) the hysteresis model of Lenhard et al. (1991) to eliminate pumping by keeping track of historical reversal points, (h) new print management options, (i) dynamic, system-dependent boundary conditions, (j) flowing particles in two-dimensional applications, and (k) calculations of actual and cumulative fluxes across internal meshlines.

2.2 *Wetland module*

A multi-component reactive transport model CW2D (**Constructed Wetlands 2D**) (Langergraber and Šimůnek 2005, 2006) was developed to model the biochemical transformation and degradation processes in subsurface-flow constructed wetlands. The model was incorporated into the HYDRUS (2D/3D) variably-saturated water flow and solute transport software package. Constructed wetlands have become increasingly popular for removing organic matter, nutrients, trace elements, pathogens, or other pollutants from wastewater and/or runoff water. Such wetlands involve a complex mixture of water, substrate, plants, litter, and a variety of microorganisms to provide optimal conditions for improving water quality. The water flow regime in subsurface-flow constructed wetlands can be highly dynamic and requires the use of transient variably-saturated flow model. The biochemical components defined in CW2D include dissolved oxygen, three fractions of organic matter (readily- and slowly-biodegradable, and inert), four nitrogen compounds (ammonium, nitrite, nitrate, and dinitrogen), inorganic phosphorus, and heterotrophic and autotrophic micro-organisms. Organic nitrogen and organic phosphorus were modeled as part of the organic matter. The biochemical degradation and transformation processes were based on Monod-type rate expressions, such as for NO_3 -based growth of heterotrophs on readily biodegradable COD (denitrification):

$$r = \mu_{\text{DN}} \frac{K_{\text{DN},\text{O}_2}}{K_{\text{DN},\text{O}_2} + c_{\text{O}_2}} \frac{c_{\text{NO}_3}}{K_{\text{DN},\text{NO}_3} + c_{\text{NO}_3}} \frac{K_{\text{DN},\text{NO}_2}}{K_{\text{DN},\text{NO}_2} + c_{\text{NO}_2}} \frac{c_{\text{CR}}}{K_{\text{DN},\text{CR}} + c_{\text{CR}}} f_{\text{N,DN}} c_{\text{XH}} \quad (1)$$

We refer to Langergraber and Šimůnek (2005, 2006) for a detailed discussion of the terms in (1). All process rates and diffusion coefficients were assumed to be temperature dependent. Heterotrophic bacteria were assumed to be responsible for hydrolysis, mineralization of organic matter (aerobic growth) and denitrification (anoxic growth), while autotrophic bacteria were assumed to be responsible for nitrification, which was modeled as a two-step process. Lysis was considered to be the sum of all decay and sink processes. Langergraber and Šimůnek (2005, 2006) demonstrated the model for one- and two-stage subsurface vertical flow constructed wetlands (Fig. 1). Model simulations of water flow, tracer transport, and selected biochemical compounds were compared against experimental observations.

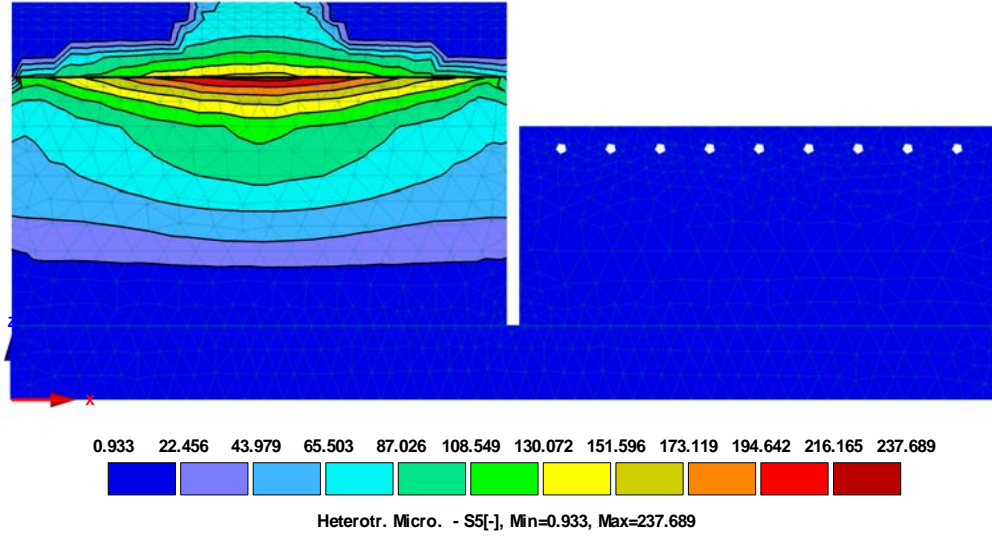


Figure 1. Simulated steady-state distribution of heterotrophic organisms XH (Langergraber and Šimůnek, 2005).

2.3 Spatial Root Distribution Functions

Following two- and three-dimensional root distribution functions are implemented into HYDRUS (Vrugt et al., 2001ab):

$$b(x, z) = \left(1 - \frac{z}{Z_m}\right) \left(1 - \frac{x}{X_m}\right) e^{-\left(\frac{p_z}{Z_m}|z^* - z| + \frac{p_x}{X_m}|x^* - x|\right)} \quad (2)$$

$$b(x, y, z) = \left(1 - \frac{x}{X_m}\right) \left(1 - \frac{y}{Y_m}\right) \left(1 - \frac{z}{Z_m}\right) e^{-\left(\frac{p_x}{X_m}|x^* - x| + \frac{p_y}{Y_m}|y^* - y| + \frac{p_z}{Z_m}|z^* - z|\right)} \quad (3)$$

where X_m , Y_m , and Z_m are the maximum rooting lengths in the x -, y -, and z - directions [L], respectively; x , y , and z are distances from the origin of the tree in the x -, y -, and z - directions [L], respectively; p_x [-], p_y [-], p_z [-], x^* [L], y^* [L], and z^* [L] are empirical parameters, and $b(x, z)$ and $b(x, y, z)$ denote two- and three-dimensional spatial distribution of the potential root water uptake [-]. Vrugt et al. (2001ab) showed that the root water uptake in (2) and (3) is extremely flexible and allows spatial variations of water uptake as influenced by non-uniform water application (e.g. drip irrigation) and root length density patterns. See Vrugt et al. (2001ab) for different configurations of normalized spatial distribution of potential root water uptake.

2.4 New features in the graphical user interface

New features of the Graphical User Interface of HYDRUS (2D/3D) include, among other things, (a) a completely new GUI based on Hi-End 3D graphics libraries, (b) the MDI (multi document interface) architecture with multiple projects and multiple views, (c) a new organization of geometric objects, (d) a navigator window with an object explorer, (e) many new functions improving the user-friendliness, such as drag-and-drop and context sensitive pop-up menus, (f) improved interactive tools for graphical input, (g) options to save cross-sections and mesh-lines for charts within a given project, (h) a new display options dialog where all colors, line styles, fonts and other parameters of graphical objects can be customized, (i) extended print options, (j) extended information in the Project Manager (including project previews), and (k) an option to export input data for the parallelized PARSWMS code (Hardelauf et al., 2007).

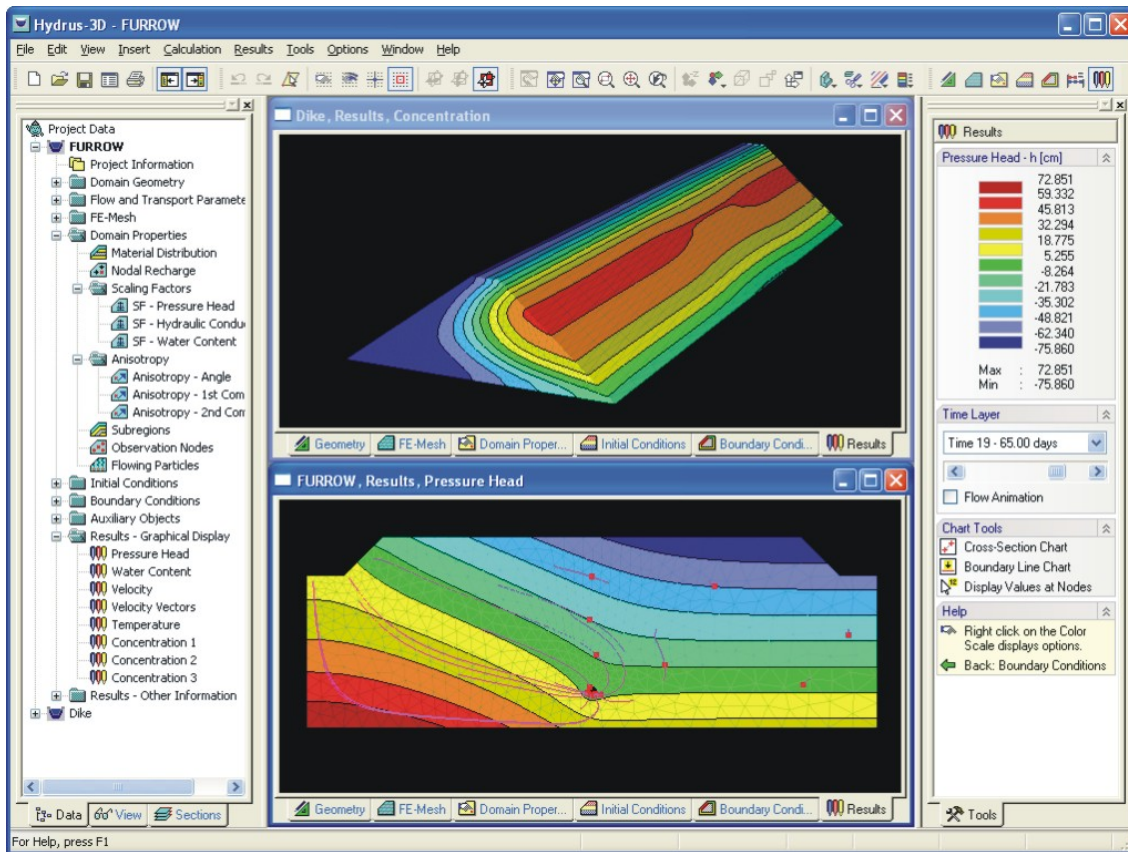


Figure 2. Main window of the HYDRUS (2D/3D) software package. Input and output data are accessible using the data tree at the Navigator Bar on the left. The computational domain with its finite element discretization, various domain properties, initial and boundary conditions, and results are displayed in one or multiple View Windows in the middle. Various tools for manipulating data in the View Window are available on the Edit Bar on the right. The tabs in the View Window allow for fast access to different types of data (Šimůnek et al., 2008b).

2.5 Website and documentation

The HYDRUS web site hosts a **discussion forum** for HYDRUS (2D/3D) (as well as other related programs) where users, after registering, can submit questions about the different software packages and how to use them for their particular applications. Users there can also discuss various topics related to modeling, or respond to questions posted by other users. The large number of users of these discussion forums has made the forums nearly self-supporting in terms of software support and feedback.

The HYDRUS website also provides **tutorials** (Figure 3), including brief downloadable videos in which these tutorials are carried out step by step, thus allowing software users to teach themselves interactively about the basic components of the software, including the process of data entry and display of calculated results.

We have also dramatically extended the **documentation** for HYDRUS (2D/3D). The installation of the latest HYDRUS (2D/3D) is accompanied with 240 pages of information in the technical manual, 200 pages of user manual, and over thousand pages of online context-sensitive help. The software package furthermore comes with a suite of test problems, some of which are described in detail in the technical manual.

Since previously published studies in which the program has been used can be a major source of information for new users, we are continuously updating the list of such publications at http://www.pc-progress.cz/Pg_Hydrus_References.htm for HYDRUS-2D (or 2D/3D) and its predecessors. Similar information is collected for HYDRUS-1D and related software packages at http://www.pc-progress.cz/Pg_Hydrus1D_References.htm.



Figure 3. HYDRUS web page with HYDRUS tutorials and brief downloadable videos, demonstrating step by step the use of the software package.

3 HYDRUS-1D

New features in version 4.0 of HYDRUS-1D (Šimůnek et al., 2008a) as compared to version 3.0 (Šimůnek et al., 2005) include a) coupled water, vapor, and energy transport, b) dual-permeability type water flow and solute transport, c) dual-porosity water flow and solute transport, with solute transport subjected to two-site sorption in the mobile zone, d) option to calculate potential evapotranspiration the Penman-Monteith combination equation or with Hargreaves equation, e) daily variations in the evaporation, transpiration, and precipitation rates, and f) support for the HP1 code, which was obtained by coupling HYDRUS with the PHREEQC biogeochemical code (Parkhurst and Appelo, 1999). Selected new features are briefly discussed below.

3.1 Coupled water, vapor, and energy transport

Version 3.0 of HYDRUS-1D numerically solved the Richards equation that considered only water flow in the liquid phase and ignored the effects of the vapor phase on the overall water mass balance. While this assumption is justified for the majority of applications, a number of problems exist in which the effect of vapor flow can not be neglected. Vapor movement is often an important part of the total water flux when the soil moisture becomes relatively low. Version 4.0 of HYDRUS-1D offers an option to simulate nonisothermal liquid and vapor flow, closely coupled with the heat transport (Saito et al., 2006):

$$\frac{\partial \theta(h)}{\partial t} = \frac{\partial}{\partial x} \left[(K + K_{vh}) \left(\frac{\partial h}{\partial x} + 1 \right) + (K_{LT} + K_{vT}) \frac{\partial T}{\partial x} \right] - S(h) \quad (4)$$

$$C(\theta) \frac{\partial T}{\partial t} + L_0 \frac{\partial \theta_v}{\partial t} = \frac{\partial}{\partial x} \left(\lambda \frac{\partial T}{\partial x} \right) - C_w q \frac{\partial T}{\partial x} - C_v \frac{\partial q_v T}{\partial x} - L_0 \frac{\partial q_v}{\partial x} \quad (5)$$

In eq. (4), θ = total volumetric water content, being the sum ($\theta = \theta_l + \theta_v$) of the volumetric liquid water content, θ_l , and the volumetric water vapor content, θ_v (both expressed as an equivalent water content), h = pressure head [L], T = temperature [K], K = isothermal hydraulic conductivity for the liquid phase [$L T^{-1}$], K_{LT} = thermal hydraulic conductivity for the liquid phase [$L^2 K^{-1} T^{-1}$], K_{vh} = isothermal vapor hydraulic conductivity [$L T^{-1}$], K_{vT} = thermal vapor hydraulic conductivity [$L^2 K^{-1} T^{-1}$], and S = sink term representing root water uptake [T^{-1}]. Overall water flow in (4) is given as the sum of isothermal liquid flow, isothermal vapor flow, gravitational liquid flow, thermal liquid flow, and thermal vapor flow. Since several terms of (4) are a function of temperature, this equation should be solved simultaneously with the heat transport equation (5) to properly account for temporal and spatial changes in soil temperature.

In eq. (5), λ = apparent thermal conductivity of the soil [$MLT^{-3}K^{-1}$] (e.g. $Wm^{-1}K^{-1}$); $C(\theta)$ and C_w = volumetric heat capacities [$ML^{-1}T^{-2}K^{-1}$] (e.g. $Jm^{-3}K^{-1}$) of the porous medium and the liquid phase, respectively, q = fluid flux density [$L T^{-1}$], L_0 = volumetric latent heat of vaporization of liquid water [$ML^{-1}T^{-2}$] (e.g., Jm^{-3}), and q_v = vapor flux density [$L T^{-1}$]. In equation (5), the total heat flux density is defined as the sum of the conduction of sensible heat as described by Fourier's law (the first term on the right side), sensible heat by convection of liquid water (the second term) and water vapor (the third term), and of latent heat by vapor flow (the fourth term).

3.2 Physical and chemical nonequilibrium models

3.2.1 Physical nonequilibrium models

Version 4.0 of HYDRUS-1D implements several physical nonequilibrium water flow and solute transport models. While mathematical description of these models is given in detail in Šimůnek et al. (2008c) or the HYDRUS-1D manual, here we will present only the conceptual description. A hierarchical set of physical nonequilibrium flow and transport models can be derived from the Uniform Flow Model (Figures 4a). The equilibrium flow and transport model can be modified by assuming that the soil particles or aggregates have their own micro-porosity and that water present in these micropores is immobile (the *Mobile-Immobile Water Model* in Figure 4b). While the water content in the micropore domain is constant in time, dissolved solutes can move into and out of this immobile domain by molecular diffusion. This simple modification leads to physical nonequilibrium solute transport while still maintaining uniform water flow.

The mobile-immobile water model can be further expanded by assuming that both water and solute can move into and out of the immobile domain (Šimůnek et al., 2003), leading to the *Dual-Porosity Model* in Figure 4c. While the water content inside of the soil particles or aggregates is assumed to be constant in the Mobile-Immobile Water Model, it can vary in the Dual-Porosity Model since the immobile domain is now allowed to dry out or rewet during drying and wetting processes. Water flow into and out of the immobile zone is usually described using a first-order rate process. Solute can move into the immobile domain of the Dual-Porosity Model by both molecular diffusion and advection with flowing (exchanging) water. Since water can move from the main pore system into the soil aggregates and vice-versa, but not directly between the aggregates themselves, water in the aggregates can be considered immobile from a larger scale point of view.

The limitation of water not being allowed to move directly between aggregates is overcome in *Dual-Permeability Models* (e.g., Gerke and van Genuchten, 1993). Water and solutes in such models move also directly between soil aggregates as shown in Figure 4d. Dual-Permeability Models assume that the porous medium consists of two overlapping pore domains, with water flowing relatively fast in one domain (often called the macropore, fracture, or inter-porosity domain) when close to full saturation, and slow in the other domain (often referred to as the mi-

cropore, matrix, or intra-porosity domain). Like the Dual-Porosity Model, the Dual-Permeability Model allows the transfer of both water and solutes between the two pore regions.

Finally, the Dual-Permeability Model can be further refined by assuming that inside of the matrix domain an additional immobile region exists into which solute can move by molecular diffusion (the *Dual-Permeability Model with MIM* in Figure 4e) (Pot et al., 2005; Šimůnek et al., 2008c).

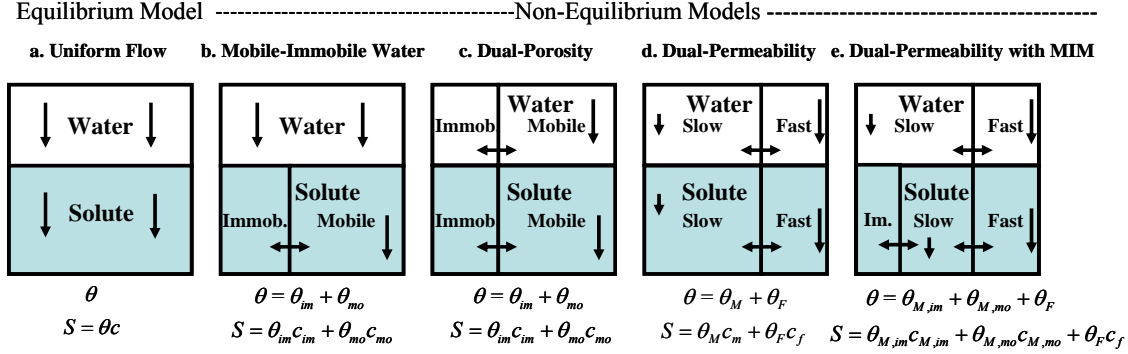


Figure 4. Conceptual physical nonequilibrium models for water flow and solute transport. In the plots, θ is the water content, θ_{mo} and θ_{im} in (b) and (c) are water contents in the mobile and immobile flow regions, respectively; θ_M and θ_F in (d) are water contents in the matrix and macropore (fracture) regions, respectively, and $\theta_{M,mo}$, $\theta_{M,im}$, and θ_F in (e) are water contents in the mobile and immobile flow regions of the matrix domain, and in the macropore (fracture) domain, respectively; c are concentrations in corresponding regions, with subscripts having the same meaning as for water contents, while S is the total solute content of the liquid phase (Šimůnek et al., 2008c).

3.2.2 Chemical nonequilibrium models

Chemical nonequilibrium models implemented into HYDRUS-1D are schematically shown in Figure 5. The simplest chemical nonequilibrium model assumes that sorption is a kinetic process (the *One Kinetic Site Model* in Figure 5a), usually described by means of a first-order rate equation. The one-site kinetic model can be expanded into a Two-Site Sorption model by assuming that the sorption sites can be divided into two fractions. The simplest two-site sorption model arises when sorption on one fraction of the sorption sites is assumed to be instantaneous, while kinetic sorption occurs on the second fraction (*Two-Site Model* in Figure 5b). This model can be further expanded by assuming that sorption on both fractions is kinetic and proceeds at different rates (the *Two Kinetic Sites Model* in Figure 5c). The Two Kinetic Sites Model reduces to the Two-Site Model when one rate is so high that it can be considered instantaneous, to the One Kinetic Site Model when both rates are the same, or to the chemical equilibrium model when both rates are so high that they can be considered instantaneous.

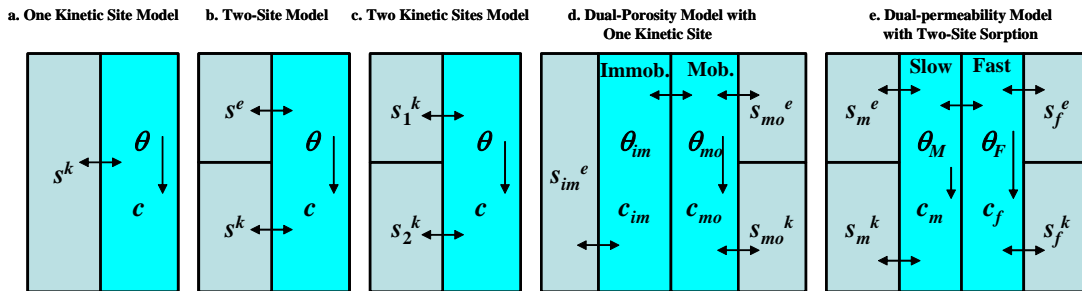


Figure 5. Conceptual chemical nonequilibrium models for reactive solute transport. In the plots, θ is the water content, θ_{mo} and θ_{im} in (d) are water contents of the mobile and immobile flow regions, respectively; θ_M and θ_F in (e) are water contents of the matrix and macropore (fracture) regions, respectively; c are concentrations of the corresponding regions, s^e are sorbed concentrations in equilibrium with the liquid concentrations of the corresponding regions, and s^k are kinetically sorbed solute concentrations of the corresponding regions (Šimůnek et al., 2008c).

3.2.3 Physical and chemical nonequilibrium models

The combined physical and chemical nonequilibrium approach may be simulated with HYDRUS-1D using the *Dual-Porosity Model with One Kinetic Site* (Figure 5d). This model considers water flow and solute transport in a dual-porosity system (or a medium with mobile-immobile water), while assuming that sorption in the immobile zone is instantaneous. However, following the two-site kinetic sorption concept, the sorption sites in contact with the mobile zone are now divided into two fractions, subject to either instantaneous or kinetic sorption. Since the residence time of solutes in the immobile domain is relatively large, equilibrium likely exists between the solution and the sorption complex here, in which case there is no need to consider kinetic sorption in the immobile domain. The model, on the other hand, assumes the presence of kinetic sorption sites in contact with the mobile zone since water can move relatively fast in the macropore domain and thus prevent chemical equilibrium (Šimůnek et al., 2008c).

Finally, chemical nonequilibrium can also be combined with the Dual-Permeability Model. This last nonequilibrium option implemented into HYDRUS-1D (the *Dual-Permeability Model with Two-Site Sorption* in Figure 5e) assumes that equilibrium and kinetic sites exist in both the macropore (fracture) and micropore (matrix) domains. Applications of this transport model that considers simultaneously both physical and chemical nonequilibrium has recently been presented by Pot et al., (2005), Köhne et al. (2006), and Kodešová et al. (2008).

3.3 Calculation of potential evapotranspiration

Potential evapotranspiration may be calculated in HYDRUS-1D using either the FAO recommended Penman-Monteith combination equation for evapotranspiration (ET_0) (FAO, 1990) or the Hargreaves equation (Jensen et al., 1997). With the Penman-Monteith approach, ET_0 is determined using a combination equation that combines the radiation and aerodynamic terms as follows [FAO, 1990]:

$$ET_0 = ET_{rad} + ET_{aero} = \frac{1}{\lambda} \left[\frac{\Delta(R_n - G)}{\Delta + \gamma(1 + r_c/r_a)} + \frac{\rho c_p (e_a - e_d)/r_a}{\Delta + \gamma(1 + r_c/r_a)} \right] \quad (6)$$

where ET_0 is the evapotranspiration rate [mm d^{-1}], ET_{rad} is the radiation term [mm d^{-1}], ET_{aero} is the aerodynamic term [mm d^{-1}], λ is the latent heat of vaporization [MJ kg^{-1}], R_n is net radiation at surface [$\text{MJ m}^{-2}\text{d}^{-1}$], G is the soil heat flux [$\text{MJ m}^{-2}\text{d}^{-1}$], ρ is the atmospheric density [kg m^{-3}], c_p is the specific heat of moist air [i.e., $1.013 \text{ kJ kg}^{-1} \text{ }^\circ\text{C}^{-1}$], $(e_a - e_d)$ is the vapor pressure deficit [kPa], e_a is the saturation vapor pressure at temperature T [kPa], e_d is the actual vapor pressure [kPa], r_c is the crop canopy resistance [s m^{-1}], and r_a is the aerodynamic resistance [s m^{-1}].

The potential evapotranspiration can also be evaluated using the much simpler Hargreaves formula (e.g., Jensen et al., 1997):

$$ET_p = 0.0023 R_a (T_m + 17.8) \sqrt{TR} \quad (7)$$

where R_a is extraterrestrial radiation in the same units as ET_p [e.g., mm d^{-1} or $\text{J m}^{-2}\text{s}^{-1}$], T_m is the daily mean air temperature, computed as an average of the maximum and minimum air temperatures [$^\circ\text{C}$], TR is the temperature range between the mean daily maximum and minimum air temperatures [$^\circ\text{C}$].

3.4 Daily variations in the evaporation, transpiration, and precipitation rates

Variations in potential evaporation and transpiration during the day can be generated with HYDRUS-1D using the assumptions that hourly values between 0-6 a.m. and 18-24 p.m. represent 1% of the total daily value and that a sinusoidal shape is followed during the rest of the day (Fayer, 2000), i.e.,

$$\begin{aligned} T_p(t) &= 0.24 \overline{T_p} & t < 0.264\text{d}, t > 0.736\text{d} \\ T_p(t) &= 2.75 \overline{T_p} \sin\left(\frac{2\pi t}{1\text{day}} - \frac{\pi}{2}\right) & t \in (0.264\text{d}, 0.736\text{d}) \end{aligned} \quad (8)$$

where $\overline{T_p}$ is the daily value of potential transpiration (or evaporation). Similarly, variation of precipitation can be approximated using a cosine function as follows:

$$P(t) = \overline{P} \left[1 + \cos \left(\frac{2\pi t}{\Delta t} - \pi \right) \right] \quad (9)$$

where \overline{P} is the average precipitation rate of duration Δt .

3.5 GUI support for the HP1 code

Graphical User Interface of HYDRUS-1D provides a support for the biogeochemical transport code HP1. This is a complex modeling tool that was recently developed by coupling HYDRUS-1D with the PHREEQC geochemical code (Parkhurst and Appelo, 1999). This coupling resulted in a new comprehensive simulation tool, HP1 (acronym for HYDRUS1D-PHREEQC) (Jacques and Šimůnek, 2005; Jacques et al., 2006, 2008ab). The combined code contains modules simulating (1) transient water flow in variably-saturated media, (2) the transport of multiple components, (3) mixed equilibrium/kinetic biogeochemical reactions, and (4) heat transport. HP1 is a significant expansion of the individual HYDRUS-1D and PHREEQC programs by combining and preserving most of their original features and capabilities into a single numerical model. The code still uses the Richards equation for variably-saturated flow and advection-dispersion type equations for heat and solute transport. However, the program can now simulate also a broad range of low-temperature biogeochemical reactions in water, the vadose zone and in ground water systems, including interactions with minerals, gases, exchangers, and sorption surfaces, based on thermodynamic equilibrium, kinetics, or mixed equilibrium-kinetic reactions.

Jacques and Šimůnek (2005), (Šimůnek et al., 2006b), and Jacques et al. (2008a,b) demonstrated the versatility of HP1 on several examples such as a) the transport of heavy metals (Zn^{2+} , Pb^{2+} , and Cd^{2+}) subject to multiple cation exchange reactions, b) transport with mineral dissolution of amorphous SiO_2 and gibbsite ($Al(OH)_3$), c) heavy metal transport in a medium with a pH-dependent cation exchange complex, d) infiltration of a hyperalkaline solution in a clay sample (this example considers kinetic precipitation-dissolution of kaolinite, illite, quartz, calcite, dolomite, gypsum, hydrotalcite, and sepiolite), e) long-term transient flow and transport of major cations (Na^+ , K^+ , Ca^{2+} , and Mg^{2+}) and heavy metals (Cd^{2+} , Zn^{2+} , and Pb^{2+}) in a soil profile, f) cadmium leaching in acid sandy soils, g) radionuclide transport (U and its aqueous complexes), and h) the fate and subsurface transport of explosives (TNT and its daughter products 2ADNT, 4ADNT, and TAT).

4 HYDRUS PACKAGE FOR MODFLOW

Although computer power has increased tremendously during the last few decades, large scale three-dimensional applications evaluating water flow in the vadose zone are often still prohibitively expensive in terms of computational resources. To overcome this problem, Seo et al. (2007) developed a computationally efficient one-dimensional unsaturated flow HYDRUS package and linked it to the three-dimensional modular finite-difference ground water model MODFLOW-2000 (Harbaugh et al. 2000). The HYDRUS unsaturated flow package used HYDRUS-1D to simulate one-dimensional vertical variably-saturated flow. MODFLOW zone arrays were used to define the cells to which the HYDRUS package was applied. MODFLOW used the time-averaged flux from the bottom of the unsaturated zone as recharge, and calculated a water table depth which was then used as a pressure head bottom boundary for HYDRUS. Twarakavi et al. (2008) provided a comparison of the HYDRUS package to other MODFLOW packages that evaluate processes in the vadose zone and presented a field application demonstrating the functionality of the package.

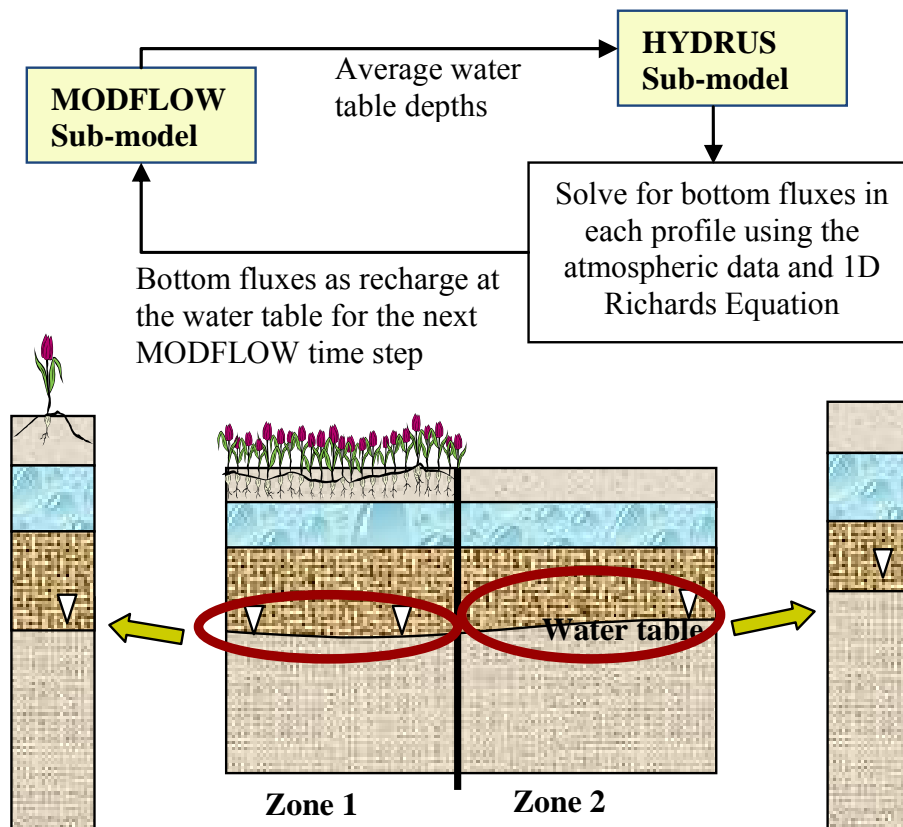


Figure 6. Schematic description of the coupling procedure for water flow in HYDRUS package for MODFLOW.

5 CONCLUSIONS

Over the last 15 years the close collaboration between the University of California Riverside, and the U.S. Salinity Laboratory, and more recently with PC-Progress in Prague, Czech Republic, and SCK•CEN, Mol, Belgium, resulted in the development of a large number of computer tools that are currently being used worldwide for a variety of applications involving the vadose zone. The need for codes such as HYDRUS is reflected by the frequency of downloading from the HYDRUS web site. For example, HYDRUS-1D was downloaded more than 200 times in March of 2007 by users from 30 different countries, and over one thousand times in 2006. The HYDRUS web site receives on average some 700 individual visitors each day. We hope that the HYDRUS family of models will remain as popular in the future as it is now.

REFERENCES

- Bradford, S. A., S. R. Yates, M. Bettehar, and J. Šimůnek, Physical factors affecting the transport and fate of colloids in saturated porous media, *Water Resour. Res.*, 38(12), 1327, doi:10.1029/2002WR001340, 63.1-63.12, 2002.
- Durner, W., Hydraulic conductivity estimation for soils with heterogeneous pore structure, *Water Resour. Res.*, 32(9), 211-223, 1994.
- Fayer, M. J. UNSAT-H version 3.0: Unsaturated soil water and heat flow model, theory, user manual, and examples, *Rep. 13249*, Pacific Northwest National Laboratory, Richland, Washington, 2000.
- Food and Agriculture Organization of the United Nations, Expert consultation on revision of FAO methodologies for crop water requirements, *ANNEX V*, FAO Penman-Monteith Formula, Rome Italy, 1990.
- Gerke, H. H., & van Genuchten, M. Th., A dual-porosity model for simulating the preferential movement of water and solutes in structured porous media, *Water Resour. Res.* 29, 305-319, 1993.

- Harbaugh, A.W., E. R., Banta, M. C. Hill, and M. G. McDonald, MODFLOW-2000, the U.S. Geological Survey modular ground-water model user guide to modularization concepts and the ground-water flow process, Denver, CO, Reston, VA, U.S. Geological Survey, 2000.
- Hardelauf, H., M. Javaux, M. Herbst, S. Gottschalk, R. Kasteel, J. Vanderborgh, and H. Vereecken, PARSWMS: a parallelized model for simulating 3-D water flow and solute transport in variably saturated soils, *Vadose Zone Journal*, 6(2), 255-259, 2007.
- Jacques, D., and J. Šimůnek, User Manual of the Multicomponent Variably-Saturated Flow and Transport Model HP1, Description, Verification and Examples, Version 1.0, *SCK•CEN-BLG-998*, Waste and Disposal, SCK•CEN, Mol, Belgium, 79 pp., 2005.
- Jacques, D., J. Šimůnek, D. Mallants, and M. Th. van Genuchten, Operator-splitting errors in coupled reactive transport codes for transient variably saturated flow and contaminant transport in layered soil profiles, *J. Contam. Hydrology*, 88, 197-218, 2006.
- Jacques, D., J. Šimůnek, D. Mallants, and M. Th. van Genuchten, Modeling coupled hydrological and chemical processes in the vadose zone: A case study on long term uranium migration following mineral phosphorus fertilization, *Vadose Zone Journal*, doi:10.2136/VZJ2007.0084, Special Issue "Vadose Zone Modeling", 7(2), 698-711, 2008a.
- Jacques, D., J. Šimůnek, D. Mallants and M. Th. van Genuchten, Modelling coupled water flow, solute transport and geochemical reactions affection heavy metal migration in a Podzol soil, *Geoderma*, 2008b (in press).
- Jensen, D. T., G. H. Hargreaves, B. Temesgen, and R. G. Allen, Computation of Eto under nonideal conditions, *J. Irrig. Drainage*, 123(5), 394-400, 1997.
- Kodešová, R., M. Kočárek, V. Kodeš, J. Šimůnek, and J. Kozák, Impact of soil micromorphological features on water flow and herbicide transport in soils, *Vadose Zone Journal*, Special Issue "Vadose Zone Modeling", doi:10.2136/VZJ2007.0079, Special Issue "Vadose Zone Modeling", 7(2), 798-809, 2008.
- Köhne, J. M., S. Köhne, and J. Šimůnek, Multi-process herbicide transport in structured soil columns: Experiment and model analysis, *J. Contam. Hydrology*, 85, 1-32, 2006.
- Kosugi K., Lognormal distribution model for unsaturated soil hydraulic properties, *Water Resour. Res.*, 32(9), 2697-2703, 1996.
- Langergraber, G. and J. Šimůnek, Modeling variably-saturated water flow and multi-component reactive transport in constructed wetlands, *Vadose Zone Journal*, 4, 924-938, 2005.
- Langergraber, G., and J. Šimůnek, The Multi-component Reactive Transport Module CW2D for Constructed Wetlands for the HYDRUS Software Package, Manual – Version 1.0, *HYDRUS Software Series 2*, Department of Environmental Sciences, University of California Riverside, Riverside, CA, 72 pp., 2006.
- Lenhard, R. J., J. C. Parker, and J. J. Kaluarachchi, Comparing simulated and experimental hysteretic two-phase transient fluid flow phenomena, *Water Resour. Res.*, 27(8), 2113-2124, 1991.
- Parkhurst, D. L., and C. A. J. Appelo, User's guide to PHREEQC (version 2) – A computer program for speciation, batch-reaction, one-dimensional transport, and inverse geochemical calculations, Water Resources Investigation, *Report 99-4259*, Denver, Co, USA, 312 pp, 1999.
- Pot, V., J. Šimůnek, P. Benoit, Y. Coquet, A. Yra, and M.-J. Martínez-Cordón, Impact of rainfall intensity on the transport of two herbicides in undisturbed grassed filter strip soil cores, *J. of Contaminant Hydrology*, 81, 63-88, 2005.
- Saito, H., J. Šimůnek, and B. Mohanty, Numerical analyses of coupled water, vapor and heat transport in the vadose zone, *Vadose Zone Journal*, 5, 784–800, 2006.
- Šejna, M., and J. Šimůnek, HYDRUS (2D/3D): Graphical User Interface for the HYDRUS Software Package Simulating Two- and Three-Dimensional Movement of Water, Heat, and Multiple Solutes in Variably-Saturated Media, published online at www-pc-progress.cz, PC-Progress, Prague, Czech Republic, 2007.
- Seo, H. S., J. Šimůnek, and E. P. Poeter, Documentation of the HYDRUS Package for MODFLOW-2000, the U.S. Geological Survey Modular Ground-Water Model, *GWMI 2007-01*, International Ground Water Modeling Center, Colorado School of Mines, Golden, Colorado, 96 pp., 2007.
- Šimůnek, J., K. Huang, and M. Th. van Genuchten, The SWMS_3D code for simulating water flow and solute transport in three-dimensional variably saturated media. Version 1.0, *Research Report No. 139*, U.S. Salinity Laboratory, USDA, ARS, Riverside, California, 155 pp., 1995.
- Šimůnek, J., M. Šejna, and M. Th. van Genuchten, The HYDRUS-2D software package for simulating two-dimensional movement of water, heat, and multiple solutes in variably saturated media. Version 2.0, *IGWMC - TPS - 53*, International Ground Water Modeling Center, Colorado School of Mines, Golden, Colorado, 251 pp., 1999.
- Šimůnek, J., N. J. Jarvis, M. Th. van Genuchten, and A. Gärdenäs, Review and comparison of models for describing non-equilibrium and preferential flow and transport in the vadose zone, *Journal of Hydrology*, 272, 14-35, 2003.

- Šimůnek, J., M. Th. van Genuchten, and M. Šejna, The HYDRUS-1D software package for simulating the one-dimensional movement of water, heat, and multiple solutes in variably-saturated media. Version 3.0, *HYDRUS Software Series 1*, Department of Environmental Sciences, University of California Riverside, Riverside, CA, 270 pp., 2005.
- Šimůnek, J., M. Th. van Genuchten, and M. Šejna, The HYDRUS Software Package for Simulating Two- and Three-Dimensional Movement of Water, Heat, and Multiple Solutes in Variably-Saturated Media, Technical Manual, Version 1.0, PC Progress, Prague, Czech Republic, pp. 241, 2006.
- Šimůnek, J., D. Jacques, M. Th. van Genuchten, and D. Mallants. Multicomponent geochemical transport modeling using the HYDRUS computer software packages, *J. Am. Water Resour. Assoc.*, 42(6), 1537-1547, 2006b.
- Šimůnek, J. and R. Kodešová (eds.), *Proc. of The Second HYDRUS Workshop*, March 28, 2008, ISBN: 978-80-213-1783-3, Dept. of Soil Science and Geology, Czech University of Life Sciences, Prague, Czech Republic, pp. 105, 2008.
- Šimůnek, J., M. Šejna, H. Saito, M. Sakai, and M. Th. van Genuchten, The HYDRUS-1D Software Package for Simulating the Movement of Water, Heat, and Multiple Solutes in Variably Saturated Media, Version 4.0, *HYDRUS Software Series 3*, Department of Environmental Sciences, University of California Riverside, Riverside, California, USA, pp. 315, 2008a.
- Šimůnek, J., M. Th. van Genuchten, and M. Šejna, Development and applications of the HYDRUS and STANMOD software packages, and related codes, *Vadose Zone Journal*, doi:10.2136/VZJ2007.0077, Special Issue "Vadose Zone Modeling", 7(2), 587-600, 2008b.
- Šimůnek, J. and M. Th. van Genuchten, Modeling nonequilibrium flow and transport with HYDRUS, *Vadose Zone Journal*, doi:10.2136/VZJ2007.0074, Special Issue "Vadose Zone Modeling", 7(2), 782-797, 2008c.
- Torkzaban, S. and S. M. Hassanizadeh (eds.), *Proc. of Workshop on HYDRUS Applications*, October 19, 2005, Department of Earth Sciences, Utrecht University, The Netherlands, ISBN 90-39341125, pp. 94, 2005.
- Twarakavi, N. K. C., J. Šimůnek, and H. S. Seo, Evaluating interactions between groundwater and vadose zone using HYDRUS-based flow package for MODFLOW, *Vadose Zone J.*, doi:10.2136/VZJ2007.0082, Special Issue "Vadose Zone Modeling", 7(2), 757-768, 2008.
- Vrugt, J. A., J. W. Hopmans, and J. Šimůnek, Calibration of a two-dimensional root water uptake model, *Soil Sci. Soc. Am. J.*, 65(4), 1027-1037, 2001a.
- Vrugt, J.A., M. T. van Wijk, J. W. Hopmans, and J. Šimůnek, One-, two-, and three-dimensional root water uptake functions for transient modeling, *Water Resour. Res.*, 37(10), 2457-2470, 200b.

Water and heat flow in a directionally frozen silty soil

K. Watanabe

Graduate School of Bioresources, Mie University, 1577 Kurima-Machiya, Tsu 514-8507, Japan

ABSTRACT: Directional freezing experiments on silty soil were carried out. The water and heat flows were calculated using the modified version of the HYDRUS-1D code, which includes a soil freezing model. In this model, the liquid water pressure at subzero temperatures was determined using temperatures, and the liquid (unfrozen) water content was estimated from soil water characteristic (retention curve) at room temperature. Unfrozen water content profiles can be simulated when proper temperature profiles are calculated. The model can also simulate water flow from the unfrozen region to the freezing front and the moisture profile in the unfrozen region. The calculated ice content roughly agreed with the column experiment when an impedance factor for the hydraulic conductivity was adjusted. However, water flow in the frozen region was not obtained since the impedance factor reduced the hydraulic conductivity too much. Better estimation of the hydraulic conductivity of frozen soils will be needed in future.

1 INTRODUCTION

In soil, some water remains unfrozen at subzero temperatures and the amount of unfrozen water decreases with the temperature. The relationship between the amount of unfrozen water, θ_l , and temperature, T , is called the soil freezing curve (SFC). Understanding how unfrozen water flows through frozen ground is important in investigations of water and solute redistribution (Baker & Spaans, 1997), soil microbial activity (Watanabe & Ito, 2008), mechanical stability and frost heaving (Wettlaufer & Worster, 2006), waste disposal (McCauley *et al.*, 2002), and climate change in permafrost areas (Lopez, 2007). To simulate the unfrozen water flow in unsaturated frozen soils, it is necessary to know not only how to express the hydraulic and thermal conductivities of the frozen soil but also how to determine its soil retention curve (soil water characteristics SWC; relationship between θ_l and the pressure head, h) and the SFC.

Williams (1964) and Koopmans & Miller (1966) measured the SFC and SWC of the same soils under freezing and drying processes and found a unique relationship between the negative temperature at which a given unfrozen water content occurs and the suction, corresponding to a similar moisture content at room temperature. Harlan (1973) derived the SFC from SWC using this relationship and analyzed the coupled heat and water flow in partially frozen soil numerically. In the Harlan's simulation, the unsaturated hydraulic conductivity of soil at room temperature was also applied to that of frozen soil, assuming the same pore water geometry for frozen and unfrozen soils. However, numerical simulations have suggested that this assumption overestimates water flow near the freezing front (Harlan, 1973; Taylor & Luthin, 1974; Jame & Norum, 1980). When the soil is frozen, the presence of ice in some pores may block water flow. To account for this blocking, several impedance factors have been introduced (*e.g.*, Jame & Norum, 1980; Lundin, 1990; Smirnova *et al.*, 2000). However, Black & Hardenberg (1991) criticized the use of an impedance factor, stating that it is a potent and wholly arbitrary correction function for determining the hydraulic conductivity of frozen soils. Newman & Wilson (1997) also concluded that an impedance factor is unnecessary when an accurate SWC and the relationship between hydraulic conductivity and water pressure are defined.

Harlan's concept and the impedance factor have been improved in several numerical studies (e.g., Flerchinger & Saxton, 1989; Zhao *et al.*, 1997; Stähli *et al.*, 1999). Hansson *et al.* (2004) also included these models in the HYDRUS-1D code and analyzed both laboratory and field soil-freezing experiments. In this study, we performed a laboratory directional freezing experiment of unsaturated silty soil and simulated movement of water and heat in the soil using the modified HYDRUS-1D code to verify the models with the impedance factor and to estimate the thermal and hydraulic conductivity of the frozen soil.

2 SOIL FREEZING MODEL

2.1 Water and heat flow equations

Assuming that vapor and ice flows are negligible, variably saturated water flow in above-freezing and subzero soil is described using a modified Richards' equation as follows (e.g., Noborio *et al.*, 1996; Hansson *et al.*, 2004):

$$\frac{\partial \theta_i(h)}{\partial t} + \frac{\rho_i}{\rho_l} \frac{\partial \theta_i(T)}{\partial t} = \frac{\partial}{\partial z} \left(K_h \frac{\partial h}{\partial z} + K_h + K_T \frac{\partial T}{\partial z} \right) \quad (1)$$

where θ_i is the volumetric ice content, t is time, z is the spatial coordinate, ρ_i is the density of ice, and K_h and K_T are the hydraulic conductivities of the flow due to a pressure head gradient and due to a temperature gradient, respectively. When ice is formed in soil pores, it releases latent heat, L_f , and the heat transport is described as follows:

$$C_p \frac{\partial T}{\partial t} - L_f \rho_i \frac{\partial \theta_i}{\partial t} = \frac{\partial}{\partial z} \left(\lambda \frac{\partial T}{\partial z} \right) - C_l q_l \frac{\partial T}{\partial z} \quad (2)$$

where C_p and C_l are the volumetric heat capacity of the soil particles and liquid water, respectively, λ is the thermal conductivity, and q_l is the liquid water flux. The left-hand side of equation (2) can be rewritten using the apparent volumetric heat capacity, C_a .

$$\left(C_p - L_f \rho_i \frac{\partial \theta_i}{\partial T} \right) \frac{\partial T}{\partial t} = \left(C_p + L_f \rho_i \frac{\partial \theta_i}{\partial T} \right) \frac{\partial T}{\partial t} = C_a \frac{\partial T}{\partial t} \quad (3)$$

Equations (1) and (2) are a tightly coupled duet due to their mutual dependence of the water content, pressure head, and temperature, and can be solved when the SWC and SFC are available.

2.2 Soil water pressure in a frozen soil

When ice and liquid water coexist, a state equation of phase equilibrium, known as a generalized form of the Clausius-Clapeyron equation (GCCE), arises.

$$v_l \frac{dP_l}{dT} - v_i \frac{dP_i}{dT} = \frac{L_f}{T} \quad (4)$$

where P_l and P_i are the liquid water and ice pressures, and v_l and v_i are the specific volumes of liquid water and ice, respectively. Assuming that GCCE is also valid in frozen soil with $P_l = \rho g h$ and $P_i = 0$, the matric potential of unfrozen water in frozen soil at an equilibrium state can be estimated from the temperature:

$$h = \frac{L_f}{g} \ln \frac{T}{T_m} \quad (5)$$

where T_m is the freezing temperature of bulk water in Kelvin.

When the soil pores illustrated in Figure 1a are filled with solute-free water and cooled below 0°C, water near the centers of the pores freezes easily, whereas water near the soil particles and at the corners among particles tends to remain in a liquid state due to the decrease in free energy resulting from surface and capillary forces. Further lowering of the temperature induces more ice formation, resulting in a decrease in the unfrozen water thickness with decreasing tempera-

ture. Williams (1964) and Koopmans & Miller (1966) regarded unfrozen water in freezing soil as having the same geometry as water in drying unsaturated soils (Fig. 1b), and assumed the same pressure difference between unfrozen water-ice interfaces and water-air interfaces. Under these assumptions, frozen soil at an h corresponding to the T from equation (5) contains the same amount of liquid water as unfrozen unsaturated soil at h ; that is the SFC can be estimated from the SWC. Furthermore, the slope of the SFC appearing in equation (3) is derived from the slope of SWC through GCCE:

$$\frac{d\theta_l}{dT} = \frac{d\theta_l}{dh} \frac{dh}{dT} = \frac{\rho g L_f}{v_w T} \frac{d\theta_l}{dh} \quad (6)$$

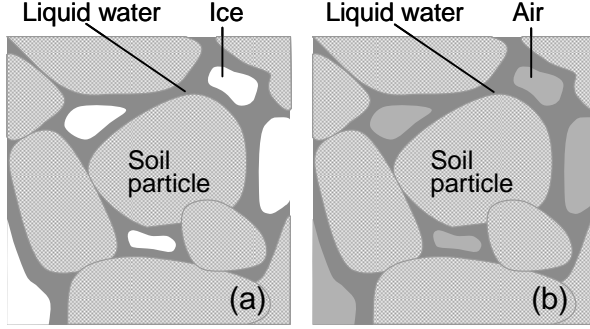


Fig. 1 Schematic illustration of liquid water geometry in soil pores: (a) freezing with the ice-liquid water interface in a saturated soil; (b) drying with the air-liquid water interface under room temperature.

2.3 Hydraulic and thermal properties

The water retention curve (SWC) and hydraulic conductivity, K_h , of unsaturated soil at room temperature are sometimes expressed using a formula proposed by Mualem (1976) and van Genuchten (1980):

$$S_e = \frac{\theta(h) - \theta_r}{\theta_s - \theta_r} = \left(1 + |\alpha h|^n\right)^{-m} \quad (7)$$

$$K_h = K_s S_e^l \left[1 - \left(1 - S_e^{1/m}\right)^m\right]^2 \quad (8)$$

where S_e is the effective saturation, θ_s and θ_r are the saturated and residual water content, respectively, K_s is the saturated hydraulic conductivity, and α , n , m , and l are empirical parameters. The soil water pressure at -1°C is estimated as $-12,500$ cm from equation (5), indicating that a SWC model that can express a relatively low pressure region is preferable for simulating frozen soil. For this purpose, in this study, we use the following equation, derived by Durner (1994), which combines two van Genuchten equations (7) using a weighting factor w :

$$S_e = w_1 \left[1 + (\alpha_1 h)^{n_1}\right]^{-m_1} + w_2 \left[1 + (\alpha_2 h)^{n_2}\right]^{-m_2} \quad (9)$$

$$K_h = K_s \frac{\left(w_1 S_{e1} + w_2 S_{e2}\right)^l \left(w_1 \alpha_1 \left[1 - \left(1 - S_{e1}^{1/m_1}\right)^{m_1}\right] + w_2 \alpha_2 \left[1 - \left(1 - S_{e2}^{1/m_2}\right)^{m_2}\right]\right)^2}{\left(w_1 \alpha_1 + w_2 \alpha_2\right)^2} \quad (10)$$

The hydraulic conductivity K_T for liquid water flow due to a temperature gradient is defined as (e.g., Hansson *et al.*, 2004):

$$K_T = K_{th} \left(hG \frac{1}{\gamma_0} \frac{d\gamma}{dT}\right) \quad (11)$$

where G is the enhanced factor, γ is the surface tension, and γ_0 is the tension at 25°C. If we assume the same liquid water geometry as shown in Figure 1, it is thought that the decrease in hydraulic conductivity of frozen soil with decreasing unfrozen water is also estimated by equation (8). However, several studies have reported that the use of the unsaturated hydraulic conductivity for unfrozen soil for frozen soil overestimates the water flow in frozen soil (*e.g.*, Jame & Norum, 1980; Lundin, 1990). Therefore, in this study, we invoke a modification of equation (8) using an impedance factor, Ω :

$$K_{fh} = 10^{-\Omega\theta_i/\phi} K_h \quad (12)$$

where ϕ is the porosity and θ_i/ϕ_T is the degree of ice saturation of the soil.

The soil heat capacity, C_p , can be estimated by summing the heat capacity, C , multiplied by the volumetric fraction, θ , of each soil element. With subscripts n , o , a , l , and i , for soil particles, soil organic matter, air, liquid water, and ice, respectively, and assuming that unfrozen water has the same heat capacity as liquid water at room temperature:

$$C_p = \theta_n C_n + \theta_o C_o + \theta_a C_{air} + \theta_l C_l + \theta_i C_i \quad (13)$$

Campbell (1985) introduced the relationship between the amount of liquid water and the thermal conductivity of soils, and Hansson *et al.* (2004) expanded this model to frozen soils by using the ice fraction parameter, F ,

$$\lambda = C_1 + C_2(\theta + F\theta_i) - (C_1 - C_4) \exp\left\{-[C_3(\theta + F\theta_i)]^{C_5}\right\} \quad (14)$$

$$F = 1 + F_1\theta_i^{F_2} \quad (15)$$

where C_1 ... C_5 , F_1 , and F_2 are empirical parameters.

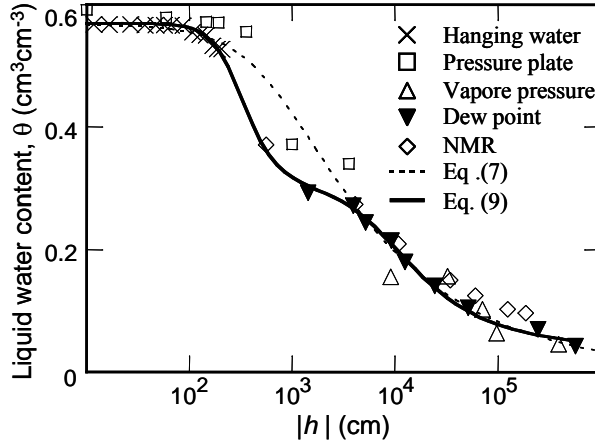


Fig. 2 Soil water characteristics of Fujinomori silt.

3 COLUMN FREEZING EXPERIMENT

3.1 Material and Methods

The samples used in this study consisted of Fujinomori silt, which is highly susceptible to frost and retains much liquid water, even when $T < -1^\circ\text{C}$. Figure 2 shows the SWC measured using several physical methods. Silt was mixed with water at $\theta = 0.4$ and packed at a bulk density of 1.18 into an acrylic column with an internal diameter of 7.8 cm and a height of 35 cm. Fifteen copper-constantan thermocouples and seven time domain reflectometry (TDR) probes were inserted into each column, and the side wall of the column was insulated. The TDR probes were initially calibrated for the measured unfrozen water content by comparison with a pulsed nuclear magnetic resonance (NMR) measurement. The column was allowed to settle at an ambient temperature of 2°C for 24 h to establish the initial water and temperature profiles and was then frozen from the upper end by controlling the temperature at both ends of the column ($T_L = -8^\circ\text{C}$

and $T_H = 2^\circ\text{C}$). During the experiment, no water flux was allowed from either end, and the profiles of temperature and water content were monitored using the thermocouples and TDR probes. A series of experiments with different durations of freezing was then performed for each freezing condition. At the end of the experimental series, the sample was cut into 2.5-cm sections to measure the total water content using the dry-oven method. The thermocouple and TDR readings confirmed that each column had the same temperature and water profiles during the series of experiments.

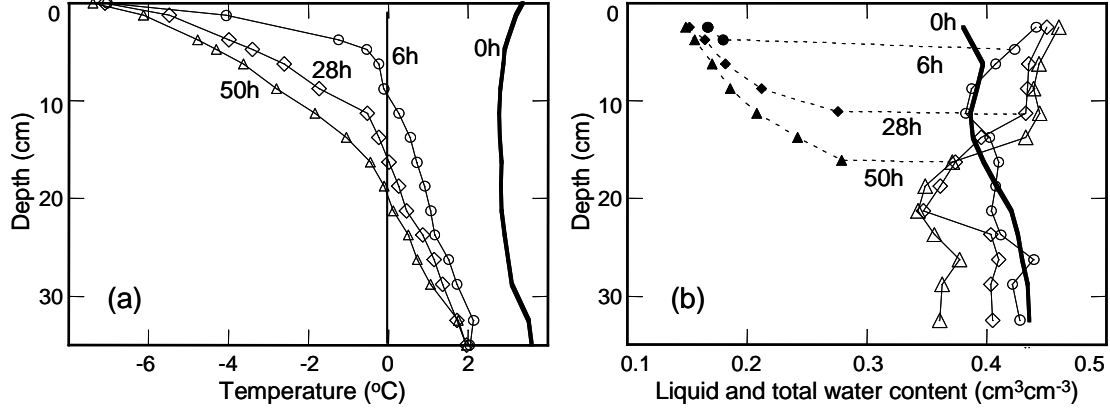


Fig 3. (a) Temperature and (b) moisture profiles measured in the frozen silt column (0, 6, 28, 50 h after freezing started). The solid line and dashed line in moisture profiles represent total water and unfrozen water contents, respectively.

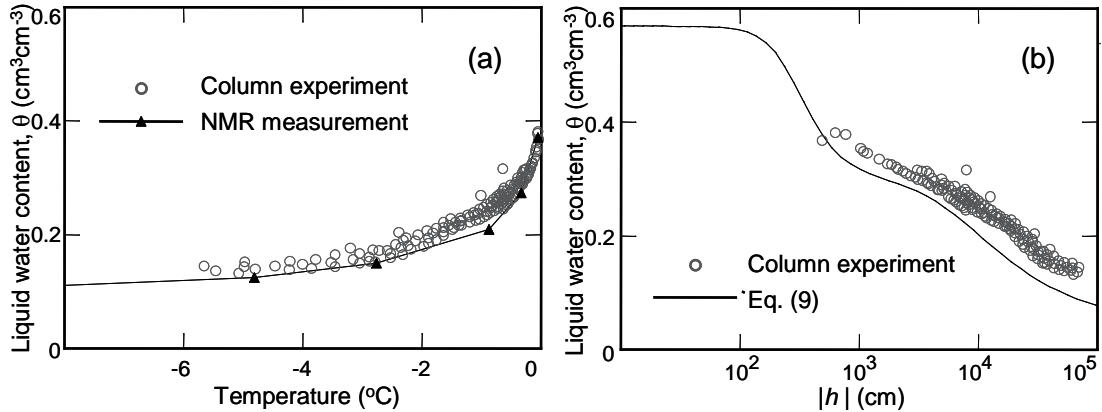


Fig. 4 (a) Soil freezing curve observed during the freezing experiment and measured by pulsed NMR methods under thermal equilibrium condition. (b) Soil water characteristics of Fujinomori silt estimated from (a).

3.2 Experimental results

Figure 3a shows the temperature profile of the freezing silt. When both ends of the column were set at different temperatures, the soil near the column ends reached the required temperatures quickly. The 0°C isotherm advanced at 1.57 , 0.34 , and 0.16 cm h^{-1} for 0–6, 6–24, and 24–48 h, respectively, and lowering of the freezing point by approximately 0.5°C was observed. The changes in the temperature profiles were smaller than expected from the thermal conductivity, implying heat flow from the side wall that prevented soil freezing. Although complete insulation was difficult in the laboratory experiment, the differences in the temperature and the location of the freezing front in soils at the center and near the wall of the column can be estimated within 0.5°C and to less than 1 cm, so we still regard it as directional freezing.

Figure 3b presents water profiles in silt at the same freezing times as shown in Figure 3a. The solid line indicates total water content, θ_T , measured using the dry-oven method, and the dashed line indicates the unfrozen water content, θ_i , measured using TDR. The ice content, θ_i , was obtained by subtracting the unfrozen water from the total water content. The silt had a relatively

vertical initial $\theta_l = \theta_T$ profile, having similar θ_l values for $h < 100$ cm (Fig. 2). An increase in θ_T , decrease in θ_l in the frozen area, and decrease in θ_l in the unfrozen area with the advancing freezing front were observed, implying that the soil water flowed not only through the unfrozen area but also through the frozen area.

Figure 4a shows the amount of unfrozen water measured with TDR during the freezing experiment (SFC). The amount of unfrozen water decreased sharply with temperature, although over $0.1 \text{ cm}^3 \text{ cm}^{-3}$ of water remained as a liquid at -8°C . Figure 4b compares the unfrozen water content as a function of the corresponding pressure based on equation (5) with the fitted SWC as shown in Figure 2. Since the frozen soil characteristics reasonably agreed with the unfrozen SWC well, we confirmed SWC can be applied as the frozen soil characteristics in the numerical simulation.

4 CALCULATIONS

The water and heat flows in the freezing experiment were simulated using a modified version of the HYDRUS-1D code. The measured temperature and water content (0 h in Fig. 3) in the 35-cm vertical silt column were given as the initial conditions. No water flux and a constant temperature ($T_{\text{top}} = -8^\circ\text{C}$ and $T_{\text{bottom}} = 2^\circ\text{C}$) were applied at both ends of the silt column for 48 h. No solute effect was considered in this simulation. Table 1 lists the hydraulic and thermal parameters used. From the fitted SWC (Figs. 2 and 4b) and measured saturated hydraulic conductivity, l in equation (10) was estimated with comparison to data from Watanabe & Wake (2008). The thermal conductivity of the frozen silt at different temperatures was first measured in the laboratory and the thermal parameters were estimated.

Table 1. Hydraulic and thermal parameter values for silt

θ_s	θ_r	α_1	n_1	α_2	n_2	w_2	K_s	l	θ_n	θ_o	C_1	C_2	C_3	C_4	F_1	F_2
m^3m^{-3}	m^3m^{-3}	m^{-1}		m^{-1}			m d^{-1}		m^3m^{-3}	m^3m^{-3}						
0.57	0.06	0.35	3.1	0.011	1.7	0.461	0.06	-0.08	0.55	0	0.72	0.84	8.38	0.093	13	1

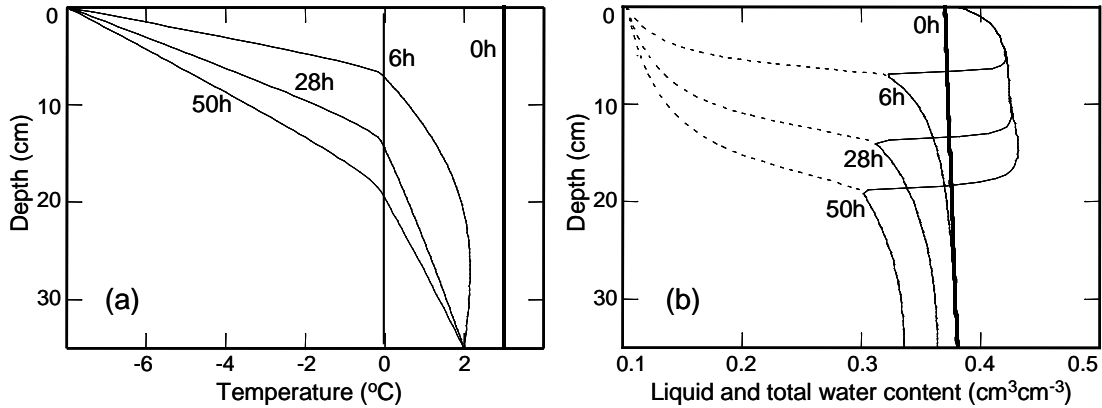


Fig. 5 Profiles of (a) temperature and (b) moisture in a directionally frozen silt calculated by using HYDRUS-1D code. The solid line and dashed line in moisture profiles represent total water and unfrozen water contents, respectively.

The calculated freezing rate underestimated the measured rate, since the heat flow from the side wall was not negligible in the laboratory experiment. Heat outflow through the wall causes quicker freezing than under fully insulated conditions, while inflow results in slower freezing. The calculated temperature profiles became congruent with the measured profiles (Fig. 5a) when the apparent thermal conductivity slightly larger than that obtained from the parameters in Table 1 was applied.

Figure 5b shows the water profile at this temperature profile. This model simulated the amounts of liquid water in both the frozen and unfrozen regions well, although the total amount of water in the frozen region was highly dependent on the impedance factor Ω (Fig. 6a). There

was a one-to-one relationship between temperature and the pressure of the unfrozen water in the frozen region. Therefore, the profile of the unfrozen water can be determined from the temperature profile directly, if the SFC is equivalent to the SWC. In other words, a reasonable unfrozen water profile can be obtained when proper temperature profiles are calculated. The water flow into and through the frozen soil appeared as a change in the total amount of water (or ice). When $\Omega = 0$, a huge pressure difference between the frozen and unfrozen regions induced water to flow to the freezing front, and the soil near the freezing front quickly reached ice saturation, so that water could no longer pass through it. Decreasing the hydraulic conductivity of frozen soil using Ω to reduce the water flow near the frozen front resulted in a decrease in the amount of ice near the frozen front; however, Ω cannot be evaluated from any soil properties and needs to be calibrated from the ice profile data itself. Furthermore, equation (12) provides an extremely small hydraulic conductivity for frozen soil according to Ω and the amount of ice (Fig. 6b) regardless of whether the amount of unfrozen water corresponds to the water path, and allows virtually no water flow in the frozen region (Fig. 5b, 6c, d). Further study of the hydraulic conductivity of frozen soil is needed to predict the total amount of water and water flow in frozen soil, which is important for estimating water balance, solute redistribution, gas emission, and snow water infiltration in cold regions.

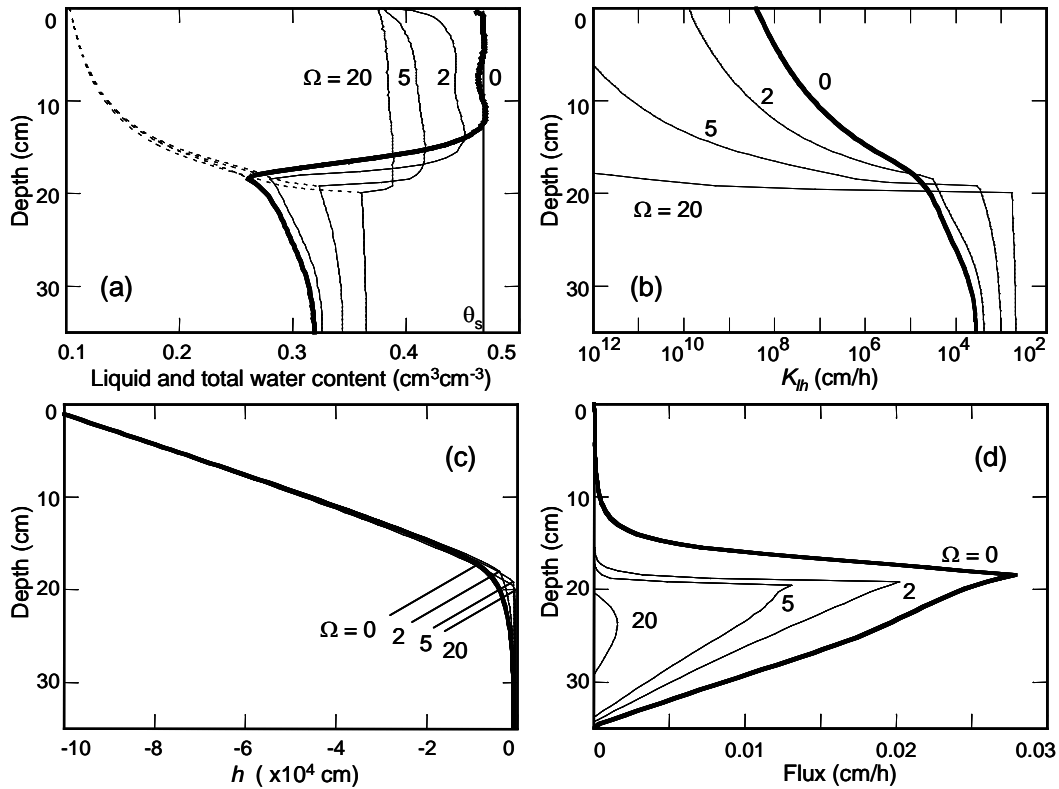


Fig.6 Profiles of (a) moisture, (b) hydraulic conductivity (c) pressure head, and (d) liquid water flux in a silt column which was directionally frozen 50 h, calculating with different impedance factor Ω .

5 SUMMARY

A freezing model for unsaturated frozen soil implemented in HYDRUS-1D could simulate water flow from the unfrozen region to the freezing front and the unfrozen water profile in the frozen region. It is very useful to consider the detailed mechanisms of water and heat flow in unsaturated soil under freezing conditions.

Since the impedance factor for the hydraulic conductivity is given as a function of ice water, it may underestimate the hydraulic conductivity as the ice water content increases. It would be necessary to describe the impedance factor in accordance with the unfrozen liquid water content instead of the ice content. Although the model assumed to reach the phase equilibrium instant-

neously, phase transition from liquid water to ice may take time to reach the equilibrium, and the transition rate would be proportional to the supercooling degree. If these time-dependent ice formations cannot be ignored, it is necessary to take into account for the non-equilibrium effects. As similar to the non-equilibrium flow and transport model, dual porosity or dual permeability formulation, for instance, may be also useful for the freezing model. Furthermore, solute concentration increases near the frozen front because of the solute exclusion, resulting in depression of freezing point of soil water. Future verification of these issues from both experiment and numerical simulation is important to evaluate water balance, solute redistribution, and snow melt infiltration in the frozen soil.

REFERENCES

- Baker, J. M. & Spaans, E. J. A. 1997. Mechanics of meltwater movement above and within frozen soil, Proc. Int. Sym. Physics, Chemistry, and Ecology of Seasonally Frozen Soils. CRREL Special Report, 97–10, pp. 31–36, US Army Cold Regions Research and Engineering Lab (CRREL), New Hampshire.
- Black, P. B. & Hardenberg, M. J. 1991. Historical perspectives in frost heave research, the early works of S. Taber and G. Beskow, CRREL Special Report, 91–23.
- Campbell, G.S. 1985. Soil physics with BASIC, Elsevier, New York.
- Dash, J. G., Fu, H. & Wettlaufer, J. S. The premelting of ice and its environmental consequences, *Rep. Prog. Phys.*, 58, 115–167.
- Durner, W. 1994. Hydraulic conductivity estimation for soils with heterogeneous pore structure. *Water Resour. Res.*, 30(2), 211–223.
- Flerchinger, G. N. & Saxton, K. E. 1989. Simultaneous heat and water model of a freezing snow-residue-soil system: I. Theory and development, *Trans. ASAE*, 32, 565–571.
- Hansson, K., Šimůnek, J., Mizoguchi, M., Lundin, L.-C. & van Genuchten, M. Th. 2004. Water flow and heat transport in frozen soil: Numerical solution and freeze-thaw applications, *Vadose Zone J.*, 3, 693–704.
- Harlan, R. L. 1973. Analysis of coupled heat-fluid transport in partially frozen soil, *Water Resour. Res.*, 9, 1314–1323.
- Jame, Y. W. & Norum, D. I. 1980. Heat and mass transfer in freezing unsaturated porous media, *Water Resour. Res.*, 16, 811–819.
- Koopmans, R. W. R., & Miller, R. D. 1966. Soil freezing and soil water characteristic curves, *Soil Sci. Soc. Am. Proc.*, 30, 680–685.
- Lopez, B. 2007. Cold Scapes, *National Geographic*, 212, 137–151.
- Lundin, L.-C. 1990. Hydraulic properties in an operational model of frozen soil, *J. Hydrolo.*, 118, 289–310.
- McCauley, C. A., White, D. M., Lilly, M. R. & Nyman, D. M. 2002. A comparison of hydraulic conductivities, permeabilities and infiltration rates in frozen and unfrozen soils, *Cold Regions Sci. Tech.*, 34, 117–125.
- Newman, G. P. & Wilson, G. W. 2004. Heat and mass transfer in unsaturated soils during freezing, *Can. Geotech. J.*, 34, 63–70.
- Smirnova, T. G., Brown, J. M., Benjamin, S. G. & Kim, D. 2000. Parameterization of cold-season processes in the MAPS land-surface scheme, *J. Geophys. Res.*, 105, 4077–4086.
- Stähli, M., Jansson, P.-E. & Lundin, L.-C. 1999. Soil moisture redistribution and infiltration in frozen sandy soils, *Water Resour. Res.*, 35, 95–103.
- Taylor, G. S. & Luthin, J. N. 1978. A model for coupled heat and moisture transfer during soil freezing. *Can Geotech. J.*, 15, 548–555.
- Watanabe, K & Ito, M. 2008. In situ observation of the distribution and activity of microorganisms in frozen soil, *Cold Regions Sci. Tech*, doi:10.1016/j.coldregions.2007.12.004.
- Wettlaufer, J. S., & Worster, M. G. 2006. Premelting dynamics, *Annu. Rev. Fluid. Mech.*, 38, 427–452.
- Williams, P. 1964. Unfrozen water content of frozen soil and soil moisture suction, *Geotechnique*, 14, 231–246.
- Zhao, L., Gray, D. M. & Male, D. H. 1997. Numerical analysis of simultaneous heat and mass transfer during infiltration into frozen ground, *J. Hydrol.*, 200, 345–363.

Simulation of fate and transport of pretilachlor in a rice paddy by PCPF-SWMS model

Watanabe Hirozumi¹, Tournebize Julien², Takagi Kazuhiro³, Nishimura Taku⁴

1. *Tokyo University of Agriculture and Technology, 3-5-8, Saiwaicho, Fuchu Tokyo, 183-0052, Japan*

2. *CEMAGREF, Parc de Tourvoie, BP 44, 92163 Antony, France*

3. *National Institute of Agro-Environmental Science, Tsukuba, Ibaraki, 305-8604, Japan*

4. *University of Tokyo, 1-1-1, Yayoi, Bunkyo-ku, Tokyo, 113-8657, Japan*

ABSTRACT: A coupled model that links PCPF-1 and SWMS-2D has been developed. This new coupled model simulates the fate and transport of pesticides in paddy water and paddy soils during the entire crop season from planting to harvest, including the mid term drainage. The monitoring data collected from experimental plots in Tsukuba, Japan, in 1998 and 1999, were used to calibrate hydraulic properties and functioning of the paddy soil. Hydraulic functioning has been additionally evaluated using the tracer (KCl) experiment. The simulation of fate and transport of an herbicide (pretilachlor) in an experimental paddy field was conducted. The tracer and pesticide travel times in the paddy soil were about 30 days after application at a 15-cm depth. A two-phase first-order process simulated well the pretilachlor movement in the paddled layer. Although improvements in predictions of processes in deeper layers are necessary, the PCPF-SWMS model can be a good tool to improve our understanding of mechanisms of degradation, sorption and transport of pretilachlor in paddy soils, and a potential tool for the aquatic risk assessment.

1 INTRODUCTION

In Japan, paddy field system accounts for 55% of total arable land. Consequently, about a half of the total pesticide has been used for rice production in paddy fields and the paddy fields seem to be the major source of the non-point source pollution in Japan. Monitoring of pesticide concentrations in river systems in Japan detected a number of herbicides commonly used in paddy fields, and these herbicides may appear to have adverse effects on the aquatic ecosystem (Inao, et al., 2008). Pesticide fate and transport through paddy soils also affects the risk of aquatic pollution via lateral seepage to the surface water and via vertical percolation to the ground water. Understanding hydraulic pathways and pollutant (nutrient and pesticide) behavior in paddy soil appears to be crucial in the aquatic risk assessment and in defining the specific management practices for controlling non-point source pollution.

Simulation models have been used for the pesticide risk assessment in paddy rice production recently. PADDY (Inao et al., 2001), PCPF-1 (Watanabe and Takagi, 2000; Watanabe et al., 2006), and RICEWQ (Williams et al. 1999) have been used for predicting pesticide concentrations in paddy waters. For pesticide transport in paddy soil, Karpozas et al. (2005) reported a coupled model, RICEWQ-VADOFT, for Italian conditions. However, no such study has been reported for Japanese paddy conditions.

A structurally coupled model PCPF-SWMS for simulating the pesticide fate and transport in paddy fields has been recently developed (Tournebize et al., 2004; 2006). The model combines two selected models, PCPF-1 (Watanabe et al., 2006) for the surface compartment and SWMS-2D (Simunek et al., 1994) for the subsurface soil compartment of the paddy field. The aim of this paper is to present the PCPF-SWMS model and its results for a model application involving the transport of rice herbicide, pretilachlor, in a monitored experimental paddy field in Japan.

2 MATERIALS AND METHODS

2.1 Model description

2.1.1 PCPF-1

PCPF-1 is a lumped parameter model simulating the pesticide fate and transport in two compartments, a paddy water compartment having variable water depths and a 1.0 cm thick conceptual surface paddy soil layer (Watanabe et al., 2006). These two compartments are assumed to be a completely mixed reactor having uniform and unsteady chemical concentrations. The water balance of a puddled rice field is determined by the following components such as irrigation supply, rainfall, surface drainage, evapotranspiration, lateral seepage and vertical percolation. Pesticide concentrations are governed by dissipation processes such as dissolution, volatilization, biochemical and photochemical degradation, sorption and transport via surface run-off, lateral seepage, and percolation under oxidative flooded conditions. A detailed description of the model can be found elsewhere (Watanabe and Takagi, 2000; Watanabe et al., 2006).

2.1.2 SWMS

SWMS_2D is the open source FORTRAN code used in HYDRUS-2D, a Windows-based modeling environment for analysis of water flow and solute transport in variably-saturated porous media (Simunek et al., 1999). The program solves the Richards' equation for saturated-unsaturated water flow and a Fickian-based advection-dispersion equation for solute transport. The solute transport equation includes provisions for linear equilibrium adsorption, zero-order production, and first-order degradation. The governing equations are solved using a Galerkin-type linear finite element scheme. Specifically for pesticides, the degradation processes are modeled using the first-order kinetics and the sorption processes using the water/soil partitioning coefficient (K_d).

2.1.3 PCPF-SWMS modeling

The coupling of the two models is carried out by linking the percolation flux, induced by

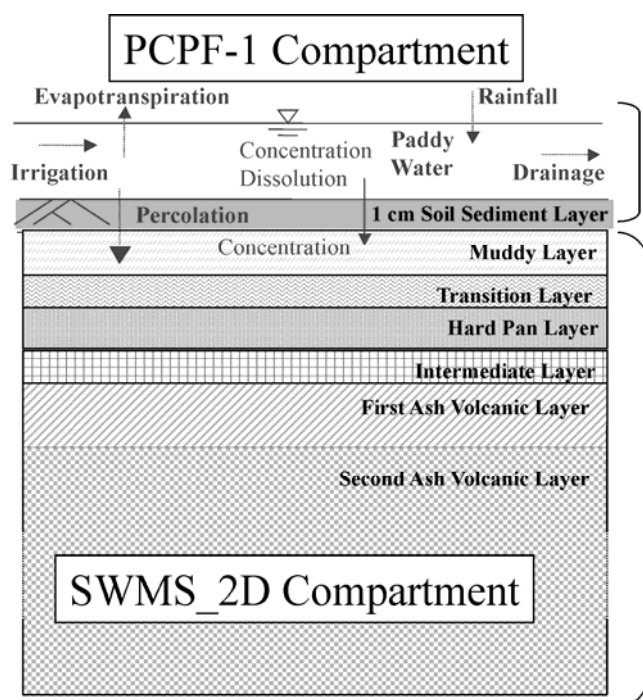


Figure. 1. Conceptual model compartments of PCPF-SWMS simulation (Tournebize et al., 2006).

ponded water depth, and the predicted concentration in the first cm of the surface soil, between a paddy water compartment and a lower paddy soil compartment using PCPF-1 and SWMS-2D. Interactions between these two model compartments for water movement and solute exchange could be summarized as follows: PCPF-1 provides a paddy water depth as the top boundary condition in SWMS-2D (pressure prescribed data) and SWMS-2D determines the vertical percolation, which is an input in the PCPF water balance equation. For the solute transport, PCPF-1 provides the top boundary solute concentration, which, associated with the percolation rate, determines the input solute flux for the SWMS-2D simulation.

A water balance equation was incorporated in the main program of SWMS-2D by calling a new subroutine, PCPF, which is a Fortran version of the PCPF-1 code. The calculation is carried out as follows: a) a daily ponded water depth is imposed as a prescribed pressure head condition in SWMS-2D where the Watflow subroutine then calculates the percolation rate; b) the calculated percolation rate is subsequently used in the water balance equation during the next simulated day. For the solute transport, the boundary concentration (c_{Bnd}) value is replaced by the predicted value from the PCPF subroutine.

The new coupled model PCPF-SWMS is applied in this paper. First, to simulate the flow of water and the transport of chloride and to assess transport parameters, and then, to simulate pesticide fate and transport through the soil profile. PCPF requires daily precipitation (cm), runoff (cm), evapotranspiration (cm) rates during the simulation period. The pesticide properties were determined from experimental soil samples in laboratory studies by Watanabe and Takagi (2000) and Fajardo et al. (2000).

For simulating different agricultural water managements, the full crop season was divided into three periods: a) a continuous water ponding period, b) a midterm drainage period with non-ponding conditions, and c) an intermittent irrigation period with alternative ponding and non-ponding conditions. While the coupled PCPF-SWMS is used to simulate conditions during water ponding, only the SWMS model is used to simulate remaining periods. A detailed modeling procedure is also described by Tournebize et al. (2006).

2.2 Pesticide fate and transport monitoring

Field experiments were conducted at the experimental rice paddy field of the National Institute for Agro-Environmental Sciences (NIAES) in Tsukuba, Japan. The local average annual precipitation and temperature are 1406 mm and 14°C, respectively. The experiments were carried out in 1998 and 1999 in two 9X9 m² plots surrounded by concrete bunds and plastic borders.

The paddy soil preparation usually comprised one or two passes of a rotary tiller about 0.15 to 0.2 m deep before the first irrigation, usually in April or May. After this pre-saturation, the soil is mechanically puddled by one or two passes of a rotary tiller in order to level and prepare the top soil or puddled layer for planting. After a few days, 17 day old rice seedlings (*Oryza sativa* L. cv. Nihonbare) were planted with 16x30cm² spacing on May 8, 1998 and on May 7, 1999. Plots were irrigated and ponded with about 4 cm of water depth until the mid-term drainage. The mid-term drainage, which drains the soil surface to control the root environment during a period from the maximum tillering stage to the panicle formation stage, was carried out for 17 days from July 17, 1998 and for 10 days from July 16, 1999, respectively. During the reproductive stage after the mid-summer drainage, an intermittent irrigation that repeats ponding every few days was performed until one week before harvesting (September 7, 1998, and September 27, 1999).

Six soil horizons were identified in the experimental area. Top three layers, i.e., a puddled layer (0-17 cm), plow sole (17-21 cm) and hard pan layer (21-23 cm) located in the upper part, are considered as an agricultural layer. This was a sandy clay loam (SCL), characterized by a high clay content (between 30 and 40%). The next three horizons were composed by a transitional subsoil clayed layer at 23-50 cm, by a first volcanic ash mixture layer (clay-Kuroboku mixture, Loam CL) at 50-65 cm, and by the original second volcanic ash layer (Kuroboku soil, SiCL) from 65 cm downward. Hydraulic properties, such as the saturated water content, the saturated hydraulic conductivity, van Genuchten parameters for water retention curves, bulk density, and cone penetrometer data were measured in the laboratory on soil core samples.

A commercial preparation of granule herbicides, Hayate® containing 1.5% of pretilachlor and other active ingredients, was applied at a rate of 4968 mg/82m² on the plot on May 12, 1998

and May 14, 1999, respectively. Those dates are used in this paper as referenced times for days after tracer/herbicide application (DATA/DAHA=0). Tracer inputs (KCl) were 1317 and 2633 g, respectively, in 1998 and 1999 for an area of 82.5 m². These amounts provided input chloride tracer concentrations of 256 and 486 mg/l in 1998 and 1999, respectively.

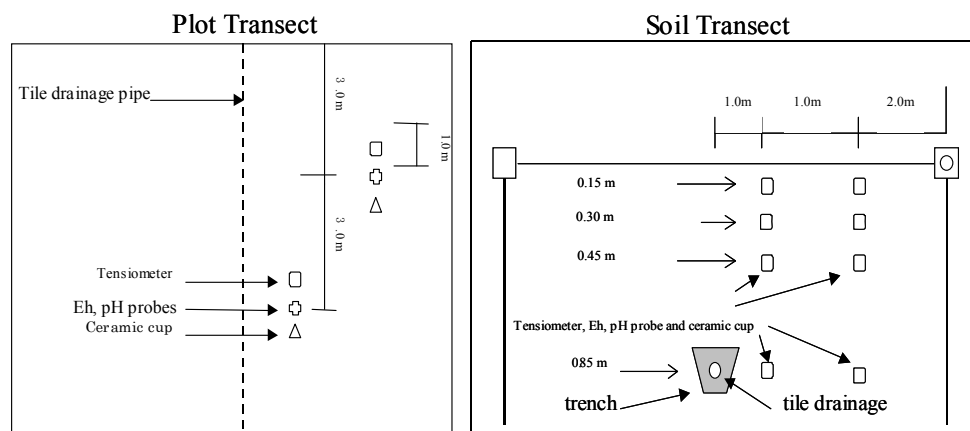


Figure 2. Field setup for tensiometers, Eh, and pH (1 and 3 cm soil depths and paddy water) probes and soil water sampling devices (Tournebize et al., 2004).

For the field monitoring of the pressure head distribution in the soil profile, a water depth sensor and two series of four tensiometers were inserted in the same plot along the soil profile at -15, -30, -45, and -85 cm depths in 1998 and one series of the same tensiometers were installed at -10, -15, -45, and -85 cm depths in 1999 (Figure 2). All data were acquired through data loggers. Data acquisition started after the tracer application (DATA=0), until the mid-term drainage (DATA=66 in 1998 and DATA=63 d in 1999).

Paddy water was sampled every day during the first week, and weekly thereafter until themid-term drainage. In addition, two series of sintered glass porous cups were installed at depths of 15, 30, 45, and 85 cm in 1998 and 15 and 45 cm in 1999 for soil water sampling (Figure 2). The soil water sampling was carried out by applying a vacuum of 500 cm (H₂O) continuously and sampled as weekly average about 500 ml.

For the chloride anion analysis, a TOSOH ion chromatography system equipped with an electric conductivity detector (CM-8020) was used. For the pesticide analysis, pretilachlor was extracted through solid phase C-18 cartridges for water samples and liquid phase (acetone and hexane) for soil samples. The pretilachlor concentration was determined by the gas chromatography with NPD for paddy water and soil, and by LC-MS/MS for soil water samples. Detailed experimental procedures were found in Fajardo et al. (2000) and Watanabe and Takagi (2000).

3 RESULTS AND DISCUSSION

3.1 Soil water regime in paddy field

Table 1 shows soil profile data and model parameters for the simulation of soil water movement in a paddy soil by the SWMS model. Figure 3 shows the evolution of the measured matric potential from day 0 to 63 for 1998. While tensiometer readings were positive and fluctuated with small variations in the top layers of 0–20 cm, they were negative in the subsurface layers. The hydraulic condition during continuous ponding stage was considered as a slow transient state in subsurface layers and depended on initial conditions and the K_S value of the hard pan layer. Comparing monitored values of 1998 and 1999, the inter-seasonal variations were low, indicating a seasonal reproducibility. Measured matric potential values were used to calibrate the model to determine the unknown K_S value during continuous ponding stage (Table 1).

Measured matric potential profiles during the 2 years were compared with predicted values using calibrated soil hydraulic parameters in Figure 4. Simulated and observed pressure head distributions for both years were almost identical during the ponding period. However, a new K_S value had to be assigned to have a better fit of the gradual decline of the matric potential in 1998

after day 40. The shape of the curves in the Figure 4 was similar to the observations reported by Adachi and Sasaki (1999). In the puddled layer, the soil-water pressure heads increased linearly with depth with a slope close to the unit gradient until about 17 cm at the bottom of the puddle layer (Figure 4). This relationship confirmed that the puddled layer did not impose any substantial resistance to water flow (Chen and Liu 2002).

The pressure head started decreasing thereafter. In the layer with more compacted and dense profile, the pressure heads decreased rapidly and became negative from the middle of the hard pan layer, generating a high hydraulic gradient. In the unsaturated zone, the pressure head decreased according to the properties of each layer until the measured value of about $-85 \text{ cm H}_2\text{O}$, which is imposed by the unit gradient bottom boundary condition (Figure 4). This relatively high value of the pressure head for an unsaturated soil corresponded to more than 90% saturation (99% saturation in the transitional layer, 98% saturation in the first ash volcanic layer, and 90% saturation in the second ash volcanic layer). This suggested that as water between soil particles was linked, vertical water movement in this region was dominated by gravitational flow, highlighting the similar potential risk of chemical movement as in the saturated condition.

For the soil water movement in the paddy soil, the percolation rate was directly calculated using Darcy's law in the SWMS code. The simulated percolation rate of the paddy soil profile depended strongly on K_s of the least permeable layer, such as the hard pan layer. The average simulated percolation rate for the period from 1 to 44 d and from 45 to 65 d in 1998 were 0.24 and 0.084 cm d^{-1} , respectively. For the period from 1 to 63 d in 1999, the percolation rate was 0.24 cm d^{-1} . These values were in accordance with the average percolation rate (0.2 cm d^{-1}) in previous studies of Watanabe and Takagi (2000). Comparing obtained results with the single PCPF-1 model, the new coupled model was able to adjust the percolation rate according to the ponded water depth and hydraulic properties.

Table 1. Soil profile data and hydraulic parameters of the experimental plot (Tournebize et al., 2006)

	Layer					
	Muddy	Plow sole	<i>Hard pan calibrated</i>	Transition	1 st Vol-canic Ash	2 nd Vol-canic Ash
Depth (cm)	0-17	17-21	21-23	23-50	50-65	95-135
Texture	SCL	SCL		C	SiL	SiL
Coarse sand 2.0-0.2mm (%)		13.1		5.6	3.7	1.9
Fine sand 0.2-0.02mm (%)	46.7	34.8		29.6	36.2	27.3
Silt 0.02-0.002mm (%)	19.4	21.6		24.4	42.8	51.2
Clay < 0.002mm (%)	33.9	30.5		40.4	17.4	19.6
Total Carbon Content (%)	1.78	1.43		1.29	4.80	8.11
Total N Content (%)	0.16	0.12		0.10	0.31	0.43
pH (H ₂ O)	5.20	6.38		6.54	6.54	5.62
pH (KCl)	4.1	5.10		5.23	5.23	4.83
Bulk Density (kg/m ³)	1.28	1.43		1.36	0.70	0.57
Cône Penetrometer (cm)	12	25		20	17	17
Saturated Water Content (cm ³ .cm ⁻³)		0.438		0.475	0.709	0.717
α (cm ⁻¹)		0.0054		0.0047	0.005	0.0098
n		1.10		1.051	1.068	1.156
Ks measured (standard deviation) (cm.d ⁻¹)	27 (23)	13.2 (5.5)		5.9 (4.3)	11.1 (9.5)	93 (82)
Calibrated Ks (cm.d ⁻¹)	27	13.2	0.08	4	8	10

For the soil water regime after the midterm drainage period, when ponding water was drained, the soil surface was then subjected to natural climatic conditions such as evapotranspiration and precipitation. During the mid term drainage, the simulated soil matric potentials fluctuated according to these conditions. After the midterm drainage period, the matric potential increased as

intermittent irrigation was performed (Figure 3). Changes in the soil structure and soil properties, especially cracks generated during the drying process, were ignored in the simulation.

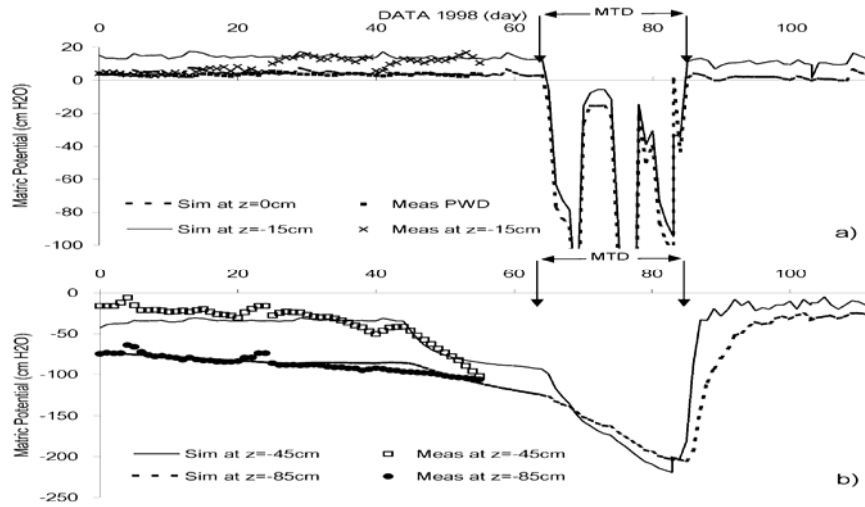


Figure. 3 Measured and simulated matric potentials (at depths of (a) 0, -15 cm and (b) -45 and -85 cm) and ponded water depths (PWD) versus time after the tracer application (DATA), from May 13 to September 3, 1998 (MTD: mid-term drainage) after Tounabize et al., (2006).

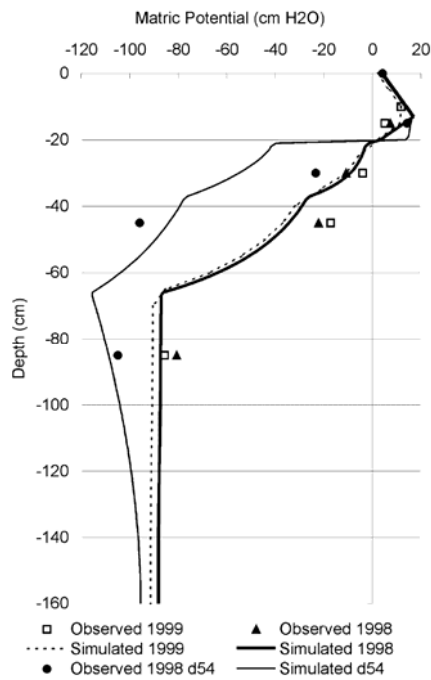


Figure. 4. Measured and simulated matric potential profiles using optimized K_S in 1998 and 1999 during ponding and a new optimized K_S at day 54 (Tounabize et al., 2006).

The peak of the chloride concentration in paddy water was observed immediately after application, followed by a sharp decrease due to dilution and losses from irrigation and runoff during the first 3 days after tracer application. After 10 d, concentrations in paddy water decreased to as low values as those of irrigation water. The maximum concentration at the 15-cm depth occurred during the period of 25–35 d, and was higher in 1999 (52 mg l^{-1}) than in 1998 (23 mg l^{-1}) due to different application rates. Peak amplitudes decreased with depth, due to dilution, dispersion, and partially due to higher background concentrations of 15, 22, and 32 mg l^{-1} at 15, 45 and 85 cm depths, respectively. Because of high background concentrations, the tracer transport phenomena in the soil profile was analyzed using reduced or relative concentrations (Tournebize et al. 2006).

Tracer concentrations were accurately simulated using the PCPF-SWMS model (Figure 5) because of the accurate estimation of the top boundary concentrations that quantify the amount of tracer entering the soil profile. The longitudinal dispersivity coefficient was fitted using the trial and error procedure during the continuous ponding period up to 60 d for 1998. Considering the high variability of the background concentrations in paddy soil water, simulated results with longitudinal dispersivity of 1 cm were considered to be in a good agreement with measured data. The time needed to reach the peak of the tracer concentration at a depth of 15 cm was simulated to be 30 d for both 1998 and 1999, while observed values ranged between 27 and 31 days. At the end of the continuous ponding stage, the simulated tracer front was located between 27 and 29 cm depths.

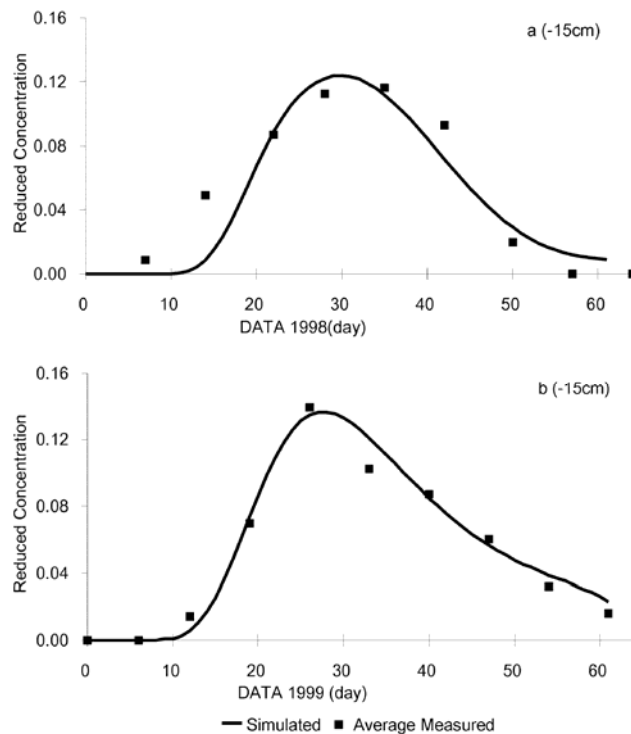


Figure 5. Measured average and simulated concentrations at a depth of 15 cm versus day after the tracer application (DATA) in 1998 (a) and 1999 (b) (Tournebize et al., 2006)

3.2 Fate and transport of pretilachlor

Simulated pretilachlor concentrations in paddy water during the ponding period using PCPF-SWMS model (Figure 6) were again in a good agreement with observations, as well as with those simulated with the PCPF-1 model alone (Watanabe and Takagi, 2000). The maximum ob-

served concentrations were 0.79 mg l^{-1} and 2.51 mg kg^{-1} (dry soil), respectively, for paddy water and the 1-cm thick surface paddy soil layer (Watanabe and Takagi, 2000).

The dissipation of pretilachlor in this field experiment was specifically studied by Fajardo et al. (2000) for paddy soils under laboratory oxidative and reductive conditions. In this simulation, we treated the 1-17 cm puddle layer to be under reductive conditions and the 17-50 cm subsoil layer to be under oxidative conditions. Therefore, the soil partitioning coefficient of 13.0 l kg^{-1} and degradation rate constants reported by Fajardo et al. (2000) were used. In the reductive puddled layer, a two-phase first-order kinetics was considered for the pretilachlor degradation process. The first-order kinetics was applied for the initial 0-21 days with a half-life of 6 days (the degradation rate constant of 0.114 day^{-1}) and for the 22-63 days with a half-life of 23 days (the degradation rate constant of 0.03 days^{-1}).

Observed pretilachlor concentrations at a 15-cm depth in the puddled layer were well simulated with these parameters described above (Figure 7). The observed pretilachlor concentration peaked at 0.043 ng ml^{-1} 29 days after application in the 15-cm puddled layer. The residence time in this layer is evaluated to be about 41 days. Although further evaluation is needed in this simulation, the sensitivity of the soil-water partition coefficient seems to be rather low and degradation rate constant may have more effect on the break through phenomena of pretilachlor.

Below the hard pan layer up to 50 cm of the subsoil layer, pesticide concentrations ranged mostly below 0.02 ng ml^{-1} during the monitoring period. Simulated concentrations underestimated the herbicide concentrations in the earlier period and the simulated peak occurred after about 90 days (Tourné et al., 2004). However observed pretilachlor concentrations at 45 and 85 cm depths ranged between 0.01 and 0.04 ng ml^{-1} without any clear peak during the monitoring period, probably due to residual herbicide concentrations from previous applications in 1996

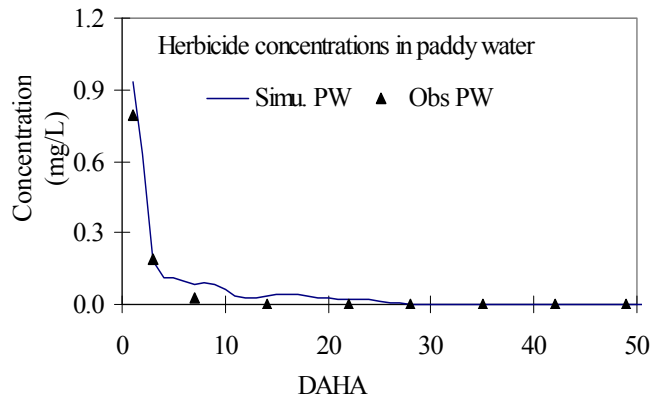


Figure 6. Observed and simulated concentrations of pretilachlor (PTC) in paddy water (PW) in 1998

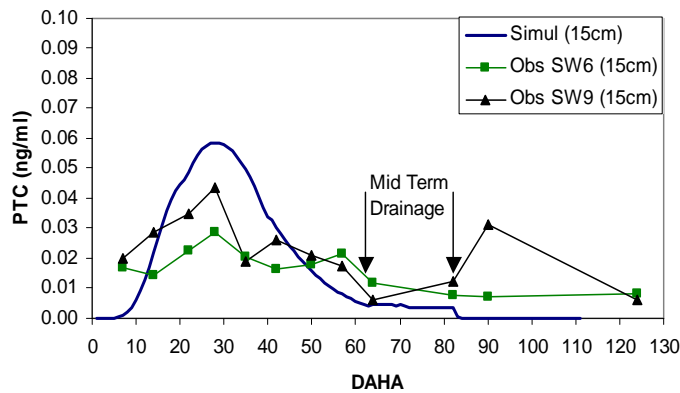


Figure 7. Measured and simulated pretilachlor concentrations in soil water at a 15-cm depth in 1998

and 1997. Simulated pesticide transport below the hardpan layer was considerably less significant and consideration of chemical residues from previous applications is necessary for improving the predictability of the model simulation below the 50-cm depth.

For the pretilachlor mass balance in the paddy field, surface runoff represented 52% of applied pesticide rate. Soil degradation was simulated to be 42% and occurred mainly in the puddled layer. 6% of pretilachlor remained in the soil below the hard pan layer at the end of the crop season (Tournebize et al., 2004).

4 CONCLUSIONS

A lumped parameter model simulating pesticide concentrations in paddy fields, PCPF-1, and a two-dimensional model simulating water flow and solute transport in soils, SWMS-2D, were coupled as a Fortran code PCPF-SWMS. Soil hydraulic and solute transport parameters were calibrated using monitored field data from the Japanese paddy field. An analysis of simulation results for the movement of water and chemical for the entire crop season using fitted parameters provided the following conclusions:

The analysis of the hydraulic functioning of the paddy soil revealed that the hardpan layer was the key factor controlling the percolation rate and tracer transport. PCPF-SWMS simulated the time to the tracer concentration peak at a depth of 15 cm to be 30 d for both 1998 and 1999, while observed values ranged between 27 and 31 days.

The pretilachlor concentrations peaked at 0.043 ng l⁻¹ after 29 days at the 15-cm paddled layer. A two-phase first-order process simulated well the pretilachlor movement in the paddled layer. Although improvements in predictions for the deeper layer are needed, the PCPF-SWMS model can be a good tool to improve our understanding of mechanisms of degradation, sorption and transport of pretilachlor in paddy soils, and a potential tool for the aquatic risk assessment.

ACKNOWLEDGMENTS

This research was funded by the Innovative Technology Research Project in the Ministry of Agriculture, Forestry and Fisheries and partially supported by a Domestic Research Fellowship from Japan Science Technology Corporation and JAPAN- FRANCE integrated action program SAKURA by the Japan Society for the Promotion of Science (JSPS, number 1522) and the Ministère des Affaires Étrangères in France (MAE number 06986).

REFERENCES

- Adachi, K. & Sasaki, C. 1999. Percolation and seepage, In: Miztani M.: Hasegawa S., Koga K., Goto A., Murty V.V.N. (eds) *Advanced paddy field engineering*. JSIDRE, pp 72– 88
- Chen S-K. & Liu CW. (2002) Analysis of water movement in paddy rice fields (I) experimental studies. *J Hydrolo* 260:206–215
- Fajardo, FF., Takagi, K., Iahizaka M., & Usui K. 2000. Pattern and rate of dissipation of pretilachlor and mefenacet in plowlayer and paddy water under lowland field conditions: A Three-year Study. *J. Pesticide Sci.* 25: 94-100.
- Inao, K., Ishii, Y., Kobara, Y., & Kitamura, Y. 2001. Prediction of pesticide behavior in paddy field by water balance on the water management using pesticide paddy field model PADDY. *J. Pestic. Sci.* 26, 229–235.
- Inao, K., Watanabe, H., Karpouzas, D. & Capri, E. 2008. Simulation Models of Pesticide Fate and Transport in Paddy Environment for Ecological Risk Assessment and Management. *Japan Agricultural Research Quarterly* 42(1), 13-21.
- Karpouzas, DG, Ferrero, A., Vidotto F. & Capri E. 2005. Application of the RICEWQ-VADOFT model for simulating the environmental fate of pretilachlor in rice paddies. *Environ Toxicol Chem* 24:1007–1017.
- Šimůnek, J., Vogel T. & van Genuchten, MTh. (1994) The SWMS 2D Code for simulating water flow and solute transport in tow dimensional variably saturated media (Version 1.21). Research Report No. 132. US Salinity Laboratory Agricultural Research Service, US Department of Agriculture, Riverside, California

- Šimůnek, J., Šejna M. & van Genuchten, MTh. (1999) The Hydrus-2D Software Package for Simulating the Two-dimensional Movement of Water, Heat, and Multiple Solutes in Variably Saturated Media, Version 2.0. IGWMC-TPS-70, International Ground Water Modeling Center, Colorado School of Mines, Colorado
- Tournebize, J., Watanabe, H., Takagi, K. & Nishimura, T. 2004. New coupled model of pesticide fate and transport in paddy field, Proceedings of the Conference, Challenges and Opportunities for Sustainable Rice-based Production Systems, Vercelli, Italy, 497-507.
- Tournebize, J., Watanabe, H., Takagi, K. & Nishimura, T. 2006. The development of a coupled model (PCPF-SWMS) to simulate water flow and pollutant transport in Japanese paddy fields, Paddy Water Environment, 4, 39-51.
- Watanabe, H. & Takagi, K. 2000. A simulation model for predicting pesticide concentrations in paddy water and surface soil II. Model validation and application. Environmental Technology 21:1393-1404.
- Watanabe, H., Takagi, K. & Vu, SH. 2006. Simulation of mefenacet concentrations in paddy fields by an improved PCPF-1 model. Pest Manag Sci 62:20–29.
- Williams, W.M., Ritter, A.M., Cheplick, J.M. & Zdinak, CE, 1999. RICEWQ: Pesticide Runoff Model for Rice Crops – User’s Manual and Program Documents Version 1.6.1. Waterborne Environmental Inc., SE Leesburg, VA, USA.

Determination of Irrigation Amounts Using a Numerical Model

H. Fujimaki

Graduate School of Life and Environmental Sciences, University of Tsukuba, 305-8577, Japan

ABSTRACT: A method of decision making of irrigation amount using a numerical model of crop response to irrigation was outlined. To optimize each irrigation amount, a concept of virtual income, which is proportional to increment attained during the irrigation interval is introduced. A numerical model that simulates water, solute, and heat transport and crop response to them is presented and used in a numerical experiment. Results indicated that the optimized irrigation amount can be smaller than the value which attains maximum yield and that simply required to recover to field capacity.

1 INTRODUCTION

Soaring food price and intensified scarcity of water resources bring a new emphasis on efficient use of water in irrigation. The determination of irrigation amount has still widely relied on experience (i.e. fixed amount) or intuition of farmers even in industrialized countries. Such conventional scheme may cause yield reduction or be wasting water. To precisely meet crop water requirement and respond water/salinity stresses quickly, automatic irrigation systems using sensors have been developed and spreading. Such “water stat” systems, however, requires high initial investment and has difficulty in adjusting irrigation amount to weather forecast. For example, it is obviously wasting to apply much water when rain is forecast on next day. But “water stat” systems may do it if currently monitored value reaches its threshold one.

Expensive monitoring using sensors can be altered by numerical simulation of water, solute, and heat transport in soil and crop response to them. High-spec personal computers are getting affordable even for farmers in developing countries, at least for farmers who can afford modern irrigation equipments. Not only monitoring current status, numerical model can predict near future. Numerical prediction requires atmospheric boundary condition: numerical weather forecast. Today, freely accessible numerical weather forecast, whose accuracy is improving, has been provided on the web. These progresses are enabling the optimization of irrigation amounts using numerical weather forecast as input data for numerical models such that net return is maximized.

This paper presents a scheme of the determination of irrigation amounts using numerical weather forecast.

2 METHOD

2.1 *Maximization of virtual net return*

Like other inputs such as labor or fertilizer, the purpose of irrigation is not necessarily to obtain the highest yields, nor water use efficiency, but to maximize the net returns. Irrigation scheduling is the optimization of timing and amount of irrigation. Timing of irrigation is generally restricted to social factors such as rotation or availability of labor. In contrary, irrigator has more

discretion with regard to the amount of irrigation, at least for reducing direction. Thus, let us focus on the optimization of the amount.

If we can calculate net return until the next irrigation, the irrigation amount can be optimized such that it is maximized. Although in reality income is realized when harvest is sold, let us assume that a farmer can obtain virtual income which is proportional to an increment of dry matter attained during an interval. Also, water must be priced high enough to give incentive to save water. Net return, N_r ($\$ a^{-1}$), during a period is then defined as

$$N_r = P_c \epsilon \tau - P_w W - C_{ot} \quad (1)$$

where P_c is the price of crop ($\$ \text{kg}^{-1}\text{DM}$), ϵ is water use efficiency of the crop, τ is cumulative transpiration ($\text{cm} = 10^3 \text{ kg } a^{-1}$), P_w is the price of water ($\$ \text{kg}^{-1}$), W : irrigation amount ($\text{cm} = 10^3 \text{ kg } a^{-1}$), and C_{ot} is the other costs ($\$ a^{-1}$). The amount of valuable part (fruit, grain etc..) of the crop is assumed to be proportional to dry matter production, which is well known to be proportional to cumulative transpiration. Under given conditions, N_r is thus the function of W . The problem is therefore, simple one-dimensional search.

To estimate transpiration amount, τ , which dynamically responds to matric and osmotic potential in soil and therefore, irrigation, a sophisticated model of the response of crop to irrigation is required. Numerical models developed in the realm of soil physics can be such a model.

2.2 Procedure

First, using the records of climatic condition, numerical simulation is performed to estimate the current status. Then, download numerical weather forecast as input data and repeat simulations changing irrigation amount until maximum anticipated N_r is obtained. Then perform irrigation. On the early morning of the next irrigation day, current status is estimated by simulation using the actual records of irrigation amount and climatic condition from the last irrigation till the moment. This cycle continues until the last irrigation.

2.3 Numerical model

Algorithm and user interface described above was incorporated into a numerical model, WASH_1D, which solves governing equations for one-dimensional movement of water, solute and heat in soils with the finite difference method. The one-dimensional maximization was implemented with the golden section method with searching range 0 to 10cm. Governing equation of water flow is Richards equation including water vapor movement. Solute and heat transport are described with the convection-dispersion equation. It can be applied to layered soil, and consider thermal vapor diffusion and hysteresis. Time steps, Δt , are adjusted automatically

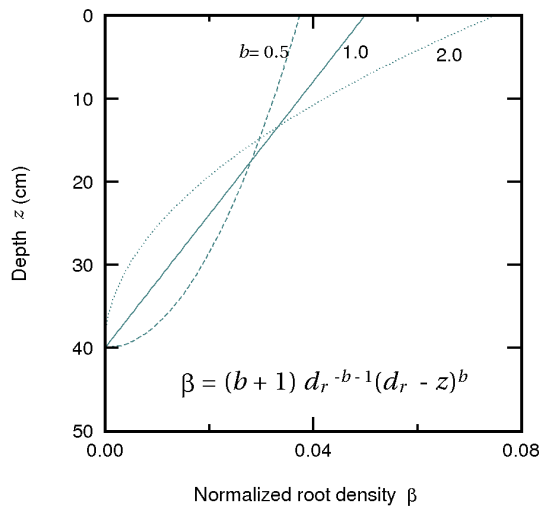


Fig.1 Examples of normalized root density profile

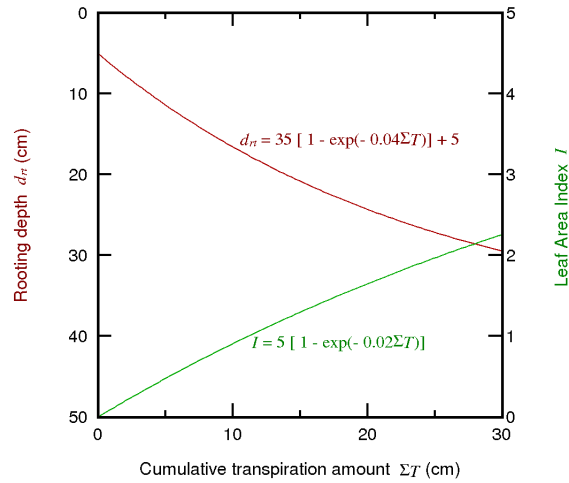


Fig.2 Examples of rooting depth and leaf area index as functions of cumulative transpiration amount

such that at each time step the number of iterations was approximately five and the maximum change in the logarithm of pressure head be less than 0.693 (= ln (2)).

2.4 Root water uptake and crop growth sub-models

The simplest crop growth modeling may be to describe the growth of the each part as a function of cumulative transpiration amount. In WASH_1D, root activity distribution, $\beta(\text{cm}^{-1})$, is given as

$$\beta = (b+1) d_{rt}^{-b-1} (d_{rt} - z)^b \quad (2)$$

where b is plant-specific parameter, d_{rt} is the depth of lower boundary of the root zone(cm), and z is the depth(cm). Figure 1 demonstrates the examples of the distribution. The d_{rt} is described as a function of cumulative transpiration amount, $\Sigma T(\text{cm})$:

$$d_{rt} = a_{drt} [1 - \exp(b_{drt} \Sigma T)] + c_{drt} \quad (3)$$

where a_{drt} , b_{drt} , and c_{drt} are plant-specific parameters. Figure 2 presents the examples.

Leaf area index, I , which affects both radiation and wind, is also handled as a function of ΣT .

$$I = a_{LAI} [1 - \exp(b_{LAI} \Sigma T)] \quad (4)$$

where a_{LAI} , and b_{LAI} are plant-specific parameters.

Transpiration, $T(\text{cm s}^{-1})$, is the integration of root water uptake rate, $S(\text{s}^{-1})$, over the root zone:

$$T = \int_0^{d_{rt}} S dz \quad (5)$$

The S at each depth is given as the product of potential transpiration rate, $T_p(\text{cm s}^{-1})$, β , and reduction coefficients which express the extent of water/salinity stress (Feddes and Raats, 2004).

$$S = T_p \beta \alpha_w \alpha_s \quad (6)$$

where α_w and α_s are the reduction coefficients for water(drought) and salinity, respectively. The T_p is given by multiplying potential evapotranspiration, $E_p(\text{cm s}^{-1})$, from Penman equation by crop coefficient, K_c :

$$T_p = E_p K_c \quad (7)$$

The K_c is also assumed to be a function of ΣT (Fig.3).

$$K_c = a_{kc} [1 - \exp(b_{kc} \Sigma T)] + c_{kc} \quad (8)$$

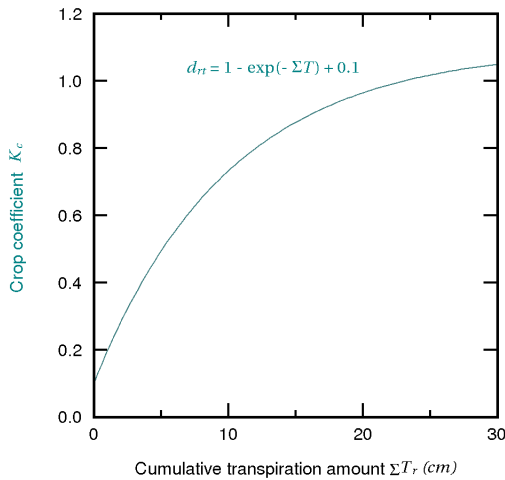


Fig.3 An example of crop coefficient as a function of cumulative transpiration amount

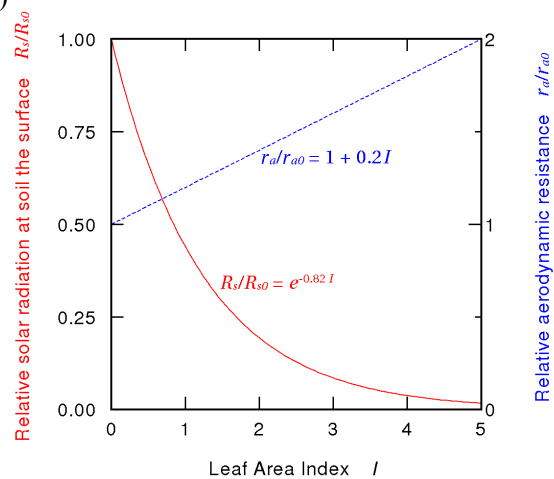


Fig.4 Assumed effects of leaf area on solar radiation and aerodynamic resistance at soil the surface

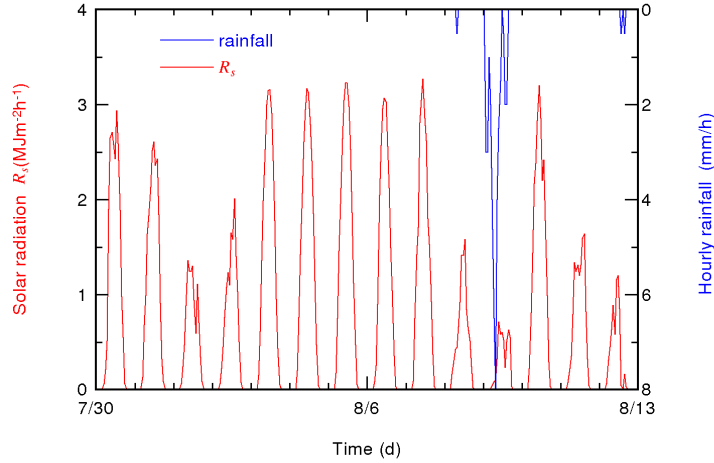


Fig.5 Solar radiation and rainfall during the numerical experiment (Tsukuba, 2006)

where a_{kc} , b_{kc} , and c_{kc} are plant-specific parameters.

The evaporation rate is calculated with the bulk transfer equation (Daamen and Simmonds, 1996; Noborio et al., 1996; Yakirevich et al., 1997):

$$E = \frac{\rho_{vs}^* h_{rs} - \rho_{va}^* h_{ra}}{r_a} \quad (9)$$

where ρ_v^* is the saturated water vapor density (g cm^{-3}), h_r is the relative humidity, r_a is the aerodynamic resistance (s cm^{-1}), and where the subscripts s and a denote the soil surface and air at the reference height, respectively. Since ρ_{vs}^* is a function of surface temperature, heat movement also must be analyzed. The main energy input, solar radiation, is absorbed and reflected by leaves. Such attenuation is commonly described as (e.g, Campbell, 1985)

$$R_s = R_{s0} \exp(-a_{rs} I) \quad (10)$$

where R_{s0} is $R_s (\text{W m}^{-2})$ above canopy and a_{ra} is plant-specific parameter. As crops grow, r_a is increased as leaves restrict water vapor transport. Such an additional resistance is expressed as a function of leaf area index, I :

$$r_a = r_{a0} (1 + a_{ra} I) \quad (11)$$

where r_{a0} is r_a from bare soil surface, and a_{ra} is plant-specific parameter. Figure 4 shows examples of R_s and r_a as functions of I .

3 NUMERICAL EXPERIMENT

3.1 Scenario and conditions

To demonstrate how irrigation amount is determined, numerical experiment was performed. Hypothetical scenario was as follows: On July 29, irrigation with a 1.0 mg cm^{-3} NaCl solution large enough to replace all the soil solution and let the water content became at field capacity on the next day, was carried out. Eight days later (early morning of August 6), the records of climatic condition for the past seven days were downloaded, and numerical simulation is performed to estimate the current status, which is used as the initial condition of prediction. Then, numerical weather forecast for the next seven days was downloaded as input data and simulations were automatically repeated changing irrigation amount until maximum anticipated N_r is obtained.

Meteorological conditions measured at Tsukuba (140E36N), Japan, from July 30 till August 13, 2006(Fig.5). Soil properties of Masa loamy sand and plant specific parameter values shown

in the figures were used in the simulation. Shape factor of root distribution, b , was set at unity. Reduction coefficients, α_w and α_s , were set such that they took 0.5 at -4,000cm. Initial (July 30 0:00) cumulative transpiration amount was set at 10cm. Initial conditions for water and solute movement were assumed to be uniform at -100cm and 1.0 mg cm^{-3} , respectively.

Supposed parameter values in the net return equation are listed in Table 1. Irrigation was started 9:00 of August 6 and irrigation intensity was 1.0 cm h^{-1} , concentration of irrigation water was supposed to be 1.0 mg cm^{-3} .

Table 1. Supposed parameter values in the net return equation.

parameter	value	unit
P_c	2	$\$ \text{ kg}^{-1}$
P_w	0.0001	$\$ \text{ kg}^{-1}$
ϵ	0.001	
C_{ot}	0	$\$$

3.2 Results

Cumulative transpiration amount at 0:00 of August 6 was increased by 0.93 cm. On the other hand, cumulative evaporation during the seven days was 1.7cm. Profiles of water content and solute concentration at 0:00 of August 6 are shown in Figure 6. Solute accumulated near the soil surface. At this moment, the plant was subject to slight water stress and heavy salinity stress in the surface layer. If irrigation was carried out simply to recover to field capacity (i.e. the integration over difference between field capacity and current water content), it would become 2.8cm.

Figure 7 shows net return and cumulative transpiration during the seven days as a function of irrigation amount, W . Both sharply increased with W , but gradients were gradually diminished, and N_r reached the peak at $W = 2.1\text{cm}$, beyond which the N_r decline with W . Note that maximum cumulative transpiration (i.e. yield) is achieved at larger irrigation amount. In this case, 4.2cm rainfall would enable 73% of the maximum N_r , even cancelling irrigation. In contrary, if there were no rain, the optimized irrigation amount would increase to 3.3cm, and N_r at no irrigation would be only 24% of the optimum value as shown in Fig.7.

Figure 6 also shows solute concentration profile at 0:00 of Aug. 13 simulated with the optimum irrigation amount. Although salt in the root zone was leached out by rainfall of Aug. 9, high concentration zone was formed below the root zone. In such case, capillary supply from the deeper layer should not be expected.

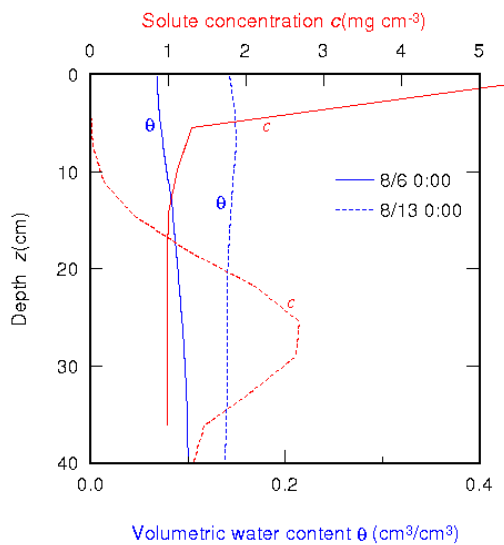


Fig.6 Profiles of water content and solute concentration

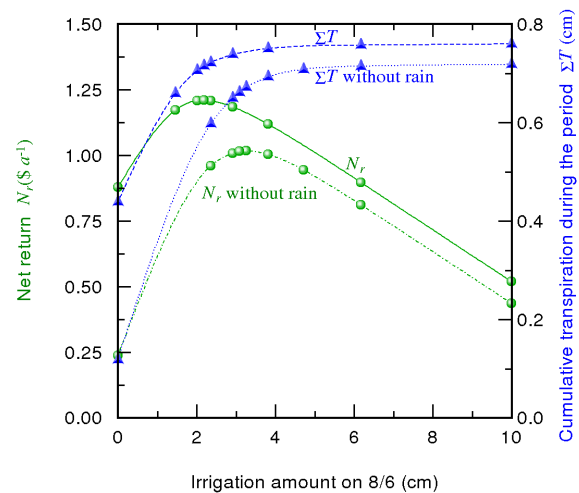


Fig.7 Net return and transpiration amount as functions of irrigation amount

4 CONCLUDING REMARKS

In this paper, a method of decision making of irrigation amount using a numerical model of crop response to irrigation was outlined. Numerical experiment showed encouraging results. Still, all of the employed plant specific parameter values were hypothetical. We are performing an experiment to determine these parameter values and test the effectiveness of this method by comparing with an automatic irrigation system. Whether the integration of short-term maximization gives maximum net return in the entire growing season should also be tested.

WASH_1D is available both for Linux and Windows, and freely distributed under the general public license from <http://www.agbi.tsukuba.ac.jp/~fujimaki/download/en/>

REFERENCES

- Campbell, G. S. 1985. *Soil Physics with Basic*. Elsevier, New York
- Daamen, C. C. and L. Simmonds. 1996. Measurement of evaporation from bare soil and its estimation using surface resistance. *Water Resour. Res.* 32(5): 1393-1402.
- Feddes, R.A., and P.A.C. Raats. 2004. Parameterizing the soil–water–plant root system. p. 95–141. In R.A. Feddes et al. (ed.) *Unsaturated-zone modeling: Progress, challenges, and applications*. Wageningen UR Frontis Ser., Vol. 6. Kluwer Academic, Dordrecht, The Netherlands.
- Noborio, K., K.J. McInnes and J. L. Heilman. 1996. Two-dimensional model for water, heat, and solute transport in furrow-irrigated soil. I. Theory. *Soil Sci. Soc. Am. J.* 60, 1001–1009.
- Yakirevich, A., P. Berliner and S. Sorek. 1997. A model for numerical simulation of evaporation from bare saline soil. *Water. Resour. Res.* 33(5): 1021-1033.

The Study of Diurnal Soil Water Dynamics in Coarse Sand with Modified HYDRUS1D Code

Y. Zeng¹⁾ L. Wan¹⁾, Z. Su²⁾, and H. Saito³⁾

1) School of Water Resources and Environment, China University of Geosciences, Beijing 100083, China

2) International Institute for Geo-information Science and Earth Observation, Enschede 7500 AA, The Netherlands

3) Institute of Symbiotic Science and Technology, Tokyo University of Agriculture & Technology, Fuchu, Tokyo 183-8509, Japan

ABSTRACT: Because of the relatively low soil moisture in arid or semi-arid regions, vapour movement often predominates in the vadose zone and affects the partitioning of energy among various land surface fluxes. In an outdoor sand bunker experiment, the soil water content at 10cm and 30cm depth were measured at hourly intervals for 2.5 days during October 2004. It was found that the soil moisture reached the daily maximum value (5.9%~6.1% at 10cm & 11.9%~13.1% at 30cm) and minimum value (4.4%~4.5% at 10cm & 10.4%~10.8% at 30cm) at midday (0 p.m.~1 p.m. for 10cm & 2 p.m.~3 p.m. for 30cm) and before dawn (2 a.m.~3 a.m. for 10cm & 4 a.m.~5 a.m. for 30cm), respectively. The modified HYDRUS-1D code, which refers to the coupled water, vapour and heat transport in soil, was used to simulate the moisture and vapour flow in the soil. The numerical analyses provided insight into the diurnal movement of liquid water and water vapour driven by the gradients of pressure heads and temperatures in the subsurface zone. The simulated temperature and water content were in good agreement with the measured values. The spatial-temporal distribution of liquid water flux, water vapour flux and soil temperature showed a detailed diurnal pattern of soil water dynamics in relatively coarse sand.

1 INTRODUCTION

Soil moisture in the unsaturated zone near the soil surface plays a critical role in partitioning precipitation into surface runoff, evaporation, and groundwater recharge. Simultaneously, soil moisture affects the conversion of incoming solar and atmospheric radiation into sensible, latent, and radiant heat losses. Along with solar radiation and soil nutrients, the availability of soil moisture is the key to plant growth and to production of crops. As such, soil moisture is not only important to agriculture but may also potentially affect the global climate and is therefore considered as a critical area for global climate change studies (Kerr et al. 2001; Entekhabi et al. 2004).

There are many existing land surface schemes, which provide boundary conditions for global climate models and numerical weather prediction models, estimating exchanges of the fluxes of energy, heat and water vapour between the land surface and the atmosphere (Dickinson et al. 2006). All these schemes are based on parameterizing plot scale sensible heat and moisture transfers in the soil-vegetation-atmosphere system and are scaled up to a model grid using a statistical approach. The treatment of soil moisture processes determines to a large extent the volume of the exchanges in these schemes, which consequently influences other variables in the atmosphere (e.g. clouds and precipitation). The importance of soil moisture has resulted in a very large number of models, which simulate water transport both in the liquid and vapour phase. Most of these models are based on theories that describe the coupled energy and mass flow in soil, considering the microscopic structure of a porous medium (Philip 1957; Philip and De Vries 1957; De Vries 1958; Milly and Eagleson 1980; Milly 1984b). There are also other

models, which are based on the thermodynamics theory of irreversible process, adopted to analyze the transport of heat and mass (Taylor and Stewart 1960; Taylor and Cary 1964; Groenevelt and Kay 1974; Kay and Groenevelt 1974).

The soil moisture variation in arid and semi-arid regions is characterized by vapour transport in the surface soil layer, since liquid water movement could be infinitesimal due to extremely dry soil conditions (Grifoll and Cohen 1999; Salzmann et al. 2000). This dominant vapour transport can result in the conservation of liquid water in the unsaturated zone (Scanlon 1992; Scanlon and Milly 1994); subsequently, it plays an important role in maintaining vegetation and ecosystems in arid or semi-arid areas (Shiklomanov et al. 2004). Moreover, the way of accumulating liquid water from vapour transport has been applied in order to produce fresh drinking water in dry areas by burying perforated pipes in the soil (Hausherr and Ruess 1993; Gustafsson and Lindblom 2001; Lindblom and Nordell 2006).

Due to the importance of soil moisture, many field or laboratory experiments were conducted in order to observe the changes in water content due to vapour transport and subsequently to analyze the soil water dynamics that involve the movement of liquid water, water vapour and heat. In order to verify the numerical model for the coupled flow derived from the thermodynamic theory of irreversible process (Cary and Taylor 1962a b), from 1962 to 1979, Cary and co-workers conducted a number of indoor experiments (Cary 1963, 1964, 1965, 1979). In the same period, Rose published a series of papers (Rose 1963a, b, 1968a, b, 1971) in order to test the theory of coupled transport in porous medium, which was developed by Philip and de Vries (1957). Except for the laboratory experiments, quantitative study of soil moisture transport in the field environment has been conducted by some other investigators, such as: Cary 1966, Jackson 1973, etc. After almost two decades of discussing the aforementioned experiments, the Philips and de Vries model (hereafter, referred to as the PDV model) remains as prominent as ever, even though the contemporary version has been slightly modified. (Milly 1982, 1984a, b; Braud et al. 1995; Shurbaji and Phillips 1995; Milly 1996; Nassar and Horton 1997).

The reason for the wide use of the PDV model is mainly due to the enhancement factor for water vapour transport. There are two postulated mechanisms for enhanced vapour transfer (Philip and De Vries 1957): the first assumption is that the water vapour can flow through the liquid island between solid particles by condensing on one side of the liquid island and subsequently evaporating on the other side; the second postulate considers local temperature gradients in the air-filled pores, which might be significantly higher than the average temperature gradient. According to these assumptions, the humidity of the air adjacent to the water in soil pores, which is determined by the local equilibrium hypothesis, is often substituted for the land surface humidity. However, such substitution is invalid, except for the humid conditions below the evaporation front, which takes place near the surface when the evaporative demand is greater than the ability of the soil to conduct water in the liquid phase and a liquid-vapour phase discontinuity occurs (Asghar 1996; Rose et al. 2005). This invalidation triggers the studies on the changes in soil water content in the topsoil, which includes the parameterization of evaporation from the soil surface (Kondo and Okusa 1990; Kondo et al. 1992; Yamanaka and Yonetani 1999; Konukcu et al. 2004; Gowing et al. 2006) and the exploration of the mechanisms by which water is added to the surface soil layer (Jacobs et al. 1999, 2000; Agam et al. 2004, 2006).

Although the theory of coupled water, vapour and heat transport in soil is widely recognized and thus extensively tested and reinforced, very few studies have demonstrated and evaluated soil water dynamics in time and space, both simultaneously and continuously. The common approach to address this issue is either to analyze the profile soil water and temperature information at specific times (Zhang and Berndtsson 1991; Athavale et al. 1998; Mmolawa and Or 2003; Grifoll et al. 2005; Saito et al. 2006) or to assess the time-series information at specific depths (Kemp et al. 1997; Schelde et al. 1998; Starr and Paltineanu 1998; Wang 2002; Starr and Timlin 2004). In this study, observed soil water content and temperature were used in order to calibrate the performance of the modified HYDRUS-1D code in sand. Then, the modified HYDRUS-1D code was used to produce temporal and spatial information of the coupled water, vapour and heat transport. The space-time information represents a two-dimensional field and a dependent specific flux (e.g. thermal water vapour flux) or temperature as a third dimension. The space-time information and dependent specific fluxes or temperatures (all of which contain discrete values) were used directly in an interpolation and smoothing procedure. This was done

to create a continuous three-dimensional field for the diurnal pattern interpretation of soil water dynamics.

2 MATERIALS AND METHODS

2.1 Model Description

In this section, the measured water contents, soil temperatures were compared with those that were calculated by the modified HYDRUS-1D code. The modified HYDRUS-1D code has two major new features, as compared to HYDRUS-1D version 3.0: (i) solving the coupled equations governing liquid water, vapor, and heat transport, together with the surface water and energy balance, and (ii) providing flexibility in accommodating various types of meteorological information to solve the surface energy balance (Saito et al. 2006).

The governing equation for one-dimensional vertical flow of liquid water and water vapour in variably saturated media is given by the following mass conservation equation (Saito et al. 2006):

$$\frac{\partial \theta}{\partial t} = -\frac{\partial q_L}{\partial z} - \frac{\partial q_v}{\partial z} \quad (1)$$

Where, q_L and q_v are the flux densities of liquid water and water vapour (cm d^{-1}), respectively; t is time (d); z is the vertical axis positive upward (cm).

The flux density of liquid water, q_L , is defined as (Philip and de Vries, 1957)

$$q_L = q_{Lh} + q_{LT} = -K_{Lh} \left(\frac{\partial h}{\partial z} + 1 \right) - K_{LT} \frac{\partial T}{\partial z} \quad (2)$$

Where, q_{Lh} and q_{LT} are respectively the isothermal and thermal liquid water flux densities (cm d^{-1}); h is the matric potential head (cm); T is the temperature (K); and K_{Lh} (cm d^{-1}) and K_{LT} ($\text{cm}^2 \text{K}^{-1} \text{d}^{-1}$) are the isothermal and thermal hydraulic conductivities for liquid-phase fluxes due to gradients in h and T , respectively.

Using the product rule for differentiation and assuming the relative humidity in soil pores keeps constant with temperature (Philip and de Vries 1957), the flux density of water vapour, q_v , can be written as

$$q_v = q_{vh} + q_{vT} = -K_{vh} \frac{\partial h}{\partial z} - K_{vT} \frac{\partial T}{\partial z} \quad (3)$$

Where, q_{vh} and q_{vT} are the isothermal and thermal water vapour flux densities (cm d^{-1}), respectively; K_{vh} (cm d^{-1}) and K_{vT} ($\text{cm}^2 \text{K}^{-1} \text{d}^{-1}$) are the isothermal and thermal vapour hydraulic conductivities, respectively. Combining Eq. (1), (2), and (3), we obtain the governing liquid water and water vapour flow equation:

$$\begin{aligned} \frac{\partial \theta}{\partial t} &= \frac{\partial}{\partial z} \left[K_{Lh} \frac{\partial h}{\partial z} + K_{Lh} + K_{LT} \frac{\partial T}{\partial z} + K_{vh} \frac{\partial h}{\partial z} + K_{vT} \frac{\partial T}{\partial z} \right] \\ &= \frac{\partial}{\partial z} \left[K_{Th} \frac{\partial h}{\partial z} + K_{Lh} + K_{TT} \frac{\partial T}{\partial z} \right] \end{aligned} \quad (4)$$

Where, K_{Th} (cm d^{-1}) and K_{TT} ($\text{cm}^2 \text{K}^{-1} \text{d}^{-1}$) are the isothermal and thermal total hydraulic conductivities, respectively, and where:

$$K_{Th} = K_{Lh} + K_{vh} \quad (5)$$

$$K_{TT} = K_{LT} + K_{vT} \quad (6)$$

For the sake of brevity, the detailed description of the modified HYDRUS-1D code is not given here, but any interested readers are referred to Saito et al. (2006).

2.2 *Field Measurement*

The soil temperature and moisture data set were collected using the mercury thermometers and TSCII sensors, while the surface temperature was measured by an infrared thermometer. Before and during the observation period, there was no precipitation, and the conditions in the field were reported as but clear skies and light winds. Maximum and minimum air temperatures in this field ranged from 28.3°C to 35°C (0 p.m. ~2 p.m.) and 10.8°C to 12°C (5 a.m.~7 a.m.), respectively; the maximum and minimum relative humidity ranged from 85.5% to 97.9% (4 a.m. ~ 7 a.m.) and 33.2% to 34% (0 p.m.~3 p.m.), respectively. In addition, the atmospheric pressure and wind speed ranged from 1012.25 hPa to 1017.54 hPa and from 0m/s to 1.45m/s.

The measurement of soil water content by TSCII is based on the determination of soil dielectric constant using the principle of standing-wave ratio (Zhao et al. 2002), according to which the soil dielectric constant is proportional to the voltage difference measured by TSCII. In this experiment, the measurement of TSCII in sand had been calibrated; the relative root mean square error between the calibration equation and the weighted soil water content was 0.0031.

The soil temperature was measured by the bent stem mercury thermometers, which were designed to measure the soil temperature at depths of 5cm, 10cm, 15cm, 20cm and 30cm. The infrared thermometer (Fluck66, Fluke UK Ltd, Norwich, Norfolk) was used to measure the surface temperature. As for the infrared thermometer, the ratio of the distance and spot size was 30:1, and the emissivity was set as 0.95 suitable for sand at the spectral range from 8 μ m to 14 μ m..

2.3 *Initial and Boundary Conditions*

The soil profile was considered to be 80cm deep. The spatial discretization of 1 cm was used, leading to 81 nodes across the profile. The calculations were performed for a period of 2.5 days from 4 October to 7 October in 2004. Discretization in time is varying between a minimum and a maximum time-step, controlled by some time-step criterion (Saito et al. 2006). Except for the aforementioned geometry and time information, it is necessary to specify initial conditions for temperature and matric potential in order to solve this problem by the modified HYDRUS-1D code. The initial matric potentials and soil temperatures were determined from measured values on 4 October by interpolating the measured values between different depths (Fig.1). Boundary conditions at the soil surface for liquid water, water vapour, and heat transport were determined from the meteorological data. The modified HYDRUS1D uses the continuous meteorological data in the energy balance equation, which is calculated in order to get the surface heat flux, which is subsequently used as a known heat flux boundary condition on the soil surface. At the same time, the surface evaporation is calculated as the surface boundary condition for the soil moisture transport (Saito et al. 2006). The free drainage was considered as the bottom boundary condition and the discharge rate assigned to bottom node was determined by the program (Simunek et al. 2005). The lower boundary condition for heat transport was a Neumann type boundary condition with a zero temperature gradient.

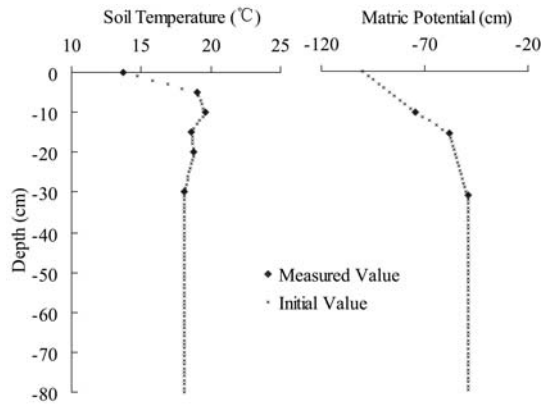


Figure.1 Initial soil temperature and matric potential values

2.4 Simulation Results

The hydraulic parameters used in the modeling, for van Genuchten-Mualem model, were $\theta_r = 0.01 \text{ cm}^3 \text{ cm}^{-3}$, $\theta_s = 0.39 \text{ cm}^3 \text{ cm}^{-3}$, $\alpha = 0.0316 \text{ cm}^{-1}$, $K_s = 103 \text{ cm d}^{-1}$, and $n = 3.3$. The predicted and observed soil temperatures at depths of 5cm, 10cm, 15cm, 20cm and 30cm were showed in Figure.2. The simulation's goodness of fit was quantified with the following relative root mean square error measure:

$$RRMSE = \frac{\sqrt{\sum_{i=1}^{N_w} (M_i - C_i)^2 / N_w}}{\text{Max}(M_1, M_2, \dots, M_{N_w}) - \text{Min}(M_1, M_2, \dots, M_{N_w})} \quad (7)$$

Where, N_w is the number of the measurements; M_i and C_i are measurements and calculations, respectively; $\text{Max}(M_1, M_2, \dots, M_{N_w})$ and $\text{Min}(M_1, M_2, \dots, M_{N_w})$ are the maximum and minimum value of the measurements. The $RRMSE$ is dimensionless and $RRMSE=0$ indicates the best fit. The smaller is the $RRMSE$, the better the fit of simulation. The $RRMSE$ s of the temperature at depths of 5cm, 10cm, 15cm, 20cm and 30cm were respectively 0.094, 0.108, 0.152, 0.184 and 0.199. Although there were spiky points at depths of 15cm and 20cm, simulated and measured temperatures generally agreed at all five depths and both showed typical sinusoidal diurnal variation, with the maximum absolute deviation of 5.794 °C at 20cm depth.

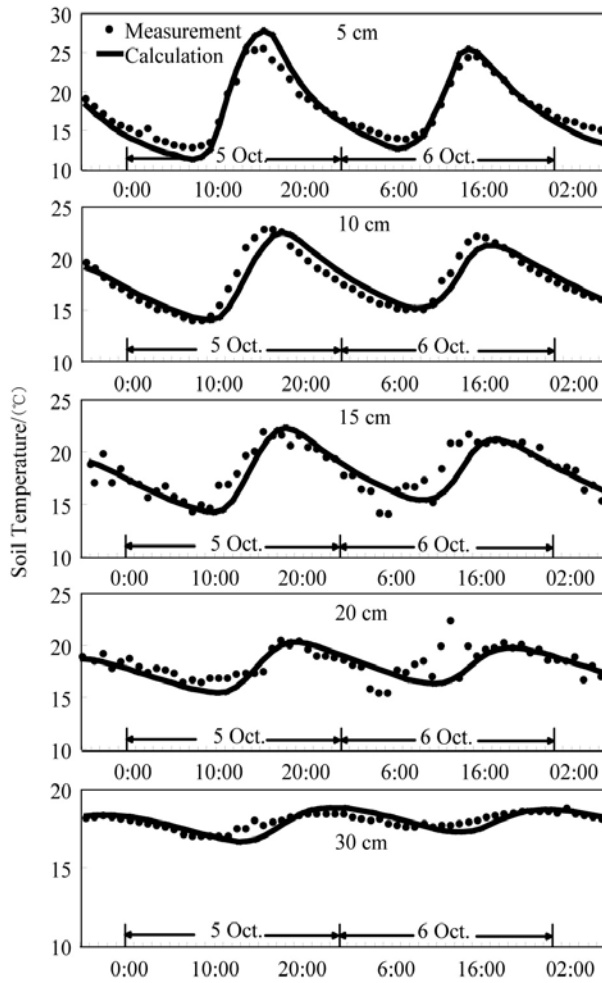


Figure.2 Simulated and measured soil temperatures at all observed depths.

Figure.3 depicts simulated and measured soil water content at two depths. As seen, there is a discrepancy between the observed and simulated water contents. The *RRMSEs* of the water content at depths of 10cm and 30cm are 0.289 and 0.211, respectively. At 10cm depth, the simulated water content can follow the general trend of observation merely; while at 30cm depth, the simulation shows a decreasing trend instead of a variation like the measurement has. However, apart from the poor fit of the simulation to the trend of water content variation at 30cm depth, the mean of the simulated water contents is close to that of the measurements. The means of simulated and observed water contents are 5.002% and 5.076% at 10cm depth, and 11.222% and 11.236% at 30cm depth, respectively. Furthermore, the average relative errors at depths of 10cm and 30cm are 1.022 and 1.001; both are close to one. It indicated that the simulated water contents could fit the most of measured values fairly well. The average relative error is defined as (Kleijnen et al. 2001)

$$AVRE = \sum (C_i / M_i) / N_w \quad (8)$$

Where, the symbols were the same as in Eq.7. To summarize, the modified HYDRUS1D code could be applied in the analysis of coupled liquid water, water vapour and heat transport in this specific case.

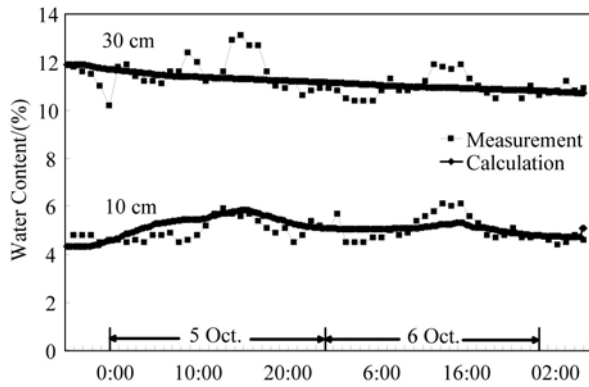


Figure.3 Simulated and measured soil moistures

3 DISCUSSIONS

Numerical modelling of isothermal and non-isothermal liquid and vapour flow plays a critical role in evaluating the physical processes, that governing soil heating, spatial distribution of water, and gaseous exchange between the soil and the atmosphere. In this section, the modified HYDRUS1D code was used to produce the hourly profiles of isothermal and non-isothermal water vapour fluxes, liquid water fluxes and soil temperatures from 4 October to 7 October 2004. Then, an interpolation and smoothing program (SURFER) was used to create continuous three-dimensional fields for the diurnal pattern interpretation of soil water dynamics. The three dimensional fields consisted of a space-time field (two-dimensional field) and a dependent specific flux or temperature (third dimension). Finally, the basic soil water dynamics were conceptualized with a schematic figure.

3.1 *Distribution of Thermal Fluxes in Space and Time Field*

In order to understand the diurnal variation and the mechanism of heating of the soil, there is a need to look at the temperature variation in the soil profile. The contour chart of temperature, in Figure 4a, shows the hourly variation of soil temperature profiles. Where, the interval of contours was 2°C.

Before 7 a.m. 5 October, the contours at the surface were sparse and the surface temperature varied slowly with the rate of 0.53°C per hour. From 7 a.m. to 7 p.m. 5 October, the contours became dense and the surface temperature fluctuated strongly with the rate of 5.2°C per hour. During this period, the surface temperature increased from 7.4°C at 7 a.m. to the highest value of 42°C at 1 p.m., and dropped to 14°C at 7 p.m., which was the changing point for the contours that varied from denseness to sparseness.

From 7 p.m. 5 October to 6 a.m. 6 October, the contours were sparse again and the variations of the surface temperature were reduced. In this period, the surface temperature changed from 14°C (at 7 p.m. 5 October) to 8.2°C (at 6 a.m. 6 October) with the rate of 0.52°C per hour. After 6 a.m., the contours would experience the period of denseness again, in which the surface temperature varied strongly. It was important to note that the denseness and sparseness indicated the rapid variation and slow variation of soil temperature, respectively.

As shown in Figure 4a, the density of contours decreased with depth. It indicated that the variation of soil temperature was reduced with depth. During the observation period, the surface temperature varied from 6.8°C to 42°C, while from 17°C to 18.8°C at depth of 30cm. At a depth of 40cm, the variation of temperature was less than 0.3°C. Note that, since the variation of temperature was close to zero below a depth of 40cm, the soil temperature profile information below a depth of 40cm depth is not shown herein.

Figure 4b shows the space-time temperature gradient field, which clearly shows how heat transport in soil controls the dependence of the temperature gradient profiles in time and space. The temperature gradients were derived from $\Delta T = (T_{i+1} - T_i)$ (°C/cm), where T_i represented the soil temperature at a depth of i cm. The variation of contours in Figure 4b was accordant with that in Figure 4a. The contours experienced alternatively the sparseness and denseness with time released, and developed downwards from denseness to sparseness with depth.

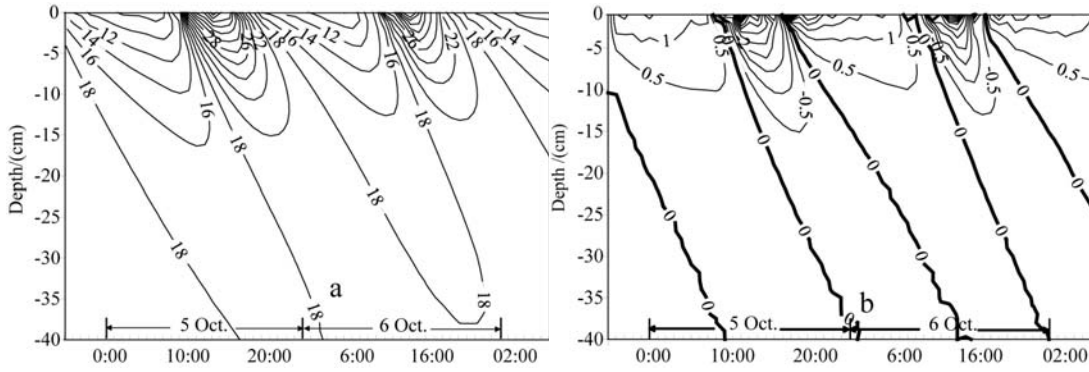


Figure.4 Distributions of soil temperatures (a) and temperature gradients (b) in space and time

From temperature gradient profiles, it was seen that there was an active layer for heat exchange, which was about 10 cm thick right below the ground surface. Between depths of 0cm and 1cm, the temperature gradient could reach $6.9^{\circ}\text{C}/\text{cm}$. At a depth of 10cm, the gradients were between $0\sim 0.6^{\circ}\text{C}/\text{cm}$, and there was very small temperature gradient below depths greater than 10cm. In addition, there were five contours for the temperature gradient of $0^{\circ}\text{C}/\text{cm}$, which indicated no heat conduction in the space-time field. Accordingly, these five contours were defined as zero heat flux planes.

There were two types of zero heat flux planes: one was the divergent plane, where the temperature gradient, above and below this plane was respectively positive and negative (upwards and downwards); the other was the convergent plane, where the directions of the temperature gradient were completely reversed (i.e. downwards and upwards) compared with those to the divergent plane. During the whole observation, there were three divergent zero heat flux planes and two convergent zero heat flux planes. The zero heat flux plane could be regarded as the ‘changing point’, i.e. the point at which the direction of the temperature gradient reversed. The divergent planes started in afternoon (4 p.m. ~ 5 p.m.), while the convergent planes happened in morning (6 a.m. ~ 7 a.m.).

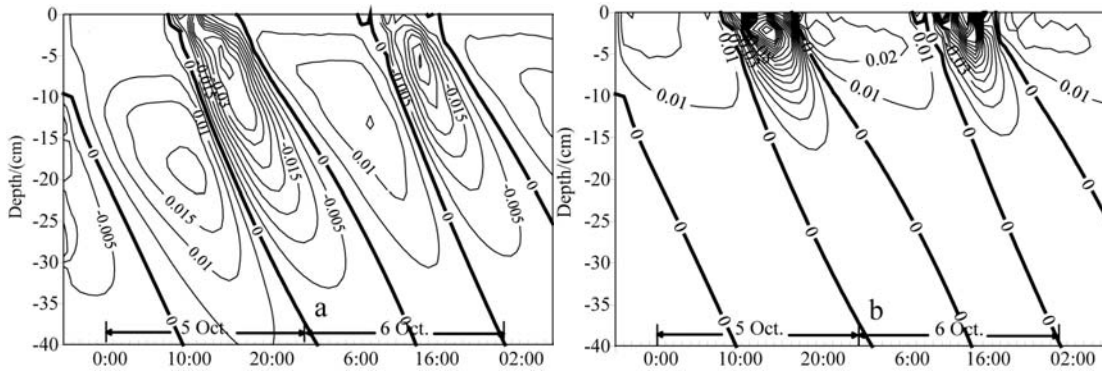


Figure.5 Distributions of the thermal liquid fluxes (a) and the thermal vapour fluxes (b) in space and time

The space-time fields of thermal liquid and vapour fluxes were showed in Figure 5. Corresponding to the zero heat flux planes in Figure 4b, the q_{LT} and q_{VT} field had the zero thermal liquid flux planes (Fig.5a) and the zero thermal vapour flux planes (Fig.5b), both of which were sub-classified into divergent and convergent planes according to the definitions of zero heat flux planes. The downward propagation of the zero thermal liquid and the vapour flux planes were accordant with that of the zero heat flux planes over the simulation period.

There were ellipses between the planes of divergence and convergence in both q_{LT} and q_{VT} fields. The ellipses in q_{LT} field were much more obvious than those in q_{VT} field. The occurrence of ellipses was dependent on the thermal liquid and vapour fluxes profiles. According to the q_{LT} field (Fig.5a), there were three types of liquid flux profiles:

a) The first type occurred before dawn (1 a.m. ~ 7 a.m.). During this period, there were only the divergent planes existed in the profile. After 7 a.m., the plane of divergence had almost

reached a depth of 40cm, and liquid flux was upward almost throughout the entire profile above 40cm. In addition, the bulge of thermal liquid flux moved deeper and deeper with time and the peak flux increased with time, which varied from 0.012cm/d at 1 a.m. to 0.02cm/d at 7 a.m. (Fig.6a). The increasing upward flux showed that liquid water in deeper soil was drawn to the surface layer at night by a temperature gradient. The propagation of the bulge of fluxes indicated the formation of the ellipses in Figure 5a;

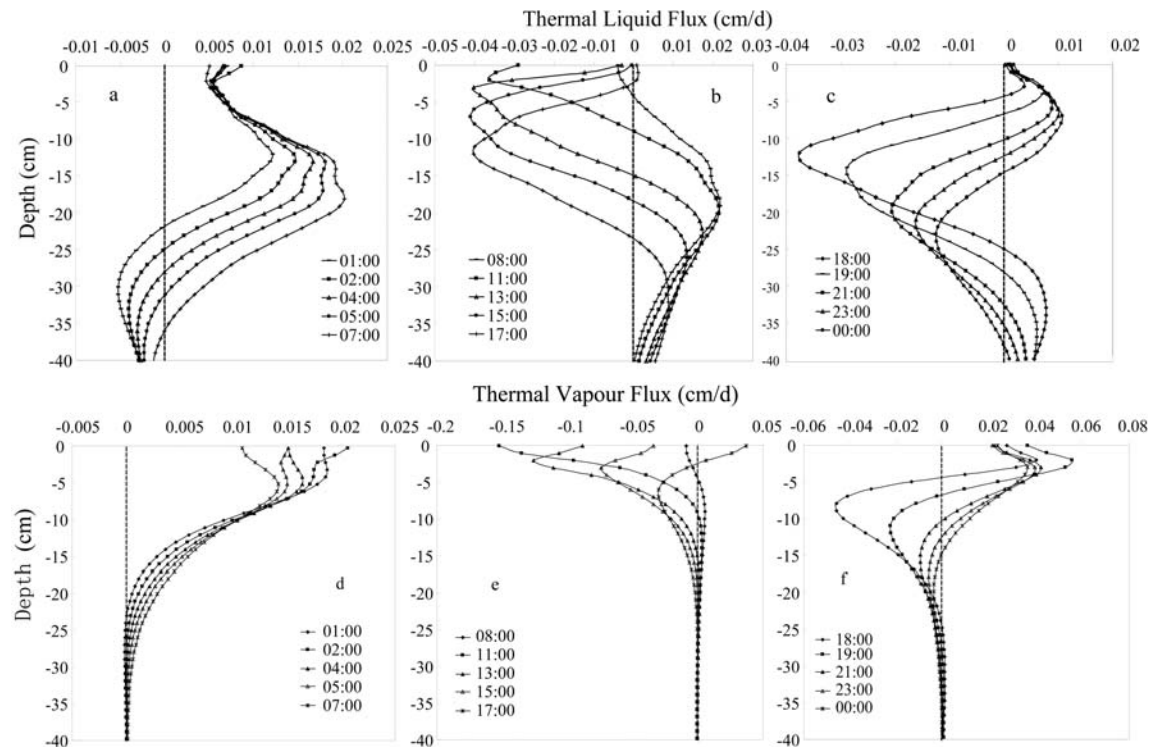


Figure.6 Different types of thermal liquid flux profiles (a, b, c) and thermal vapour flux profiles (d, e, f)

b) There were only the convergent planes of zero thermal liquid flux that existed in the second type profile. The directions of the thermal liquid fluxes were opposite to those in the first type. The propagation of the bulge of fluxes was accordant with that in type one, but the direction was reversed; the peak flux varied from -0.036cm/d at 8 a.m. to -0.04cm/d at 5 p.m. (Fig.6b). The second type profiles happened during the day (8 a.m. ~ 5 p.m.), where the convergent plane reached the depth of 24cm. This indicated that the downward flow of the thermal liquid water occurred during day and in the top ~24cm; below a depth of 24cm, the liquid water was upward and the peak flux decreased from 0.022cm/d to 0.009cm/d;

c) The third type profile was the transition between the first type and the second type. Both the divergent planes and convergent planes were seen in this profile. The divergent plane was above the convergent plane, which indicated that the profile was changing from the second type to the first type. The third type profile occurred before midnight (6 p.m. ~12 p.m.). During this period, the divergent plane moved from the surface to -15cm, and the convergent plane moved from -25cm to -38cm. This indicated that the liquid water flux in the top layer (above -25cm) started to be upward and increased after 6 p.m., from 0.004cm/d to 0.01cm/d; below -25cm, the liquid water flux started to decrease from 0.008cm/d to 0.001cm/d (Fig.6c). After the upward peak flux at greater depth reached zero, the flux profile became the first type again.

As for the space-time field of the thermal vapour flux (Fig.5b), there were three corresponding types of vapour flux profiles, compared with those in $q_{v,T}$ field. From the thermal vapour flux profiles, it was seen that the bulges of vapour fluxes, above -20cm, fluctuated from 0.061cm/d to -0.177cm/d throughout all profiles (from Fig.6d to Fig.6f); below -20cm, the fluctuation of the bulge of flux was small and varied from 0.003cm/d to -0.004cm/d.

The range of variation for the thermal vapour flux was 0.238cm/d above -20cm and 0.009cm/d at greater depth, and the corresponding variation range of the thermal liquid flux was 0.063cm/d and 0.042cm/d. The variation of thermal vapour flux was one order of magnitude

more than that of the thermal liquid flux in the subsurface layer, while one order of magnitude less than that in deeper layer. It indicated that the thermal vapour flux dominated in the top ~20cm, while the thermal liquid flux dominated at greater depth.

As shown in Fig.6d, the flow of thermal vapour was upward throughout the entire profile after 5 a.m., which indicated the first type of thermal vapour flux profile (1 a.m. ~ 7 a.m.). The second type of thermal vapour flux profile was showed in Fig.6e, and the thermal vapour flux was moving downward in day (from 8 a.m. ~ 5 p.m.). The transition type profile of the thermal vapour flux was not obvious due to the small variation of the vapour flux at greater depth (Fig.6f). Thus, the maximum thermal vapour flux was only 0.003cm/d below the plane of convergence. However, it was still seen that the evaporation started to develop from the uppermost soil to the deeper soil, and that the thermal vapour flux was changing from the second type to the first type.

3.2 Distribution of Isothermal Fluxes in Space and Time Field

The hourly variation of matric potential was largest near the surface and decreased with depth, which indicated that there was an upward driving force for liquid water and water vapour during the whole simulation period. The matric potential fluctuated from -3084cm to -94.109cm at surface, while varied from -54.582cm to -49.26cm at -40cm. The rapid variation of the matric potential happened from 10 a.m. to 11 p.m., and was restricted to the uppermost soil layer.

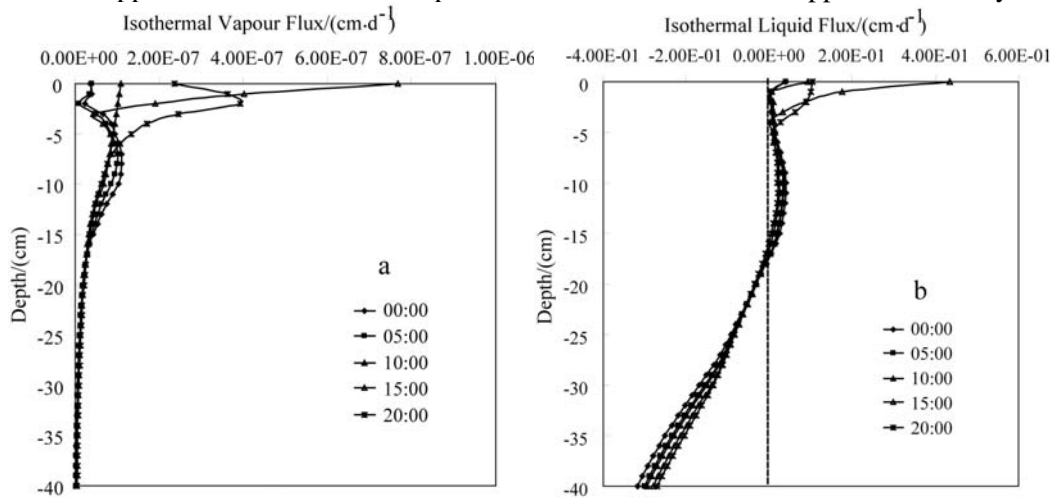


Figure.7 Distribution of the isothermal vapour flux profiles (a) and isothermal liquid flux profiles (b)

The matric potential gradient were decided by $\Delta h = (h_{i+1} - h_i)$ (cm/cm), where h_i represented the soil matric potential at a depth of i cm. The variation of the potential gradient, between 0cm and -5cm, was most intensive, which indicated the fluctuation of the matric potential gradient was strongest near the surface. The gradient varied from 2923.627cm/cm to 1.027cm/cm at surface, and varied from 4.229cm/cm to 1.281cm/cm at -5cm. The top 5cm layer could be regarded as the active layer for the isothermal flux driven by the matric potential. Below -5cm, the variation of the gradient tended to be steady, except for the occurrence of the bulge of gradient in the initial period. The matric potential gradient was positive throughout the entire profile.

The variation of the isothermal vapour flux was determined by the matric potential discussed above. In the top ~5cm layer, the fluctuation was strong. The isothermal vapour flux varied from 4.018×10^{-4} cm/d to 6.749×10^{-9} cm/d at surface, and from 2.365×10^{-7} cm/d to 5.132×10^{-8} cm/d at -5cm. At deeper soil layers, there was almost no fluctuation. For example, at -40cm, the maximum flux was 5.309×10^{-9} cm/d and the minimum flux was 1.743×10^{-11} cm/d. During the whole simulation period, the direction of the isothermal vapour flux was upwards throughout the entire profile (Fig.7a). Although the matric potential gradient was upwards throughout the entire profile during the simulation period, the isothermal liquid water flux was not only upward, but also downward in the space-time filed. There was a reversal in the direction from upward to downward. From the isothermal liquid flux profiles, there was a plane of divergence developed from -16cm that fluctuated between -13cm and -17cm. The reason for this was that the isothermal liq-

uid water was driven not only by the matric potential gradient, but also the gravitational gradient (Fig.7b).

4 SOIL WATER DYNAMICS

Generally, three stages could be recognized from the spatial-temporal distributions of liquid water flux and water vapour flux (Fig.8). Due to the isothermal flux profiles kept fixed during the whole simulation period, the determination of the stages was corresponding to the occurrences of the three types of thermal flux profiles. The isothermal vapour flux was upward through all three stages, and it was at least two orders of magnitude less than other fluxes. Considering its stability and small magnitude, the isothermal vapour flux would not be discussed in these specific stages.

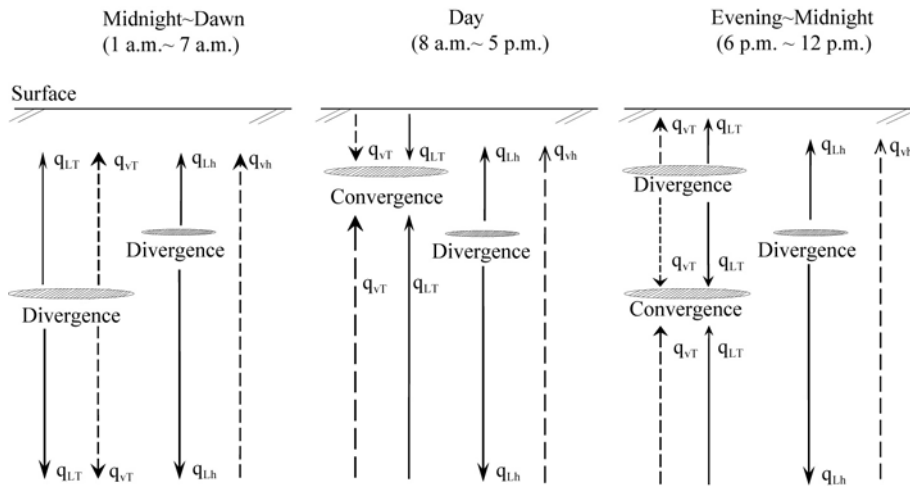


Figure.8 Schematic illustration of the diurnal soil water dynamics

The first stage started from midnight and ended before dawn (1 a.m. ~ 7 a.m.) (Fig.8, left part). During this stage, the isothermal liquid flux, the thermal liquid and vapour flux were upward above the plane of divergence, and downward below this plane. The magnitude of the upward value of thermal vapour flux ($0.238\text{cm/d} \sim 0.0007\text{cm/d}$) was similar with that of thermal liquid flux ($0.202\text{cm/d} \sim 0.0002\text{cm/d}$). Compared to the thermal liquid and vapour flux, the isothermal liquid flux ($0.064\text{cm/d} \sim 0.0001\text{cm/d}$) was less significant in this stage. However, below the divergent plane, the downward isothermal liquid flux ($-0.329\text{cm/d} \sim -0.378\text{cm/d}$) dominated, while the thermal vapour flux ($-2.146 \times 10^{-6}\text{cm/d} \sim 3.833 \times 10^{-4}\text{cm/d}$) was most insignificant. The divergent plane of thermal fluxes developed from -23cm at the beginning of this stage and propagated downward to -36cm at the end. This stage indicated that the upward thermal flux dominated in the upper soil layer, while the downward isothermal flux dominated in the deeper soil layer.

The second stage was in day between 8 a.m. and 5 p.m. (Fig.8, middle part). In this stage, the convergent plane of thermal fluxes occurred at -3cm and moved downward to the depth of 24cm . Above this convergent plane, the magnitude of the downward thermal vapour flux ($-0.244\text{cm/d} \sim -2.409 \times 10^{-3}\text{cm/d}$) was larger than the thermal liquid flux ($-0.04\text{cm/d} \sim -5.509 \times 10^{-5}\text{cm/d}$). However, the thermal vapour flux was not the dominant flux. The magnitude of upward isothermal liquid flux ($0.423\text{cm/d} \sim 0.029\text{cm/d}$) exceeded the thermal flux above the convergent plane. In addition, the downward isothermal liquid flux was over the upward thermal flux below the convergent plane. It indicated that the isothermal liquid flux dominated during day throughout the entire profile.

The third stage was from evening to midnight (6 p.m. to 12 p.m.) (Fig.8, right part). It was the transition stage between the second stage and the first stage. The divergent plane of thermal fluxes started from -5cm and ended at -15cm . In the initial period of this stage (6 p.m. ~ 7 p.m.), the upward isothermal liquid flux was over the thermal flux above this divergent plane. In the top $\sim 5\text{cm}$ soil layer, the average of the isothermal liquid flux was 0.033cm/d , compared with

0.031cm/d of thermal vapour flux and 0.004cm/d of thermal liquid flux. During the rest of this stage, the average of the thermal vapour flux (0.022cm/d) was close to the average isothermal liquid flux (0.021cm/d) and over the average thermal liquid flux (0.005cm/d). The convergent plane of thermal fluxes occurred at -24cm and developed downward to -38cm. The direction of the thermal liquid flux, thermal vapour flux and isothermal liquid flux were the same between -15cm and -24cm; however, the isothermal liquid flux was dominant in this soil layer. Below -24cm, the downward isothermal liquid flux was still the most dominant type of flux. During this transition stage, the dominant flux in the top ~5cm soil layer changes from the isothermal liquid flux to the thermal vapour flux; at the mean time, the isothermal kept the dominance at greater depth. It indicated that the third stage was changing toward the situation in the first stage.

5 CONCLUSION

The modified HYDRUS1D code, which refers to the coupled transport of liquid water, water vapour and heat, could be applied to further evaluate the mechanisms affecting unsaturated flow at the site. It was convenient to use the space-time fields to investigate the propagation of the heat and water flow in soil. According to the space-time fields of the nonisothermal and isothermal flux, three stages of the soil water dynamics were determined. Generally, the thermal vapour and liquid flux was dominant in uppermost soil layer at night, while the isothermal liquid water dominated during the day and in the deeper soil layer. The numerical simulations suggested that the isothermal liquid flux, the thermal liquid flux and the thermal vapour flux should be considered in the conceptualization of the unsaturated flow in soil. Although this study was for the relative coarse sand in the sand bunker, further studies for sand in natural conditions (particularly in desert) are necessary.

REFERENCES

- Agam, N. and P. R. Berliner. 2006. Dew formation and water vapor adsorption in semi-arid environments--A review. *Journal of Arid Environments* 65(4): 572-590.
- Agam, N., P. R. Berliner, A. Zangvil and E. Ben-Dor. 2004. Soil water evaporation during the dry season in an arid zone. *Journal of Geophysical Research* 109: 161-173.
- Asgar, M. N. 1996. Computer simulation of salinity control by means of an evaporative sink. PhD Thesis, University of Newcastle upon Tyne.
- Athavale, R. N., R. Rangarajan and D. Muralidharan. 1998. Influx and efflux of moisture in a desert soil during a 1 year period. *Water Resources Research* 34(11): 2871-2877.
- Braud, I., A. C. Dantasantonino, M. Vauclin, J. L. Thony and P. Ruelle. 1995. A Simple Soil-Plant-Atmosphere Transfer Model (Sispat) Development and Field Verification. *Journal of Hydrology* 166(3-4): 213-250.
- Carsel, R. F. and R. S. Parrish. 1988. Developing joint probability distributions of soil water retention characteristics. *Water Resources Research* 24(5): 755-769.
- Cary, J. W. 1963. Onsager's relation and the non-isothermal diffusion of water vapor. *The Journal of Physical Chemistry* 67(1): 126-129.
- Cary, J. W. 1964. An evaporation experiment and its irreversible thermodynamics. *Int. J. Heat Mass Transfer* 7: 531-538.
- Cary, J. W. 1965. Water flux in moist soil: thermal versus suction gradients. *Soil Sci.* 100(3): 168-175.
- Cary, J. W. 1966. Soil moisture transport due to thermal gradients: practical aspects. *Soil Sci. Soc. Am. Proc* 30: 428-433.
- Cary, J. W. 1979. Soil Heat Transducers and Water Vapor Flow. *Soil Science Society of America Journal* 43(5).
- Cary, J. W. and S. A. Taylor. 1962a. Thermally Driven Liquid and Vapor Phase Transfer of Water and Energy in Soil. *Soil Science Society Am. Proc* 26: 417-420.
- Cary, J. W. and S. A. Taylor. 1962b. The Interaction of the Simultaneous Diffusions of Heat and Water Vapor. *Soil Science Society Am. Proc* 26: 413-416.
- De Vries. 1958. Simultaneous transfer of heat and moisture in porous media. *Trans. Am. Geophys. Union* 39(5): 909-916.

- Dickinson, R. E., K. W. Oleson, G. Bonan, F. Hoffman, P. Thornton, M. Vertenstein, Z. Yang and X. Zeng. 2006. The Community Land Model and Its Climate Statistics as a Component of the Community Climate System Model. *Journal of Climate* 19(11): 2302-2324.
- Entekhabi, D., E. Njoku, P. Houser, M. Spencer, T. Doiron, J. Smith, R. Girard, S. Belair, W. Crow and T. Jackson. 2004. The Hydrosphere State (HYDROS) mission concept: An earth system pathfinder for global mapping of soil moisture and land freeze/thaw. *IEEE Trans. Geosci. Remote Sens* 42(10): 2184-2195.
- Gowing, J. W., F. Konukcu and D. A. Rose. 2006. Evaporative flux from a shallow watertable: The influence of a vapour-liquid phase transition. *Journal of hydrology(Amsterdam)* 321: 77-89.
- Griffoll, J. and Y. Cohen. 1999. A front-tracking numerical algorithm for liquid infiltration into nearly dry soils. *Water Resour. Res* 35(8): 2579-2585.
- Griffoll, J., J. M. Gast and Y. Cohen. 2005. Non-isothermal soil water transport and evaporation. *Advances in Water Resources* 28: 1254-1266.
- Groenevelt, P. H. and B. D. Kay. 1974. On the interaction of water and heat transport in frozen and unfrozen soils: II. The Liquid Phase. *Soil Sci. Soc. Am. Proc* 38: 400-404.
- Gustafsson, A. M. and J. Lindblom. 2001. Underground condensation of humid air-a solar driven system for irrigation and drinking-water production. Master Thesis 2001:140 CIV, Luleå University of Technology, Sweden.
- Hausherr, B. and K. Ruess. 1993. Seawater Desalination and Irrigation with Moist Air. Ingenieurbüro Ruessund Hausherr, Switzerland.
- Jackson, R. D. 1973. Diurnal changes in soil water content during drying. Field soil water regime, Madison.
- Jacobs, A.F.G., G. Bert and Heusinkveld. 2000. Force-restore technique for ground surface temperature and moisture content in a dry desert system. *Water Resour. Res* 36(5): 1261-1268.
- Jacobs, A.F.G., G. Bert, Heusinkveld and S. M. Berkowicz. 1999. Dew deposition and drying in a desert system: a simple simulation model. *Journal of Arid Environments* 42: 211-222.
- Jury, W. A., W. R. Gardner and W. H. Gardner. 1991. *Soil Physics*, 328 pp, John Wiley, New York.
- Kay, B. D. and P. H. Groenevelt. 1974. On the interaction of water and heat transport in frozen and unfrozen soils: I. Basic Theory: The Vapor Phase. *Soil Sci. Soc. Am. Proc* 38: 395-400.
- Kemp, P. R., J. F. Reynolds, Y. Pachepsky and J. L. Chen. 1997. A comparative modeling study of soil water dynamics in a desert ecosystem. *Water Resources Research* 33(1): 73-90.
- Kerr, Y. H., P. Waldteufel, J. P. Wigneron, J. Martinuzzi, J. Font and M. Berger. 2001. Soil moisture retrieval from space: the Soil Moisture and Ocean Salinity (SMOS) mission. *Geoscience and Remote Sensing* 39(8): 1729-1735.
- Kleijnen, J. P. C., R. C. H. Cheng and B. Bettonvil. 2001. Validation of Trace-Driven Simulation Models: Bootstrap Tests. *Management Science* 47(11): 1533-1538.
- Kondo, J. and N. Okusa. 1990. A Simple Numerical Prediction Model of Nocturnal Cooling in a Basin with Various Topographic Parameters. *Journal of Applied Meteorology* 29(7): 604-619.
- Kondo, J., N. Saigusa and T. Sato. 1992. A Model and Experimental-Study of Evaporation from Bare-Soil Surfaces. *Journal of Applied Meteorology* 31(3): 304-312.
- Konukcu, F., A. Istanbuluoglu and I. Kocaman. 2004. Determination of water content in drying soils: incorporating transition from liquid phase to vapour phase. *Australian Journal of Soil Research* 42(1): 1-8.
- Lindblom, J. and B. Nordell. 2006. Water production by underground condensation of humid air. *Desalination* 189: 248-260.
- Milly, P. C. 1982. Moisture and Heat Transport in Hysteretic, Inhomogeneous Porous Media: A Matrix Head-Based Formulation and a Numerical Model. *Water Resources Research* 18(3).
- Milly, P.C. 1984a. Linear Analysis of Thermal Effects on Evaporation From Soil. *Water Resources Research* 20(8).
- Milly, P.C. 1984b. Simulation Analysis of Thermal Effects on Evaporation From Soil. *Water Resources Research* 20(8).
- Milly, P.C. 1996. Effects of thermal vapor diffusion on seasonal dynamics of water in the unsaturated zone. *Water Resources Research* 32(3): 509-518.
- Milly, P. C. D. and P. S. Eagleson. 1980. The coupled transport of water and heat in a vertical soil column under atmospheric excitation, Massachusetts Institute of Technology, Dept. of Civil Engineering, Ralph M. Parsons Laboratory for Water Resources and Hydrodynamics.
- Mmolawa, K. and D. Or. 2003. Experimental and numerical evaluation of analytical volume balance model for soil water dynamics under drip irrigation. *Soil Science Society of America Journal* 67(6): 1657-1671.

- Nassar, I. N. and R. Horton. 1997. Heat, Water, and Solution Transfer in Unsaturated Porous Media: I-- Theory Development and Transport Coefficient Evaluation. *Transport in Porous Media* 27(1): 17-38.
- Philip, J. R. 1957. Evaporation, and moisture and heat fields in the soil. *Journal of the Atmospheric Sciences* 14(4): 354-366.
- Philip, J. R. and V. D. De Vries. 1957. Moisture movement in porous materials under temperature gradient. *Trans. Am. Geophys. Union* 38(2): 222-232.
- Rose, D. A. 1963a. Water movement in porous materials: Part 1- Isothermal vapour transfer. *British Journal of Applied Physics* 14(5): 256-262.
- Rose, D. A. 1963b. Water movement in porous materials: Part 2- The separation of the components of water movement. *British Journal of Applied Physics* 14(8): 491-496.
- Rose, D. A. 1968a. Water movement in dry soils:1. physical factors affecting sorption of water by dry soil. *J. Soil Sci.* 19(1): 81-93.
- Rose, D. A. 1968b. Water movement in porous materials. 111. Evaporation of water from soil. *Brit. J. Appl. Phys.* 2(1): 1779-1791.
- Rose, D. A. 1971. Water movement in dry soils.II. An analysis of hysteresis. *J. Soil Sci.* 22(4): 490-507.
- Rose, D. A., F. Konukcu and J. W. Gowing. 2005. Effect of watertable depth on evaporation and salt accumulation from saline groundwater. *Australian Journal of Soil Research* 43(5): 565-573.
- Saito, H., J. Simunek and B. P. Mohanty. 2006. Numerical analysis of coupled water, vapor, and heat transport in the vadose zone. *Vadose Zone Journal* 5(2): 784-800.
- Salzmann, W., K. Bohne and M. Schmidt. 2000. Numerical experiments to simulate vertical vapor and liquid water transport in unsaturated non-rigid porous media. *Geoderma* 98(3): 127-155.
- Scanlon, B. R. 1992. Evaluation of liquid and vapor water flow in desert soils based on chlorine 36 and tritium tracers and nonisothermal flow simulations. *Water Resources Research* 28(1): 285-297.
- Scanlon, B. R. and P. C. D. Milly. 1994. Water and heat fluxes in desert soils 1. Field studies. *Water Resources Research* 30(3): 709-720.
- Schelde, K., A. Thomsen, T. Heidmann, P. Schjoenning and P. E. Jansson. 1998. Diurnal fluctuations of water and heat flows in a bare soil. *Water Resources Research* 34(11): 2919-2929.
- Shiklomanov, I. A., W. Gu and J. Lu. 2004. Experimental research on the role of dew in arid ecosystem of Gobi desert, Inner Mongolia [A]. A A Balkema Publishers.
- Shurbaji, A. R. M. and F. M. Phillips. 1995. A Numerical-Model for the Movement of H₂O, H-2 O-18, and (Hho)-H-2 in the Unsaturated Zone. *Journal of Hydrology* 171(1-2): 125-142.
- Starr, J. L. and I. C. Paltineanu. 1998. Soil water dynamics using multisensor capacitance probes in non-traffic interrows of corn. *Soil Science Society of America Journal* 62(1): 114-122.
- Starr, J. L. and D. J. Timlin. 2004. Using high-resolution soil moisture data to assess soil water dynamics in the vadose zone. *Vadose Zone Journal* 3(3): 926-935.
- Taylor, S. A. and J. W. Cary. 1964. Linear equations for the simultaneous flux of matter and energy in a continuous soil system. *Soil Science Society American Journal* 28: 167-172.
- Taylor, S. A. and G. L. Stewart. 1960. Some thermodynamic properties of soil water. *Soil Sci. Soc. Am. Proc.* 24: 243-247.
- Wang, D. 2002. Dynamics of soil water and temperature in aboveground sand cultures used for screening plant salt tolerance. *Soil Science Society of America Journal* 66(5): 1484-1491.
- Yamanaka, T. and T. Yonetani. 1999. Dynamics of the evaporation zone in dry sandy soils. *Journal of Hydrology* 217(1-2): 135-148.
- Zhang, T. and R. Berndtsson. 1991. Analysis of Soil-Water Dynamics in Time and Space by Use of Pattern-Recognition. *Water Resources Research* 27(7): 1623-1636.
- Zhao, Y., W. Paul and W. Yiming. 2002. "Comparison of soil water content measurements with SWR-, FD- and TDR sensors." *Z Bewässerungswirtsch* 37(1): 17-31.

Surface Boundary Conditions from Meteorological Data Using HYDRUS-1D

M. Sakai & J. Šimůnek

Department of Environmental Sciences, University of California Riverside, Riverside, CA 92521, USA

H. Saito

Department of Ecoregion Science, Tokyo University of Agriculture and Technology, Fuchu, Tokyo 183-8509, Japan

ABSTRACT: Evapotranspiration rates strongly affect the movement of water and solute in the vadose zone. We have implemented into the HYDRUS-1D code Penman-Monteith and Hargreaves equations to estimate potential evapotranspiration rates. While Penman-Monteith equation requires information about net radiation, wind speed, minimum and maximum temperatures and relative humidity, Hargreaves equation requires only minimum and maximum temperatures. The developed code provides users with a lot of flexibility by allowing an input of various combinations of meteorological information. The performance of the code is demonstrated using meteorological data for Tokyo, Japan (humid climate) and Riverside, CA (semi-arid climate). Liquid water flux, water vapor flux, heat transport, root water uptake, and evapotranspiration rates were quantitatively evaluated using meteorological data publicly available from local weather stations.

1 INTRODUCTION

Evaluating evapotranspiration rates from soils is needed for many research applications involving lysimeter and field studies, as well as for water management of agricultural fields. Potential evapotranspiration rates from vegetated soils can be calculated from meteorological data using either the Penman-Monteith combination equation (Monteith and Unsworth, 1990; FAO, 1990) or Hargreaves equation (Jensen et al., 1997). Since actual evaporation from soils and transpiration from crops are additionally also affected by water contents in the root zone, their evaluation requires simultaneous calculations of water flow and root water uptake in soils.

Penman-Monteith and Hargreaves equations were implemented into the HYDRUS-1D software package (Šimůnek et al., 2008). Various combinations of meteorological and crop data can be entered in the graphical user interface (GUI) of HYDRUS-1D to evaluate potential evapotranspiration rates. Example simulations are presented here to demonstrate this new feature of HYDRUS-1D and to evaluate evaporation rates, transpiration rates, water contents, and root water uptake using readily available data during the year 2007 from weather stations at Tokyo in Japan and Riverside in California.

2 MODELS

2.1 *Potential evapotranspiration*

The FAO-recommended Penman-Monteith combination equation is as follows (FAO, 1990):

$$ET_p = \frac{1}{\lambda} \left[\frac{\Delta (R_n - G)}{\Delta + \gamma (1 + r_c / r_a)} + \frac{\rho c_p (e_a - e_d) / r_a}{\Delta + \gamma (1 + r_c / r_a)} \right] \quad (1)$$

where ET_p is the potential evapotranspiration rate [mm d^{-1}], λ is the latent heat of vaporization [MJ

kg^{-1}], R_n is the net radiation at the surface [$\text{MJ m}^{-2}\text{d}^{-1}$], G (≈ 0 in this study) is the soil heat flux [$\text{MJ m}^{-2}\text{d}^{-1}$], ρ is the atmospheric density [kg m^{-3}], c_p is the specific heat of moist air [$\text{kJ kg}^{-1}\text{C}^{-1}$], e_a is the saturation vapor pressure [kPa], e_d is the actual vapor pressure [kPa], Δ is the slope of the vapor pressure curve [$\text{kPa}^\circ\text{C}^{-1}$], γ is the psychrometric constant [$\text{kPa}^\circ\text{C}^{-1}$], r_c is the crop canopy resistance [s m^{-1}], and r_a is the aerodynamic resistance [s m^{-1}].

The potential evapotranspiration can also be evaluated using the much simpler Hargreaves equation (Jensen et al., 1997; Droogers and Allen, 2002):

$$ET_p = 0.0023 \cdot 0.408 \cdot R_a (T_m + 17.8) \sqrt{TR} \quad (2)$$

where R_a is the extraterrestrial radiation [$\text{MJ m}^{-2}\text{s}^{-1}$], T_m is the daily mean air temperature [$^\circ\text{C}$], and TR is the temperature range between mean daily maximum and minimum air temperatures [$^\circ\text{C}$]. Potential evaporation, E_p , and transpiration, T_p , fluxes can be calculated from potential evapotranspiration using Beer's law (Ritchie, 1972):

$$\begin{aligned} T_p &= ET_p \cdot SCF = ET_p (1 - e^{-k \cdot LAI}) \\ E_p &= ET_p \cdot (1 - SCF) = ET_p e^{-k \cdot LAI} \end{aligned} \quad (3)$$

where SCF is the soil cover fraction [-], LAI is the leaf area index [-], k ($= 0.463$) is the constant governing radiation extinction by the canopy [-].

2.2 Root water uptake

The root water uptake rate can be defined according to Feddes et al. (1978) as follows:

$$S = \alpha(h) S_p = \alpha(h) b(z) T_p \quad (4)$$

where S is the sink term in Richards' equation [s^{-1}], $\alpha(h)$ is the water stress response function [-], S_p is the potential root water uptake rate [s^{-1}], and $b(z)$ is the normalized water uptake distribution [m^{-1}].

3 HYDRUS-1D GUI FOR METEOROLOGICAL INFORMATION

Different meteorological data are available for different applications. While a complete set of meteorological variables (net radiation, wind speed, temperature, relative humidity, vapor pressure, etc) may be available for one application, limited information (or no information at all) may be available for other applications. FAO suggested various equations to compensate for the lack of data (FAO, 1990). Some of these were implemented in the version 4 of HYDRUS-1D to calculate potential evapotranspiration rates from several combinations of data. Figure 1 shows the "Meteorological Parameters" dialog window of the HYDRUS-1D GUI where users select what type of information they have available. While parameters in the upper part of the window relate mainly to net radiation calculations, parameters in the lower part concern crop information (crop height, root depth, and LAI). Figure 2 shows the "Meteorological Conditions" dialog window of the HYDRUS-1D GUI where one inputs time variable meteorological data (e.g. radiation, air temperature, and relative humidity, etc) and time variable crop data (crop height, root depth, and LAI).

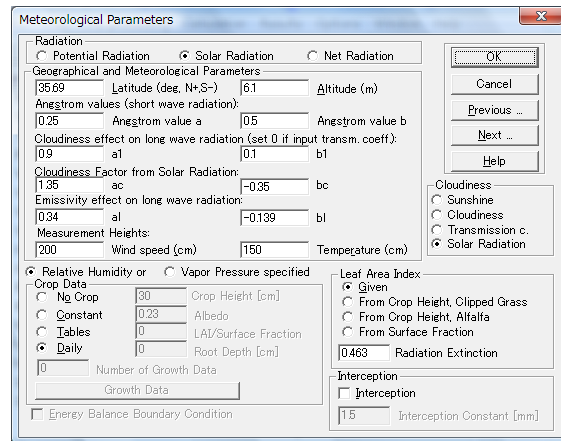


Figure 1. The Meteorological Parameters dialog window of the HYDRUS-1D GUI.

Time [days]	Radiation [MJ/m ² /d]	T _{max} [-C]	T _{min} [-C]	Humidity [%]	Wind [km/d]	No In form.	Crop Height [cm]	Albedo [-]	LAI/SCF [-]	Root Depth [cm]
1	11.3386	19.4444	4.4444	50.9	307.2	0	0	0.23	0	0
2	10.9621	22.7778	10	19.75	268.8	0	0	0.23	0	0
3	10.711	22.2222	7.2222	32.1	115.2	0	0	0.23	0	0
4	10.711	15	3.3333	68.95	115.2	0	0	0.23	0	0
5	12.301	12.7778	7.7778	47.3	537.6	0	0	0.23	0	0
6	12.2591	21.1111	4.4444	22.7	192	0	0	0.23	0	0
7	11.506	23.3333	8.3333	21.15	230.4	0	0	0.23	0	0
8	12.0081	25	10	19	230.4	0	0	0.23	0	0
9	11.8826	27.2222	10.5556	23.7	153.6	0	0	0.23	0	0
10	7.9495	20	7.7778	36.15	115.2	0	0	0.23	0	0
11	5.23	13.8889	3.3333	68.4	153.6	0	0	0.23	0	0
12	11.2131	9.4444	1.6667	51.75	268.8	0	0	0.23	0	0
13	12.803	7.7778	2.2222	18.15	384	0	0	0.23	0	0
14	12.8867	11.1111	-3.3333	25.95	115.2	0	0	0.23	0	0

Figure 2. The Meteorological Conditions dialog window of the HYDRUS-1D GUI.

4 EXAMPLE SIMULATIONS

Model performance is demonstrated using meteorological data for 2007 for two sites, i.e., Tokyo in Japan (35°41'N, 139°46'E, Altitude 6 m) and Riverside in California (33°58'N, 117°21'W, Altitude 311 m). Daily maximum and minimum air temperatures, averaged relative humidity, wind speed, sunshine hour, and rainfall data for Tokyo were downloaded from the Japan Meteorological Agency. Daily maximum and minimum air temperatures, averaged relative humidity, wind speed, solar radiation, and rainfall data for Riverside were downloaded from the University of California, Agriculture and Natural Resources. Time variable LAI and root depth shown in Figure 3 were used as crop data for both sites.

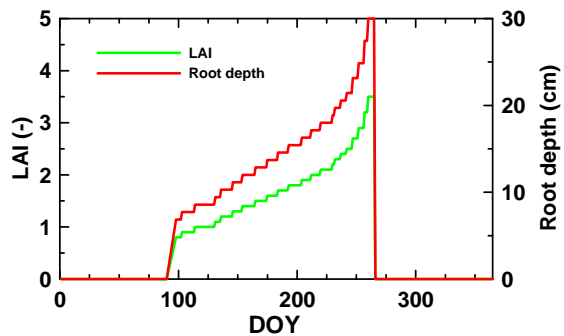


Figure 3. LAI and root depth as a function of time for example simulations.

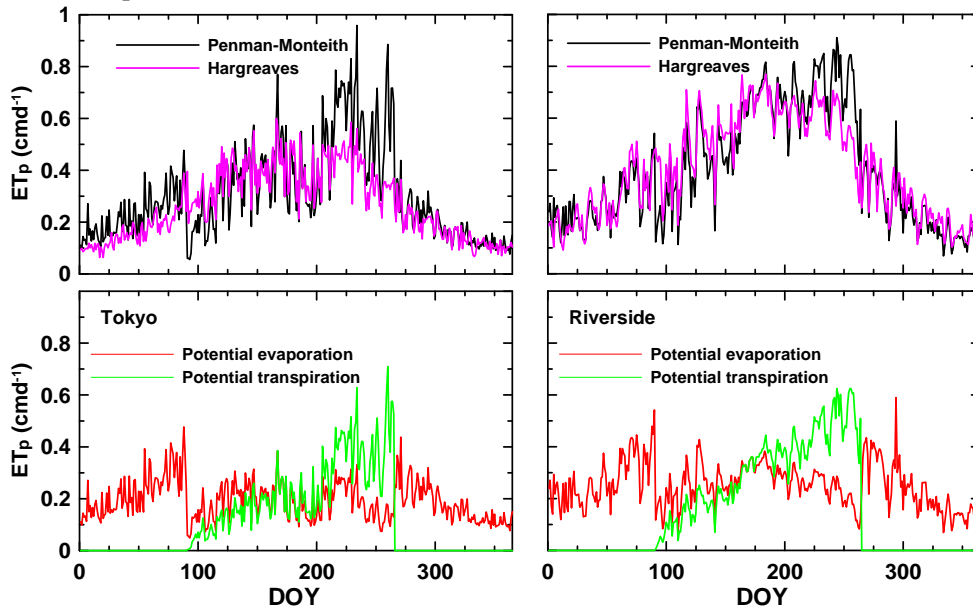


Figure 4. Estimated potential evapotranspiration rates (top), and potential evaporation and transpiration rates (bottom) for the Tokyo (left) and Riverside (right) sites during the year 2007.

Potential evapotranspiration rates, ET_p , calculated using Penman-Monteith equation (eq. (1)), and precipitations were used as a surface boundary condition. Free drainage was used as the lower boundary condition. Loam and sandy loam from the HYDRUS catalog were used for soil hydraulic properties of Tokyo and Riverside, respectively. Coupled movement of liquid water, water vapor, and heat (Saito et al., 2006) was simulated using HYDRUS-1D.

Figure 4 (top) shows ET_p calculated using both Penman-Monteith equation (eq. (1)) and Hargreaves equation (eq. (2)). Although ET_p calculated using Penman-Monteith equation fluctuated more than the one calculated using Hargreaves equation, reflecting more pronounced changes of radiation, relative humidity, and wind speed, the two estimated values agreed well. ET_p for Riverside was larger than for Tokyo, because of its semi-arid climate. Figure 4 (bottom) shows potential evaporation and transpiration rates obtained by dividing ET_p calculated with Penman-Monteith equation using Beer's law (eq. (3)). The potential transpiration rate increased from 90th day to 250th day depending on the growth of the crop (LAI and root depth).

Figure 5 shows simulated actual evaporation rates, transpiration rates, and water contents for Tokyo and Riverside. Both in Tokyo and Riverside, large evaporation or transpiration rates occurred immediately after precipitations. Since Tokyo has large amounts of precipitation all year round, soil water evaporation was large throughout the year, while transpiration reflected the growth of the crop. Water contents in the soil also fluctuated throughout the year due to precipitation events and evapotranspiration. Water content changes at a depth of 50 cm were smaller than those at other depths because of a decreasing impact of evaporation and root water uptake. On the other hand, it was raining only during the first 110 days of the year in the semi-arid climate of Riverside. Therefore actual evaporation rates were much smaller in Riverside than in Tokyo in spite of its larger values of potential evaporation rate. The transpiration rate was negligibly small in Riverside because of the shortage of soil water in the root zone.

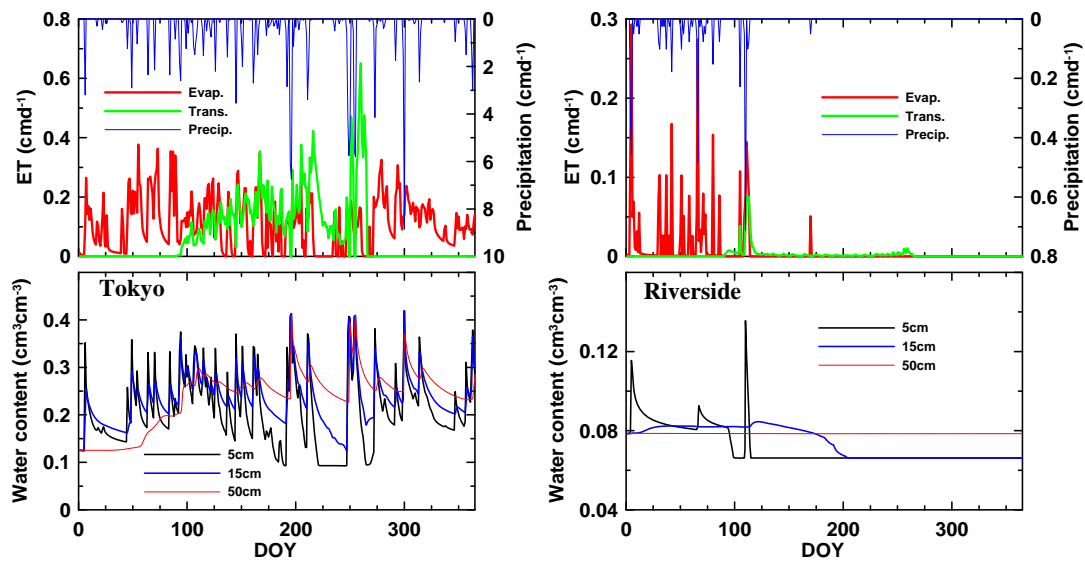


Figure 5. Precipitations and simulated actual evaporation and transpiration rates (top), and water contents (bottom) for the Tokyo (left) and Riverside (right) sites during the year 2007.

SUMMARY

This study demonstrates capabilities of the new version (4.0) of the HYDRUS-1D program that implements Penman-Monteith equation for calculating potential evapotranspiration rates. Estimations of evapotranspiration rates and water contents in the root zone using readily available meteorological information can be useful for water management decisions involving irrigation and drainage systems.

REFERENCES

- Droogers, P., and R. G. Allen, Estimating reference evapotranspiration under inaccurate data conditions, *Irrigation and Drainage Systems*, 16, 33-45, 2002.
- Feddes, R. A., E. Bresler, and S. P. Neuman, Field test of a modified numerical model for water uptake by root systems, *Water Resour. Res.*, 10(6), 1199-1206, 1974.
- Food And Agriculture Organization of the United Nations, Expert consultation on revision of FAO methodologies for crop water requirements, *ANNEX V*, FAO Penman-Monteith Formula, Rome Italy, 1990.
- Jensen, D. T., G. H. Hargreaves, B. Temesgen, and R. G. Allen, Computation of Eto under nonideal conditions, *J. of Irrig. Drainage*, 123(5), 394-400, 1997
- Monteith, J. L. and M. H. Unsworth, Principles of Environmental Physics, Edward Arnold, London, 1990.
- Ritchie, J. T., Model for predicting evaporation from a row crop with incomplete cover, *Water Resour. Res.*, 8(5), 1204-1213, 1972.
- Saito, H., J., J. Šimůnek, and B. Mohanty, Numerical analyses of coupled water, vapor and heat transport in the vadose zone, *Vadose Zone Journal*, 5, 784-800, 2006.
- Šimůnek, J., M. Šejna, H. Saito, M. Sakai, and M. Th. van Genuchten, The HYDRUS-1D Software Package for Simulating the Movement of Water, Heat, and Multiple Solutes in Variably Saturated Media, Version 4.0, *HYDRUS Software Series 3*, Department of Environmental Sciences, University of California Riverside, Riverside, California, USA, pp. 315, 2008.

Applications and Problems of Numerical Modeling of Nitrogen Transport in Agricultural Soils Using HYDRUS

K. Nakamura & S. Watanabe

Graduate School of Agriculture, Kyoto University, Kyoto, JAPAN

Y. Hirono

National Institute of Vegetable and Tea Science, Shizuoka, JAPAN

ABSTRACT: The HYDRUS code is considered to be useful for the numerical simulation of the simultaneous movements of water and nitrogen in soil. Application of the nitrogen transport model to the upland field reveals splitting up the fertilizer applications into at least two times could lower the risk of N leaching to groundwater. Another application of the model to the paddy field applied with manure liquid is to estimate the amounts of N transformations (mineralization, nitrification, and denitrification) which could not be measured directly. The nitrogen model is expected to establish the fertilizer application scheduling and irrigation scheduling for reducing the nitrogen effluent to environment while supporting and nutrient uptake and profitable yields. In the applications of the model, it is very important to determine the appropriate first-order reaction rate coefficients of N transformations. These coefficients depend on various factors such as temperature, water content, redox potential, pH, and so on, and should include the effect of these factors. We demonstrate the dependencies of nitrification in the upland soil on soil temperature and soil water content, the dependencies of mineralization, nitrification, and denitrification of the paddy soil on soil depth, and the dependency of denitrification of the paddy soil on infiltration rate. Incorporating of these dependences to the nitrogen transport model is needed.

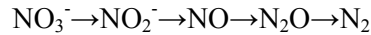
1 INTRODUCTION

Groundwater nitrate contamination and eutrophication of water bodies are common problems in the world. Quantitative, technical information related to nitrogen is needed to help farmers make management decisions that support profitable yields while avoiding environmental degradation. Nitrogen transport in soils is modeled numerically incorporating solute transport equation with water movement and nitrogen transformations. Various forms of nitrogen exists in soils and soil microbes convert nitrogen forms intricately by mineralization, immobilization, nitrification, denitrification, and nitrogen fixation. The HYDRUS-1D code (Šimůnek et al., 2005; 2008) for simulating the one-dimensional movement of water, heat, and multiple solutes in variably-saturated media is considered to be very useful for the numerical modeling of the simultaneous water and nitrogen transports in soils using the Richards' equation, the convection-dispersion equation and the first-order reaction rate equations for nitrogen transformations. We showed some examples of applications to upland and paddy soils. Determination of the first-order reaction rate coefficients of N transformations is critical for the appropriate nitrogen transport estimation. N transformations depend on some soil environmental factors. Here, the dependences of the reaction rate coefficients of N transformations on soil temperature, soil water content, soil depth, and infiltration rate are examined.

2 MODEL DESCRIPTION

2.1 Nitrogen transformation

Various forms of nitrogen exist in soil. Nitrogen transformations are the cycling of N among organic forms, inorganic forms (ammonium: NH_4^+ , nitrate: NO_3^- , nitrite: NO_2^-), and gaseous forms (molecular nitrogen: N_2 , nitrous oxide: N_2O , ammonia: NH_3 , nitric oxide: NO). Mineralization is defined as the transformation of N from the organic state into the inorganic forms of NH_4^+ or NH_3 (Jansson and Persson, 1982). N immobilization is defined as the transformation of inorganic N compounds (NH_4^+ , NH_3 , NO_3^- , NO_2^-) into the organic state through the assimilation by soil organisms (Jansson and Persson, 1982). The net mineralization is the difference between the mineralization and the immobilization and depends on the C/N ratio of soil organic matter. Nitrification is the process of the oxidation of NH_4^+ into NO_2^- and NO_2^- into NO_3^- by the nitrifying bacteria. Nitrification takes place in virtually all soils where NH_4^+ is present and conditions are favorable with respect to the major factors of temperature, moisture, pH, and aeration (Schmidt, 1982). Nitrifying bacteria are strictly aerobic and prefer nearly neutral conditions (pH=7). It was reported that N_2O emitted during nitrification of NH_4^+ (Cheng et al., 2004). Denitrification is the respiratory process by the denitrifying bacteria in the absence of molecular oxygen (O_2) while reducing NO_3^- or NO_2^- to N_2 and/or N_2O . The pathway of N oxide reduction during denitrification is generally thought to be (Firestone, 1982):



In paddy soil, NO_3^- moves to the reduced layer just below the surface layer with infiltration and is denitrified in the reduced layer in paddy soil. Biological N fixation is the transformation of atmospheric N_2 into NH_4^+ by the nitrogen-fixing microorganisms. Volatilization of NH_3 is the chemical process through which NH_4^+ in soil is returned to the atmosphere and depends on soil pH, wind speed, and NH_3 concentration in the atmosphere (Ritter and Bergstrom, 2001). Volatilization of NH_3 increases from alkaline soil induced by the excessive fertilization and from ponding water, in which the activity of photosynthetic organism is high, in a paddy field. Atmospheric NH_3 returns to soil by dry and wet depositions.

As mentioned above, N transformations are very complicated processes which are affected by various soil environmental factors (temperature, water content, pH, redox potential, C amount, etc.). It is important to simplify the N transformation processes in order to incorporate them into the convection-dispersion equation. Oxidation of NO_2^- in the process of nitrification is more rapid than that of NH_4^+ , so that only rarely in natural soils is there more than trace amounts of NO_2^- present (Schmidt, 1982). Furthermore, we can lump N_2 , N_2O , NO , and NH_3 together as gaseous N (Gas-N). Simplified N transformation model is given in **Figure 1**.

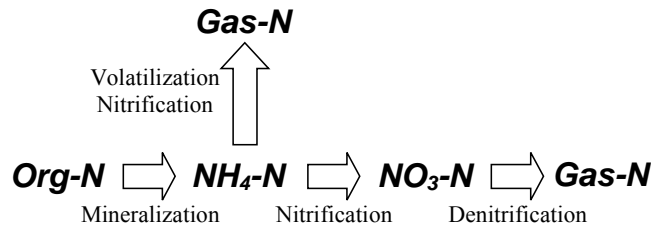


Figure 1. Simplified soil N transformation model.

N transformation processes are considered to be the chain reactions in chemical kinetics as shown in **Figure 1**. Temporal change in concentration of each form is expressed by the reaction rate equation. Most N transformations can be formulated by the first-order reaction rate equations,

$$\frac{dC_{\text{Org-N}}}{dt} = -k_{\text{min}} C_{\text{Org-N}} \quad (1)$$

$$\frac{dC_{\text{NH}_4\text{-N}}}{dt} = k_{\text{min}} C_{\text{Org-N}} - k_{\text{nit}} C_{\text{NH}_4\text{-N}} - k_{\text{los}} C_{\text{NH}_4\text{-N}} \quad (2)$$

$$\frac{dC_{\text{NO}_3\text{-N}}}{dt} = k_{\text{nit}} C_{\text{NH}_4\text{-N}} - k_{\text{den}} C_{\text{NO}_3\text{-N}} \quad (3)$$

where C is the concentration of N component in soil (mgN g^{-1}), t is time (h), and k is the first-order reaction rate coefficient (h^{-1}). Subscript min means mineralization, nit means nitrification, den means denitrification, and los means loss of N to the atmosphere by volatilization and nitrification. For examples, Tanji et al. (1979) and Zak et al. (1999) provided the value of k for mineralization. Ma et al. (1999) estimated the values of k for nitrification and denitrification.

2.2 Nitrogen transport

Governing equations of N components transport are the combination of the N transformation model and the convection-dispersion equation considering the adsorption of organic N and $\text{NH}_4\text{-N}$ and the nutrient uptake by the plant root. The one-dimensional partial differential equations governing three N components transport and transformations in a variably saturated porous media without the loss to the atmosphere by volatilization and nitrification ($k_{\text{los}}=0$) are

$$\frac{\partial \theta c_{\text{Org-N}}}{\partial t} + \frac{\partial \rho s_{\text{Org-N}}}{\partial t} = \frac{\partial}{\partial z} \left(\theta D_{\text{Org-N}} \frac{\partial c_{\text{Org-N}}}{\partial z} \right) - \frac{\partial q c_{\text{Org-N}}}{\partial z} - k_{\text{min(w)}} \theta c_{\text{Org-N}} - k_{\text{min(s)}} \rho s_{\text{Org-N}} \quad (4)$$

$$\begin{aligned} \frac{\partial \theta c_{\text{NH}_4\text{-N}}}{\partial t} + \frac{\partial \rho s_{\text{NH}_4\text{-N}}}{\partial t} = & \frac{\partial}{\partial z} \left(\theta D_{\text{NH}_4\text{-N}} \frac{\partial c_{\text{NH}_4\text{-N}}}{\partial z} \right) - \frac{\partial q c_{\text{NH}_4\text{-N}}}{\partial z} \\ & + k_{\text{min(w)}} \theta c_{\text{Org-N}} + k_{\text{min(s)}} \rho s_{\text{Org-N}} \\ & - k_{\text{nit(w)}} \theta c_{\text{NH}_4\text{-N}} - k_{\text{nit(s)}} \rho s_{\text{NH}_4\text{-N}} - S c_{\text{NH}_4\text{-N}} \end{aligned} \quad (5)$$

$$\begin{aligned} \frac{\partial \theta c_{\text{NO}_3\text{-N}}}{\partial t} = & \frac{\partial}{\partial z} \left(\theta D_{\text{NO}_3\text{-N}} \frac{\partial c_{\text{NO}_3\text{-N}}}{\partial z} \right) - \frac{\partial q c_{\text{NO}_3\text{-N}}}{\partial z} \\ & + k_{\text{nit(w)}} \theta c_{\text{NH}_4\text{-N}} + k_{\text{nit(s)}} \rho s_{\text{NH}_4\text{-N}} - k_{\text{den}} \theta c_{\text{NO}_3\text{-N}} - S c_{\text{NO}_3\text{-N}} \end{aligned} \quad (6)$$

where c is the soluble concentration (mgN cm^{-3}), s is the adsorbed concentration (mgN g^{-1}), ρ is the bulk density (g cm^{-3}), D is the dispersion coefficient ($\text{cm}^2 \text{h}^{-1}$) for soluble component, θ is the volumetric water content, q is the Darcian fluid flux density (cm h^{-1}), z is the vertical coordinate (cm), t is time (h), and S is the root uptake term ($\text{cm}^3 \text{cm}^{-3} \text{h}^{-1}$). Adsorption isotherms for organic N and $\text{NH}_4\text{-N}$ obtained from the measurements were fitted to the linear adsorption equation or the Freundlich type equation. Sorption of nitrate was considered to be negligible. The dispersion coefficient of soluble substance is calculated by the longitudinal dispersivity (D_L), the molecular diffusion coefficient in free water (D_w), the tortuosity factor in the liquid phase (τ), and q .

$$\theta D = D_L |q| + \theta D_w \tau \quad (7)$$

D_L can be determined using the optimization based on the measured concentrations of N components (Nakamura et al., 2004). D_w was 0.064 and 0.069 $\text{cm}^2 \text{h}^{-1}$ for $\text{NH}_4\text{-N}$ and $\text{NO}_3\text{-N}$, respectively (Ma et al., 1999). D_w of organic N was assumed to be 0.06 $\text{cm}^2 \text{h}^{-1}$. The k means the first-order transformation rate constant. Subscript (w) and (s) for the k_{min} and k_{nit} mean the conversion of soluble N component and adsorbed N component, respectively. But, it is impossible to specify exactly whether soluble component only, adsorbed component only, or both forms of N are converted in the processes of mineralization and nitrification. There are no research examples on this issue. It is assumed in the later model applications that both forms of N components

were simultaneously converted at the same rate ($k_{\min(w)}=k_{\min(s)}$ and $k_{\text{nit}(w)}=k_{\text{nit}(s)}$). These first-order reaction constants can be estimated based on the batch tests (Nakamura et al., 2004).

Vertical water movement in isotropic soil is computed by solving Richards' equation,

$$\frac{\partial \theta}{\partial t} = \frac{\partial}{\partial z} \left[K(\theta) \frac{\partial h}{\partial z} + K(\theta) \right] - S \quad (8)$$

where K is the unsaturated hydraulic conductivity (cm h^{-1}) and h is the pressure head (cm).

The numerical simulation of Equations (4)-(6) with soil water movement which is formulated by Equation (8) was conducted by using Version 3.0 of HYDRUS-1D, a software package for simulating water, heat, and solute movement in one-dimensional variably saturated media on the basis of finite element representation of the governing equations (Šimůnek et al., 2005). Nakamura and Toride (2007) demonstrated the possibility of the application to the upland soil and the paddy soil by setting the first-order reaction rate coefficients for the oxidized layer and the reduced layer.

3 APPLICATIONS OF MODEL TO AGRICULTURAL FIELDS

3.1 Fertilizer management in an upland field

3.1.1 Introduction

Inadequate management of N in agricultural environment has induced various environmental problems related to N, for example, eutrophication of lakes or ponds, global warming by N_2O , and groundwater NO_3^- contamination. Groundwater NO_3^- contamination caused by excessive fertilizer application is a common problem in field crops and dairy areas all over the world. Japanese agricultural areas are no exception.

Various management practices have been proposed to control NO_3^- leaching to groundwater. Adequate fertilizer application is a key issue. Split-application of N fertilizer during a cropping period is generally known to reduce the leaching potential for NO_3^- -N (Nakamura et al., 2004).

3.1.2 Materials and methods

We performed a long-term assessment of split-application practices for reducing N leaching in cultivated Japanese upland soils (sand and andosol, which were sampled in Tottori Prefecture, Japan) combining experimental and simulation approaches. N transformation considered in this study was only nitrification because batch tests showed that only nitrification occurred in both unsaturated upland soils. We used the HYDRUS software package to simulate several irrigation and fertilizer management scenarios based on 1992-2000 meteorological data including water and nutrient uptakes by two crops, watermelon and tomato. They are grown during each calendar year. The root zone was set to be 30cm deep with uniform root distribution during the entire two growing seasons of each year. Availability of HYDRUS was confirmed through the results of transient nitrogen and water transport experiments using soil columns with an inside diameter of 5cm and a length of 30cm.

3.1.3 Results and discussions

Figure 2 shows the simulated temporal changes in the cumulative seepage N fluxes for the andosol. It was concluded that two split applications instead of a single lumped application reduced the N leaching fraction by approximately one-third for the specific Japanese soils and climate conditions simulated. In the sandy soil, a three-way split resulted in further leaching reductions compared to the two-way split. Six-way split applications did not result in further N leaching improvements in either sand or andosol. Split application increased N root uptake and lowered the amount of soluble N in the deeper soil profiles.

We can recommend that in fertigation, combining irrigation and fertilizer application, where it is easy to control the amount and frequency of water and fertilizer, split fertilizer application should be implemented to the maximum extent possible. This will also reduce the risk of leach-

ing losses due to unforeseen rainfall events. In conventional broadcast application of fertilizer, it is recommended to split the necessary amount of fertilizer into at least two applications to lower the risk of N leaching to groundwater.

The leaching risk simulations showed that timing of rainfall or irrigation relative to fertilizer application is as critical as the total amount of precipitation or irrigation during growing season and the large amount of interannual variability in N leaching was observed. These explain the difficulties encountered in field experiments to establish definite benefits based on only 1 to 3 yr of experimental data. Simplified models and sensitivity analyses such as the one implemented here considering more realistic physical transient water and N movement in the root zone can provide a significant scientific basis for the evaluation of alternative nutrient management methods.

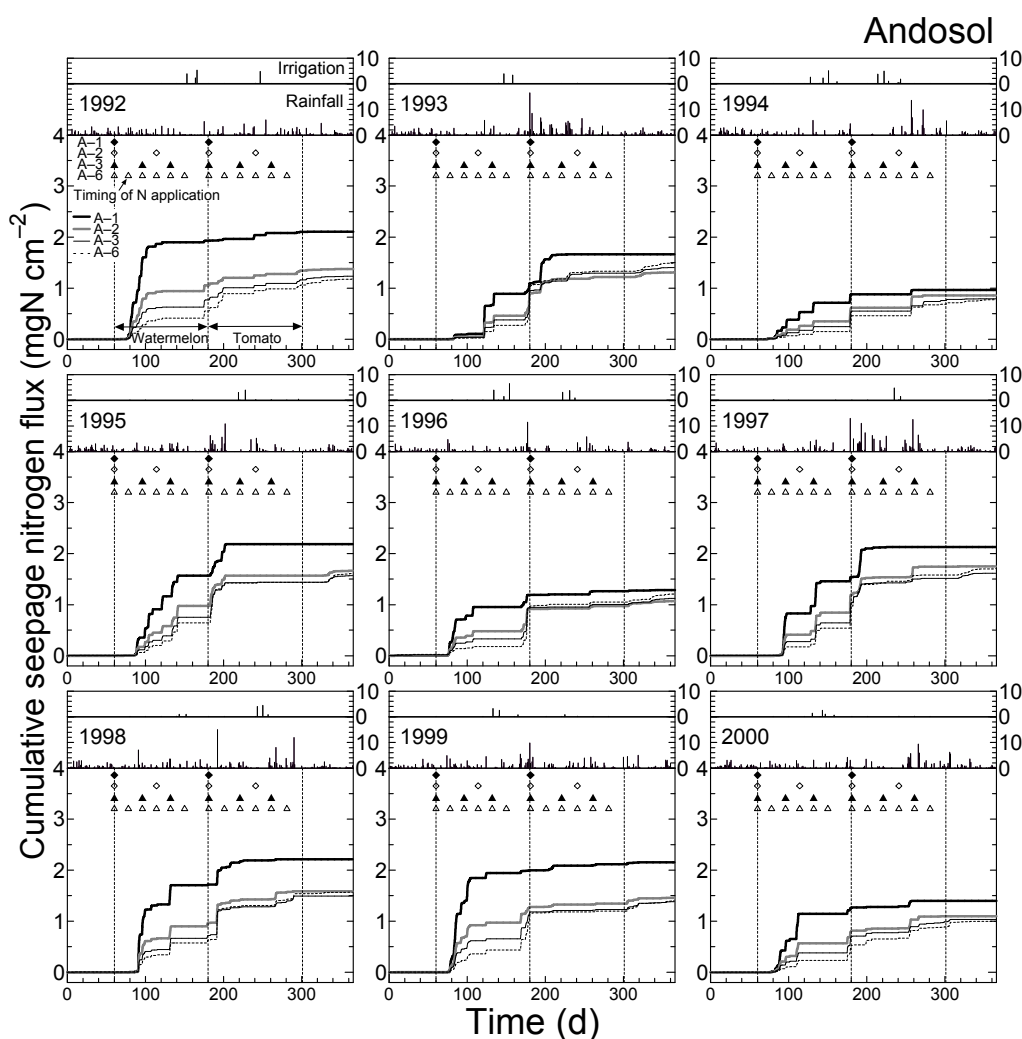


Figure 2. Temporal changes in the precipitation and irrigation (cm d^{-1}) and simulated temporal changes in the cumulative seepage N fluxes for the andosol. Heavy solid, heavy gray solid, thin solid, and thin dotted lines represent the case of lumped (A-1), two-split (A-2), three-split (A-3), and six-split (A-6) applications, respectively. Symbols represent the timing of $\text{NH}_4\text{-N}$ applications for each scenario.

3.2 Nitrogen transformations in paddy soil applied with manure liquid

3.2.1 Introduction

The methane fermentation technique produces power and heat by the treatment of animal waste and leftover food. This technique is nowadays drawing public attention as a good option for utilization of biomass resources. However, treatment of the by-product of fermentation, called methane fermentation manure liquid (ML), has been very costly. For establishing the sustainable recycle system of the by-product in a region, we should examine the possibility to apply this ML to paddy fields as a fertilizer because it contains $\text{NH}_4\text{-N}$, organic N, phosphorous, and potassium. When the ML application to paddy plots is considered, it is important to examine whether specific application design is necessary since the ML contains high level of organic compound unlike in the case of the chemical fertilizer.

Most of existing researches on nitrogen fate in the agricultural soils applied with organic matter such as dairy effluent, compost, or crop residues have covered various upland fields. For example, Woodard et al. (2002) evaluated forage system with dairy effluent; Nendel et al. (2004) derived the N-mineralization potential for vineyard soils applied with bio-waste compost; Zaman et al. (2002) conducted a pasture field experiment applied with dairy shed effluent. Nitrogen mineralization in aerobic paddy soils was estimated by Roelcke et al. (2002). Only a limited amount of research for the actual paddy plot and under the condition of water flow has been carried out. Therefore, there is a need to improve our understanding for the actual paddy plot applied with organic compounds and to model nitrogen transformation with water and nitrogen transport phenomena. Details were reported in Nakamura et al. (2007).

3.2.2 Materials and methods

We set up one field plot applied with the ML in Kyoto Prefecture, Japan and measured soil quality and ponding water quality in 2005 and 2006. Soil was sampled from three zones (soil surface to 10cm deep, 10cm to 20cm deep, and 20cm to 30cm deep) at the same locations as ponding water sampling. Concentrations of DTN (dissolved total N), $\text{NH}_4\text{-N}$, $\text{NO}_2\text{-N}$, and $\text{NO}_3\text{-N}$ in the soil solution were measured after the extraction with distilled water. Total DTN and $\text{NH}_4\text{-N}$ including adsorbed components were determined after extraction with 100g L^{-1} of KCl solution.

In order to estimate the first-order reaction rate coefficients for N transformations in the paddy soil, three types of batch tests were conducted. The first experiment was the oxidized soil test, in which the ML was titrated onto the paddy soil in containers to ensure homogeneous soil moisture distribution corresponding to 0.8 of saturation and the $(\text{NH}_4)_2\text{SO}_4$ solution was similarly titrated corresponding to 200mgN kg^{-1} dry soil to the separate containers. After the solution was added, containers were incubated in the dark at 25°C for 0, 2, 7, 14, 21, and 28d. At the end of each incubation period, concentrations of items in each soil similar to the above were analyzed. The second one was the reduced soil test, in which the ML or the KNO_3 solution was applied to the soil corresponding to 1.0 of saturation. The KNO_3 solution was applied corresponding to 200mgN kg^{-1} . Then, distilled water was added in order to set the submerged condition in containers. Analyzed items and manner were same as in the case of the oxidized soil test. The third one is the ML volatilization test, in which original ML was stood still in the 1L of container with air vents and concentration of $\text{NH}_4\text{-N}$ was measured in order to estimate volatilization rate in the above two batch tests.

Furthermore, the experiment was conducted to investigate the amount of volatilized NH_3 at the ML application using a cylindrical soil column with an inside diameter of 24cm and a length of 30cm. Original ML was diluted to have the almost same $\text{NH}_4\text{-N}$ concentration (107mgN L^{-1}) as the actual ponding water in the ML plot after the basal application in 2006, and applied to the soil columns saturated with distilled water. Steady drainage flux from the bottom outlet of a column was 0.025cm h^{-1} . Ponding depth was kept to be 5cm by applying distilled water. Experimental period was about 140 hours. During the experimental period, NH_3 volatilized from ponding water was trapped in sulfuric acid solution and $\text{NH}_4\text{-N}$ concentration in this solution was measured.

A numerical N transformation and transport model was applied to determine the amount and the timing of mineralization. The numerical simulation model used was Version 3.0 of HYDRUS-1D (Šimůnek et al., 2005). We considered three N components (organic N, $\text{NH}_4\text{-N}$, and $\text{NO}_3\text{-N}$) in paddy soil applied with the ML. In the model here, volatilization of $\text{NH}_4\text{-N}$ was assumed to occur not from the soil, but from the ponding water because the ML was applied along

with irrigation water and then only irrigation water was run into a ML plot until the ML went around the plot. When the ML was applied as basal fertilizer, soil puddling was conducted at the same time. It was considered that almost $\text{NH}_4\text{-N}$ existed in the murky ponding water. We estimated the amount of mineralization after the ML application as the basal fertilizer in 2006 based on the simulation model neglecting water and nutrient uptakes due to the early growing stage of rice. Calculation duration was 33 days from June 3 to July 6 after the basal application. Because the surface of paddy plot was flooded during this period, we assumed that saturated steady water flow occurred in soil layer and set the saturated hydraulic conductivity to be 0.1cm h^{-1} as water flux. In general, paddy soil layer consists of oxidized layer and reduced layer (Kyuma, 2004). Oxidized layer is formed at the surface layer and its thickness is reported a few millimeters to 1 centimeter (Suzuki et al., 1999). Reduced layer is formed under the oxidized layer. In this simulation, the thickness of oxidized layer was assumed to be 0.5cm and that of reduced layer to be 49.5cm. The upper boundary conditions for organic N and $\text{NH}_4\text{-N}$ were given by the concentrations. We set organic N concentration as the amount of applied organic N divided by the infiltrated amount by soil water flow during 12 days. The rate of infiltrated amount of organic N was assumed to be constant. We set $\text{NH}_4\text{-N}$ concentration as the amount of applied $\text{NH}_4\text{-N}$ divided by the infiltrated amount and the volatilized amount from ponding water, which was estimated based on the NH_3 volatilization experiment, during 12 days because nitrogen concentrations in ponding water went down to lower values in about 12 days after the ML application.

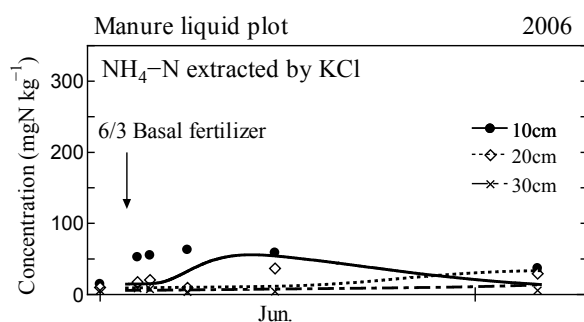


Figure 3. Measured and calculated soil $\text{NH}_4\text{-N}$ concentration changes in the plot applied with the ML. Dots represent measured data and lines calculated results.

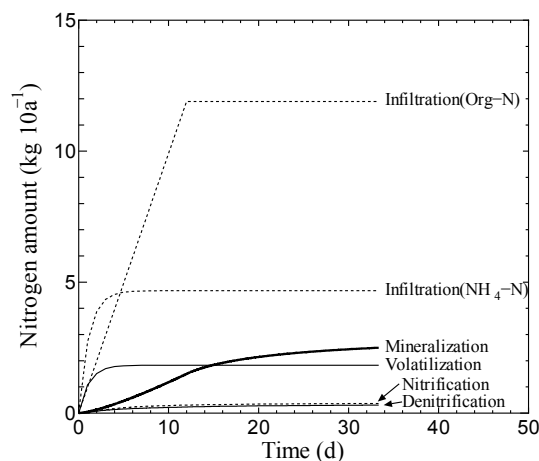


Figure 4. Simulated amount of N transformations (mineralization, nitrification, denitrification, and volatilization) and infiltrated N components after the basal ML application.

3.2.3 Results and discussions

The upper N boundary conditions were considered to be adequate because the change in $\text{NH}_4\text{-N}$ concentration at the upper boundary estimated in this calculation was consistent with the measured concentrations of ponding water. Simulated $\text{NH}_4\text{-N}$ concentration including adsorbed and soluble components is shown in **Figure 3** with measured data. Calculated $\text{NH}_4\text{-N}$ at the surface soil layer could represent the changing trend, but the rapid increasing of $\text{NH}_4\text{-N}$ could not be represented in the simulation. This is considered to be due to the effect of soil puddling at the

ML application and the uncertainty of soil water flux. Though there is room for improvement of the simulation conditions, we could figure out the trend of N transformations in soil.

The cumulative amounts of mineralization, nitrification, and denitrification, volatilization and infiltration of organic N and NH₄-N are shown in **Figure 4**. The cumulative volatilization amount (1.8 kg (10a)⁻¹) reached 28% of applied NH₄-N (6.5kg (10a)⁻¹). The cumulative mineralized nitrogen was 2.5 kg (10a)⁻¹. Loss of NH₄-N by volatilization was compensated by mineralization of organic nitrogen. The amounts of nitrification and denitrification were very small.

It is necessary to determine the timing of manure liquid application for higher N use efficiency considering mineralization rate and amount in soil and the rate of volatilization. The simulation model developed here is useful for the adequate plan of the ML application for rice growth. Future task is the establishment of the improved N transport model including N uptake by rice, evapotranspiration, rainfall, and distribution of oxidized and reduced zone during irrigation and non-irrigation period.

4 CHARACTERISTICS OF THE REACTION RATE OF N TRANSFORMATION

The N transport model in upland soil and paddy soil using HYDRUS code is useful tool to design the best management practices of water and fertilizer in the agricultural field. However, in spite of N transformation depends on various soil environmental factors as mentioned in section 2.1, we should give the first-order reaction rate coefficients of N transformations for each soil material set in the computational domain. Determination of the first-order reaction rate coefficients is critical for the appropriate simulation results. Here, characteristics of dependence of N transformation on some factors are described.

4.1 Temperature dependence and soil water content dependence

We conducted the batch tests to examine the temperature dependence and the soil water content dependence of nitrification of andosol sampled at an upland plot in Tottori Prefecture, Japan. The (NH₄)₂SO₄ solution was titrated onto the soil in containers to ensure homogeneous soil water distribution corresponding to 0.6 of saturation. Soil containers were incubated in the dark at 5, 15, 25, and 35 °C. Similarly, the (NH₄)₂SO₄ solution was titrated onto the soil to ensure soil water content corresponding 0.25, 0.4, 0.8, and 1.0 of saturation. These soil containers were incubated at 25 °C. Measured items were same as mentioned in section 3.2.2. The first-order reaction rate coefficients for nitrification were estimated for the rate of NO₃-N increase. Symbols in **Figure 5** showed the temperature dependence and the water content dependence of nitrification reaction rate coefficient.

N transformation depends on soil water and soil temperature. In the latest version 4 of HYDRUS-1D (Šimůnek et al., 2008), temperature dependence and water content dependence of reaction parameters can be newly incorporated.

The temperature dependence of reaction parameters is expressed by the modified Arrhenius equation in HYDRUS.

$$a_T = a_r \exp\left[\frac{E_a(T^A - T_r^A)}{R_u T^A T_r^A}\right] \quad (9)$$

where a_r and a_T are the values of the coefficient being considered at a reference absolute temperature T_r^A and absolute temperature T^A , respectively, R_u is the universal gas constant, and E_a is the activation energy of the particular reaction or process being modeled. Solid line in **Figure 5(a)** showed the fitted curve at temperature in the range of 5 to 25°C. The nitrification rate coefficient at 35°C was not explained by the Equation (9). It is necessary to incorporate the limitation factor to decrease the reaction rate coefficients of N transformations at higher temperature related to soil microbes.

The soil water dependence of reaction parameters is expressed by the following equation in HYDRUS.

$$a(\theta) = a_r (\theta_{ref}) \min \left[1, \left(\frac{\theta}{\theta_{ref}} \right)^B \right] \quad (10)$$

where a_r and a are the values of the coefficient being considered at a reference water content θ_{ref} and actual water content θ , respectively, and B is the substance dependent value (usually 0.7). The reference water content, θ_{ref} which can be different for different soil layers is calculated from the reference pressure head h_{ref} , which is considered to be constant for a particular compound. When the actual water content θ is more than θ_{ref} , a equals to a_r , which is the maximum value of a . It means that the increase of soil water content induces the increase of the value of reaction parameters. N transformation, however, also depends on soil redox condition. The increase of soil water content and the oxygen consumption might cause the development of reduction state and the decrease of nitrification rate. It is insufficient to consider only water content dependence.

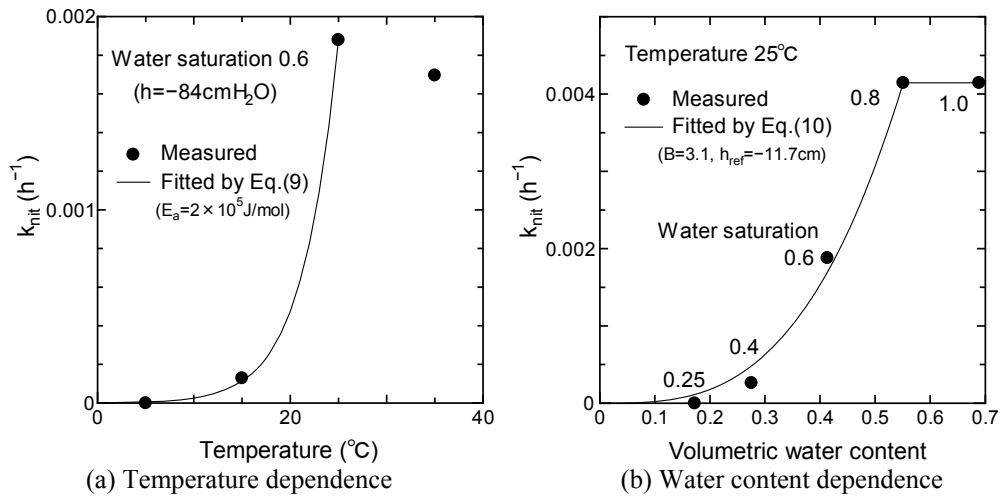


Figure 5. Temperature dependence and the soil water content dependence of the first-order reaction rate coefficient of nitrification for the andosol. Symbols represent the measured values. Solid lines represent fitted curves by Equations (9) and (10).

4.2 Soil depth dependence

N transformation reaction rate coefficients for mineralization, nitrification, and denitrification are expected to be dependent on soil depth. We conducted the batch tests for paddy soil sampled from the three layers (soil surface to 30cm deep, 30cm to 60cm deep, and 60cm to 90cm deep) at a paddy plot in Shiga Prefecture, Japan. Two types of batch tests were conducted. The first experiment was under the condition of the oxidized and unsaturated paddy soil, in which the $(\text{NH}_4)_2\text{SO}_4$ solution was titrated onto the soil in containers to ensure homogeneous soil moisture distribution corresponding to 0.8 of saturation. Added $\text{NH}_4\text{-N}$ corresponded to 0, 100, 200, and 300 mg N kg⁻¹. After the solution was added, containers were incubated in the dark at 25°C for 0, 2, 7, 14, 21, and 28 d. Measurements were similar to section 3.2.2. Additionally, total N and total C of soil were analyzed by dry combustion method. The second one was under the condition of the reduced and submerged soil, in which the KNO_3 solution was applied to the soil corresponding to 1.0 of saturation. The KNO_3 solution was applied corresponding to 0, 9, 19, and 280 mg N kg⁻¹. Then, distilled water was added in order to set the submerged condition in containers. Incubation periods were 0, 2, 6, 11, 21, and 37 d. Analyzed items were same as in the case of the oxidized soil test.

Temporal changes in measured N forms exhibited the zero-order N transformation reaction rate as shown in **Figure 6**. Because temporal changes in concentrations of N components in these batch tests were fitted more adequately by the zero-order reaction equations rather than the first-order reaction equations, reaction rate coefficients for the soil used here were assumed to zero-order. Reaction rate coefficients are derived into a chain reaction as follows. The zero-

order reaction rate coefficient of mineralization k_{\min} could be estimated from the temporal change in organic N. The zero-order reaction rate coefficient of denitrification k_{den} could be estimated from the temporal change in inorganic N ($\text{NH}_4\text{-N} + \text{NO}_2\text{-N} + \text{NO}_3\text{-N}$) and the value of k_{\min} estimated already. The zero-order reaction rate coefficient of nitrification k_{nit} could be estimated from the temporal change in the sum of $\text{NO}_2\text{-N}$ and $\text{NO}_3\text{-N}$ and k_{den} . Volatilization of NH_3 from the containers was neglected because soil solution was not alkaline. **Figure 7** shows the soil depth dependence of reaction rate coefficients and the concentration of total C at the start of the tests.

The reaction rate coefficients of all N transformations were the highest in the soil layer near the soil surface. The concentration of total C was also the highest near the soil surface. Especially, the denitrification rate coefficient might be affected by the total C distribution in soil profile. The number of soil microorganisms contributing to mineralization, nitrification, and denitrification might be smaller in deeper soil zone. In HYDRUS, different reaction rate coefficients can be given by setting different soil materials. Because the decrease of reaction rate coefficient with depth is in an exponential or a linear manner, it is considered to be convenient to set up some functions of the soil depth dependence of reaction rate coefficients.

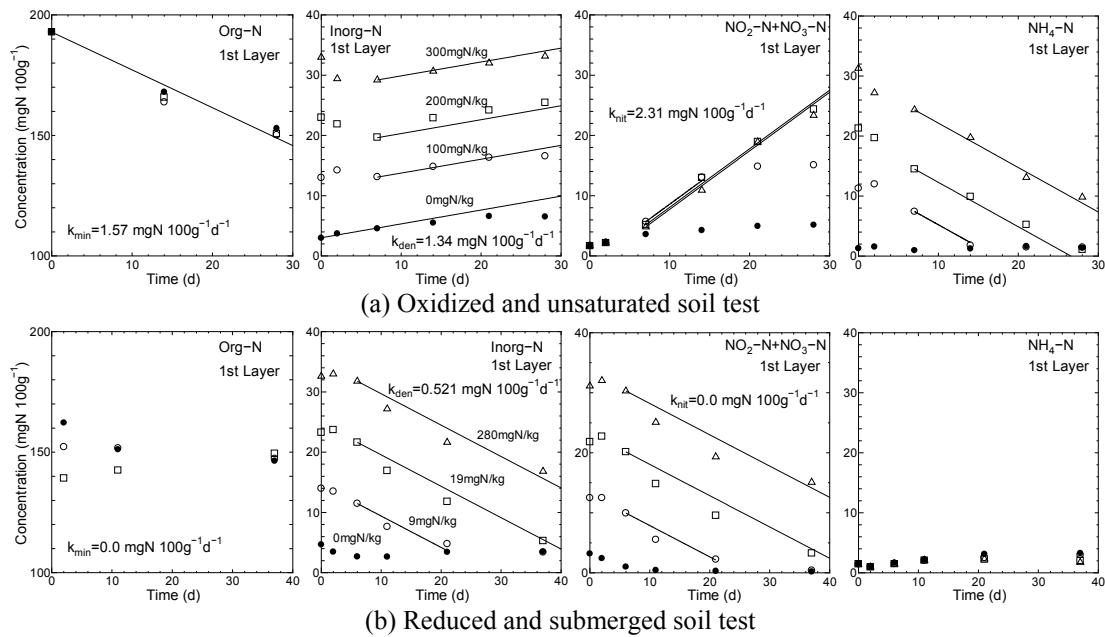


Figure 6. Temporal changes in the concentrations of organic N, inorganic N, $\text{NO}_2\text{-N} + \text{NO}_3\text{-N}$, and $\text{NH}_4\text{-N}$ in the soil layer from the soil surface to 30cm deep in (a) the oxidized and unsaturated soil test and (b) the reduced and submerged soil test. Organic N and $\text{NH}_4\text{-N}$ are total amounts including soluble and adsorbed components. Solid lines represent are fitted by using the zero-order reaction formula for N transformations.

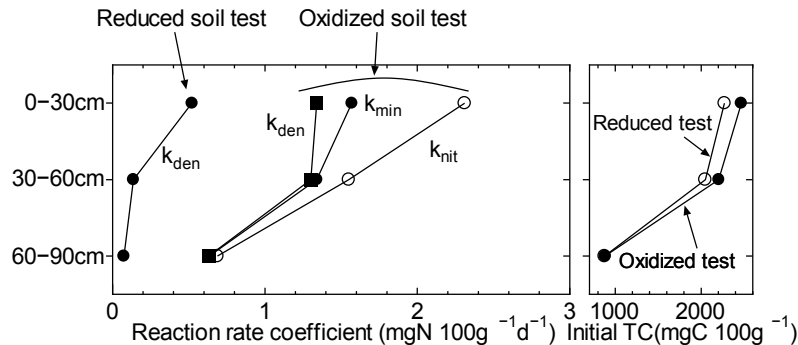


Figure 7. Soil depth dependence of the zero-order reaction rate coefficients of N transformations and the initial total C concentration for the oxidized soil test and the reduced soil test using the paddy soil.

4.3 Infiltration rate dependence

It is considered that the infiltration rate may affect on the amounts of denitrification. We conducted a laboratory experiment using the soil column (Watanabe et al., 2008). Paddy soils, which were sampled in Kyoto Prefecture, Japan, were packed in soil columns with inside diameters of 10.5cm and lengths of 40cm, and subsequently saturated by ponding. Different infiltration rate was given to each soil column by setting different hydraulic gradient. Top-dressing of the KNO_3 solution was given continuously during the experimental period and methanol, which is a hydrogen donor and carbon source for denitrification, was additionally applied from 8 days after the start of the experiment till the end. Concentrations of cations and anions including $\text{NO}_3\text{-N}$ in leachate and soil solution at three different depths (2.5, 17.5, and 32.5cm deep) were measured. We investigated the relationship between the ratio of denitrified nitrogen to $\text{NO}_3\text{-N}$ input and the infiltration rate (**Figure 8**). Under the soil condition limited by methanol, the ratio of denitrification to $\text{NO}_3\text{-N}$ input decreased linearly with increasing infiltration rate from 100 to 450 mm d^{-1} . Below the infiltration rate of 200 mm d^{-1} under rich methanol condition, the denitrification rate was not controlled by the infiltration rate. The relationship between denitrification rate and infiltration rate depended on the amount of carbon in the soil.

We estimated the first-order denitrification rate coefficients for the low infiltration rate (192.5 mm d^{-1}) and the high infiltration rate (447.1 mm d^{-1}) from the measured $\text{NO}_3\text{-N}$ concentration of the leachate under the condition limited by methanol using the inverse solution procedure of HYDRUS-1D version 4 (Šimůnek et al., 2008). The steady water flow was assumed. The estimated first-order denitrification rate coefficient was 0.505 d^{-1} for the low infiltration rate and 0.104 d^{-1} for the high infiltration rate. The possibility of the infiltration rate dependence of the first-order reaction rate coefficient of N transformation was shown.

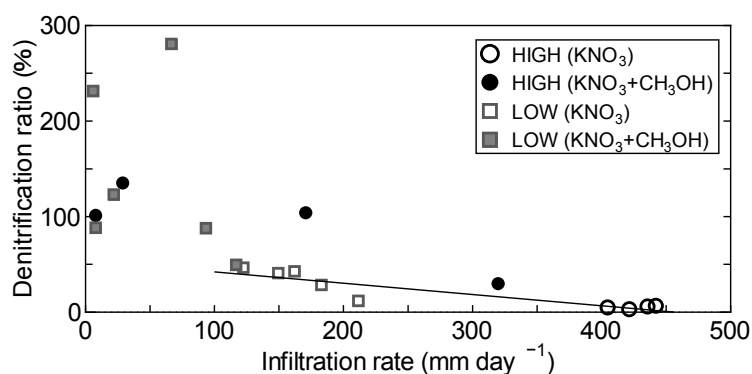


Figure 8. Relationship between the denitrification ratio, defined as the ratio of denitrified N to $\text{NO}_3\text{-N}$ input, and the infiltration rate in a paddy soil. HIGH and LOW mean high and low hydraulic gradient, respectively. Solid line represents the approximate relationship under the condition limited by methanol.

5 CONCLUSIONS

If we can set the first-order reaction rate coefficients of N transformations adequately considering the redox characteristics of soil profiles, the temperature dependence, the soil water content dependence, the soil depth dependence, the soil C dependence, and the infiltration rate dependence, and so on, it is possible to establish the appropriate N transport model for agricultural soils, estimate the amount of N transformations, and suggest the best water and N management practices to reduce N loads to environment. More examination on the characteristics of N transformation rate should be conducted. Furthermore, the simultaneous water, heat, and nitrogen transport model including redox potential, pH, and the concentration of C as variables may be necessary.

REFERENCES

- Cheng, W., Tsuruta, H., Chen, G., and Yagi, K. 2004. N_2O and NO production in various Chinese agricultural soils by nitrification, *Soil Biology & Biochemistry*, 36, pp.953-963.
- Firestone, M.K. 1982. Biological denitrification. *Nitrogen in agricultural soils*, Agronomy No.22 (Stevenson, F.J. (ed.)), pp.289-326, ASA, CSSA, SSSA, Medison, WI.

- Jansson, S.L. and Persson, J. 1982. Mineralization and immobilization of soil nitrogen. *Nitrogen in agricultural soils*, Agronomy No.22 (Stevenson, F.J. (ed.)), pp. 229–252, ASA, CSSA, SSSA, Madison, WI.
- Kyuma, K. 2004. *Paddy Soil Science*, Kyoto University Press, Trans Pacific Press, pp.255-277.
- Ma, L., Lindau, C.W., Hongprayoon, C., Burhan, W., Jang, B.C., Patrick, W.H., and Selim, H.M. 1999. Modeling urea, ammonium, and nitrate transport and transformations in flooded soil columns, *Soil Sci.*, 164, pp.123-132.
- Nakamura, K., Harter, T., Hirono, Y., Horino, H., and Mitsuno, T. 2004. Assessment of Root Zone Nitrogen Leaching as Affected by Irrigation and Nutrient Management Practices, *Vadose Zone Journal*, 3, pp.1353-1366.
- Nakamura, K., Funamoto, K., and Mitsuno, T. 2007. Nitrogen Management in a Paddy Plot Applied with Methane Fermentation Manure Liquid, *Proceeding of PAWEES 2007 6th International Conference on Sustainable Rural Development and Management*, pp.202-221.
- Nakamura, K. and Toride, N. 2007. Numerical Modeling of Nitrogen Transport with First-Order Transformation Processes in Soils, *Journal of the Japanese Society of Soil Physics*, 105, pp.83-97. (in Japanese)
- Nendel, C., Reuter, S., Kubiak, R., and Nieder, R. 2004. Nitrogen mineralization from manure bio-waste composts in vineyard soils 1, Long-term laboratory incubation experiments, *J. Plant Nutr. Soil Sci.*, 167, pp.397-407.
- Ritter, W.F. and Bergstrom, L. 2001. *Agricultural nonpoint source pollution – Watershed management and hydrology* – (Ritter, W.F. and A. Shrimohammadadi (ed.)), pp.59-89, Lewis Publishers, USA.
- Roelcke, M., Han, Y., Cai, Z., and Richter, J. 2002. Nitrogen mineralization in paddy soils of the Chinese Taihu Region under aerobic conditions, *Nutrient Cycling in Agroecosystems*, 63, pp.255-266.
- Schmidt, E.L. 1982. Nitrification in soil. *Nitrogen in agricultural soils*, Agronomy No.22 (Stevenson, F.J. (ed.)), pp.253-288, ASA, CSSA, SSSA, Madison, WI.
- Šimůnek, J., van Genuchten, M. Th., and Sejna, M. 2005. *The HYDRUS-1D software package for simulation the one-dimensional movement of water, heat, and multiple solutions in variably-saturated media*, Version 3.0., HYDRUS software series 1, Dep. of Environmental Sciences, UCR, Riverside, CA.
- Šimůnek, J., Sejna, M., Saito, H., Sakai, M., and van Genuchten, M.Th. 2008. *The HYDRUS-1D software package for simulation the one-dimensional movement of water, heat, and multiple solutes in variable-saturated media*, Version 4.0, Dep. of Environmental Sciences, UCR, Riverside, CA.
- Suzuki, S., Okazaki, M., Kosaki, T. 1999. Characteristics of paddy soils, *Advanced Paddy Field Engineering*, Editorial committee of advanced paddy field engineering, The Japanese society of irrigation, drainage and reclamation engineering, Shizan-sha Sci.&Tech., pp.11-30.
- Tanji, K.K., Broadbent, F.E., Mehran, M., and Fried, M. 1979. An extended version of a conceptual model for evaluating annual nitrogen leaching losses from croplands, *J. Environ. Qual.*, 8(1), pp.114-120.
- Zak, D.R., Hilmes, W.E., MacDonald, N.W., and Pregitzer, K.S. 1999. Soil temperature, matric potential, and kinetics of microbial respiration and nitrogen mineralization, *Soil Sci. Soc. Am. J.*, 63, pp.575-584.
- Zaman, M., Cameron, K.C., Di, H.J., and Inubushi, K. 2002. Changes in mineral N, microbial biomass and enzyme activities in different soil depths after surface applications of dairy shed effluent and chemical fertilizer, *Nutrient Cycling in Agroecosystems*, 63, pp.275-290.
- Watanabe, S., Nakamura, K., Hama, T., and Kawashima, S. 2008. Effect of infiltration rate on denitrification in a ponded soil column, *Proceeding of 5th International Conference Interfaces Against Pollution 2008*, p.253.
- Woodard, K.R., French, E.C., Sweat, L.A., Graetz, D.A., Sollenberger, L.E., Macoon, B., Portier, K.M., Wade, B.L., Rymph, S.J., Prine, G.M., and Van Horn, H.H. 2002. Nitrogen removal and nitrate leaching for forage systems receiving dairy effluent, *J. Environ. Qual.*, 31, pp.1980-1992.

Transport and Retention of Colloid-sized Materials in Saturated Porous Media: Experimental and Numerical Analysis

D.T.K.K. Chamindu¹⁾, K. Kawamoto¹⁾, H. Saito²⁾, T. Komatsu¹⁾ and Per Moldrup³⁾

1) Department of Civil and Environmental Engineering, Saitama University, Saitama, Japan

2) Institute of Symbiotic Science and Technology, Tokyo University of Agriculture and Technology, Japan

3) Department of Biotechnology, Chemistry and Environmental Engineering, Alborg University, Denmark

ABSTRACT: Transport of colloids in subsurface is the underlying process governing colloid-facilitated contaminant transport in soils causing groundwater contamination. Colloid attachment and straining are known as key mechanisms of colloid retention/filtration in porous media. This study investigated attachment and straining of colloid-sized glass beads (diameter 1-10 μm) and soil colloids (diameter less than 1 μm) extracted from a volcanic ash soil in saturated sand (Toyoura sand) by means of a series of column experiments at several colloid concentrations and flow rates. In the column experiments, colloid breakthrough and breakdown curves in the effluents as well as colloid deposition profiles in sand columns were examined. Results revealed strong dependence of colloid transport on flow rates. Numerical analysis was carried out using HYDRUS 1D program code based on one-site (first-order Langmuirian attachment & detachment) as well as two-site (first-order Langmuirian attachment, detachment and straining) deposition models. Numerical analysis revealed that both analyses failed to capture the multi peaks in deposition profiles.

1 INTRODUCTION

Colloidal particles with effective diameter less than 10 μm (e.g. clays, metal oxides, humic substances, microorganisms etc.) are ubiquitous in soil pore waters. Owing to their smaller size (high specific surface area) and high surface charge (predominantly electronegative), colloids are highly reactive in subsurface environments. As a result, highly sorptive contaminants adsorb onto mobile colloids and transport into groundwater causing groundwater contamination. Growing body of literature bears strong evidences to colloid-facilitated transport of various contaminants such as radionuclides, heavy metals, pesticides, microorganisms etc. Transport and retention of colloids in porous media is the underlying process governing colloid facilitated contaminant transport.

Both colloid attachment and straining play the dominant role in retention/filtration of colloids on porous media. Colloid attachment/detachment is a result of net interaction potential of colloids and grains i.e. the sum of the electrostatic double layer force, van der Waals forces, etc. (DeNovio et al., 2004) whereas colloid straining is the entrapment of colloid particles at the pore throats in down gradient flow that are too small for particle passage (Bradford et al., 2004). Further, colloid retention is influenced by various physicochemical parameters including initial colloid concentration and flow rate.

Although the understanding of colloid transport and retention has improved quite significantly over the past decade, mutual interactions among colloids and porous media still remains poorly understood.

This study investigated transport and retention of colloid-sized glass beads (1-10 μm) and soil colloids (less than 1 μm) in saturated Toyoura sand. Breakthrough and breakdown profiles of

colloids and tracer (Bromide) were observed at different colloid concentrations and flow rates by means of a series of column experiments. Colloid retention profiles for glass beads colloids were also observed.

HYDRUS 1D program was used to simulate colloid transport and deposition kinetics. Results of two different approaches to model colloid deposition kinetics are presented herein; One-site deposition model (including first-order Langmurian attachment and first-order detachment models) and two-site deposition model (including first-order straining model coupled with depth dependant straining function in addition to the aforementioned attachment and detachment models).

2 MATERIALS AND METHODS

2.1 Artificial rain water and colloidal solutions

Artificial Rain Water (ARW) was used as the eluent solution in all column experiments. The composition of ARW was 0.085mM NaCl₂ and 0.015mM CaCl₂. The ionic strength of the solution is close to that of natural rainwater.

Two kinds of colloidal solutions, Barium-Titanate glass beads solution and water dispersible soil colloidal solution (WDC), were employed in this study. For glass beads, colloidal solution was prepared by mixing correct mass of glass beads (MBP 1-10, The Association of Powder Process Industry and Engineering, Japan.) in ARW and by stirring for 1hour to obtain a uniform solution. The procedure of the preparation of soil colloidal solution is illustrated in Fig.1. The particle size distribution of each colloid type is shown in Fig.2. Table 1 shows the properties of both colloidal solutions. 0.01M NaBr was also added to colloidal solutions to observe the simultaneous transport of conservative tracer (bromide).

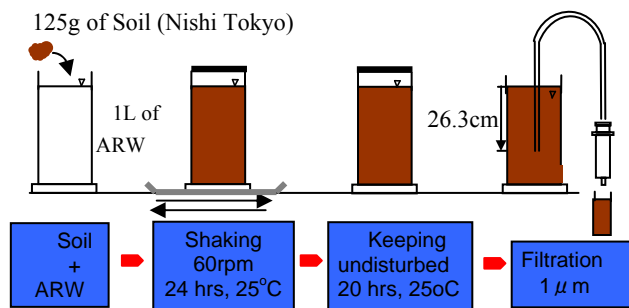


Fig.1 Main steps in extraction of soil colloids

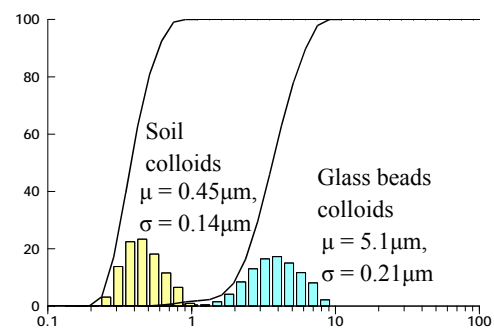


Fig.2 Particle size distribution of two colloid types

Table 1. Properties of colloidal solutions

Solution	Initial Concentration(C _o) (mg/L)	pH	EC (mS/m)	†ζ- Potential (mV)
BT glass beads (d _c =5.1μm)	250	6.1~6.8	1.3~1.5	-25.3
Soil Colloids (d _c =0.45μm)	30~110	6.4~7.1	9.3~9.6	-13.4

† measured at natural pH.

2.2 Column Experiments

Toyoura sand was used as the porous media in all column experiments. The mean diameter (d_{50}), particle density, dry bulk density and hydraulic conductivity are 0.18 mm, 2.64 g/cm³, 1.58 g/cm³ and 78.1 cm/hr respectively. The height and internal diameter of the column were 10cm and 4.91cm (Fig.3). A porous plate covered with a 105 μ m nylon mesh was placed at the bottom of the column to prevent loss of sand in the column. The cleaned Toyoura sand was wet packed (water level kept above sand surface) inside the column incrementally in 1cm layers. Initially 3 pore volumes of ARW was applied downward at a steady flow rate, after which a three-way valve was used to switch to the colloidal solution with 10 pore volumes, followed by another 5 pore volumes of ARW. The effluents were collected at an automatic fraction collector and the volume of the effluents, turbidity (turbidimeter 2100P, HACH), tracer concentration (Ion chromatograph, SHIMADZU, JP) particle size distribution (nano particle size analyzer, SALAD 7100, SHIMADZU, JP), EC and pH were determined.

Following completion of colloid transport experiment, the packed bed was dissected into 1cm sections and retained colloids were resuspended by ultrasonic vibration and extruded by filtration in order to obtain spatial distribution of retained colloids. Linear relationships between measured turbidity (NTU) and colloid concentration (mg/L) was developed and used to estimate colloid concentration.

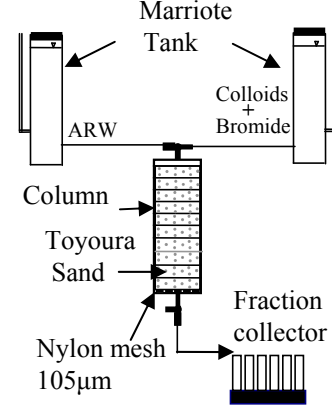


Fig. 3. Schematic of set up of column experiment

3 NUMERICAL MODELLING

The governing equation of colloid transport was based on the classical Fickian-based one dimensional convection-dispersion equation, but modified to take account for colloid deposition.

$$\frac{\partial \theta_w C_c}{\partial t} + \rho_s \frac{\partial S_c}{\partial t} = \frac{\partial}{\partial z} \left(\theta_w D_c \frac{\partial C_c}{\partial z} \right) - \frac{\partial q_c C_c}{\partial z} \quad [1]$$

where C_c [ML⁻³] is the aqueous phase colloid concentration, S_c [mM⁻¹] is the solid phase (deposited) colloid concentration, ρ_s [ML⁻³] is soil bulk density, θ_w [-] is colloid accessible water content (assumed to be equal to total water content in this study), D_c [L²T⁻¹] is hydrodynamic dispersion coefficient and q_c [LT⁻¹] is the volumetric flux density of the colloids.

In order to describe the essential features of colloid breakthrough as well as colloid deposition, the applicability of two filtration models was examined in this study. The one-site deposition model, including first-order attachment and detachment can be presented as follows;

$$\rho_s \frac{\partial S_c}{\partial t} = \rho_s \frac{\partial S_c^{att}}{\partial t} = \theta_w \psi_s k_{ac} C_c - \rho_s k_{dc} S_c \quad [2]$$

where S_c^{att} [mM⁻¹] is the attached solid phase concentration, k_{ac} [T⁻¹] and k_{dc} [T⁻¹] are first-order attachment and detachment coefficients respectively. Here, ψ_s [-], the colloid retention function, is assumed to be a Langmurian dynamic blocking function as expressed below;

$$\psi_s = 1 - \frac{S_c}{S_{max}} \quad [3]$$

where S_{max} [mM⁻¹] is the maximum solid phase concentration.

Two-site deposition model, on the other hand, included straining in addition to attachment and detachment through a first-order straining coefficient coupled with a depth-dependant straining function as follows;

$$\rho_s \frac{\partial S_c}{\partial t} = \rho_s \frac{\partial S_c^{att}}{\partial t} + \rho_s \frac{\partial S_c^{str}}{\partial t} = \theta_w \psi_s k_{ac} C_c - \rho_s k_{dc} S_c + \theta_w \psi_{str} k_{str} C_c \quad [4]$$

$$\psi_{str} = \left(\frac{d_{50} + z}{d_{50}} \right)^{-\beta} \quad [5]$$

where $k_{str} [T^{-1}]$ is first-order straining coefficient, $\psi_{str} [-]$ is the depth-dependant straining function and $\beta [-]$ is the shape factor.

Schematically, the two-site deposition model can be illustrated as shown in Fig.4. In the absence of straining, the two-site deposition model reduces to the one-site deposition model.

In this study, numerical simulation was carried out using HYDRUS 1D program code (Simunek et al., 2005). The HYDRUS 1D simulates water, heat and solute movement in one-dimensional variably saturated media and is coupled to a nonlinear least squares optimization routine based upon the Marquardt-Levenberg algorithm (Marquardt, 1963) to facilitate the estimation of transport parameters from experimental data. The governing flow and transport equations are solved numerically using Galerkin-type linear finite element schemes. (Simunek et al., 2006).

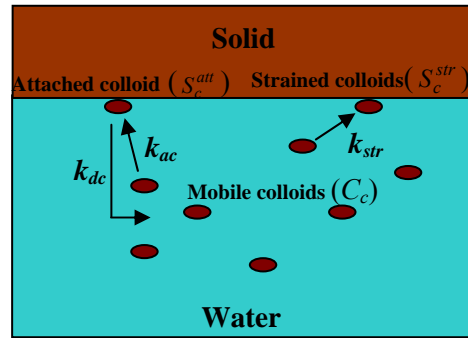


Fig.4. Schematic of two-site deposition model

4. RESULTS AND DISCUSSION

4.1 Glass beads Colloid Breakthrough and Deposition Profiles

The observed and simulated breakthrough curves and colloid deposition profiles of glass beads colloids at two different flow rates are illustrated in Fig.5. It can be seen that, for both flow rates, glass beads colloids showed essentially no breakthrough, suggesting that all glass beads colloids have been deposited inside sand. The simulated results showed that two-site deposition model significantly overestimated the colloid recovery whereas one-site model could reasonably predict the observed data. Both models, however, failed to predict the observed deposition multi peaks.

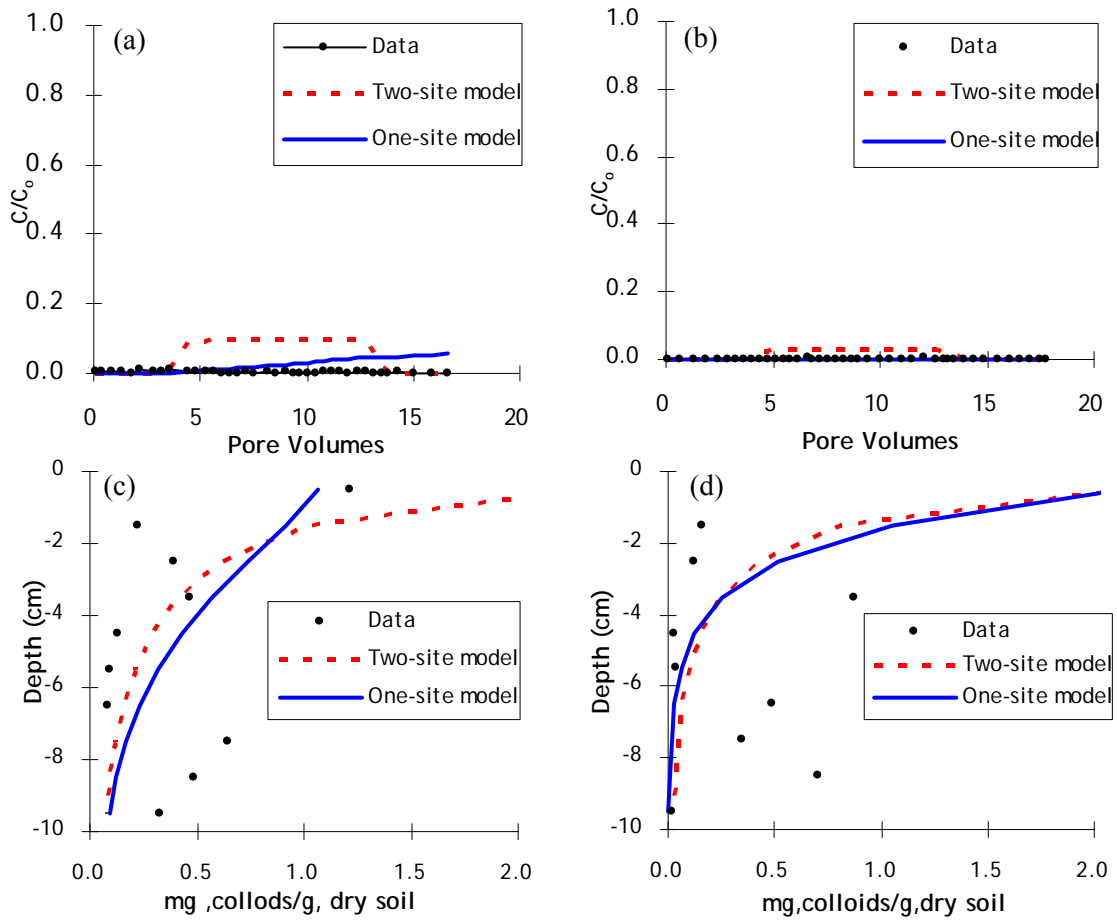


Fig.5. Breakthrough and breakdown curves of glass beads colloids at Darcy flow rates of (a) 0.45cm/min and (b) 0.42 cm/min. deposition profiles corresponding to (a) and (b) are shown in (c) and (d) respectively

The tracer Bromide, however, showed a distinct breakthrough curve for both flow rates (see Fig.6).

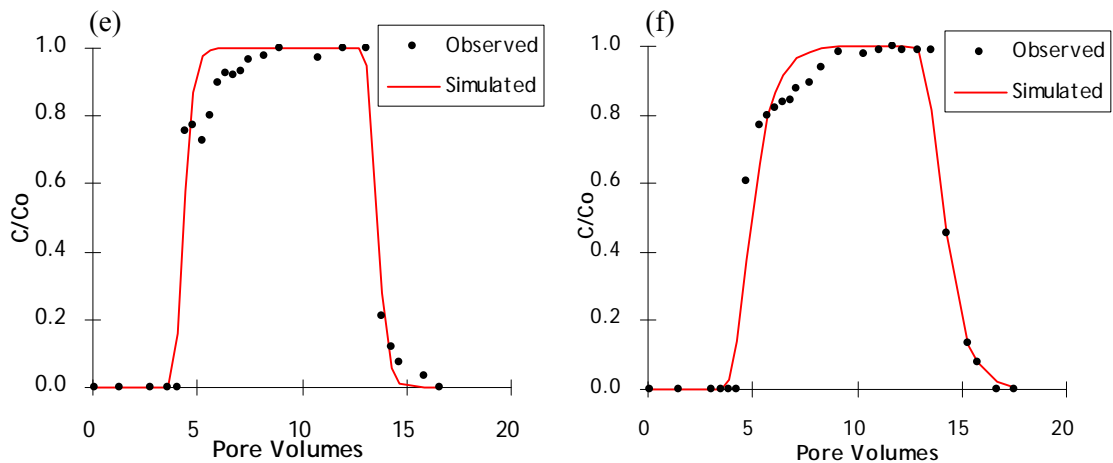


Fig.6 Observed and simulated breakthrough curves of bromide transport at Darcian velocities of (e) 0.45cm/min and (f) 0.42cm/min.

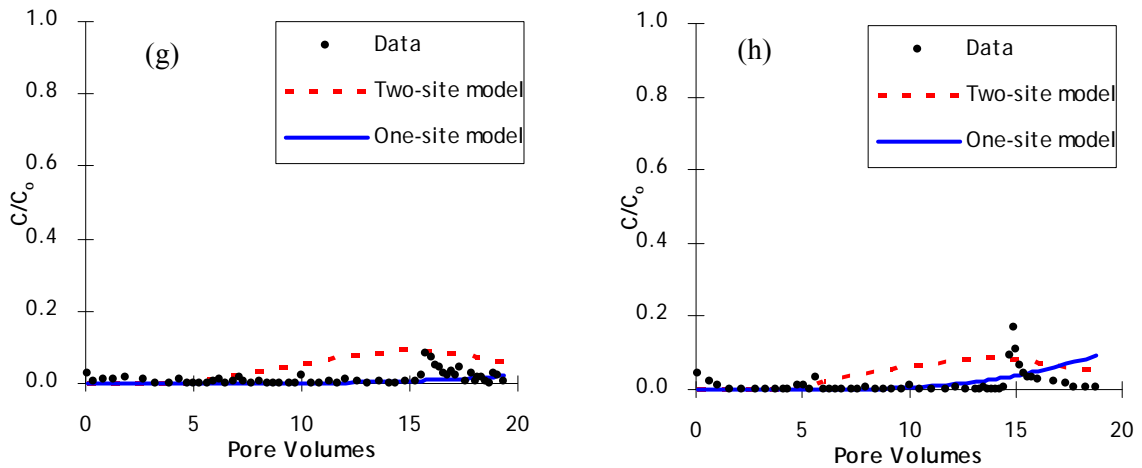


Fig.7. Breakthrough and breakdown curves of soil colloids at Darcy flow rate of (g) 0.08cm/min and (h) 0.09 cm/min.

4.2 Soil Colloid Breakthrough and Deposition Profiles

The observed and simulated breakthrough curves of soil colloids at two low flow rate conditions are illustrated in Fig.7. It could be seen that at low flow rates soil colloids showed an insignificant breakthrough. Similar to previous observation, of two models, one-site deposition model underestimated the recovered colloid mass whereas two-site model largely overestimated it (see Fig.8).

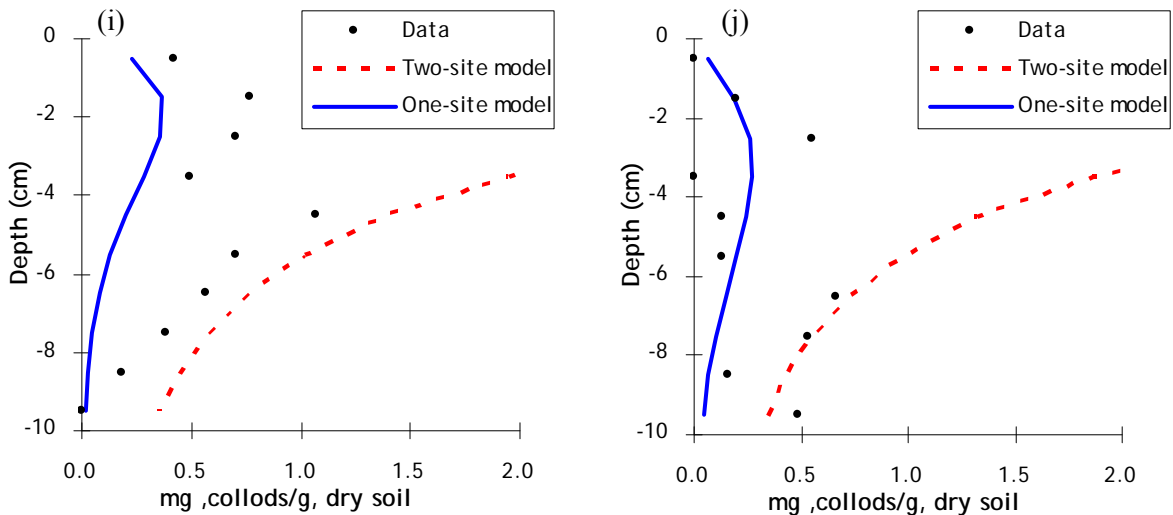


Fig.8. Deposition profiles of soil colloids at Darcy flow rates of (i) 0.08cm/min and (j) 0.09cm/min

Contrary to the observations at low flow rate conditions, soil colloids showed a significant breakthrough at middle flow rates and high flow rates as illustrated in the Fig. 9.

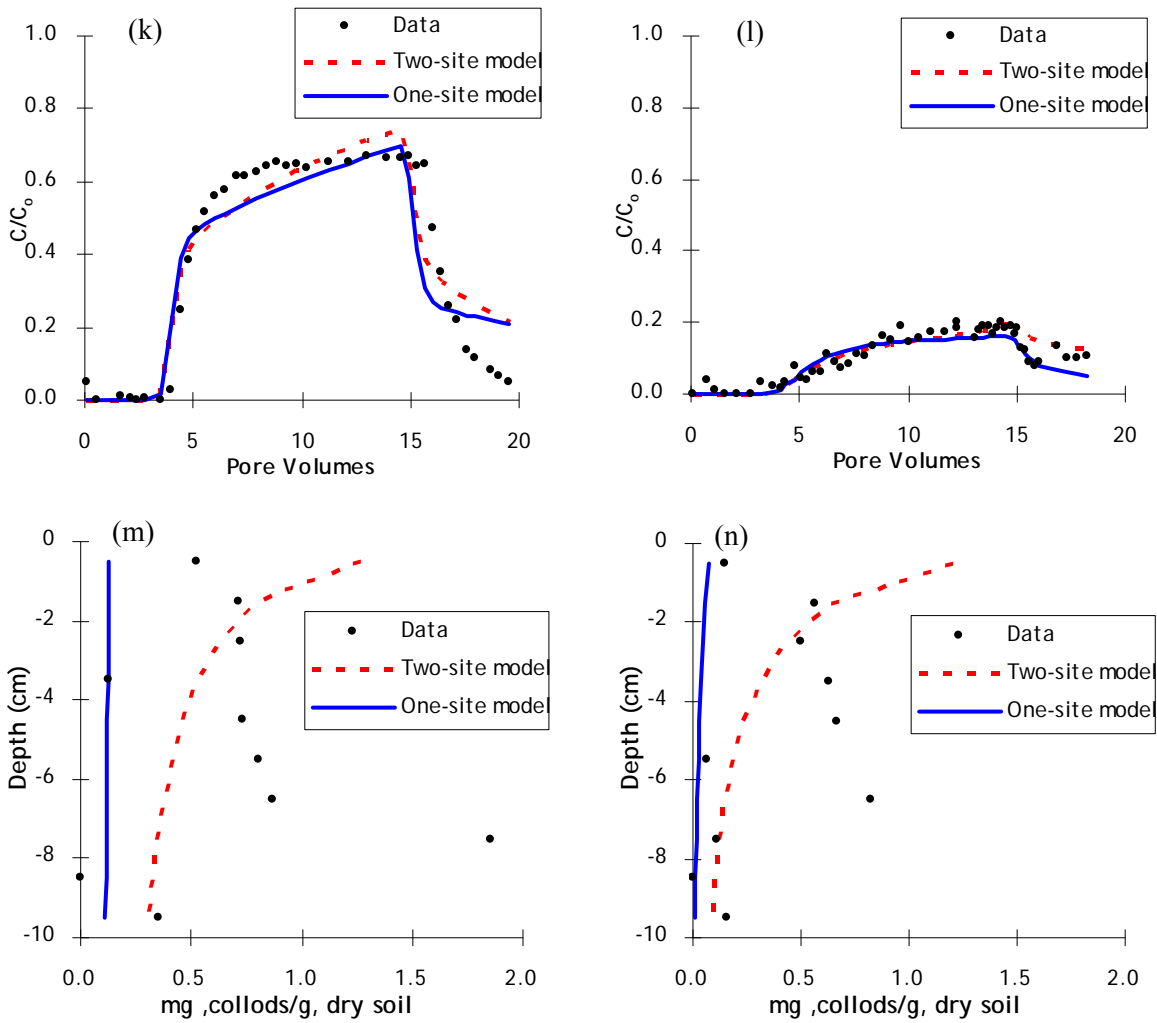


Fig.9. Breakthrough and breakdown curves of soil colloids at Darcy flow rates of (k) 0.29cm/min and (l) 0.52 cm/min. Deposition profiles corresponding to (k) and (l) are shown in (m) and (n) respectively

It should be noted here that, at very high flow rates, colloids exhibited lower recovery compared to that at middle flow rates, suggesting that there is an optimum flow rate at which colloid recovery is maximum. Similar to low flow rate conditions, at middle and high flow rates, simulated soil colloid deposition showed significant underestimation with one-site deposition model. Although the two-site model failed to capture essential deposition peaks, the estimated overall mass balance was fairly accurate.

The observed bromide breakthrough curves for all column experiments are similar to those shown in Fig.6 hence not shown here.

Table 2. Experimental conditions, estimated parameters from both deposition models and the mass balance analysis results

Expt.	Experimental Conditions			From Br data			One-site Model		Two-site model			Mass Balance analysis		
	Colloid Type	d_{50} μm	Initial Concentration mg/L	Darcy Flux (cm^2/min)	Diffusion Coeff (cm^2/min)	R^2	fitted		Fixed from batch kinetics			M_E	M_S	M_{BT}
							k_{ac} min^{-1}	k_{dc} min^{-1}	k_{ac} min^{-1}	k_{dc} min^{-1}	k_{str} min^{-1}			
1	BT glass beads	5.1	250	0.42	0.54	0.98	0.834	1.9×10^{-2}	0	0	3.19	0	0.98	0.98
2	BT glass beads	5.1	250	0.45	0.67	0.98	1.38	3.4×10^{-3}	0	0	5.93	0	1.12	1.12
3	Soil colloids	0.48	139	0.08	0.60	0.96	0.465	1.7×10^{-2}			0.510	0.69	1.47	1.47
4	Soil colloids	0.48	126	0.09	0.07	0.98	0.629	3.5×10^{-2}	1.17×10^{-1}	2.94×10^{-2}	0.635	0.02	0.90	0.92
5	Soil colloids	0.48	167	0.29	0.02	0.99	0.113	1.5×10^{-2}			0.158	0.17	1.40	2.09
6	Soil colloids	0.48	81.5	0.52	1.85	0.99	0.123	2.7×10^{-3}			0.341	0.08	1.67	1.84

[†] Experimental results from the batch kinetics were analyzed to derive k_{ac} and k_{dc} using the equation by Schijven and Hassanizadeh (2000). Maximum solid phase concentration of colloids on deposition site was set as 1000 for each condition.

[¶] Maximum solid phase concentration of colloids on deposition site was set as 1000 for each condition.

[‡] Measured colloid mass fraction in the effluent (M_E) in the sand (M_S) and total (M_{BT})

The estimated colloid transport and retention parameters and the results of mass balance analysis in each experiment are summarized in Table.2. It can be seen that the estimated attachment and detachment coefficients of soil colloids from both models are of same order of magnitude (except for the detachment coefficients of Expt. 6). Glass beads, however, showed a higher value of attachment coefficient estimated from the one-site model compared to the assumed (zero) value of the two site model. Further investigation, therefore, is warranted to estimate accurately the attachment and detachment coefficients of glass beads onto sand grains.

The estimated parameters of the two-site model suggest that straining plays the major role on deposition of both colloid types in saturated porous media. Since the smallest glass beads colloids ($1\mu\text{m}$) satisfy the criteria for colloid straining (i.e., colloid diameter/ mean grain diameter ratio exceeds the threshold value of straining (Bradford et al., 2004)), all glass beads can be assumed to be retained in potential straining sites. The observed particle size distribution profiles of soil colloids in the influent and effluents revealed that significant amount of larger colloids deposited in sand, presumably due to straining. These observations, therefore, corroborate the numerical analysis results of two-site model. Further research, however, is being carried out to confirm the results.

5. CONCLUSIONS

Glass beads colloids (diameter $1\text{-}10\mu\text{m}$) completely deposited in saturated sand for both high and low initial concentrations and the effect of flow rate was insignificant. On the other hand, volcanic ash soil colloids (diameter less than $1\mu\text{m}$) exhibited complete deposition at low flow rates but significant recovery at middle and high flow rates. soil colloid recovery was highest at middle flow rate compared to lower and higher flow rates.

The numerical analysis carried out by means of HYDRUS 1D software based on one-site and two-site deposition models provided sound insight to examine deposition kinetics of colloids in saturated porous media. The results of two-site deposition model highlighted the dominant role of straining in colloid deposition.

REFERENCES

- Bradford, S.A., Bettahar, M., Simunek, J. and M.Th . van Genuchten. 2004. Straining and attachment of colloids in physically heterogeneous porous media. *Vadose Zone J.* 3:384- 394.
- DeNovio, N.M., Saiters, J.E. and Ryan J.N. Colloid Movement in Unsaturated Porous Media: Recent Advances and Future Directions. 2004. *Vadose Zone J.* 3:338-351.
- Schijven, J.F. and Hassanizaden, S.M. 2000. Removal of viruses by soil passage: Overview of modeling processes and parameters, *Crit.Rev.Envirn.Sci.Technol.*,31,49-125.
- Simunek, J., van Genuchten, M.Th. 2005. The HYDRUS-1D software package for simulating the one-dimensional movement of water, heat, and multiple solutes in variably saturated media. Version 3.0. Dept. of Environmental Sciences. University of California Riverside. Riverside, California.
- Simunek, J., Changming, Pang, L. and Bradford S.A. 2006. Colloid-Facilitated Solute Transport in Variably Saturated Porous Media: Numerical Modeling and Experimental Verification. *Vadose Zone J.*

Acknowledgement:

This work is partially supported by the Saitama University Project Grant and a grant from the Japanese Ministry of Education, Science and Culture (Research no. 18360224).

下層土のNO₃⁻吸着特性が森林流域からのNO₃⁻の長期流出に及ぼす影響

Effects of NO₃⁻ adsorption characteristics by subsoil on long-term NO₃⁻ leaching from the forest watershed

浦川梨恵子・戸田浩人・生原喜久雄・崔 東寿

R.Urakawa, H.Toda, K.Haibara, and D.S.Choi

東京農工大学農学府

Graduate School of Agriculture, Tokyo Univ. of Agric. and Technol., Fuchu 183-8509, Tokyo, Japan

ABSTRACT: 北関東地方の高齢スギ・ヒノキ人工林小流域で斜面下部の伐採前後の土壌および渓流水質の長期的変動パターンを調査し、下層土の変異荷電によるNO₃⁻吸着が森林伐採流域からの長期にわたるNO₃⁻流出に及ぼす影響について検討した。土壌水のNO₃⁻濃度変動は比較的速やかで、伐採直後の植生による養分吸収の減少、表層土壌での窒素無機化の促進や、伐採から数年後の後継樹による養分吸収の増進など、伐採後の窒素循環の変化を直接的に反映していた。一方、渓流水のNO₃⁻濃度変動は緩慢で、伐採6年目でも伐採前よりも高い傾向が継続していた。渓流水のNO₃⁻濃度と流出速度の関係より、それぞれ直接流出、基底流出が優勢している高水、低水時のNO₃⁻濃度を求め、これらの伐採前後の年変動より、土層中のNO₃⁻濃度の分布が渓流水質に影響を及ぼしていることが明らかになった。このため、土層中の水・溶質移動モデルであるHYDRUS-1Dで下層土におけるNO₃⁻濃度分布の時間変動を予測し、その結果、火山灰下層土のNO₃⁻吸着特性が溪流へのNO₃⁻流出に大きな影響を与えていることが示された。今後、人工林の長伐期化やその方法が土壌水や渓流水の窒素動態に及ぼす影響を明らかにするために、火山灰土壌のNO₃⁻吸着特性を考慮する必要がある。

1 はじめに

森林は、大気沈着物等に含まれて生態系外から供給される物質を吸収・固定し、流域から流出する渓流水質を清浄に保つ機能を有している。森林流域における溪流の水質形成は、土壌での炭素窒素の無機化、硝化、樹木根による養分吸収、粘土鉱物や腐植物質による陽イオン交換、母材での化学的風化等、様々な過程が関わっている。環境変化や森林施業等に伴う渓流水質の変化を明らかにするためには、土壌層全体での、植物・水・土壌の生物地球化学的な相互作用を把握することが重要である。

森林流域からの渓流水質に関する研究は数多く行われている。特に、森林伐採は森林生態系の養分循環を最も大きく変化させる施業であり、これまでに伐採に伴う渓流水質変化に関する多くの研究が行われ、渓流水のNO₃⁻濃度を大きく上昇させることが示されている(たとえば、Bormann et al., 1968; Sollins and McCorison, 1981; Swank et al., 2001)。筆者らも北関東地方の高齢スギ・ヒノキ小流域において、斜面下部の皆伐が土壌および溪流の水質に及ぼす影響を継続的に調査しており、伐採後に濃度変動が最も大きかったイオンはNO₃⁻だった。表層の土壌水では伐採1年目に伐採前の3倍以上に上昇した一方、渓流水の濃度上昇は伐採前年比の1.5倍と小さく、そして土壌水のNO₃⁻濃度が検出限界以下に低下した5年目以降も、渓流水では伐採前よりも濃度が高い状態が継続している(浦川ら, 2007a)。これは、NO₃⁻が下層土の変異荷電による陰イオン吸着によって保持されるためと考えられ(浦川ら, 2007b)、伐採による渓流水質への影響が長期にわたることが予測された。本発表では、伐採が溪流からのNO₃⁻流出に影響する期間やその機構を明らかにするため、NO₃⁻濃度の時間経過にともなう変動と、土層中のNO₃⁻移動の関係について実測値の解析やHYDRUS-1Dによる数値計算を通じて検討を行った。

2 方法

2.1 調査地の概況

調査地は、群馬県みどり市東町の東京農工大学フィールドミュージアム大谷山内のスギ・ヒノキ人工林小流域(1.8 ha)である。本流域は、1907年に斜面上部(0.76ha)にヒノキ、斜面中～下部(1.04ha)にスギが植栽され、94年生時の2000年11月に流域面積の18%(0.33 ha)にあたる斜面下部スギ林を部分皆伐し、翌年の2001年5月にスギを再植林した。林齢は2008年現在、斜面上部ヒノキおよび中部スギ林が102年、斜面下部のスギ幼齢林が8年である。土壌母材は秩父中古生層の砂岩・粘板岩であるが、火山灰土壌の影響を少なからず受けている(浦川ら, 2007b)。

2.2 水量の測定・水質試料の採取・分析方法

降水量は転倒マス式雨量計(1転倒0.5 mm)を流域近傍の露場に設置し測定した。流出水量は、流域末端の量水堰にて測定した。土壌水は、斜面下部の伐採(予定)区の5、15、50、80 cm深より、ポーラスカップ法で原則として月1回採取した。渓流水は流域末端の量水堰で、原則として週1回の定期採水を行った。また、台風等の降雨イベント時に1～3時間間隔で自動採水装置(ISCO, 3700 Portable Samplers)による採水を行った。

土壌水、渓流水のNO₃⁻濃度は0.20 μmのシリンジフィルターでろ過した後、イオンクロマト(島津, HIC-6A)で分析した。本報告では、土壌水の水質データは伐採前年の2000年から伐採6年目の2006年までの計7年間、渓流水は2000年から伐採7年目の2007年目までの計8年間のデータを解析に用いた。

2.3 土層中のNO₃⁻移動のシミュレーション

本流域では、80 cm深の土壌水中NO₃⁻濃度が検出限界以下(0.1 mgN L⁻¹以下)に低下した伐採5年目以降も、渓流水のNO₃⁻濃度は伐採前よりも高い傾向が続いており(後述)、下層土中に保持されているNO₃⁻が伐採後の渓流水質に影響を及ぼしていると考えられた。このため、土中の水・溶質移動予測モデルであるHYDRUS-1D(Simunek et al., 2005)を用いて、実測が困難な下層土中のNO₃⁻濃度の経時変化のシミュレーションを行った。このシミュレーションでは、本流域の斜面最下部の土層厚(Shiraki et al., 2007)を考慮して2 mの長さの土壌カラムに、長期間にわたって水とNO₃⁻溶液を流す試験を想定している。

土壌カラムの層位を0-10、10-30、30-60、60-100、100-150、150-200 cmに区切り、それぞれの層位の土壌の水分特性曲線(水分保持曲線)はvan Genuchtenモデル(van Genuchten, 1980)、不飽和透水係数はvan Genuchten-Mualemモデル(van Genuchten, 1980; Mualem, 1976)を用いた。各パラメータは各層位の採土円筒試料で実測した水分保持曲線を用い、非線形最小二乗法(van Genuchten et al., 1991)により求めた。また飽和透水係数はShiraki et al. (2007)による土壌の深さと飽和透水係数の関係により求めた。表-1に各土層の水分特性パラメータを示す。

表-1. 土壌の水分特性・NO₃⁻吸着特性のパラメータ

Table 1. Soil hydraulic parameters and NO₃⁻ adsorption characteristics.

Soil depth (cm)	K_s (cm d ⁻¹)	θ_s (cm ³ cm ⁻³)	θ_r (cm ³ cm ⁻³)	α (cm ⁻¹)	n (-)	K_d (cm ³ mg ⁻¹)
0-10	4.11 × 10 ³	0.679	0.000	4.72 × 10 ⁻²	1.17	—
10-30	3.54 × 10 ³	0.682	0.000	2.68 × 10 ⁻²	1.15	—
30-60	2.75 × 10 ³	0.682	0.000	4.15 × 10 ⁻²	1.14	—
60-100	1.94 × 10 ³	0.682	0.000	4.15 × 10 ⁻²	1.14	—
100-150	1.24 × 10 ³	0.656	0.361	3.61 × 10 ⁻¹	1.16	2.94 × 10 ⁻³
150-200	7.51 × 10 ²	0.668	0.355	1.25 × 10 ⁰	1.16	2.94 × 10 ⁻³

K_s , saturated hydraulic conductivity; θ_s , saturated soil water content; θ_r , residual soil water content; α , n , parameters in the soil water retention function; K_d , adsorption isotherm coefficient.

本シミュレーションでは、カラム上端に蒸発散量を考慮して計算期間の日降水量の1/2の水量を実際の降水と同じタイミングで与え、1 m深から流出する水フラックスを得た。次にこの得られた水フラックスで80 cm深の土壌水のNO₃⁻濃度をもとに補間した濃度のNO₃⁻溶液を1 m深以下のカラムに与え、2 m深から流出する水フラックスとNO₃⁻濃度を得た。下層土によるNO₃⁻吸着特性については、線形の吸着等温線で表した。本流域の斜面下部のB層土壌を用いたカラム実験(浦川ら, 2007b)より、吸着等温線の傾きである分配係数($K_d=2.94 \text{ cm}^3 \text{ g}^{-1}$)を求めた。

今回のシミュレーションでは特に下層土によるNO₃⁻吸着が渓流水質に及ぼす影響を検討するため、対照として下層土による吸着がない場合($K_d=0 \text{ cm}^3 \text{ g}^{-1}$)のシミュレーションも行い、吸着ありの場合との比較を行った。なお、計算期間は伐採前年の2000年～伐採6年目の2006年の7年間とした。

3 結果と考察

3.1 渓流水質の時間経過に伴う変動特性

図-1の上段に深さ別の土壌水および渓流水のNO₃⁻濃度の伐採前後の月変動を、下段には渓流水のみレンジを拡大し、月流出水量と合わせて示した。本流域は樹木の生育期である5～10月に年間降水量の約8割が集中する夏雨型気候である。渓流水のNO₃⁻濃度は、流出水量の増加する地温の高い夏季に上昇する明瞭な季節変化を示している。

伐採後の土壌水のNO₃⁻濃度上昇は伐採1年目が最も大きく、特に伐採後の5 cm深のNO₃⁻濃度は、伐採1年目の2001年8月に伐採前年の約3倍の1.5 mmol_c L⁻¹に上昇した。しかし、時間の経過とともに上昇幅は小さくなり、伐採3年目には伐採前年と同程度、伐採5年目以降は全ての深度で検出限界以下まで低下した。渓流水のNO₃⁻濃度は、伐採1年目～6年目の夏季に伐採前年の同時期の1.5倍以上に上昇し、伐採の影響が明瞭に現れていた。しかし、土壌水が検出限界以下(0.1 mgN L⁻¹以下)に低下した伐採5年目以降も、冬季・夏季ともに伐採前年よりも高い傾向が続いており、伐採から5年以上経過すると土壌水よりも渓流水の方がNO₃⁻濃度が高い逆転状態となっている。

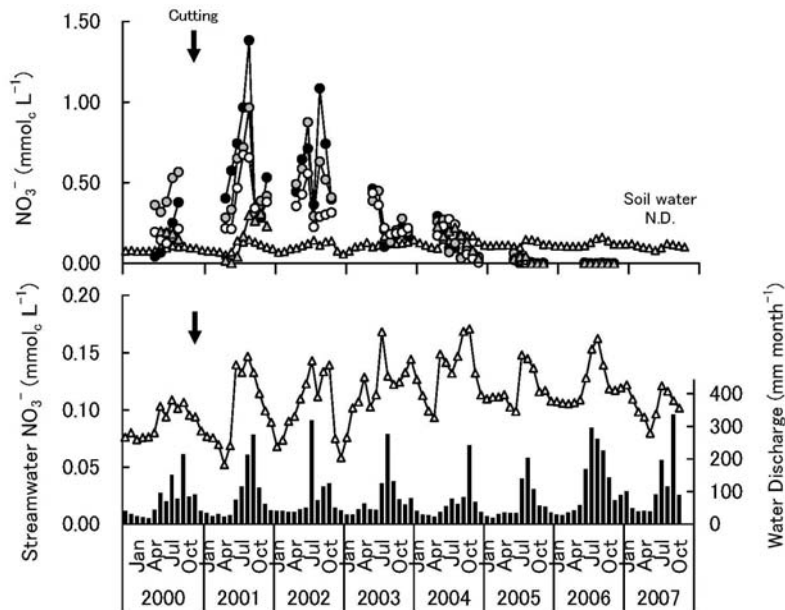


図-1. 土壌水・渓流水のNO₃⁻濃度および流出水量の伐採前後の経時変化

Figure 1. Changes of NO₃⁻ concentration in soil water and streamwater and water discharge before and after cutting.

- , 5 cm; ○, 15 cm; □, 50 cm; △, 80 cm;
- △, Streamwater; ■, Monthly water discharge.

伐採前後とも、流出速度が増加すると渓流水のNO₃⁻濃度も上昇し、流出水量を対数軸にとると右上がりの直線の関係がみられたため、流出速度とNO₃⁻濃度の回帰式を年ごとに作成した。これらの回帰式から流出水量が0.05 mm hr⁻¹の時の濃度を低水時、1 mm hr⁻¹の時の濃度を高水時のNO₃⁻濃度とし、それぞれの伐採後の時間経過に伴う変化をみると(図-2)、ピークが現れる時間(年)が高水時は伐採2年目の2002年、低水時は伐採4年目の2004年であり、低水時は高水時よりもNO₃⁻濃度の上昇が遅い。

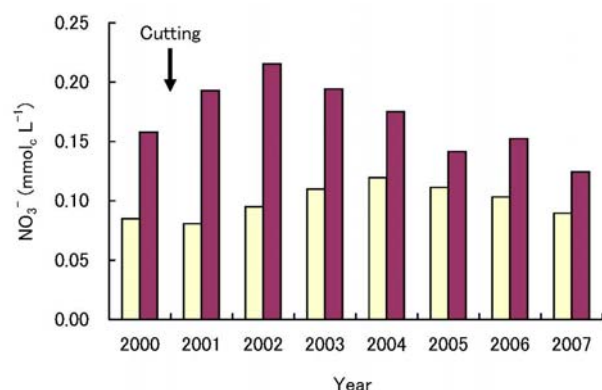


図-2. 低水時・洪水時の渓流水NO₃⁻濃度の経時変化
Figure 2. Changes of NO₃⁻ concentration in streamwater at low and high discharges before and after cutting.

□, low discharge (at discharge rate 0.05mm hr⁻¹);
■, high discharge (at discharge rate 1mm hr⁻¹)

渓流水質には斜面中を流動している水の流出経路が強く影響するといわれ、特に高水時にNO₃⁻濃度が上昇するのは、NO₃⁻が集積している比較的土壌上層部の影響を受けるためと指摘されている(大類ら, 1992)。高水時、低水時のNO₃⁻濃度はそれぞれ表層、下層に分布しているNO₃⁻の影響が強いと考えられ、伐採直後に表層土壌で多量に生成されたNO₃⁻が時間経過とともに徐々に下層へ移動しているため、ピークが現れるのにこのような時間差が生じたと考えられる。

3.2 下層土のNO₃⁻分布と渓流水のNO₃⁻濃度変動との関係

図-3に、下層土によるNO₃⁻吸着を考慮したとき、考慮しないときの土壌の深さ100、200 cmにおける土壌水のNO₃⁻濃度の予測値と、80 cm深の土壌水および実測の渓流水NO₃⁻濃度を示す。

NO₃⁻吸着の有無にかかわらず100 cm深の予測値は、実測の80 cm深のNO₃⁻濃度の範囲やその変動の傾向がほぼ一致しており、季節変動や伐採直後の濃度上昇およびその後の濃度低下が顕著に現れていた。一方、200 cm深の予測値は吸着の有無で濃度変動が大きく異なった。下層土によるNO₃⁻吸着を考慮しない場合、伐採後の濃度上昇が伐採の1年後に現れた。また、伐採5年目(2005年)の80 cm深の土壌水NO₃⁻濃度の検出限界以下の低下の伝播も速やかで、2006年の夏季にはシミュレーションを行った全ての深度でNO₃⁻濃度が0 mmolc L⁻¹まで低下している。一方、吸着を考慮した方は季節変化がほとんどみられず、伐採から2年半後の2003年の夏季に濃度上昇が始まっている。同深度のNO₃⁻濃度が大きく低下し始めるのは2006年の後半からで、図には示していないが、年間降水量が平年並み(約1650 mm)であった2004年の降水を2007年以降反復させていくと、200 cm深のNO₃⁻濃度は2008年に伐採前以下、そして伐採から8年が経過した2009年にはほぼ0 mmolc L⁻¹に低下すると算出された。下層土による吸着のあり・なしのいずれの場合も実測値と大きな隔たりはあるが、本シミュレーションによって下層土のNO₃⁻吸着特性が、渓流水のNO₃⁻濃度が長期にわたって高濃度を維持する要因として重要であると考えられた。

以上のように下層土中のNO₃⁻動態のシミュレーションを行うことにより、NO₃⁻吸着の有無によって、土壌水のNO₃⁻濃度変動パターンが大きく異なり、下層土におけるNO₃⁻吸着特性が伐採後の渓流水のNO₃⁻濃度変動に大きな影響を及ぼしていることが明らかになった。

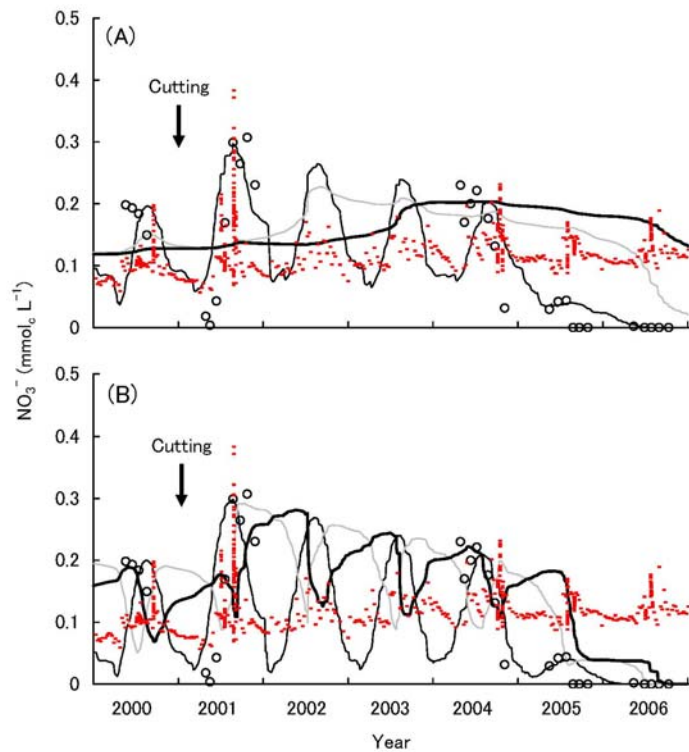


図-3. 下層土および渓流水中の NO_3^- 濃度の変動
 Figure 3. Changes of NO_3^- concentration in streamwater and subsoil,
 A) with NO_3^- adsorption capacity, B) without NO_3^- adsorption capacity.

○, 80 cm (Soil water, observed value); - , streamwater (observed value);
 — , 100 cm; — , 150 cm; — , 200 cm (Simulated value below 100 cm).

4 おわりに

土壌水および渓流水の伐採前後の NO_3^- 濃度の経時変化より、渓流水の伐採に伴う変動は土壌水と比較して非常に緩慢であること、また降雨イベント時を含めた渓流水 NO_3^- 濃度と流出速度の解析から、低水・高水の流出経路の違いによって NO_3^- 濃度変動の時間的スケールが異なること、さらに下層土中の NO_3^- 移動をシミュレーションすることにより、下層土の NO_3^- 吸着が伐採後の渓流水質の変動パターンに大きな影響を与えていることが明らかになった。

変異正荷電を多く含む火山灰土壌が分布する森林流域は、日本国内に広く存在する(吉永ら, 1994)。このような流域では植生と表層土壌間での窒素循環の変化が渓流水質にダイレクトに結びつかないため、環境変化や施業の影響を明らかにするためには、長期的なモニタリングが必要である。また今後、変異荷電による陰イオン吸着をはじめとする火山灰土壌の特性が、森林生態系における窒素等の養分動態に及ぼす影響を解明していくことが重要であり、森林の持つ公益的機能をより効果的に発揮できる施業につなげていく必要がある。

5 引用文献

- Bormann, F. H., Likens, G. E., Fisher, D. W., and Pierce, R. S. 1968. Nutrient loss accelerated by clear-cutting of a forest ecosystem. *Science* 159: 882-884.
 Mualem, Y. 1976. A new model for predicting the hydraulic conductivity of unsaturated porous media. *Water Resour. Res.* 12: 513-522.

- 大類清和・生原喜久雄・相場芳憲 1992. 降雨イベントでの渓流水の溶存物質の流出特性と流出成分の分離. *日林誌* 74: 203-212.
- Simunek, J., van Genuchten M. Th., and Sejna, M. 2005. The HYDRUS-1D software package for simulating the movement of water, heat, and multiple solutes in variably saturated media, Version 3.0, *HYDRUS Software Series 1*, Department of Environmental Sciences, University of California Riverside, California, USA, 270 pp.
- Shiraki, K., Shinomiya, Y., Urakawa, R., and Toda, H. 2007. Numerical calculation of secondary discharge peak from a small watershed by a physically based watershed scale infiltration simulation. *J. For. Res.* 12: 201-208.
- Sollins, P. and McCorison, F. M. 1981. Nitrogen and Carbon solution chemistry of an old growth coniferous forest watershed before and after cutting. *Water Resour. Res.* 17: 1409-1418.
- Swank, W. T., Vose, J. M., and Elliott, K. J. 2001. Long-term hydrologic and water quality responses following commercial clearcutting of mixed hardwood on a southern Appalachian catchment. *For. Ecol. Manage.* 143: 163-178.
- 浦川梨恵子・戸田浩人・生原喜久雄 2007a. スギ・ヒノキ流域における渓流水質形成に及ぼす斜面下部土壌系の重要性. *118回日林講* P3d38.
- 浦川梨恵子・戸田浩人・生原喜久雄 2007b. 高齢化したスギ・ヒノキ人工林小流域における下層土のNO₃吸着による窒素流出の遅延効果. *日林誌* 89: 190-199.
- van Genuchten, M. Th. 1980. A closed-form equation for predicting the hydraulic conductivity of unsaturated soils. *Soil Sci. Soc. Am. J.* 44: 892-898.
- 吉永秀一郎・鈴木裕一・松倉公憲・小林 守・新井 正 1994. 国土数値情報を用いた酸性雨に対する感受性分布図の作成. *土肥誌* 65: 565-563.

Fluctuation of Salt Content Profile of the Field in Northwest China under Repetitious Border Irrigation

C. Kato, T. Nishimura & T. Miyazaki

Graduate School of Agriculture and Life Sciences, University of Tokyo, Bunkyo, Tokyo, Japan

M. Kato

Graduate school of Tokyo University of Agriculture and technology, Fuchu, Tokyo, Japan

ABSTRACT: Salt accumulation in semi-arid field irrigated with salty ground water in Gansu province, China was evaluated using numerical simulations with Hydrus-1D and with measured soil hydraulic and solute transport parameters. The experimental site is above deep ground water and is irrigated with water having EC of 1.7 dS m^{-1} . Salt was stored in the vadose zone following irrigated cropping season without any contribution from ground water. It was observed that a repetition of irrigation caused wavy salt concentration profile near surface. This may be due to a combination of downward leaching and upward evaporation driven transport of soluble salts during cropping season.

1 INTRODUCTION

While agricultural land development has been promoted over several decades and crop yields have been substantially increased, acreage of cultivated soils has remained at the almost same level. An increase in food production is mainly attributed to the development of irrigation technology.

While irrigated agricultural land occupies 17% of total arable land in the world (FAO, 2007), irrigated agricultural land produces about 40% of total agricultural food production. However, in arid and semi-arid regions, inappropriate irrigation practices have been deteriorating agricultural lands (Oster and Shainberg, 2001). For example, instead of using limited fresh water, saline ground water is often used for surface irrigation. This could cause salt accumulation and reduction of productivity of the land. According to the IPCC Fourth Assessment Report (2007), global warming will cause the decrease of the water availability and the deterioration of the water quality. It indicates that the risk of occurrence of salt damage will be great due to the use of low-quality water for agriculture.

To prevent problems caused by salt accumulation and to improve efficiency of irrigation, it is necessary to fully understand mechanisms involved in salt damage. It is usually said that the main cause of salt accumulation is a rising groundwater level. However, groundwater rise cannot always explain the cause of salt problems.

Gansu province, China (Fig.1), is one of the provinces, which have lower agricultural production in China. At our study site, Wuwei city, Gansu province, salt accumulation has been observed under repetitious irrigation during the cropping period. The groundwater level in Wuwei is more than 10 m deep, and the soil texture is sandy. The rise of the groundwater level is thus not likely to be the reason for salt accumulation. The purpose of this study is to analyze water and salt movement in the soil in order to define mechanisms involved in salt accumulation, especially for areas where groundwater is deep.



Fig.1 The location of Wuwei city, Gansu Province, China

2 MATERIALS AND METHODS

2.1 Field Experiment

The experimental field is located at the Wuwei city in the Gansu province, China. Annual precipitation is between 100 and 200 mm yr⁻¹ and potential evaporation is about 2900 mm yr⁻¹. As a result, Wuwei is classified as the arid land. Groundwater, which exists at depths lower than 10 meters, is the main source of irrigation water. Electrical conductivity of the irrigation water was 1.71 dS m⁻¹, or about 0.005 mol-NaCl L⁻¹. In 2006, irrigation was repeated over the cropping period (Table 1). The field was covered by thick Yellow loess. Texture of the soil was approximately 80%:10%:10% for sand: silt: clay, respectively, and the bulk density of the top soil layer was 1.5 g cm⁻³.

Table 1. The irrigation schedule (Sato et al., 2007)

Cycle	Time t (day)	Irrigation (cm day ⁻¹)
0	0(2006/4/15)	0
1	1	6.8
2	54	13.6
3	65	6.8
4	82	6.8
5	93	6.8
6	104	10.2
7	115	6.8
8	125	6.8
9	139	6.8
	154	0

2.2 Numerical Simulation

To reproduce temporal changes in vertical distributions of water and salt contents over the irrigation period, a numerical simulation was conducted using Hydrus-1D (Simunek et al., 2005). Parameters used in the numerical simulation were collected from laboratory experiments.

Soil hydraulic properties of the top soil layer were determined using the multi-step outflow method (Eching and Hopmans, 1993). The van Genuchten-Mualem model was used to describe soil water retention, $\theta(h)$, and hydraulic conductivity function, $K(h)$:

$$S_e(h) = \frac{\theta(h) - \theta_r}{\theta_s - \theta_r} = \frac{1}{(1 + |\alpha h|^n)^m} \quad (1)$$

$$K(h) = K_s S_e^l \left\{ 1 - (1 - S_e^{1/m})^m \right\}^2 \quad (2)$$

where θ_r = residual volumetric water content, θ_s = saturated water content, $S_e(h)$ = degree of saturation, K_s = saturated hydraulic conductivity, l = pore connectivity parameter, and α , m , n = fitting parameters.

Miscible displacement experiments have been conducted to determine the salt transport parameters under both saturated and unsaturated conditions. Transport parameters were determined using CXTFIT (Toride et al., 1995). Convection-dispersion equation was employed to simulate solute transport.

$$R \frac{\partial C}{\partial t} = D \frac{\partial^2 C}{\partial z^2} - u \frac{\partial C}{\partial z} \quad (3)$$

$$D = \lambda v \quad (4)$$

where R = solute retardation factor, C = solute concentration, t = time, z = position, D = dispersion coefficient, v = mean water pore velocity, and λ = dispersivity.

The soil profile in numerical simulations was considered to be 750 cm deep, and initial and boundary conditions were determined according to field observations (Table 2). The model validation was carried out by comparing simulation results with field observations of Sato et al. (2007).

Table 2. Initial and boundary conditions for the numerical simulation

Initial and boundary conditions	
Suction (cm H ₂ O)	174
Salt Content (mmol cm ⁻³)	0.01
Potential evaporation (cm day ⁻¹)	0.57
Potential transpiration (cm day ⁻¹)	0
Bottom boundary condition	dh/dz=0

3 RESULTS AND DISCUSSION

3.1 Soil hydraulic properties

Soil hydraulic parameters determined using the multi-step outflow method are shown in the Table 3.

Table 3. Soil hydraulic parameters

θ_r [cm ³ cm ⁻³]	θ_s [cm ³ cm ⁻³]	α [cm ³ cm ⁻³]	n	K_s [cm day ⁻¹]	l
0.052	0.43	0.0246	1.84	101	0.986

3.2 Solute transport properties

Figure 2 shows the relationship between the mean water pore velocity v [cm s⁻¹] and the dispersion coefficient D [cm² s⁻¹] under saturated and unsaturated conditions. In both cases, D is proportional to v , but the slope λ [cm] (longitudinal dispersivity) under unsaturated conditions (0.311 cm) was about twice as large as under saturated conditions (0.155 cm).

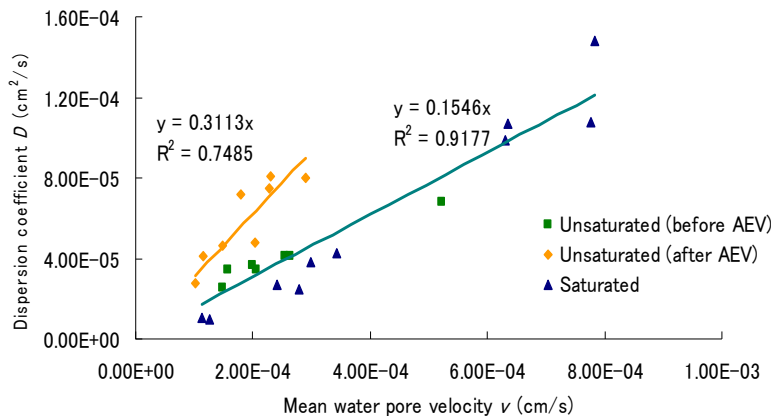


Figure 2. The relationship between the mean water pore velocity v and the dispersion coefficient D (AEV stands for the Air Entry Value).

3.3 Numerical simulation

Figures 3 to 5 show the influence of λ on solute transport. Here, λ_1 ($=0.155$ cm) is the dispersivity under saturated conditions and λ_2 ($=0.311$ cm) under unsaturated conditions. Figures present salt content profiles after the last day of the cycle 1 ($t=53$ d), cycle 5 ($t=103$ d) and after the last cycle 9 ($t=250$ d), respectively. In the beginning, the difference in λ does not affect the results. However, as irrigations were repeated, λ_1 produces smaller concentration peaks and smaller overall fluctuations in concentration values than λ_2 .

Since the field was under unsaturated conditions during most of the cropping period, $\lambda = 0.311$ cm was employed in the simulation of solute transport in the remainder of this paper.

Figures 6 and 7 show changes in water and salt content during the irrigation cycle 1. During the dry period after the first irrigation, the wetting front moved downward while the water content near the soil surface decreased due to evaporation. Since salt was transported with moving liquid water, the front of the high salt concentration in soil water also moved downward. As days passed, concentrations near the surface soil became high. After 9 consecutive irrigations were carried out (Figures 8 and 9), the salt content profile fluctuated independently of changes in the water content.

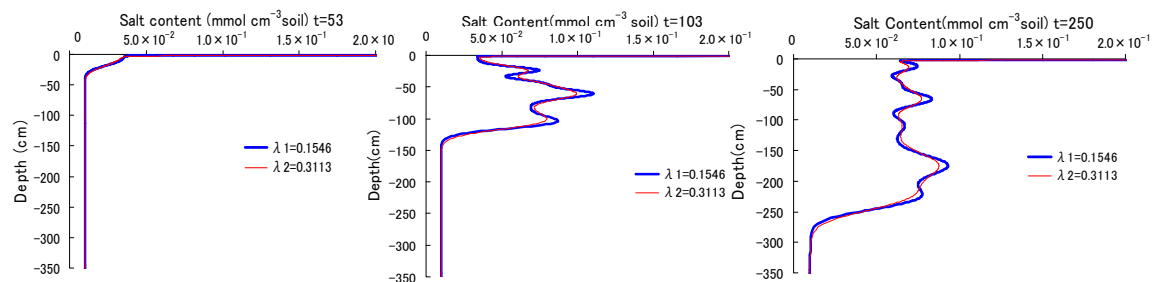


Figure 3. Salt content profile at the last day of cycle 1.

Figure 4. Salt content profile at the last day of cycle 5.

Figure 5. Salt content profile at the day after cycle 9

Observed results (Figure 10) also revealed that the vertical distribution of the salt content was spatially variable. This phenomenon was also reported in other areas (e.g., Endo et al., 2000) and spatial heterogeneity of soil properties has been considered to be a cause of it. However, this study indicated that repeated salty water irrigations may also produce fluctuations in salt contents.

At this experimental site, applied salt with irrigation water moved upward and accumulated near the surface as evaporation proceeded. The high salt concentration was then pushed down-

ward by the following irrigation. However, accumulated salt was not completely leached away by the following irrigation, and remaining salt concentrated near the soil surface between the irrigation events. Applied salt moved up and down through the vadose zone during the cropping season and could form waved concentration profiles as shown in Figures 4 and 5. This phenomenon may be strongly affected by saturated and unsaturated conductivities, dispersivity, water retention of the soil and irrigation schedule.

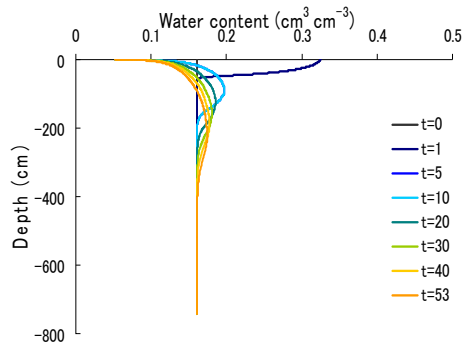


Figure 6. Water content changes during Cycle 1.

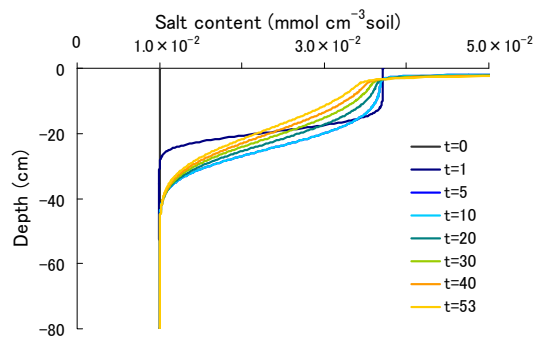


Figure 7. Salt content changes during Cycle 1.

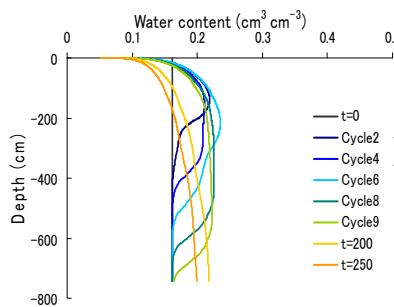


Figure 8. Water content changes during the irrigation period

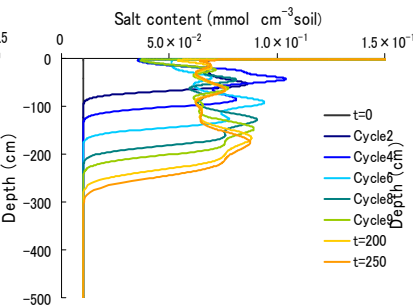


Figure 9. Salt content changes during the irrigation period

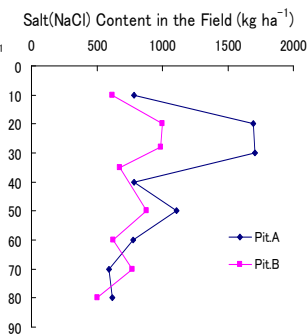


Figure 10. Salt content observed in the field in 2005

4 CONCLUSIONS

Accumulation of salts due to irrigation with salty groundwater at areas with deep groundwaters is discussed in this paper. Salt contained in irrigated water accumulates near the soil surface as evaporation proceeds, and is then pushed down by irrigation water. However, a significant amount of the salt is not leached away and is returned to the near-surface as evaporation dominates after irrigation. As a result, the vadose zone may experience the salt accumulation in the surface layer after repeated irrigation events without any rise of the ground water level. This process may form waved salt concentration profiles near the soil surface and may be affected by soil hydraulic properties and irrigation schedule.

REFERENCES

- Endo, T., Yamamoto, S., Honna T., Takashima, M., Iimura, K., Lopez, R. & Benson, M., Behavior and Distribution of Salts under Irrigated Agriculture in the Middle of Beja California, Mexico
 Eching, S.O. & Hopmans, J.W., 1993, Optimization of Hydraulic functions from transient outflow and soil water pressure data, *Soil Sci. Soc. Am. J.*, 57(5), 1167-1175

- Oster, J.D. & Shainberg, I., 2001, Soil response to sodicity and salinity: challenges and opportunities. *Aust. J. of Soil Res.*, 39, 1219-1224
- Sato, Y., Nishimura, T., Kato, M., & Xinmin, L., 2007, More sustainable irrigation regarding water and solute dynamics in semi-arid region of Gansu Province, China, Conference Abstracts of The Japanese Society of Irrigation, Drainage and Rural Engineering, 246-247
- Šimůnek, J., M. Th. van Genuchten, and M. Šejna, The HYDRUS-1D software package for simulating the one-dimensional movement of water, heat, and multiple solutes in variably-saturated media. Version 3.0, *HYDRUS Software Series 1*, Department of Environmental Sciences, University of California Riverside, Riverside, CA, 270 pp., 2005.
- Toride, N., Leij, F.J. & van Genuchten, M. Th., 1995, The CXTFIT code for estimating transport parameters from laboratory or field tracer experiments, U.S. Salinity Lab., Agric. Res. Service, U.S. Dep. of Agric., Research Report No. 137, Riverside (CA)

Analysis of Water Movement in a Wick Sampler Using HYDRUS-2D Code

K. Inosako

Faculty of Agriculture, Tottori University, Tottori, 680-8553, Japan

S. Kozaki

Graduate School of Agriculture, Tottori University, Tottori, 680-8553, Japan

M. Inoue

Arid Land Research Center, Tottori University, Tottori, 680-0001, Japan

K. Takuma

Faculty of Agriculture, Tottori University, Tottori, 680-8553,

ABSTRACT: A container wick sampler (CWS) was applied to a Tottori sand dune field. The sampling rate (SR) and the volumetric water content (WC) around the sampler were measured to evaluate the effectiveness and convenience of CWS to measure water fluxes. The change of SR corresponded to WC around the sampler when rains occurred frequently. However, the time-lag between them occurred for a rainfall event after several dry days. We conducted a numerical experiment to clarify the reason using the HYDRUS-2D code. From the experiments, it was confirmed that the CWS collected percolating water immediately when it reached the sampling phase. However, the movement of water in the wick was relatively slow because the conveyance part of the wick became dry and the hydraulic conductivity low during preceding dry days. Therefore, the increase in the sampling rate occurred later than the percolating event under these conditions.

1 INTRODUCTION

Sand fields have low water retention and fertility. Hence, frequent irrigation and fertilization are essential for stable crop production. It means that the fields have a high risk for leaching of salts and nutrients to groundwater. According to research carried out on lysimeters, 41 to 67 % of fertilizing nitrogen was leached from fields (Nonaka & Kamura, 1995; Jinno and Honna, 1999). To reduce the quantity of chemicals leached from a root zone, it is necessary to take countermeasures to protect groundwater from pollution. In particular, direct measurements are very important in the field.

A wick sampler (WS) is one of the apparatuses for direct water sampling. The WS automatically collects soil water by capillary force of fiberglass wick without applying any pressure from external instruments. The production costs are relatively reasonable.

Multi-point measurements are important in order to estimate the amount of fertilizers leached from a root zone, because the distribution of fluxes in the field is highly variable. At this point, WS is a suitable apparatus. We use WS with a container as soil water sampling part (CWS) to measure the amount of chemicals leached from a root zone in a sand dune field.

There were many studies on WS in the past (Holder et al., 1991; Boll et al., 1992; Maeda et al., 1999; Zhu et al., 2002; Gee et al., 2004). However, to the best of our knowledge, there are few studies on mechanisms of collection and conveyance of water in WS. We conducted field and numerical experiments using HYDRUS-2D code to evaluate the effectiveness and convenience of CWS to measure water fluxes.

2 MATERIALS AND METHODS

2.1 Container Wick Sampler

The schematic view of the CWS is shown in Figure 1. The total length of this wick (GY96, Sakaguchi E. H. VOC CORP.) was 1.13 m. The sampling part is a 0.108-m diameter and 0.105-m thick PVC pipe. A plate with a 0.03-m diameter hole in the center was installed 5 cm below the top of the sampling part. The length of the wick above the hole was 0.13 m. The wick was spread radially on the plate and laid in the pipe. The wick layer on the plate became a sampling phase for soil water. Its thickness is about 0.03 m. The other end of the wick reached to a storage tank through the hole. The part from the hole to the tank is the conveyance part for collected water. The wick of this part is enclosed in a plastic tube (0.02-m i.d.). The water can not flow on the inner side of the tube because the inside of the tube is filled with the wick.

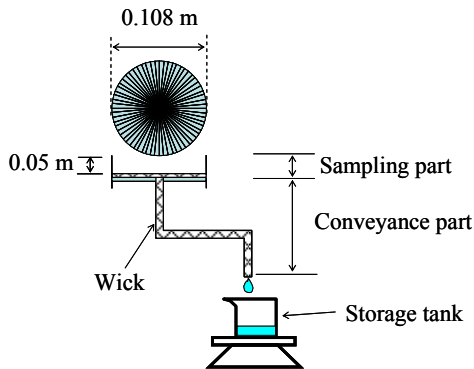


Figure 1 Schematic view of a container wick sampler

Field experiment was conducted at a bare sand dune field in Arid Land Research Center, Tottori University. This experiment was conducted from April 5 to October 7, 2006 (186 days). The CWS was installed at 0.5 m below the soil surface (sampling phase at 0.55 m). An observation pit was excavated at 0.65 m away from the installation point of the CWS. Collected leachate was conveyed from the sampling phase through the wick to storage tank in the pit. The end of conveyance part was at 0.35 m below the depth of the sampling phase. The tank was on an electric balance to measure sampling rate of the CWS (SR). Water contents at 0.55-m depth were observed using TDR sensors. Moreover, pressure heads 0.6 m below the soil surface were measured using a tensiometer with a pressure transducer.

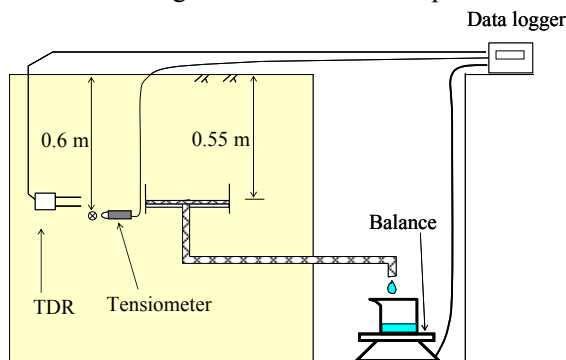


Figure 2 Outline of the experiment in sand dune field

2.2 Numerical experiments

Fiberglass wick is a kind of porous medium. Therefore, the governing equation for water movement in the wick can be given using the following two dimensional Richards' equation:

$$\frac{\partial \theta}{\partial t} = \frac{\partial}{\partial x_i} \left[K \left(K_{ij}^A \frac{\partial h}{\partial x_j} + K_{ij}^A \right) \right] \quad (1)$$

where θ = the volumetric water content; K = the unsaturated hydraulic conductivity; K_{ij}^A = components of dimensionless anisotropy tensor \mathbf{K}^A , h = the pressure head, x_i ($i=1,2$) = the spatial coordinates, and t = time (Šimůnek et al., 1999). The hydraulic properties were assumed to be expressed by the van Genuchten-Mualem model (van Genuchten, 1980):

$$S_e = \frac{1}{\left[1 + (\alpha h)^n \right]^m} \quad (2)$$

$$S_e = \frac{\theta - \theta_r}{\theta_s - \theta_r} \quad (3)$$

$$m = 1 - \frac{1}{n} \quad (4)$$

$$K = K_s S_e^{\frac{1}{2}} \left[1 - \left(1 - S_e^{\frac{1}{m}} \right)^m \right] \quad (5)$$

where, θ_s and θ_r = saturated and resident water contents, respectively, and α , n and m = experimental parameters. Hydraulic properties of the wick were measured similarly to Knutson & Selker (1994). The parameters were identified using the genetic algorithm (Inosako & Takuma, 2002).

Figure 3 shows a calculation domain for numerical experiments. Planar flow in a vertical cross-section was assumed in this study. The sampling phase was assumed to be a flat plate for simplification. The HYDRUS-2D code (Šimůnek et al., 1999) was used for the numerical experiments. Initial conditions for simulations were determined using a following procedure: First, saturated conditions were assumed in the entire transport domains. The upper boundary condition was no flux and the lower boundary condition was free drainage. The boundary condition of the end of the conveyance part of the wick was seepage face. Calculations were continued until the pressure head near the lower boundary became almost the same as observed (around -50 cm). We adopted the results of this simulation as the initial condition for the next numerical experiments.

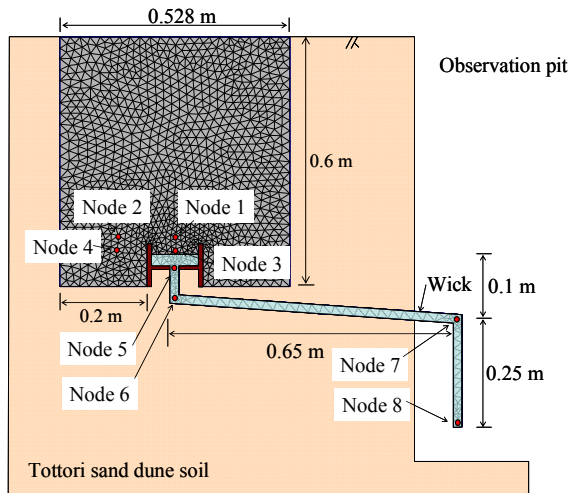


Figure 3 Computational domain for the numerical experiment

Observed precipitation fluxes were given as the upper boundary condition for numerical experiments. Evaporation loss from the bare soil surface was neglected because it was too small compared to precipitation. Variable pressure heads observed 0.6 m below the soil surface were used as the lower boundary condition. The data for these boundaries were observed in the field for 70 hours, from June 7 to 10, 2006. Seven points were set as observation nodes in the calculation domain.

3 RESULTS AND DISCUSSIONS

3.1 Field experiment

Changes in volumetric water contents (WC) 0.55 m below the soil surface and the sampling rate (SR) of the CWS are shown in Figure 4. The WC and SR began to increase later after the occurrence of precipitation. This time-lag was due to the time it took water to arrive at the depth of 0.55 m. When the interval between rainfall events was short, starting points for increases in WC corresponded to SR. This means that water percolating to the sampling phase was immediately absorbed by the wick and it then pushed antecedent water off the wick. On the other hand, both WC and SR increased during the rainfall event after more than eight no-rainy days. However, there was still a time-lag between their starting points.

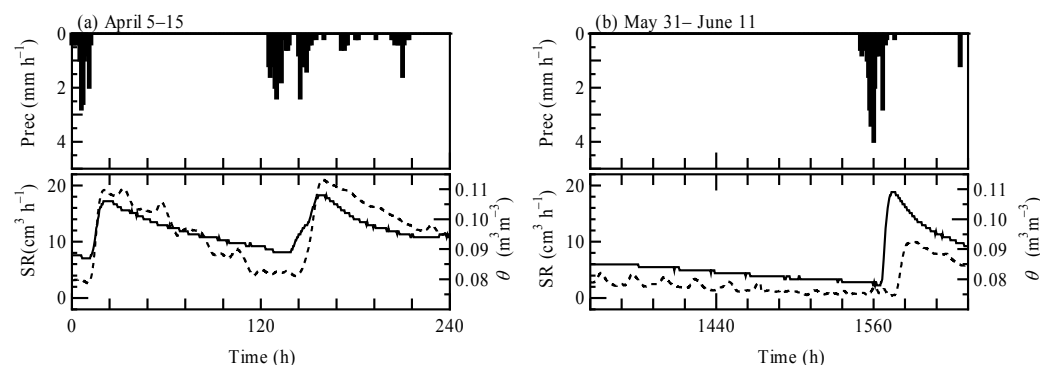


Figure 4 Change of sampling rate (SR, dot line), volumetric water content (θ , solid line) and precipitation (Prec., bar graph).

3.2 Numerical experiment

Table 1 shows hydraulic parameters used in numerical experiments.

Table 1. Hydraulic parameters of the wick and the Tottori dune sand.

Material	θ_s	θ_r	α	n	K_s (cm/s)
Wick	0.620	0.005	0.034	2.306	0.0144
Tottori sand dune soil	0.453	0.047	0.049	6.082	0.0171 =

Figure 5 shows pressure head changes around the CWS. The pressure head at the observation node 1 was greater than at node 2 before the occurrence of rainfall. Node 3 also had higher pressure head than node 4. Soils in and on the CWS were kept wet because otherwise they represented a barrier for soil water percolation. However, the difference between nodes 1 and 2 was very small after percolating water reached these points. This state continued for about 20 hours. Soil water flowed one-dimensionally in this situation. On the other hand, the pressure head at node 3 was smaller than at node 4. Flow outside of the CWS was gravitational, because pressure heads at nodes 2 and 4 were same. Although the same amount of outflow water came into node 3, the pressure head there was lower than at node 4. This was caused by the capillary force of the wick.

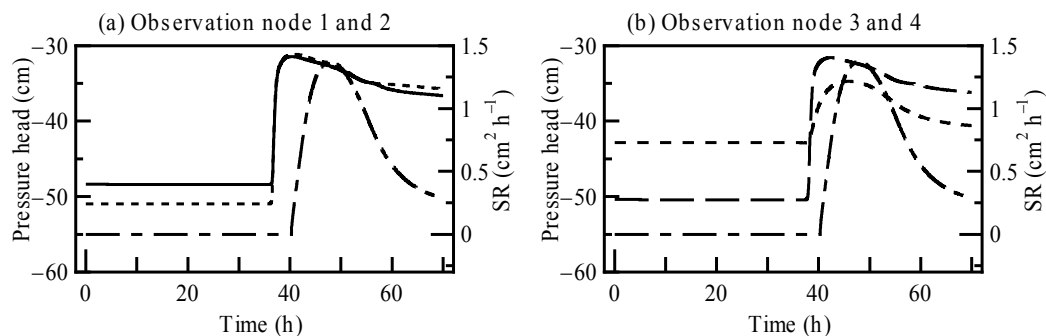


Figure 5. Pressure head changes at observation nodes around the CWS. The solid line represents node 1, the dot line node 2, the short dash line node 3, and the dash line node 4. The dot dash line represents the sampling rate (SR).

Figure 6 shows pressure head changes in the conveyance part of the wick. It can be observed that the sampling phase of the CWS collected percolating water immediately, because the pressure heads at nodes 3, 5 and 6 began to increase at the same time. It took, however, considerable time (conveyance time) for the collected water to move to the end of the wick under dry conditions. This delay resulted in the delay of the change of the seepage face from potential to actual and the initiation of seepage flux. Increases in pressure heads at nodes 7 and 8 were small due to redistribution of collected water in the wick.

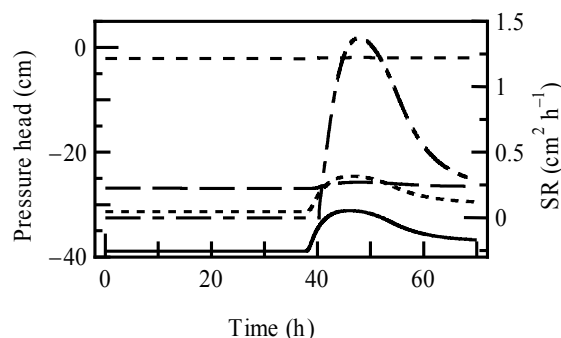


Figure 6 Pressure heads at observation nodes in the conveyance part of the CWS. The solid line represents node 5, the dot line node 6, the dash line node 7, the short dash line node 8, and the dot dash line the sampling rate (SR).

4 CONCLUSIONS

A wick sampler is one of the direct sampling instruments for monitoring soil water percolation in fields. There are only few studies investigating water sampling and conveyance of CWS under field conditions.

In this study, the CW sampler was applied to a Tottori sand dune field for 186 days. The change of the sampling rate corresponded to changes in volumetric water contents around the sampler when rains occurred frequently. However, the time-lag between these two processes was observed after rainfall that followed several dry days. We conducted a numerical experiment to clarify the reason for this phenomenon. The HYDRUS-2D code was used for numerical experiments. It was confirmed by the numerical experiment that the CWS collected immediately percolating water when it reached the sampling phase. However, the movement of water in the wick was relatively slow because the wick in the conveyance part became dry and its hydraulic conductivity low during dry periods. Therefore the increase of the sampling rate was rather delayed after the arrival of percolating water.

ACKNOWLEDGEMENT

This study was accepted financial supports by the Global COE project and the collaboration study project of the Arid Land Research Center, Tottori University.

REFERENCES

- Boll, J., Steenhuis, T. S. & Selker, J. S. 1992. Fiberglass wicks for sampling of water and solutes in the vadose zone, *Soil. Sci. Soc. Am. J.* 56: 701-707
- Gee, G. W., Zhang, Z. F. & Ward, A. L. 2003. A modified vadose zone fluxmeter with solution collection capability, *Vadose Zone J.*, 2: 627-632
- Holder, M., Brown, K. W., Thomas, J. C., Zabcik, D. & Murray, H. E. 1991. Capillary-wick unsaturated zone soil pore water sampler, *Soil Sci. Soc. Am. J.*: 1195-1202
- Inosako K. & Takuma, K. 2002. Determination of parameters of soil moisture retention curve by using genetic algorithm *Bull. Fac. Agric. Tottori Univ.*, 55: 13-20 (in Japanese with English abstract)
- Jinno, Y. & Honna, T. 1999. Analysis of nitrate leaching and nitrogen balance in Chinese yam grown in sand dune field by lysimeters, *Sand Dune Research*, 46(1): 27-36 (in Japanese with English abstract)
- Knutson, J. H. & Selker J. S., Unsaturated hydraulic conductivities of fiberglass wicks and designing capillary wick pore-water samplers, *Soil Sci. Soc. Am. J.*, 58, 721-729 (1994)
- Maeda M., Liyanage, B. C. & Ozaki, Y. 1999. Water collection efficiency of wick samplers under steady state flow conditions, *Soil. Sci. Plant Nutr.*, 45(2): 485-492
- Nonaka, M., & Kamura, T. 1995. Nitrate leaching and nitrogen balance in sand dune upland soil by lysimeter, *Japanese Journal Soil Sci. Plant Nutrition*, 66:372-380 (in Japanese with English abstract)
- Šimůnek, J., Šejna, M & van Genuchten, M. Th. 1999. *HYDRUS-2D/MESHGEN-2D simulating water flow and solute transport in two-dimensional variably saturated media*, IGWMC-TPS 53 C, Colorado school of Mines Golden, CO, 11 pp.
- van Genuchten, M. Th. 1980. A closed-form equation for predicting the hydraulic conductivity of unsaturated soil, *Soil Sci Soc. Am. J.*, 44: 892-898
- Zhu, Y., Fox, R. H. & Toth, J. D. 2002. Leachate collection efficiency of zero-tension pan and passive capillary fiberglass wick lysimeters, *Soil Sci. Soc. Am. J.*, 66: 37-43

Risk assessment of soil and groundwater contamination using HYDRUS-1D

T. Yasutaka

Kokusai Environmental Solutions Co.,Ltd, 2 rokuban-cho, Chiyoda-ku, Tokyo 102-0085, Japan

K. Nakamura

Graduate School of Agriculture, Kyoto University, Oiwake-cho, Kitashirakawa, Sakyo-ku, Kyoto 606-8502, Japan

ABSTRACT: In this study, we assessed the future risk of groundwater contamination from contaminated soil using HYDRUS-1D. We simulated an actual site polluted by boron in the Kanto region of Japan, where we measured boron concentrations at several depths. As a result of the simulation, the predicted boron concentration in groundwater was over 1.0 mg L^{-1} (the Japanese groundwater criteria) from 2025 to 2065, for about 40 years. This approach can help estimating the risk of groundwater contamination from contaminated soil more precisely and the decision-making for selecting countermeasure methods for stakeholders.

1 INTRODUCTION

Transport of pollutants to groundwater through the vadose zone depends on various factors, such as soil hydraulic properties, soil structure, the adsorption and transport characteristics of the pollutants, the depth of the groundwater table and the type of covering on the soil surface. Thus, the risk of groundwater contamination can vary, even when the concentration of the pollutants in the surface and subsurface soil is the same.

In Japan, the Soil Contamination Countermeasures Law (2003) provides standards designed to prevent groundwater contamination and to protect the health of people drinking groundwater. These standards define uniform criteria for groundwater and soil throughout Japan, regardless of the differences in their properties. There is a legal obligation to countermeasure contaminated soils that exceed these standards. Remediation is costly, but the real risk of groundwater contamination is predicted to be very low in many cases. It is important to manage soil contamination based on the risk to human health and the groundwater contamination risk based on Process-based models. Thus, there is a need to reconsider the present criteria.

The purpose of our research is to develop a risk assessment method for groundwater contamination from contaminated soil based on Process-based models and offer this model as a decision-making tool for stakeholders. In this study, we assessed the future risk of groundwater contamination rather than the risk to human health from drinking contaminated groundwater. Since, in our target region, many people consider groundwater to be a very important resource, they wish to protect the groundwater itself even if there is no risk to human health. Therefore, our target site is the one that has soil contamination, but does not yet have groundwater contamination.

In particular, we simulated an actual site polluted by boron in the Kanto region of Japan, where we measured boron concentrations at several depths. We simulated the boron concentration in the unsaturated and saturated zone and groundwater from 1980 to 2080 using a convective-dispersion equation that includes the adsorption of boron under actual and hypothetical rainfall events.

2 MATERIALS AND METHODS

2.1 Risk Assessment Procedure

In this research, we estimated the risk of groundwater contamination by boron at an old manufacturing site. We first made a conceptual model using the site investigation data. We then obtained the parameters of the soil adsorption characteristics of boron and various physical properties of the soil by laboratory experiments and from published data for the simulation. Next, we simulated water and boron transport in the unsaturated zone from 1980 to 2005 and assessed the validity of the predicted boron concentration profile with respect to the observed boron profile.

Subsequently, we simulated water and boron transport from 2005 to 2080 and obtained the boron concentration in groundwater. Finally, we assessed the risk of groundwater contamination by boron in the future by comparing our results with the Japanese groundwater criteria (1.0 mg L^{-1}).

2.2 Site Description and Conceptual Site Model

The soil sampling site was an old glass manufacturing site (about $5,000 \text{ m}^2$) located in the Kanto region of Japan. The surface and subsurface soil had been contaminated by boron; however, it had yet not reached the groundwater table. We surmised that the contamination occurred in 1980 when the factory had closed. The site was investigated in 2005.

2.2.1 Geology

The vadose zone is composed of two types of soil, an artificial layer located between ground level (G.L.) to G.L. -1.2 m and loam located between G.L. -1.2 m to G.L. -10 m at investigation point A. The aquifer is composed of sandy gravels. The unconfined aquifer is located between G.L. -10 m to G.L. -16.2 m and the groundwater level averaged 9.0 m below the ground surface at point A. Figure 1 shows the geology of point A and the conceptual site model using our simulation.

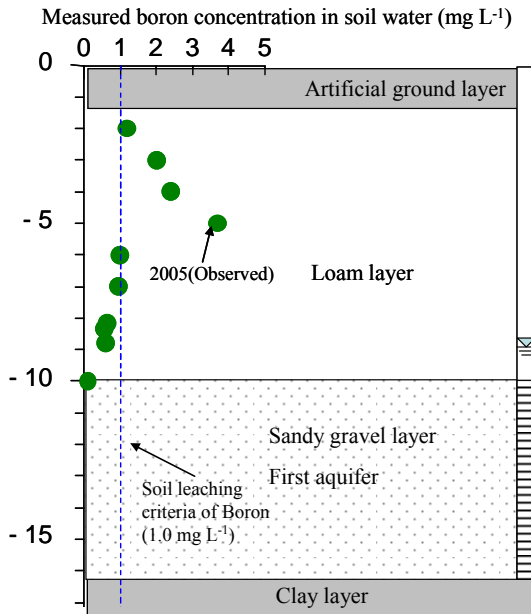


Figure 1 Geology and Boron concentration profile in soil water at point A.

2.2.2 Contamination States

The measured concentrations of boron ranged from below 50 mg kg⁻¹ to 430 mg kg⁻¹. It was measured by extraction with 1N-hydrochloric acid (this is the standard method in Japan). Since these concentrations are less than the Japanese ‘soil content criteria’ for boron, which is set to 4,000 mg kg⁻¹ to prevent risk to human health by direct ingestion of boron contaminated soils. Therefore we evaluated the human health risk by direct ingestion of boron contaminated soil at this site to be low.

In addition, there is another criteria in Japan called ‘soil leaching criteria’ measured by batch testing, in which distilled water is added to the soil to give a ratio of 10 L Kg⁻¹ dry weight (Japanese soil leaching criteria for boron is 1.0 mg L⁻¹). The purpose of these criteria’s is to prevent groundwater contamination and the risk to human health from drinking contaminated groundwater.

The measured boron concentrations by the leaching test at this site exceeded the soil leaching criterion (1.0 mg L⁻¹) at the surface soil and subsurface soil. Figure 1 shows the boron concentration profile of point A where boron transferred to the deepest depth at this site. The maximum concentration at point A (3.7 mg L⁻¹) was observed at G.L. -5.0 m. The measured boron concentrations were lower than the soil leaching criteria at depths less than G.L. -5.0 m at point A.

The boron concentration in groundwater was 0.01 mg L⁻¹, which was below the Japanese groundwater criteria for boron (1.0 mg L⁻¹). However, we do not deny that there is a future risk of groundwater contamination caused by vadose zone boron contamination.

2.3 Model Description

A numerical water flow and boron fate and transport model was applied to perform a future groundwater contamination risk analysis and profile of boron concentration at this site.

The numerical simulation model used was HYDRUS-1D Version 3, a software package for simulating the one-dimensional movement of water, heat and multiple solutes in variably-saturated media on the basis of finite element representation of the governing equations (Šimůnek et al., 2005). Table 1 shows parameters used in this simulation.

Table 1. Parameters using this simulation.

Parameters		Loam layer	Sandy gravel layer	unit
	θ_r	0 *	0.045 **	-
Soil water retention curve (van Genuchten(1980))	θ_s	0.708 *	0.43 **	-
	α	0.007 *	0.145 **	cm ⁻¹
	n	1.085 *	2.68 **	-
Saturated hydraulic conductivity	K_s	25 *	712.8 **	cm day ⁻¹
Freundlich adsorption equation **** $s=mC^n$	m	1.013	0.475	-
	n	0.066	0.43	-
Bulk density****	-	0.5	1.5 **	g cm ⁻³
D_w		0.48*****	0.48*****	cm ² day ⁻¹
D_L		100	100	cm

* Narioka et al.,(2000); ** :Using HYDRUS default value; *** :Estimated from the batch tests; **** :Obtained value by laboratory experiment ; ***** :David,(2002).

2.4 Simulation Procedure and Boundary Conditions

We only simulated at point A. The reason is that the risk of groundwater contamination at this point, judged by boron concentration and infiltrated depth, was at the highest level in this site. Since, boron existed in a solid state in the artificial ground layer in the beginning; the adsorption isotherms equation for boron was not approved in the artificial ground layer. The simulation was performed in three steps as follows.

2.4.1 *Water Movement from 1980 to 2005*

We simulated water movement from 1980 to 2005 for the total layer (which included the artificial layer, loam layer and sandy gravel layer) and calculated the water flux from the artificial layer to the loam layer.

The soil surface boundary was represented by atmospheric boundary conditions with daily precipitation rates (average 145.7 cm per year from 1980 to 2005 (Japan meteorological Agency, 1980–2005)). We assumed that evaporation was negligibly small because the site was a bare ground without vegetation.

The bottom of the layer was represented by a constant pressure head boundary condition (720 cm) which is the average groundwater level at this site.

2.4.2 *Boron Movement from 1980 to 2005*

We simulated boron movement from 1980 to 2005 in the loam layer and sandy gravel layer. The surface boundary related to water movement was represented by variable pressure head/flux with daily flux rates calculated as above. The upper boundary related to boron movement was represented by boundary condition of concentration flux. The boron input concentration was satisfied with the following conditions.

1. Total amount of boron in the loam and sandy gravel layer in 2005 seeped into the top of the loam layer from 1980 to 2005.
2. The boron flux decreased in a linear fashion from 1980 to 2005
3. The boron flux in 2005 was the same as the observed concentration of boron at the top of the loam layer in 2005.

2.4.3 *Water and Boron Movement from 2005 to 2080*

Finally, we simulated boron movement from 2005 to 2080 in the loam layer and sandy gravel layer. The surface boundary condition with water movement was the same as the above condition. We used daily flux rates from 1980 to 2005 in this period repeatedly. The upper boundary related to boron movement was represented by boundary condition of concentration flux. We assumed that the boron input concentration in 2005 was the same as the observed concentration of boron at the top of the loam layer in 2005 and decreased with the same gradient in the second condition.

2.5 *Estimating Boron Concentration in Groundwater*

We defined boron concentration in groundwater as the concentration of boron in soil water at G.L.–13.1 m the central depth of the first aquifer. We calculated secular variation in boron concentration in groundwater from 1980 to 2080, and assessed the risk of groundwater contamination by boron in the future by comparing the results with the Japanese groundwater criteria (1.0 mg L^{-1}).

3 RESULTS AND DISCUSSION

3.1 *Predicted Boron Concentration in Soil*

Figure 2 shows the simulated boron profile in soil water in 2005, 2030 and 2080. The simulated boron profile agrees well with the profile measured in 2005. However, there is a small difference in boron concentration below G.L.–5.0 m between the predicted and observed concentrations. After 2005, the predicted peak of boron concentration was less and the peak depth was deeper than that in 2005. Moreover, in 2080, the simulated boron concentration was less than the soil leaching criteria at every observed depth.

3.2 *Predicted Boron Concentration in Groundwater*

Figure 3 shows the simulated boron concentration in groundwater from 1980 to 2080 which increased rapidly in 2020 and reached a peak in 2040. The simulated peak concentration was 1.5 mg L^{-1} which exceeds the Japanese groundwater criteria (1.0 mg L^{-1}). After 2040, the concen-

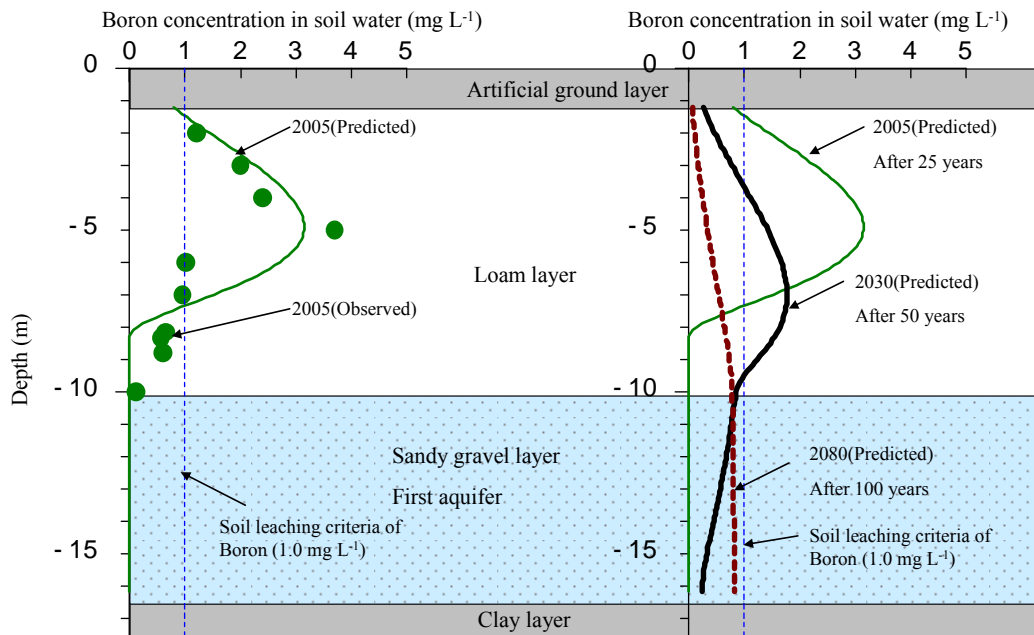


Figure 2. Measured Boron profile in soil water in 2005 and Simulated Boron profile in 2005, 2030 and 2080. Circle indicates measured boron concentration in soil water and lines are obtained by simulation.

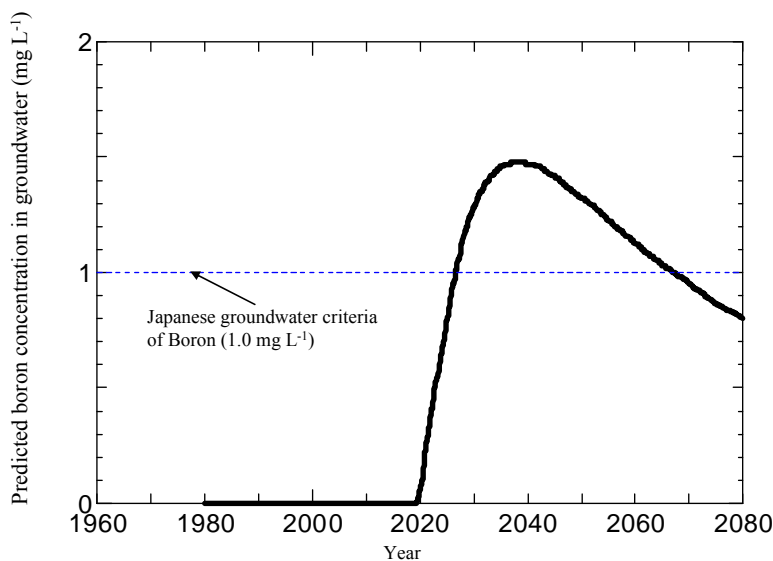


Figure 3. Simulated boron concentration in groundwater from 1980 to 2080. Lines are obtained by simulation. Boron concentration in groundwater is defined as the concentration of boron in soil water at the G.L.-13.1 m the central depth of the first aquifer.

tration decreased and was same as the Japanese groundwater criteria in 2065. The period during which boron concentration exceeded 1.0 mg L^{-1} was about 40 years.

3.3 Risk of Groundwater Contamination

As mentioned above, the period during which the boron concentration exceeded the Japanese groundwater criteria (1.0 mg L^{-1}) was about 40 years and the predicted peak concentration was about 1.5 times higher than that criteria.

We concluded that this contaminated soil should be measured, because there is a possibility that point A will become a source of groundwater contamination. For examples, we can recommend covering the contaminated soil by water interception asphalt to keep out infiltration rainfall and monitoring of groundwater quality considering these high countermeasure costs.

Using this procedure, we can estimate the risk of groundwater contamination from contaminated soil more precisely.

4 CONCLUSION

In this study, we developed a risk assessment method for groundwater contamination from contaminated soil based on process-based models and applied it to a boron contaminated site.

We simulated the boron concentration in the unsaturated and saturated zone and groundwater from 1980 to 2080, using a convective-dispersion equation that includes the adsorption of boron under actual and hypothetical rainfall events. As a result of the simulation, the predicted boron concentration in groundwater was over 1.0 mg L^{-1} (the Japanese groundwater criteria) from 2025 to 2065 for about 40 years. However, the predicted peak concentration was only about 1.5 times higher than the Japanese groundwater criteria.

We concluded that this contaminated soil should be measured, because there is a possibility that point A will become a source of groundwater contamination. As mentioned above, this method can help estimating the risk of groundwater contamination from contaminated soil more precisely and the decision-making for selecting countermeasure methods for stakeholders.

REFERENCES

- David R. Lide. 2002. CRC Handbook of Chemistry and Physics 80th Edition, CRC Press, Boca Raton.
- Šimůnek J., van Genuchten, M.Th 2005. The HYDRUS-1D Software Package for Simulating the One-Dimensional Movement of Water, Heat, and Multiple Solutes in Variably-Saturated Media, Ver.3.0. HYDRUS Software Series 1, UC Riverside, CA.
- Narioka, H. and M. Komamura 2000. Tubular Macropores formed in the Kanto Loam Formations of the Musashino plateau, Transactions of the Japanese Society of Irrigation, Drainage and Reclamation Engineering, 68(4), pp. 523~529.
- van Genuchten, M.Th. 1980. A closed-form equation for predicting the hydraulic conductivity of unsaturated soils. Soil Sci. Soc. Am. J. 44:892-898.
- Japan meteorological Agency 1980- 2005, Climatic Statistics, <http://www.data.jma.go.jp/obd/stats/etrn/index.php>, accessed at 30/8/2007.

Determination of soil hydraulic properties of undisturbed core sample using continuous suction outflow method

連続吸引流出法による不攪乱土の水分移動特性値の決定

M. Inoue¹⁾, K. Inosako²⁾, and K.C.Uzoma¹⁾

¹⁾ *Division of Afforestation and Land Conservation, Arid Land Research Center, Tottori University, Tottori, 680-0001, Japan*

²⁾ *Faculty of Agriculture, Tottori University, Tottori, 680-8550, Japan*

ABSTRACT: Simple, low-cost and portable laboratory equipment was developed to determine the unsaturated hydraulic properties of undisturbed soil sample. The significant advantages of the proposed method are the reduction of soil disturbance by measuring saturated and unsaturated hydraulic conductivities with identical equipment and quick/easy applicability in the field. Air pressure in the equipment was controlled by portable suction pump. Cumulative outflow from soil sample and bottom pressure were measured with time. The soil hydraulic properties were estimated using the inverse method in HYDRUS-1D software. Some technical know-how and detailed practical procedures were described for easy use of the method.

Key words: *soil hydraulic conductivity, inverse solution, continuous suction outflow method*

1 INTRODUCTION

Many laboratory methods such as one- and multistep outflow or evaporation method have been developed to determine soil hydraulic properties (relationship between volumetric water content θ and soil water pressure head h , relationship between θ and unsaturated hydraulic conductivity K). In many case, saturated hydraulic conductivity K_s was measured by a constant head method or a falling head method. After that, K was measured with different equipment. In this study, we used same equipment to measure K and K_s of undisturbed soil. Soil hydraulic properties were determined with simple and low-cost equipment using the inverse option in HYDRUS-1D software.

2 EXPERIMENTAL EQUIPMENT AND METHODS

2.1 Simple, low-cost and portable laboratory equipment

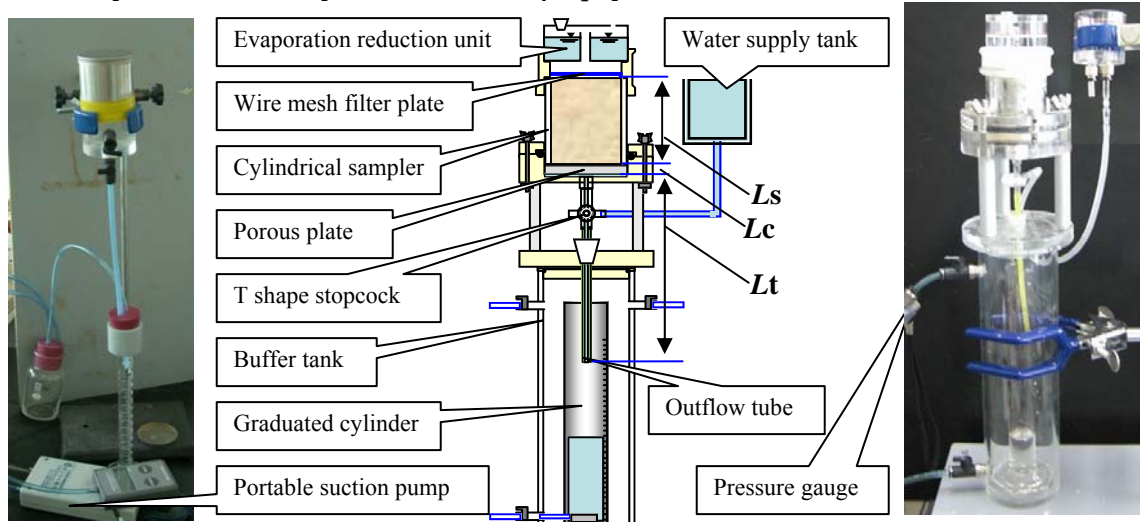


Figure 1 Simple and low-cost equipment to determine soil hydraulic properties.

The proposed equipment consists of water supply tank, evaporation reduction unit, wire mesh filter plate, cylindrical sampler, porous plate, T shape stopcock, buffer tank, vacuum pump and graduated cylinder as shown in Fig. 1.

2.2 Experimental procedure

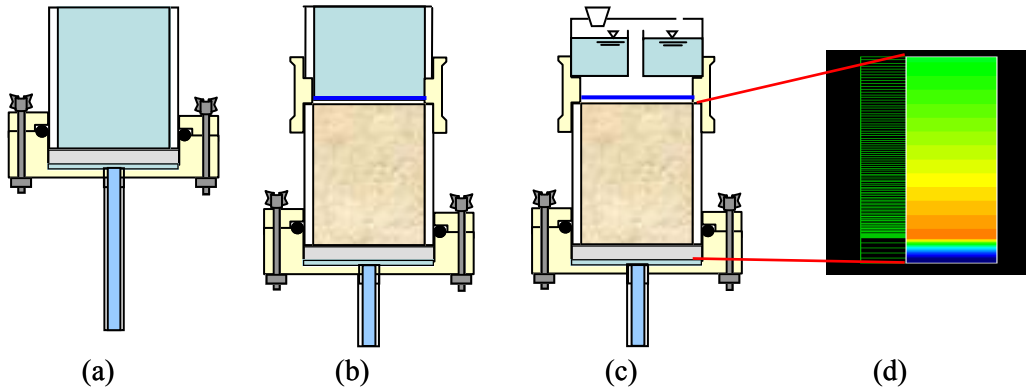


Figure 2 Apparatus for determination of (a) saturated hydraulic conductivity K_{cs} of porous plate, (b) saturated hydraulic conductivity K of soil and porous plate, (c) unsaturated hydraulic conductivity $K(h)$ and (d) initial pressure distribution in soil and porous plate using inverse technique.

Under constant vacuum condition in buffer tank, K_{cs} was estimated from upper pressure head (water depth in cylindrical sampler), bottom pressure head (air pressure P_a in buffer tank and length L_t of outflow tube) and outflow flux q (area A of cylindrical sampler and outflow rate Q), and thickness L_c of porous plate as shown in Fig.2 (a). The soil column in cylindrical sampler with inner diameter D of 5.0 cm and height L_s of 5.1cm was fitted on saturated porous plate by o-ring and screws. Soil was saturated using water supply tank and T shape stopcock as shown in Fig.2 (b). Soil saturated hydraulic conductivity K_s in cylindrical sampler was estimated from the appearance combined soil and porous plate saturated conductivity K_a , L_s , K_{cs} and L_c using following equation.

$$K_s = \frac{K_{CS} \cdot K_a \cdot L_s}{K_{CS}(L_s + L_c) - K_a \cdot L_c} \quad \dots\dots\dots (1)$$

After test of (b), T shape stopcock was closed and soil surface water was carefully removed by needle-tipped syringe. Evaporation reduction unit was set on the soil as shown in Fig.2 (c). Pressure gauge and portable suction pump were connected to buffer tank. Initially, pressure distribution in soil and porous plate should be as shown in Fig.2 (d). Bottom pressure head hb of porous plate was equal to $P_a - L_t$. We started the experiment by opening T shape stopcock and measured manually air pressure variation P_a (kPa) in buffer tank with pressure gauge and cumulative outflow rate variation $CumQ$ in graduated cylinder with time t .

Data set of variation of bottom pressure head hb (cm) and cumulative outflow flux $Cumq$ (cm) (= $CumQ/A$) with time were shown in Fig.3 (a) and (b), respectively. Difference between traditional one- or multistep method and the proposed continuous suction outflow method is that bottom pressure head at switching of air pressure does not change rapidly in the proposed method as shown in Fig.3 (a). The $Cumq$ data was obtained by manually measurement of time with stopwatch across the horizontal line in graduated cylinder such as 5mL-line, 10mL-line, 15mL and so on. Here, $P_a = -20kPa$ and $-65kPa$ (1kPa=10.2 cm). After experiment, soil water content θ_{final} was measured by dry-oven method and initial water content $\theta_{initial}$ was estimated using $CumQ$ data.

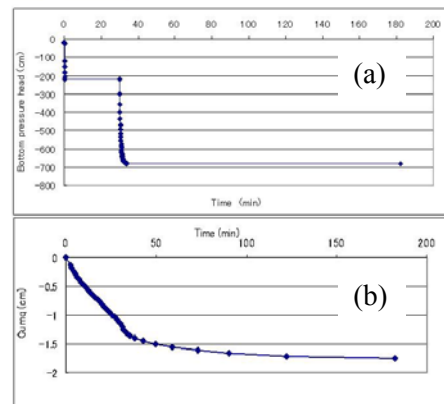


Figure 3 Variation of $Cumq$ and hb with time.

2.3 Input data for inverse option in HYDRUS-1D software

We used the recent software version 4.05 of HYDRUS-1D (2008.5.31) with van Genuchten-Mualem soil hydraulic model for determination of soil hydraulic properties.

	Qr	Qs	Alpha	n	Ks	l
Initial Estimate	0.295	0.66	0.0065	2.8	0.017	0.5
Minimum Value	0.285	0.64	0	1.1	0.001	0
Maximum Value	0.305	0.68	0	8	0.2	0
Fitted ?	<input checked="" type="checkbox"/>	<input type="checkbox"/>				

Figure 4 Input data of initial estimate, minimum and maximum values for soil.

Residual water content θ_r should be θ_{final} and saturated water content θ_s should be $\theta_{initial}$. Soil saturated hydraulic conductivity K_s was estimated using equation (1) and parameter l was 0.5. Range of parameter from minimum to maximum value was considered the measurement error such as water content of 0.01 or 0.02 cm^3/cm^3 and K of one order difference.

	Qr	Qs	Alpha	n	Ks	l
Initial Estimate	0	1	1E-020	1.001	0.0004	0.5
Minimum Value	0	0	0	0	0.0001	0
Maximum Value	0	0	0	0	0.01	0
Fitted ?	<input type="checkbox"/>	<input type="checkbox"/>	<input type="checkbox"/>	<input type="checkbox"/>	<input checked="" type="checkbox"/>	<input type="checkbox"/>

Figure 5 Input data of initial estimate, minimum and maximum values for porous plate.

Parameter α should be very small value because of saturated condition every time. Also porous plate saturated hydraulic conductivity was K_s measured as shown in Fig.2 (a).

3 RESULTS AND DISCUSSIONS

3.1 Inverse solution of HYDRUS-1D

The inverse option has proved to be very popular with many users, leading to a large number of applications in simple laboratory experiments (Šimůnek et al. 2008).

Fig. 6 shows one of the results of inverse solution based on the continuous suction outflow method. Calculation results are as follows:

SSQ: 0.000484
 Lower < 95% confidence < Upper
 WCR(θ_r): 0.286 < 0.2948 < 0.303 (cm^3/cm^3)
 WCS(θ_s): 0.653 < 0.664 < 0.676 (cm^3/cm^3)
 ALPHA: 0.00512 < 0.0066 < 0.00807 (1/cm)
 N(n): 1.24 < 6.56 < 11.87
 CONDS(K_s): 0.06 < 0.0826 < 0.105 (cm/min)
 CONDS(K_c): 0.000192 < 0.000316 < 0.00044 (cm/min)

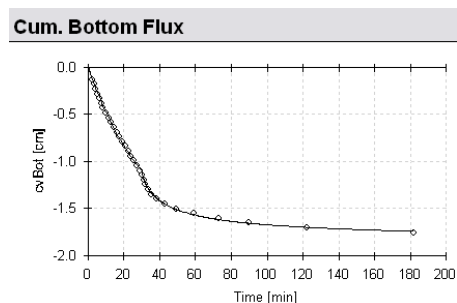


Figure 6 Fitting result of $Cumq(t)$.

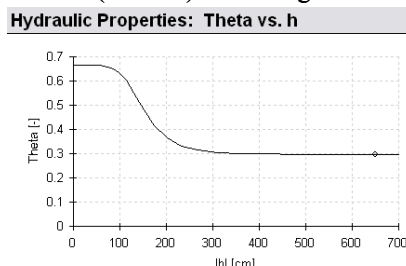
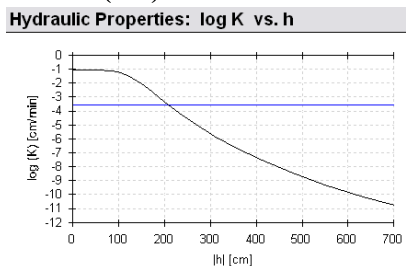


Figure 7 Relations of $\log(K)$ and θ to h obtained by HYDRUS-1D inverse solution.

3.2 Practical exercise with students

Many case studies could be used for training and practical exercise with students. But each student had different level of computer skill. Especially, inverse solution is one of the most difficult training exercises compared with normal simulation. A couple of students could not obtain final parameters because of inappropriate input data or initial parameters of *Alpha* and *n*. Another problem was wrong experimental data for inverse solution.

3.3 Special soil amendment

Good water management along with appropriate soil amendments is necessary for sustainable crop production (Inoue et al. 2008). Information of soil hydraulic properties for soil amendments is required for discussion and evaluation of irrigation scheduling, such as topics of total readily available moisture and water holding capacity.

However, the experiments on water holding capacity of sand mixed with super absorbent polymer (SAP) was difficult with some traditional methods since the material was expanded by swelling of SAP as shown in Fig.8. As a result, another soil amendment, bark treatment or bark mulching was sometime used.

In objective function of inverse method, the data of pressure head with tensiometer was used to eliminate non-uniqueness problem of traditional multistep outflow method. The measurement of soil pressure head was more difficult with tensiometer, as larger amount of bark was mixed in soil.



Figure 8 Expanded volume by swelling.



Figure 9 Sand mixed with bark.

4 CONCLUSIONS

Organic materials are often used in actual agriculture as soil amendments. The soil hydraulic properties of undisturbed core sample with organic material in actual field can be measured using the proposed continuous suction outflow method. It is important to conduct careful experiment in other to get the variation of air pressure and cumulative outflow rate with time. Also, the selection of parameter of *Alpha* and *n* in van Genuchten – Mualem equation is important for suitable inverse solution to estimate soil hydraulic properties in agricultural field. In order to accurately use the inverse solution option of HYDRUS-1D, more detail procedure information is needed.

ACKNOWLEDGEMENT

We greatly appreciate the financial supports by the Global COE program of Japan Society for Promotion of Science and the JGS company project for carrying out this research.

REFERENCES

- Šimůnek, J., van Genuchten, M. Th. And Šejna, M. 2008. Development and applications of HYDRUS and STANMOD software packages and related codes, *Vadose Zone J.* 7:587-600.
- Inoue, M., Irshad, M. and Ould Ahmed B. A., 2008. Interrelation of irrigation frequency and manuring on the growth and water use efficiency of wheat under arid condition, *Journal of Food, Agriculture & Environment*, 6(2): 290-294
- (M. Inoue: Arid Land Research Center, Tottori University, 1390 Hamasaka, Tottori, 680-0001, Japan.
Received 14 June 2008. Corresponding author: m11minoue@alrc.tottori-u.ac.jp)

Inverse Estimation of Clay Soil Unsaturated Hydraulic Conductivity Treated with Organic Material by Multistep Outflow Method

H. Andry, M. Inoue, T. Yamamoto, K.C. Uzoma

Arid Land Research Center, Tottori University, 1390 Hamasaka, Tottori 680-0001, Japan

H. Fujiyama

Faculty of Agriculture, Tottori University, Tottori, Japan

ABSTRACT: In this study, the effect of soil organic material on unsaturated hydraulic conductivity of clay soil was estimated using the inverse solution method with cumulative outflow and soil water pressure head measured simultaneously during laboratory transient multistep outflow experiments. The standard errors of the optimization parameters are less than 5 % of the parameter values. The possible use of the unimodal equation to estimate the unsaturated hydraulic conductivity of organic soil was discussed.

1 INTRODUCTION

Knowledge of the hydraulic properties of unsaturated soils is essential for most studies involving water flow and solute transport in the vadose zone. Many traditional methods to determine these properties require relatively restrictive initial and boundary conditions, and thus can be time-consuming, laborious, and expensive. Moreover, these methods generally aim at identifying either the retention or conductivity properties. Because of major advances in computational techniques and computer power, estimation of the unsaturated soil hydraulic properties by means of inverse modeling has now become an attractive alternative to traditional methods (Hopmans et al., 2002).

Popular laboratory approaches for the inverse estimation of the soil hydraulic properties have been one-step or multistep outflow methods (Durner et al., 1999). Whereas the general feasibility of outflow experiments for identifying hydraulic functions has been demonstrated in several studies (e.g., Hopmans and Simunek, 1999), the applicability and success of this method is often still limited by the ill-posedness of the problem being considered. Many studies have discussed the validity of the van Genuchten-Mualem model on the basis of direct comparisons between estimated and measured values of hydraulic conductivity (Stephens, 1992), as well as on the basis of theoretical analyses (Vogel and Cislserova, 1988). The model has produced satisfactory results in soils with a unimodal pore-size distribution, normal or log-normal shaped.

The organic matter content has been found to be one of the main factors controlling the aggregate stability of soils (Lado et al., 2004). It is often assumed that greater organic matter content in the soil will result in higher saturated hydraulic conductivity (K_s). The rationale behind such assumption is that more soil aggregation is linked to greater organic matter contents. Organic matter content and bulk density tend to be negatively correlated and therefore organic matter content and porosity are thought to be positively correlated. In well aggregated soils the pore system is frequently partitioned into intraaggregate and interaggregate (Tamari, 1994), thus resulting in bimodal pore-size distributions (Zurmühl and Durner, 1998), with one maximum in the range of textural pores and another in the range of structural pores. In such soils the independent draining of the inter- and intraaggregate pores frequently results in a steep slope of the retention curve near saturation (Thony et al., 1991), which a single van Genuchten or any unimodal-type function may not reproduce adequately (Mallants et al., 1997). In this study, an attempt to determine unsaturated hydraulic conductivity functions of clay soil treated with different concentrations of organic material with unimodal equation was conducted. The estimation was undertaken using the inverse solution method with cumulative

outflow and soil water pressure head measured simultaneously during laboratory transient multiseep outflow experiments. We compared results obtained by computer optimization using the inverse technique with the results taken directly from our laboratory measurements.

2 MATERIALS AND METHODS

The soil used in this study was taken from Tohaku in Tottori prefecture, Japan. The soil was collected from the soil surface of mountains cut, which has originated from red volcanic ash. It was air-dried, ground to an aggregate larger ≤ 5 mm, and then sieved through a 2 mm screen and the material ≤ 2 mm was used in the study. The textural composition of the soil was 539, 283, and 178 g kg⁻¹ of clay, silt, and sand, respectively.

Wood debris with clay structure provided by the Japan Green Inc. was used as soil organic amendments in this study. The organic material was mixed with the clay soil at a rate of 5, 10, 15, and 20 % in volume ratio.

2.1 Saturated hydraulic conductivity

One hundred and fifteen grams of dry treated soil were packed in 100 cm³ soil column with a soil bulk density of 1.15 Mg m⁻³. The saturation was undertaken from the bottom of the soil columns with distilled water for 24 hours under controlled room temperature at 25 °C. The saturated hydraulic conductivity was conducted by following the falling-head method described by Klute and Dirksen (1986).

2.2 Multistep outflow method

The calculation of $K(\theta)$ using the inverse solution technique uses the combination of van Genuchten's $\theta(h)$ model (1980)

$$S_e = \frac{\theta - \theta_r}{\theta_s - \theta_r} = \left[1 + |\alpha h|^n \right]^{\frac{1}{n} - 1} \quad (1)$$

with the pore-size distribution model of Mualem (1976) to yield (van Genuchten, 1980)

$$K(S_e) = K_s S_e^\ell \left[1 - \left(1 - S_e^{n-1} \right)^{\frac{1}{n}} \right]^2 \quad (2)$$

where S_e is the effective saturation ($0 \leq S_e \leq 1$), θ_r (cm³ cm⁻³) and θ_s (cm³ cm⁻³) are the residual and saturated water contents, respectively; K_s (cm s⁻¹) is the saturated hydraulic conductivity; ℓ denotes the pore-connectivity parameter fixed to be 0.5; α (cm⁻¹), and n are empirical parameters. In order to simulate outflow and pressure head in the optimization of the parameters of the hydraulic model, we used the program HYDRUS-1D model (Šimůnek et al., 1998), which is based on Marquardt's method (1963).

The experimental setup consisted of a 100 cm³ soil column stainless-steel assembled in the pressure cell with a 0.7 cm thick, and 1000 cm air-entry porous ceramic plate at the bottom connected with a burette. The saturated hydraulic conductivity of the porous ceramic plate was 1.25x10⁻³ cm s⁻¹. Soil samples were packed to predetermined bulk density of 1.15 Mg m⁻³. Soil samples were saturated from the bottom and subsequently equilibrated to an initial soil water pressure head of 0 cm at the column center. In order to keep the soil surface at the atmospheric pressure, the top of soil column was connected with plastic tube inside of perspex cylinder perforated with two different positions in both edges. The perspex cylinder was filled with

water at a depth smaller than the height of the inner plastic tube to minimize evaporation loss. Multistep pressurized outflow experiments were performed on the four soils using a pressure pump in a constant-temperature room at 25 °C. Each pressure increase will drive water out of the sample, through the ceramic plate and into the burette where the time-series of the outflow volume is recorded with a pressure transducer. Static equilibrium occurs when the outflow stops, leaving an opportunity to determine a water retention point. Subsequently, the air pressure is raised again until the maximum pressure is reached. We performed the measurements at -10, -20, -30, -40, -60, -100, -200, -300, -400, and -600 cm of head pressure. Final water content was determined by drying the samples at 105 °C.

3 RESULTS AND DISCUSSION

Table 1. Fitted parameter values for the retention data.

	θ_t cm ³ /cm ³	θ_s cm ³ /cm ³	α 1/cm	n	K_S cm/s
5 %	0.05	0.5925	$0.481 \cdot 10^{-2}$	1.274	$0.515 \cdot 10^{-4}$
10 %	0.15	0.5945	$0.768 \cdot 10^{-2}$	1.298	$0.788 \cdot 10^{-4}$
15 %	0.12	0.6075	$0.595 \cdot 10^{-2}$	1.365	$0.926 \cdot 10^{-4}$
20 %	0.2	0.6855	$0.567 \cdot 10^{-2}$	1.612	$0.210 \cdot 10^{-3}$

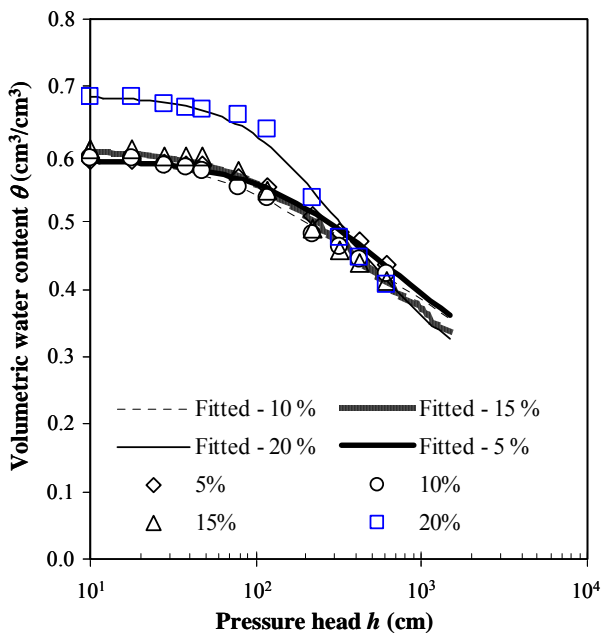


Figure 1. Soil water retention curves.

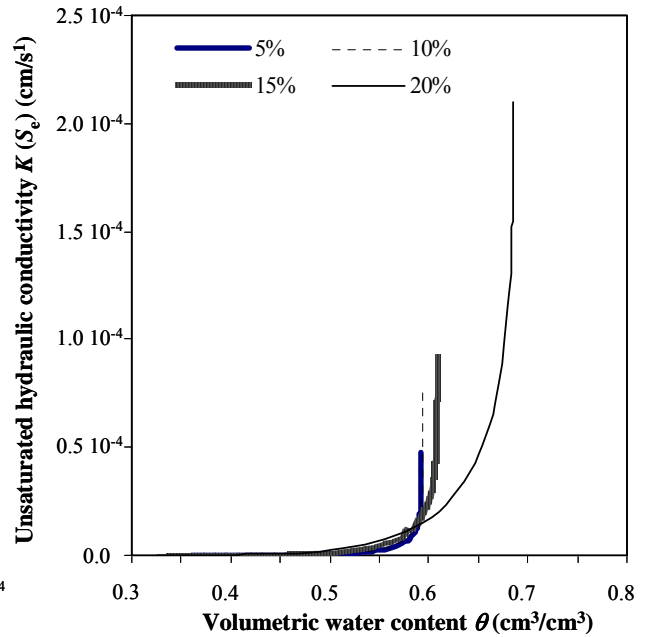


Figure 2. Soil unsaturated hydraulic conductivity.

3.1 Soil water retention curve

In Figure 1, inversely determined retention curves and observed data retention curves from near-equilibrium outflow of the treated soil with different organic material concentration are shown. It was found that both curves agreed well with the retention data for all treated soils, it implies the reliability of both the observed and the fitted curves. This experiment results suggests that the unimodal equation could be still used for estimating the water retention curve of some clay soil treated with organic materials. The parameter values used for the fitted retention curves are listed in Table 1.

3.2 Unsaturated hydraulic conductivity

The saturated hydraulic conductivity determined with falling-head of the soils treated with 5, 10, 15, and 20 % volumetric organic content was 4.89×10^{-5} , 7.55×10^{-5} , 9.55×10^{-5} , and 2.15×10^{-4} cm s^{-1} , respectively. Hydraulic conductivities, $K(S_e)$, determined from the equations (1) and (2) are given in Figure 2. The optimized parameter values were shown in Table 1. The standard errors of the parameters are less than 5 % of the parameter values. It was found from that the $K(S_e)$ increased with increasing the concentration of the organic material. This result was in agreement with the fact that organic matter improves the soil aggregate structure by increasing the aggregate size and the pore space between aggregate sizes. Based on this study, the estimation of the $K(S_e)$ affected by soil organic material could be still possible with the unimodal equation.

4 CONCLUSION

The organic matter content has been known to be one of the main factors controlling the soil aggregate structure. In this study, the effect of soil organic material on unsaturated hydraulic conductivity of clay soil was estimated using the inverse solution method with cumulative outflow and soil water pressure head measured simultaneously during laboratory transient multiseep outflow experiments. It was found that the inversely determined curves agreed well with the retention of the observed data for all treated soils, thus implies the reliability of both the observed and the fitted curves. The estimated unsaturated hydraulic conductivity was found in agreement with the positive effect of organic matter on the soil aggregate structure.

The possible use of the unimodal equation to estimate the unsaturated hydraulic conductivity of organic soil as shown in this study could help to take a decision making for the maintenance of soil organic matter content.

5 REFERENCES

- Durner, W., Schultze, B. & Zurmühl, T. 1999. State-of-the-art in inverse modeling of inflow/outflow Experiments. p. 661-681. In M.Th. van Genuchten et al. (ed.) Proc. Int. *Workshop on Characterization and Measurement of the Hydraulic Properties of Unsaturated Porous Media*. Univ. of California, Riverside.
- Hopmans, J. & Simunek, J. 1999. Review of inverse estimation of soil hydraulic properties. p. 643-659. In M.Th. van Genuchten et al. (ed.) Proc. Int. *Workshop on Characterization and Measurement of the Hydraulic Properties of Unsaturated Porous Media*. Univ. of California, Riverside.
- Hopmans, J.W., Simunek, J., Romano, N. & Durner, W. 2002. Simultaneous determination of water transmission and retention properties. Inverse methods. p. 963-1008. In J.H. Dane and G.C. Topp (ed.). *Methods of soil analysis*. Part 4. SSSA Book Ser. 5. SSSA, Madison, WI.
- Klute, A. & Dirksen, C. 1986. Hydraulic conductivity and Diffusivity, laboratory methods. p. 687-734. In A. Klute (ed.) *Methods of soil analysis*. Part I, 2nd ed., SSSA Book Ser. 5. SSSA, Madison, WI.
- Lado, M., Paz, A. & Ben-Hur, M. 2004. Organic matter and aggregate-size interactions in saturated hydraulic conductivity. *Soil Sci. Soc. Am. J.* 68: 234-242.
- Mallants, D., Tseng, P.H., Toride, N., Timmerman, A. & Feyen, J. 1997. Evaluation of multimodal hydraulic functions in characterizing a heterogeneous field soil. *J. Hydrol.* 195: 172-199.
- Marquardt, D. W. 1963. An algorithm for least-squares estimation of nonlinear parameters. *SIAM J. Appl. Math.*, 11: 431-441.
- Mualem, Y. 1976. A new model for predicting the hydraulic properties of unsaturated porous media. *Water Resour. Res.* 12: 1248-1254.
- Stephens, D.B. 1992. A comparison of calculated and measured hydraulic conductivity of two uniform soils in New Mexico. p. 249-262. In M.Th. van Genuchten, et al. (ed.) *Indirect methods for estimating the hydraulic properties of unsaturated soils*. Riverside: Univ. of California.
- Šimunek, J., van Genuchten, M. Th. Gribb, M. M. & Hopmans, J. W. 1998. Parameter estimation of unsaturated soil hydraulic properties from transient flow processes. *Soil & Tillage Research* 47: 27-36.
- Tamari, S. 1994. Relations between pore-space and hydraulic properties in compacted beds of silty-loam aggregates. *Soil Technol.* 7: 57-73.

- Thony, J.L., Vachaud, G., Clothier, B.E. & Angulo-Jaramillo, R. 1991. Field measurement of the Hydraulic properties of soil. *Soil Technol.* 4: 111-123.
- van Genuchten, M.Th. 1980. A closed-form equation for predicting the hydraulic conductivity of unsaturated soils. *Soil Sci. Soc. Am. J.* 44: 892-898.
- Vogel, T. & Cislerova, M. 1988. On the reliability of unsaturated hydraulic conductivity calculated from the moisture retention curve. *Transp. Porous Media* 3: 1-15.
- Zurmühl, T. & Durner, W. 1998. Determination of parameters for bimodal hydraulic functions by inverse modeling. *Soil Sci. Soc. Am. J.* 62: 874-880.

Integrated Modeling of Watershed Hydrologic Fluid and Heat Flows

K. Inaba

Takenaka Research & Development Institute, Inzai, Chiba, Japan

H. Tosaka & M. Yoshioka

Graduate School of Eng. The Univ. of Tokyo, Bunkyo-ku, Tokyo, Japan

ABSTRACT: The expansion of city region occurs the situation to the deterioration and decrease in the natural ecosystem according to the expansion of no infiltration area, the ground water level drawdown, groundwater pollution, and so on. It is pointed out that the watershed management at regional area from city region to mountainous takes the key role to solve these problems. From a scientific, technological point of view, the development of the modeling of hydrologic and thermal circulation processes in the watershed becomes very important. We developed the geosphere hydrological and thermal circulation modeling method which includes the physical processes related to fluid and heat transportation. This method has the possibility of becoming useful in evaluating the whole system of hydrologic and thermal circulation in the geosphere.

1 INTRODUCTION

The hydrologic circulation of water, a large-scale cycle of mass and heat movement on the earth surface is generated mainly by solar radiation in hydrosphere and gravity, transported through the atmosphere, and becomes rainfall/snowfall, surface runoff, underground infiltration/discharge, evapotranspiration at land areas.

Recent scientific predictions have warned that the promotion of the global warming through this century might cause serious changes in the hydrological cycle, might arise increase in natural disasters, and water problems related to shortage of water resources and desertification. In order to preserve local environments, we need to solve environmental problems such as the degradation of natural environment due to urbanization and the increase of drought area as well as industrially waste and contaminated lands.

Nowadays, “watershed management” plays a crucial role in administrative policy for securing water resources, preventing natural disasters, and preservation of regional environment. For practical and reasonable management, it is essential for us to provide reliable scientific/engineering understandings and evaluation methods using numerical models for management purposes because it is impossible to observe with high accuracy whole regional area and it is difficult to evaluate total system of regional area based on human experience and knowledge.

From the aspect of modeling, the watershed hydrologic environment consists of fluids and heat processes including solar short wave radiation, atmospheric/surface long wave radiations, rainfall/snowfall, surface runoff, underground infiltration/discharge, evapotranspiration at land areas. The ecosystem and man-made system are under such processes (See Fig. 1).

There are many types of numerical models practically used for river runoff and flood analyses, and groundwater analysis. Most of these simulation models deal with the mass flow of the liquid phase water. However, we realize that increasing number of environmental assessments basically needs the consideration of heat flow taking place simultaneously with the fluid transport. For example, in assessing the urban heated environment, to understand the state and finding out the mitigation measures, consideration of thermal flow becomes important. Moreover,

the thermal data from the watershed could be very useful information to improve reliability of identifying the field hydrological/hydraulic parameters, in addition to the ordinary data. Currently, no numerical code applicable for the watershed-scale fluid-heat coupled modeling is known.

In this study, the authors propose a new type environmental simulator, that is, a physically-based hydrologic fluids and heat circulation model including the near-surface atmospheric layer, the surface and subsurface regions of a watershed.

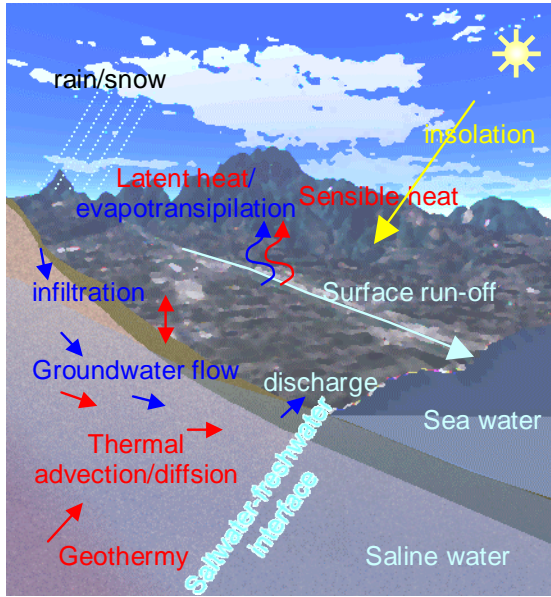


Figure 1. Conceptual water and heat circulation in a watershed

2 MATHEMATICAL MODEL

2.1 *The concept of the integrated model*

The following processes are included referring to Tosaka et al. (1996) for modeling natural water and heat circulation system in geosphere.

- Surface heat processes consisting of solar radiation, long wave emission, sensible and latent heat transport
- Water and heat input by the rainfall and/or snowfall (accumulation and melting)
- Surface flow and subsurface 2-phase flow
- Heat transport by surface and subsurface flow, and through soil and geological formations
- Thermally non-equilibrium states among air/liquid/solid phases are assumed by separating respective phase temperatures.

Primary variables to model processes are (a) atmospheric pressure (atmospheric pressure or underground vapor pressure), (b) water saturation (water depth at surface or underground water saturation), (c) concentration of dissolved matter, (d) ground snow depth, (e) water temperature (surface water or groundwater temperature), (f) air temperature (atmospheric temperature or underground vapor temperature), (g) solid phase temperature (snow temperature at surface or underground solid phase temperature).

Seven equations of the conservation of mass and energy are solved with the fully implicit finite difference method.

2.2 *Heat budget at the ground surface*

Double layer model (Kondo and Watanabe, 1992) is employed here.

In this model, the heat flux for each unit area that ground surface and the plant layer receive is shown by the following expressions.

$$\Delta Q_g = f_v R^\downarrow + (1 - f_v) \sigma T_v^4 - \sigma T_g^4 - H_g - \lambda E_g + G \quad (1)$$

$$\Delta Q_v = (1 - f_v)(R^\downarrow + \sigma T_g^4) - 2(1 - f_v)\sigma T_v^4 - H_v - \lambda(E_v + I) \quad (2)$$

$\Delta Q_{g,v}$ is the energy amount the ground or vegetation receives, f_v is the transmittance of the vegetation layer, T_v is the vegetation temperature, T_g is the surface temperature, R^\downarrow is the net radiation, $H_{g,v}$ is the sensible heat from ground or vegetation to atmosphere, $E_{g,v}$ is the evapotranspiration from the ground or vegetation, I is the blocking evaporation by the canopy, G is the soil heat flux.

2.3 Surface/Subsurface fluid flow

Hydraulically, river flow or surface flow on the slope is generally described as an open channel flow. Practical water velocity used for runoff analysis is obtained as the Kinematic Wave (KW) or Diffusion Wave (DW). In most run-off simulations, KW is used for the calculation of river networks. We here use the DW velocity because it is more appropriate and flexible than the KW in treating the flow on the topographic surface.

The diffusion wave velocity is expressed as,

$$v_w = -\frac{R^{2/3}}{n} \frac{I}{|I|^{1/2}} \quad (3)$$

where n is the Manning's coefficient of roughness of the channel floor and walls, R is the hydraulic radius defined and I is the gradient of water surface defined by

$$R = \frac{Wh}{W + 2h} \quad (4)$$

$$I = \frac{\partial z}{\partial x} + \frac{\partial h}{\partial x} \quad (5)$$

where, h is the water depth, W is the width of a rectangular channel, z is the altitude, x is the axis along the surface. For shallow surface water flow, R can be approximated as $R \approx hW$ ($W \gg h$).

For the flow velocity in porous media, we use the air-water 2-phase Darcy's law as

$$v_w = -\frac{kk_{rw}}{\mu_w} \frac{\partial \Psi_w}{\partial x} \quad (6)$$

$$v_a = -\frac{kk_{ra}}{\mu_a} \frac{\partial \Psi_a}{\partial x} \quad (7)$$

where, k : permeability, k_r : relative permeability, μ : viscosity of fluid, Ψ : hydraulic potential.

2.4 Heat transfer

The heat is transported with the mass flow as

$$q_p = \rho_p v_p H_p - \lambda_p^* \frac{\partial T_p}{\partial x} \quad (8)$$

where q_p is the heat flux for a unit section and unit time in p phase, λ_p^* is the thermal conductivity including mechanical dispersion in p phase, H_p is the enthalpy of p phase for a unit section. The affixing p shows the kind of phase ($p=w$: water, a : air, s : solid phase).

2.5 Heat exchange among phases

In the thermal model used for groundwater models, geothermal models, and petroleum reservoir models, the assumption that the water-vapor-solid phases have the same temperature, i.e., the in-

stant thermal equilibrium conditions among phases is employed. In the natural hydrological system, however, we observe usually non-equilibrium conditions thermally.

These considerations have led us to the formulation which assumes thermally non-equilibrium state among gas, liquid and solid phases. We give independent temperatures for solid, water and air within the same discretized grid block. The transient solution of heat conduction at the interface of two different temperatures (T_{p1}, T_{p2}) of each phase (p1,p2) per unit area can be expressed as

$$e_{p1 \rightarrow p2} = 2\sqrt{\frac{\lambda_e}{\pi \Delta t}} (T_{p1} - T_{p2}) \quad (9)$$

where, $e_{p1 \rightarrow p2}$ is average heat crossing the contact boundary in contact time Δt , λ_e is effective heat conductivity. In this paper, λ_e is assumed as the heat conductivity of downstream phase.

2.6 Solute transfer

The solute transfer with the flow of water is expressed by the convection-dispersion flux as

$$m_c = v_w C - D^* \frac{\partial C}{\partial x} \quad (10)$$

where C is the solute concentration, D^* is the dispersion coefficient of either the turbulent diffusion coefficient for surface flow, or the subsurface dispersion including molecular diffusion and mechanical dispersion.

2.7 Total equation system

With the mentioned velocity equations and other source terms, the mass balance equations can be written as follows.

$$\text{Independent phase: } -\nabla \rho_p v_p - \rho_p q_p = \frac{\partial(\rho_p \phi S_p)}{\partial t} \quad (11)$$

$$\text{Solution phase: } -\nabla \rho_w v_w C + \nabla D^* \nabla C - \rho_w q_w C = \frac{\partial(\rho_w \phi S_w C)}{\partial t} \quad (12)$$

where, q_p ($p=w, a, s$) is the input by precipitation or well production rate, S_p is the saturation, ϕ is the porosity. When $p=s$, the solid saturation S_s is defined as $S_s=(1-\phi)/\phi$.

The heat balances of respective phases are written as follows.

$$-\nabla \rho_p v_p H_p - \nabla \lambda_p \nabla T_p - \rho_p q_p H_p + \rho_p q_p H_p - e_{p \rightarrow p2} - e_{p \rightarrow p3} = \frac{\partial(\rho_p \phi S_p U_p)}{\partial t} \quad (13)$$

where, U_p is the inner energy of p phase per unit.

In the issue, 4 equations of mass balance (water, air, solute, solid) and 3 equations of energy balance (water, air, solid) are led. In addition, the variable is adjusted to seven using the relational expression like $S_w + S_a = 1$. Therefore, it is possible to solve in the numerical solution.

3 MODEL OPERATION

3.1 Input and output data

The constructed simulator needs ordinary data used in runoff simulation and groundwater simulation, and additional data for thermal properties and thermal conditions as shown in Table1.

Table 1. Model input and output.

Input /Output	Items	Contents	
Input	Static field data	topography of the surface subsurface 3-D geological structure basic rock properties	
	Fluid & rock data	compressibility thermal expansibility viscosity thermal coefficients capillarity relative permeability	
	Time dependent data	Meteorological data	atmospheric pressure temperature humidity wind speed solar radiation
		Precipitation	rainfall rate
		Land use	land use map LAI interception
Artificial activity		land modification underground construction well operation	
Output	Binary output	pressure water saturation concentration water temperature air temperature solid temperature	
	Text output	input data for confirmation river flow rate groundwater level fluxes at specified points convergence information	

3.2 *Numeric solution*

The simulator uses the complete implicit FDM method. The 7 difference expansion equations are solved by Newton-Rhapson method. In addition, the pre-conditioned conjugate residual method is used for solution of determinant.

4 EXAMINATION OF REPEATABILITY BY LABORATORY EXPERIMENT

4.1 *Outline of test equipment*

The test equipment measures the infiltration and heat transfer rate in vadose zone. The outline of test equipment shows in Fig. 2.

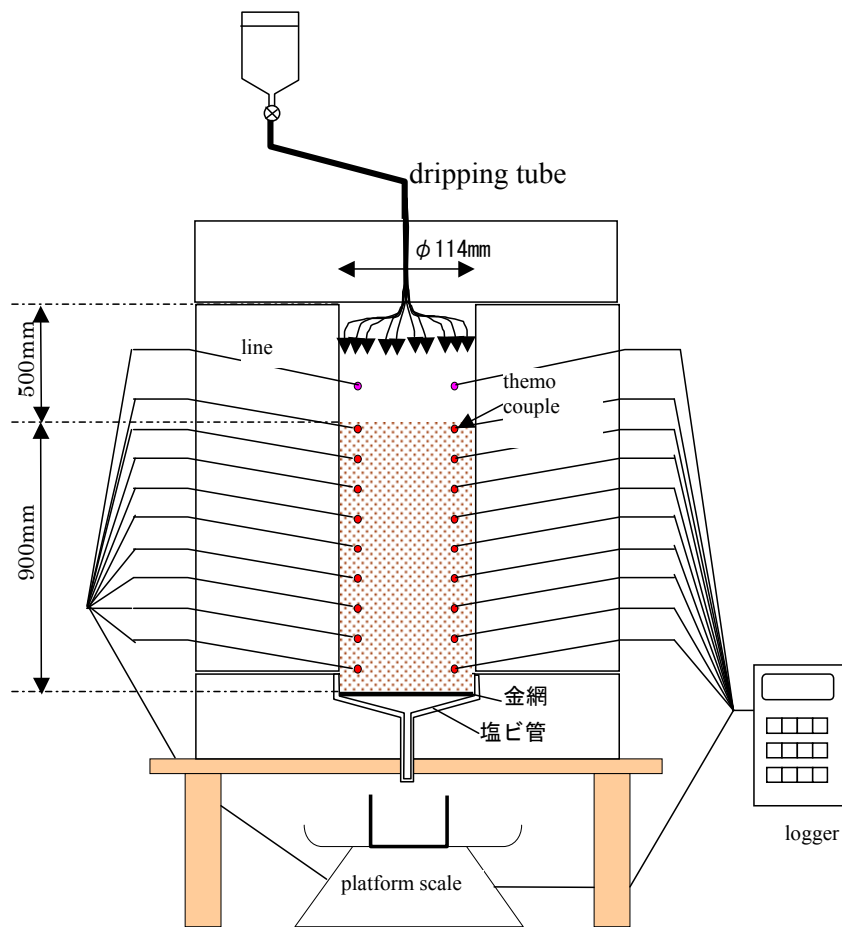


Figure 2. Outline of test equipment

The equipment consists of the test portion and the styrene form. The thermocouples are set at the surface of test portion and set -10cm to -80cm level at interval of 10cm. The portion porosity is 0.4.

4.2 Examination

Four permeability test was implemented using water which was same temperature with the laboratory. Using this result, the characteristics in unsaturated zone of the portion was identified.

The identified capillary pressure curve and the relative permeability curve shows in Fig.3.

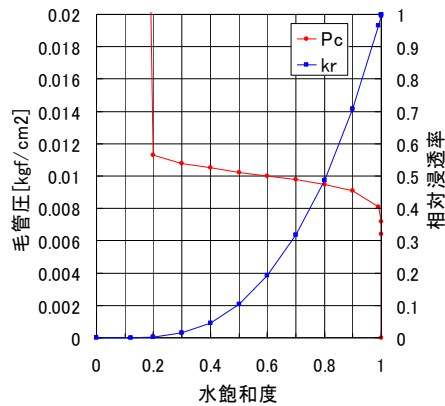


Figure 3. Capillary pressure curve and relative permeability of water

The comparison of cumulative flow rate at the bottom between observation data and calculated value is shown in Fig. 4.

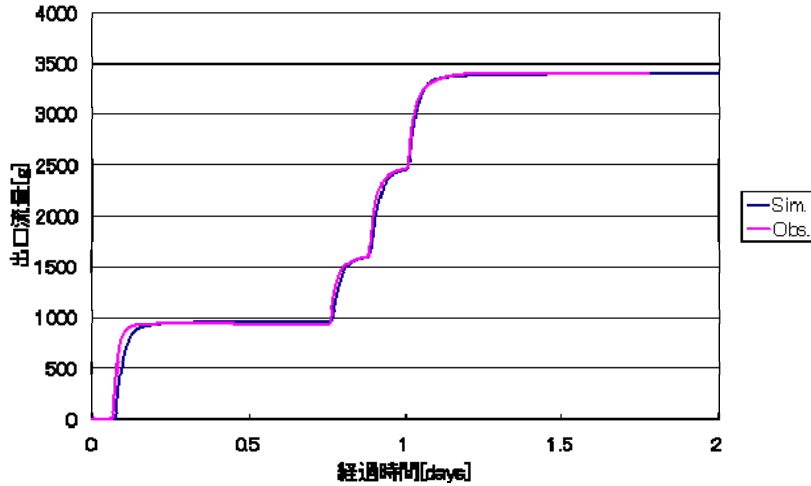


Figure 4. Cumulative flow rate

Next, the permeability test using warm water (about 42 degree) of 5 times was done. The result of heat transfer observation data by thermocouples and the simulation result are shown as follows.

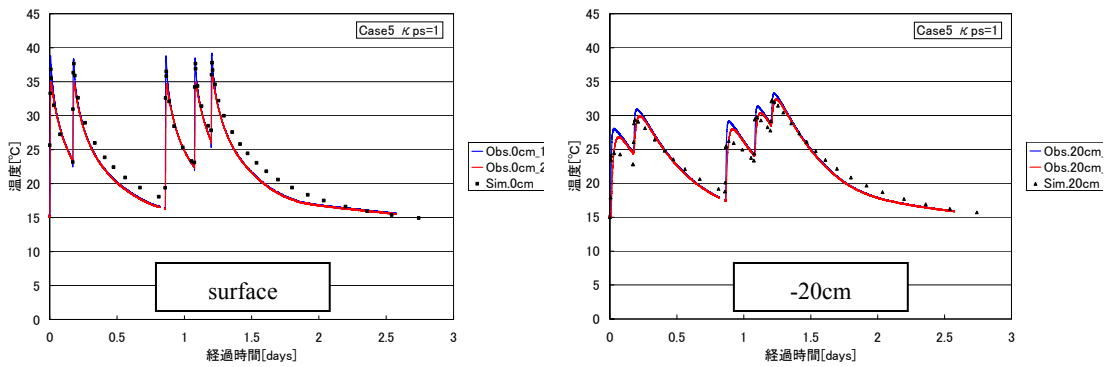


Figure 5. Temperature change at the surface and -20cm level

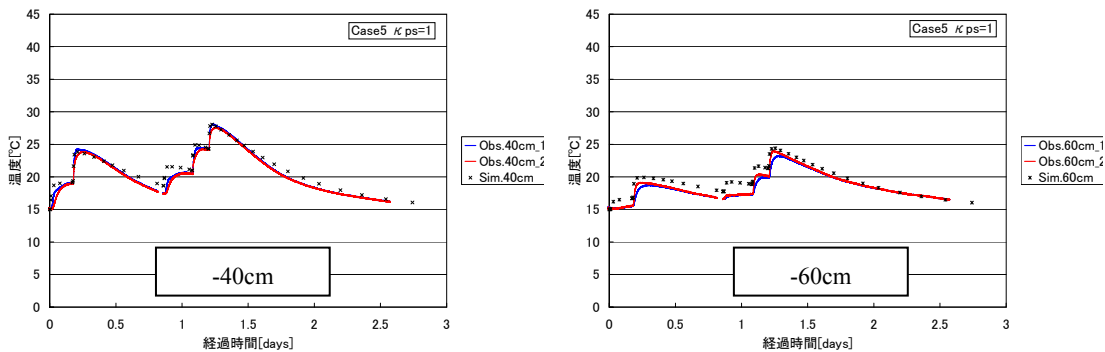


Figure 6. Temperature change at -40cm level and -60cm level

5 CONCLUSIONS

It can be said that the well-repeatable model of fluid and heat transportation in vadose zone is constructed. It is important to be going to confirm applicability in the field scale in the future.

The simulations that use 2D or 3D regional models are being executed now. Those progress reports and the problems in the regional model use are scheduled to be reported on the day.

REFERENCES

- Bear, J. 1972. *Dynamics of Fluids in Porous Media*. Dover Publication, Inc.
- Domenico, P.A. and Schwartz, F.W. 1990. *Physical and Chemical Hydrogeology*, John Wiley & Sons, Inc.
- Kondo, J. and Watanabe, T. 1992. Studies on the bulk transfer coefficients over a vegetated surface with a multilayer energy budget model. *J.Atmos. Sci.*, 49, 2183-2199.
- Saito, H., Šimůnek, J., and Mohanty, B.P. 2006. Numerical Analysis of Coupled Water, Vapor, and Heat Transport in the Vadose Zone, *Vadose Zone Journal*, Soil Science Society of America, 5, 786-800.
- Woodside, W. and Messmer, J. H. 1961. Thermal conductivity of porous media I. Unconsolidated sands, *J. Appl. Phys.*, Vol.32, pp.1688-1699.
- Tosaka, H., Kojima, K., Miki, A., and Chino, T. 1996. Numerical Simulation of Surface-Subsurface Coupled, 2-Phase, 3-Dimensional Fluid Behavior, *Journal of Groundwater Hydrology*, Japanese Association of Groundwater Hydrology, 38, 4, 253-267.
- Inaba, K., Tosaka, H., Hirai, S., and Yoshioka, M. 2007. Development of Integrated Model of Thermal/Hydro-circulation System, *Journal of Hydraulic Engineering*, Japan Society of Civil Engineers, 51, 469-474.

Estimating Hydraulic Property for a Dune Sand and a Volcanic Ash Soil Using Evaporation Method

M. Sakai

Department of Environmental Sciences, University of California Riverside, Riverside, CA 92521, USA

N. Toride

Graduate School of Bioresources, Mie University, Tsu, Mie 514-8507, Japan

ABSTRACT: The Fayer and Durner models, which modified the water retention curve of the van Genuchten (VG) model, combined with the statistical pore-size distribution model of Mualem were used to predict unsaturated hydraulic conductivity functions of Tottori dune sand and aggregated Kumamoto Andisol. Parameters of the Fayer and Durner models, as well as the VG model, were inversely estimated with the evaporation method. The Fayer model well described unsaturated hydraulic conductivity for the dune sand reflecting pore water retention for higher water contents and absorbed water retention on the surface of soil particles for lower water contents. The Durner model was suitable to the Andisol whose hydraulic properties were strongly affected with the distinct the aggregated structure. The Mualem model can predict unsaturated hydraulic conductivity for a wide range of soil water pressure when an appropriate model is used for the water retention curve and the pore-connectivity coefficient, l is estimated. Furthermore, it was also suggested that we need to use an appropriate soil water retention function to predict unsaturated hydraulic conductivity for much smaller pressure heads than the minimum pressure head observed during the evaporation experiment

1 INTRODUCTION

Although the van Genuchten-Mualem model (VG model) is widely used for the hydraulic property functions, it is not suitable to sandy soils for lower water content or aggregated soils describing stepwise shape of retention curves. Fayer and Simmons (1995) and Durner (1994) suggested modified functions for retention curves (Fayer model and Durner model). The objective of this study is to evaluate the applicability of the Fayer model to a sandy soil and the Durner model to an aggregated soil, especially for the unsaturated hydraulic conductivity functions predicted with the Mualem's pore-size distribution model. We inversely estimated parameters of the Fayer and Durner models, as well as the VG model with the evaporation method, and compared the calculated pressure heads with the observed ones (Sakai and Toride, 2007a).

2 HYDRAULIC PROPERTY FUNCTIONS

2.1 Fayer model

Fayer and Simmons (1995) modified the residual water content in the VG model to better represent the soil water retention curve at low water contents:

$$\theta/\theta_s = S_e = (1 - \chi(h)\theta_a/\theta_s) \left[1 + |\alpha h|^n \right]^{-m} + \chi(h)\theta_a/\theta_s \quad (1)$$

where θ is the volumetric water content [L^3L^{-3}], θ_s is the saturated water content [L^3L^{-3}], S_e is the

effective liquid saturation [-], h is the soil water pressure head [L], α [L^{-1}], n [-], m ($= 1-1/n$), and θ_a [L^3L^{-3}] are empirical shape parameters. The second term $\chi(h)\theta_a/\theta_s$ denotes the adsorption of water on soil, where $\chi(h) = 1 - \ln(-h)/\ln(-h_m)$, and h_m is the pressure head [L] at the water content equal to 0 (Rossi and Nimmo, 1994). We used $h_m = -10^{-6}$ cm in this study. By substituting Eq. (1) into Mualem's pore-size distribution model (1976), the closed-form of the unsaturated hydraulic conductivity is given as:

$$K(S_e) = K_s S_e^l \left[\Gamma_s(h) / \Gamma_{\max} \right]^2 \quad (2)$$

where K is the unsaturated hydraulic conductivity [LT^{-1}], K_s is the saturated hydraulic conductivity [LT^{-1}], l is the pore-connectivity coefficient [-], and Γ_s and Γ_{\max} are the integrals in Mualem model (Fayer and Simmons, 1995).

2.2 Durner model

Durner (1994) proposed a multimodal retention function which is constructed by a linear superposition of two VG models:

$$\frac{\theta - \theta_r}{\theta_s - \theta_r} = S_e = w_1 \left[1 + |\alpha h|^n \right]^{-m} + w_2 \left[1 + |\alpha_2 h|^{n_2} \right]^{-m_2} \quad (3)$$

where θ_r is the residual water content [L^3L^{-3}], α_2 [L^{-1}], n_2 [-], and m_2 ($= 1-1/n_2$) are empirical shape parameters, and w_1 and w_2 are weighting factors ($w_1 + w_2 = 1$). Combining Eq. (3) with Mualem's model leads to following closed-form model (Priesack and Durner, 2006):

$$K(S_e) = K_s \frac{(w_1 S_{e1} + w_2 S_{e2})^l \left(w_1 \alpha \left[1 - (1 - S_{e1}^{1/m})^m \right] + w_2 \alpha_2 \left[1 - (1 - S_{e2}^{1/m_2})^{m_2} \right] \right)^2}{(w_1 \alpha + w_2 \alpha_2)^2} \quad (4)$$

3 EVAPORATION METHOD

3.1 Evaporation experiment

Tottori dune sand and Kumamoto Andisol were used for soil samples. Figure 1 shows the measured soil water retention curves. The retention curve of Tottori dune sand shows an abrupt decrease at $-20 > h > -50$ cm and a gradual decrease at $h \leq -50$ cm, describing water retention at soil pores and at the surface of soil particles. Kumamoto Andisol shows a stepwise soil retention curve describing retention property inside and outside of aggregates. The Fayer and the Durner model as well as VG model were fitted to the observed data, and the resulting values are given in Table 1. The Fayer and Durner model described well the two distinct water retention properties for the sand and the Andisol, respectively.

Tottori dune sand (bulk density $\rho_b = 1.62 \text{ g cm}^{-3}$) and Kumamoto Andisol ($\rho_b = 0.48 \text{ g cm}^{-3}$) were packed uniformly in a column with a height of 8 cm and inside diameter of 3.8 cm, and a column with a height of 18.6 cm and inside diameter of 7.5 cm, respectively. The soil columns were saturated using a Mariotte tank from the bottom. After saturation, the bottom of column was closed and evaporation was allowed to start. Soil water pressure heads at each depths (0.5 and 5 cm for

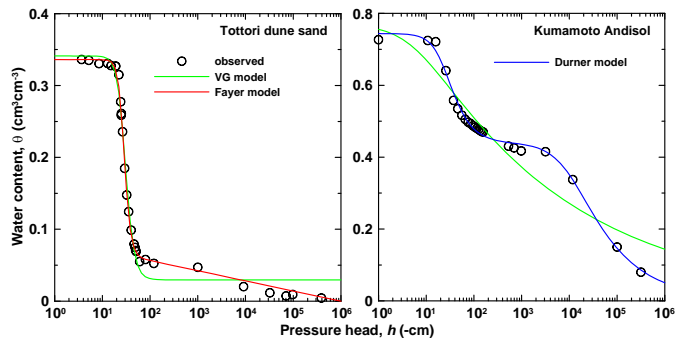


Figure. 1 Observed water retention curves for Tottori dune sand (Left) and Kumamoto Andisol (Right) with fitted curves described with the VG, Fayer, and Durner model.

sand, 5.5 and 15.5 cm for Andisol) were measured with tensiometers and the amount of water removed by evaporation was measured with an electrical balance. The average water content of whole column was determined gravimetrically at the time the evaporation experiment was terminated.

Table1 Soil water hydraulic parameters of the VG, Fayer, and Durner models fit to the observed soil water retention curves

Tottori dune sand	θ_r	θ_a	θ_s	α (cm ⁻¹)	n	w_2	α_2 (cm ⁻¹)	n_2
VG model	0.030	–	0.341	0.035	5.20	–	–	–
Fayer model	–	0.085	0.336	0.036	7.06	–	–	–
Andisol								
VG model	0	–	0.769	0.192	1.14	–	–	–
Durner model	0	–	0.744	0.041	2.44	0.59	1.01×10 ⁻⁴	1.47

3.2 Inverse analysis

The column length, initial, and boundary conditions for numerical simulations were given as corresponding experiments. The evaporation rate calculated from the measured cumulative evaporation amount was used as the upper boundary condition and no flux boundary condition was used as lower boundary condition. The pressure head profile measured at the beginning of the experiment was used as initial condition. The VG model and the Fayer model were used as the hydraulic property function for Tottori dune sand and the VG model and the Durner model were used for Kumamoto Andisol.

All the hydraulic parameters were estimated from the evaporation experiment using parameter inversion (Šimůnek et al., 1998; Sakai and Toride, 2007b). The tensiometer readings as a function of time, the average water content at the end of the experiment, the observed cumulative evaporation amount, and the observed retention curve data were used for the objective function Φ :

$$\Phi = \sum_{j=1}^m v_{h,j} \sum_{i=1}^{n_j} w_h \left[h_j^*(t_i) - h_j(t_i) \right]^2 + w_\theta \left[\theta_{ave}^* - \theta_{ave} \right]^2 + v_E \sum_{i=1}^{n_E} w_E \left[E_{cum}^*(t_i) - E_{cum}(t_i) \right]^2 + v_{\theta(h)} \sum_{i=1}^{n_\theta} w_{\theta(h)} \left[\theta(h)^* - \theta(h) \right]^2 \quad (5)$$

where the variables with superscript * indicate measured data sets and without * indicate corresponding model predictions. $h_j(t_i)$ denotes pressure head at the location j at time t_i , m is the number of measurement depth, n_j is the number of measurement, θ_{ave} denotes the average water content at the end of the experiment, $E_{cum}(t_i)$ is the cumulative evaporation amount at t_i , and $\theta(h)$ is the retention curve data. w and v are weights associated with a particular measurement set or point, respectively. v is defined as $1/(n\sigma^2)$, where σ^2 is the measurement variances. In this study, we used $w_h = 1$, $w_\theta = 10$, $w_E = 10$, $w_{\theta(h)} = 10$. Minimization of the objective function is accomplished by using the effective Levenberg-Marquardt nonlinear minimization method (Marquardt, 1963). The values shown in Table 1 and measured saturated hydraulic conductivity (550 cmday⁻¹ for dune sand, and 200 cmday⁻¹ for Andisol) $l = 0.5$ (Mualem, 1976) were used as the initial values for inverse analyses. Numerical simulations and inverse analyses were carried out using HYDRUS-1D (Šimůnek et al. 2005).

4 RESULTS AND DISCUSSIONS

4.1 Tottori dune sand

Observed and fitted pressure heads for Tottori dune sand is shown in Figure 2. The optimized retention curve and unsaturated hydraulic conductivity were shown in Figure 3 and the optimized parameters were shown in Table 2. The observed pressure head near the soil surface had a drastic decrease after 40 hours, whereas the pressure head at 5 cm depth decreased gradually.

The optimized Fayer model described well the observed pressure heads change (Figure 2) and observed retention curve (Figure 3). The $K(h)$ function shows different gradients, $d\log K/d\log h$, for higher and lower pressure heads, while the VG model decreased monotonically. This shape for the $K(h)$ function is similar to that proposed by Tuller and Or (2001), which considers film flow for lower water contents as well as pore water flow for higher water contents. This results indicates that the Fayer model not only modifies the VG model for the soil water retention curve, but that it also has a profound effect on the unsaturated hydraulic conductivity function for lower water contents. It is expected that the Fayer model with calibrated l will describe the unsaturated hydraulic conductivity for dry sandy soils better than the original VG model.

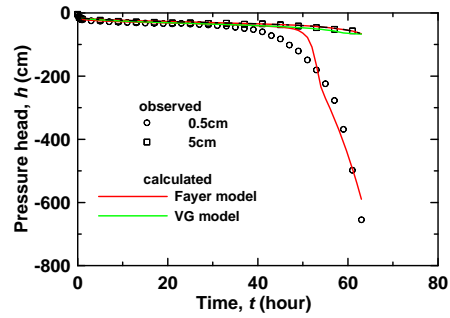


Figure. 2 Pressure heads change during the evaporation process for Tottori dune sand.

Table 2 Soil water hydraulic parameters for Tottori dune sand and Kumamoto Andisol obtained inversely with the evaporation method.

Tottori dune sand	θ_r	θ_s	α (cm ⁻¹)	n	w_2	α_2 (cm ⁻¹)	n_2	K_s (cm d ⁻¹)	l
VG model	0.0290	0.330	0.034	4.72	—	—	—	74.88	2.59×10^{-3}
Fayer model	—	0.317	0.035	7.44	—	—	—	98.88	2.83×10^{-4}
Andisol									
VG model	0.0004	0.686	0.086	1.14	—	—	—	843.6	-0.092
Durner model	0.0108	0.678	0.030	2.29	0.63	1.11×10^{-4}	1.42	49.5	0.87

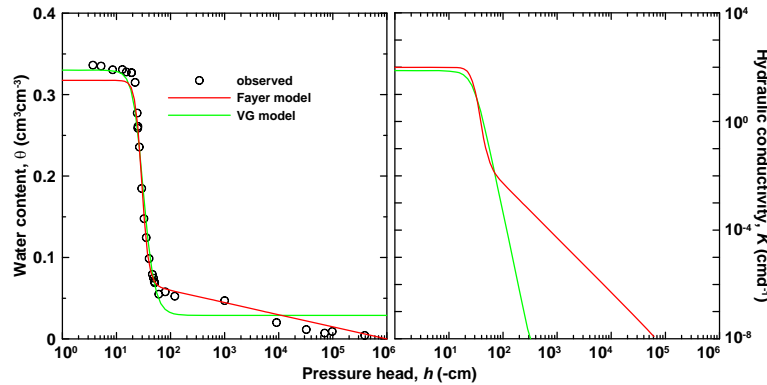


Figure. 3 Water retention curve (Left) and unsaturated hydraulic conductivity as a function of the pressure head (Right) for Tottori dune sand estimated with the evaporation method.

4.2 Kumamoto Andisol

Observed and fitted pressure heads for Kumamoto Andisol is shown in Figure 4. The optimized retention curve and unsaturated hydraulic conductivity were shown in Figure 5 and the optimized parameters were shown in Table 2. The optimized Durner model described well the observed pressure heads change and (Figure 4) and observed retention curve (Figure 5). $K(h)$ of the Durner model decreased gradually for $h < -100$ cm and showed stepwise shape. This indicates that the Durner model describes well two distinct flow properties inside and outside of aggregates as well as water retention property.

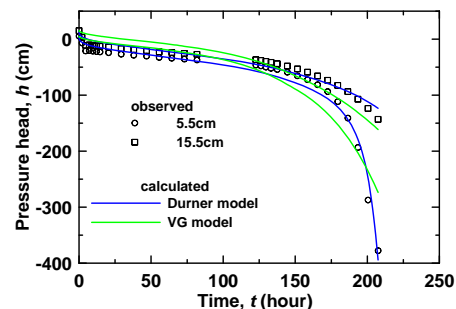


Figure. 4 Pressure heads change during the evaporation process for Kumamoto Andisol.

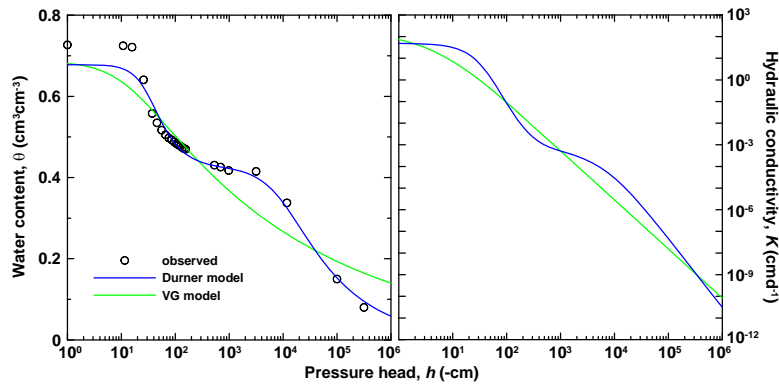


Figure. 5 Water retention curve (Left) and unsaturated hydraulic conductivity as a function of the pressure head (Right) for Kumamoto Andisol estimated with the evaporation method.

SUMMARY

The applicability of the Fayer model to a sandy soil and the Durner model to an aggregated soil was evaluated using the evaporation method. The Fayer model described the unsaturated hydraulic conductivity of Tottori dune sand well reflecting pore water retention for higher water contents and absorbed water retention on the surface of soil particles for lower water contents. The Durner model was suitable to the Andisol whose hydraulic properties were strongly affected with the distinct aggregated structure. The Mualem model, although it is based on the pore-size distribution model, can predict unsaturated hydraulic conductivity for a wide range of soil water pressure when an appropriate model is used for the water retention curve and the pore-connectivity coefficient l is estimated.

REFERENCES

- Durner, W., Hydraulic conductivity estimation for soils with heterogeneous pore structure, *Water Resour. Res.*, *30*, 211-223, 1994.
- Fayer, M. H., and C. S. Simmons, Modified soil water retention functions for all matric suctions, *Water Resour. Res.*, *31*, 1233-1238, 1995.
- Marquardt, D. W., An algorithm for least-squares estimation of nonlinear parameters, *SIAM J. Appl. Math.*, *11*, 431-441, 1963.
- Mualem, Y., A new model for predicting the hydraulic conductivity of unsaturated porous media, *Water Resour. Res.*, *12*, 513-522, 1976.
- Rossi, C., and J. R. Nimmo, Modeling of soil water retention from saturation to oven dryness, *Water Resour. Res.*, *30*, 701-708, 1994.
- Priesack, E., and D. Durner, Closed-form expression for the multi-modal unsaturated conductivity function, *Vadose Zone Journal*, *5*, 892-898, 2006.
- Sakai, M., and N. Toride, Optimum conditions for predicting unsaturated hydraulic properties using the evaporation method, *Journal of the Japanese Society of Soil Physics*, *106*, 33-46, 2007. (in Japanese)
- Sakai, M., and N. Toride, Soil water hydraulic functions for a sandy soil and an Aggregated soil, *Journal of the Japanese Society of Soil Physics*, *107*, 63-77, 2007. (in Japanese)
- Šimůnek, J., M. Th. van Genuchten, and M. Šejna, The HYDRUS-1D Software Package for Simulating the Movement of Water, Heat, and Multiple Solutes in Variably Saturated Media, Version 3.0, *HYDRUS Software Series 1*, Department of Environmental Sciences, University of California Riverside, Riverside, California, USA, pp. 270, 2005.

- Šimůnek, J., O. Wendroth, and M. Th. van Genuchten, Parameter estimation analysis of the evaporation method for determining soil hydraulic properties, *Soil Sci. Soc. Am. J.*, 62, 894–905, 1998.
- Tuller, M. and D. Or, Hydraulic conductivity of variably saturated porous media, *Water Resour. Res.*, 37, 1257-1276, 2001.
- van Genuchten, M. Th., A closed- form equation for predicting the hydraulic conductivity of unsaturated soils, *Soil Sci. Soc. Am. J.*, 44, 892–898, 1980.

Calcium Hydroxide Leaching through a Well-Buffered Volcanic-Ash Soil with pH Dependent Charges

D. Chen, N. Toride, & D. Antonov

Graduate school of Bioresources, Mie University, Tsu, Mie, Japan

ABSTRACT: Soils have a buffering capacity to moderate pH changes in soil solutions because of the pH dependent charges. A variable charge model is proposed assuming dissociation and attachment reactions of hydrogen with the hydroxyl reactive groups in soils to evaluate the soil buffering capacity. A titration experiment is conducted for a volcanic-ash soil by adding acid and alkaline solutions to estimate parameter values for the variable charge model using the PHREEQC geochemical database code (Parkhurst and Appelo, 1999). Calcium hydroxide leaching process through the well-buffered volcanic-ash soil is then simulated in accordance with the proposed variable charge model using a numerical code HP1 (Jacques and Šimůnek, 2005), which couples HYDRUS-1D for flow and transport and PHREEQC for chemical reactions. When we take into account a suitable buffering capacity based on the variable charge model, HP 1 is a promising tool for quantitative evaluation of the acid or alkaline contaminant transport through well-buffered soils.

1 INTRODUCTION

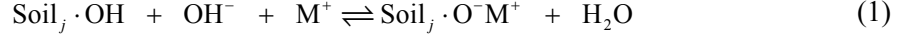
Construction sludge is usually dehydrated with a coagulant material such as lime hydrate for recycling the sludge as a soil foundation. A volcanic-ash soil is often used at the bottom of the landfill sites because of its high buffering capacity to minimize adverse effects of high pH solutions of the coagulant material to the surrounding area. For evaluating a soil buffering capacity, it is necessary properly to take into account the soil variable charges

The variable cation exchange capacity (CEC_v) and anion exchange capacity (AEC_v) of volcanic-ash soils for different pH and electrolyte concentrations have been experimentally determined by Japanese soil scientists (Wada and Ataka, 1958; Wada, 1980). Okamura and Wada (1983) proposed a general regression equation to describe the observed pH dependent CEC and AEC. Although the empirical regression formula can be used to predict the CEC_v and AEC_v at certain pH and concentration, it is necessary to describe explicit reactions of hydrogen or hydroxyl ions with soil hydroxyl reactive groups to predict transport of acid or alkaline solutes in soils.

In this study, a variable charge model is firstly proposed to describe the pH dependent charges and to evaluate the soil buffering capacity. Then, a titration experiment is conducted for a volcanic-ash soil by adding acid and alkaline solutions to the soil-water suspension. Parameter values for the variable charge model are determined based on the titration curve using the PHREEQC geochemical database code (Parkhurst and Appelo, 1999). Finally, a calcium hydroxide leaching process through the volcanic-ash soil is simulated in accordance with the proposed variable charge model. A numerical code HP1 (Jacques and Šimůnek, 2005) is used, which couples the water flow and solute transport code HYDRUS-1D (Šimůnek et al., 2005) and the geochemical code PHREEQC.

2 VARIABLE-CHARGE MODEL

A hydrogen ion dissociates from the hydroxyl reactive group j at the edge of clay minerals ($\text{Soil}_j \cdot \text{OH}$) depending on the soil solution pH. Simultaneously, exchangeable cations M^+ from the solution phase are electrically adsorbed on the surface ($\text{Soil}_j \cdot \text{O}^- \text{M}^+$) because of the electrical neutrality. The dissociated hydrogen forms water with a hydroxyl ion.



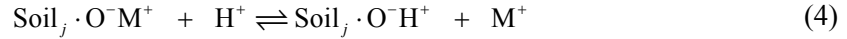
We assume the above reaction does not depend on cation species but simply depends on the total cation concentrations described as

$$[\text{M}^+] = \sum_{i=1}^{N_M} [\text{M}_i^{\nu+}] \quad (2)$$

where N_M is the number of cation species, ν is the valency, and $[\]$ is the ion concentration in terms of moles of charges. We assume higher valency cations such as Ca^{2+} also behave similar as a monovalent ion in accordance with the moles of charges. Hence we denote Ca^{2+} in Eq. (1) as $\text{Ca}_{1/2}^+$. The equilibrium constant for the dissociate reaction K_{vc-j} is given by

$$K_{vc-j} = \frac{[\text{Soil}_j \cdot \text{O}^- \text{M}^+]}{[\text{Soil}_j \cdot \text{OH}][\text{OH}^-][\text{M}^+]} \quad (3)$$

An ion exchange between M^+ and H^+ takes place according to the following exchange reaction:



$$K_{\text{H-M}} = \frac{[\text{Soil}_j \cdot \text{O}^- \text{H}^+][\text{M}^+]}{[\text{Soil}_j \cdot \text{O}^- \text{M}^+][\text{H}^+]} \quad (5)$$

where $K_{\text{H-M}}$ is the exchange constant between M^+ and H^+ . We note that $\text{O}^- \text{H}^+$ denotes the exchangeable hydrogen whereas OH is the hydroxyl group as shown in Eq. (1). It is possible to further determine a specific exchangeable cation concentration for mixed cation solutions if the corresponding exchanges reaction are defined. Since the hydroxyl group may have maximum capacity of dissociation, the parameter S_{vc-j} (mmol/g soil) is defined for the total amount of the surface reactive group:

$$[\text{Soil}_j \cdot \text{OH}] + [\text{Soil}_j \cdot \text{O}^- \text{M}^+] + [\text{Soil}_j \cdot \text{O}^- \text{H}^+] = S_{vc-j} \quad (6)$$

The sum of exchangeable M^+ and H^+ can be regarded as the amount of negative charges, which corresponds to the CEC_v , for the reaction group as a result of the hydrogen dissociation.

When the soil consists of N_{vc} reaction groups, the sum of exchangeable cations for all reaction groups is equal to the variable cation exchange capacity CEC_v for the soil. Substituting Eqs. (3) and (5) into Eq. (6) leads to

$$\text{CEC}_v = \sum_{j=1}^{N_{vc}} ([\text{Soil}_j \cdot \text{O}^- \text{M}^+] + [\text{Soil}_j \cdot \text{O}^- \text{H}^+]) = \sum_{j=1}^{N_{vc}} \frac{10^{-14} K_{\text{H-M}} K_{vc-j} S_{vc-j} + K_{vc-j} S_{vc-j} [\text{OH}^-][\text{M}^+]}{1 + 10^{-14} K_{\text{H-M}} K_{vc-j} + K_{vc-j} [\text{OH}^-][\text{M}^+]} \quad (7)$$

Parameters $K_{\text{H-M}}$, K_{vc-j} , and S_{vc-j} are strictly specific for any different type of soil. They could be determined from a titration experiment as shown in the next chapter. The variable anion capacity AEC_v can be also derived as similar to the CEC_v , as described above.

3 TITRATION EXPERIMENT

A titration experiment was conducted to determine parameters for the variable charge model. A soil sample ($m_s = 5 \text{ g}$) was firstly mixed with distilled water of $V_0 = 150 \text{ cm}^3$. After adding ΔV

cm^3 of a NaOH solution ($c_0 \text{ mmol}_c/\text{cm}^3$), pH of the supernatant solution was measured. The mass conservation for Na^+ leads to:

$$c_0 \Delta V = (V_0 + \Delta V) [\text{Na}^+] + m_s \sum_{j=1}^{N_{vc}} [\text{Soil}_j \cdot \text{O}^- \text{Na}^+] \quad (8)$$

Substituting (7) into (8) and assuming $[\text{Na}^+]$ is equal to $[\text{OH}^-]$ results in

$$\Delta \text{OH}^- (c_0 - [\text{OH}^-]) = \frac{V_0}{m_s} c_0 [\text{OH}^-] + \sum_{j=1}^{N_{vc}} \frac{K_{vc-j} S_{vc-j} c_0 [\text{OH}^-]^2}{1 + 10^{-14} K_{\text{H-M}} K_{vc-j} + K_{vc-j} [\text{OH}^-]^2} \quad (9)$$

where $\Delta \text{OH}^- (= \Delta \text{Na}^+)$ is the amount of added NaOH per unit weight of soil. The pH of the supernatant solution can be determined as a function of ΔOH^- according to Eq. (9).

The parameters K_{vc-j} and S_{vc-j} for the variable charge model as well as K_{HM} for the cation exchange were determined based on the observed titration data (Fig. 1). When the soil consists of two types of reaction groups ($N_{vc} = 2$), the fitted curve could reasonably agree well with the observed data. The corresponding variable cation exchange capacity CEC_v as function of solution pH for three ionic concentrations is calculated with Eq. 7 for the optimized parameter values (Fig. 2).

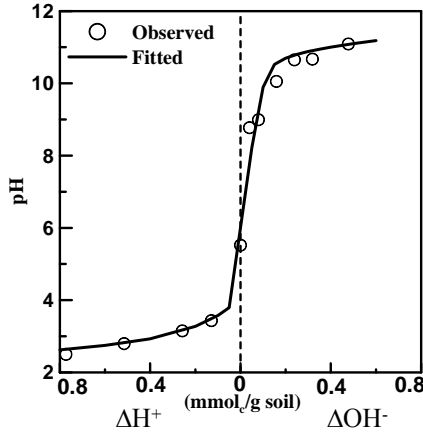


Figure 1. A titration curve for a volcanic-ash soil. Solid line is fitted with Eq. (9).

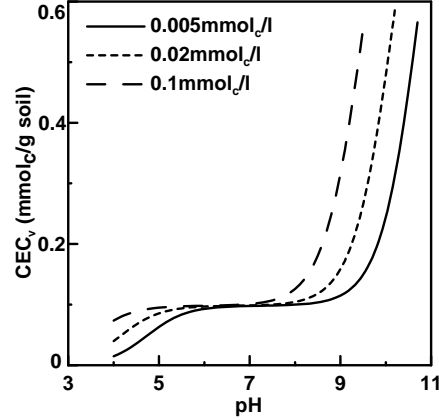


Figure 2. Calculated cation exchange capacity CEC_v based on optimized fitted parameters to an observed titration curve.

4 CALCIUM HYDROXIDE LEACHING

Calcium hydroxide leaching transport through a volcanic ash soil is numerically evaluated. The soil is uniformly packed at a bulk density of 0.53 g/cm^3 in a 20 cm length column (Fig. 3). A calcium hydroxide solution of $10 \text{ mmol}_c/\text{cm}^3$ is applied to the saturated solute-free soil with steady-state water flux of 30 cm/h . The volcanic-ash soil has a charge property as described in Fig. 1.

Transport of Ca^{2+} is described with the convection dispersion equation:

$$\frac{\partial}{\partial t} (\rho_b Q_{Ca} + \theta C_{Ca}) = \frac{\partial}{\partial x} \left(D \frac{\partial C_{Ca}}{\partial x} \right) - \frac{\partial}{\partial x} (J_w C_{Ca}) \quad (10)$$

where C_{Ca} is the Ca^{2+} aqueous concentration ($\text{mmol}_c/\text{cm}^3$), ρ_b is the soil bulk density (g/cm^3), θ is the volumetric water content (-), D is the hydrodynamic dispersion coefficient (cm^2/h), J_w is the volumetric flux (cm/h), and Q_{Ca} is the Ca^{2+} adsorbed concentration ($\text{mmol}_c/\text{g soil}$) described with the variable charge model:

$$Q_{Ca} = \sum_{j=1}^{N_{vc}} [\text{Soil}_j \cdot \text{O}^- \text{Ca}_{1/2}^+] = \sum_{j=1}^{N_{vc}} \frac{K_{vc-j} S_{vc-j} [\text{OH}^-] [\text{Ca}_{1/2}^+]}{1 + 10^{-14} K_{H-M} K_{vc-j} + K_{vc-j} [\text{OH}^-] [\text{Ca}_{1/2}^+]} \quad (11)$$

Because of the electrical neutrality of the soil solution, $[\text{OH}^-]$ is assumed to be equal to $[\text{Ca}_{1/2}^+] + [\text{H}^+]$. Furthermore, for an alkaline condition, neglecting $[\text{H}^+]$ leads to $[\text{OH}^-] \approx [\text{Ca}_{1/2}^+]$, which means the solution pH ($[\text{OH}^-]$) can be solely determined from $[\text{Ca}_{1/2}^+]$.

The numerical calculation for the Ca^{2+} transport through the profile is carried out using the HP1 code (Fig. 4): *i.e.*, water flow and nonreactive solute transport parts in Eq. (10) are evaluated in HYDRUS-1D, and chemically reactive part Q_{Ca} in Eq. (10) is evaluated in PHREEQC based on the variable charge model with the optimized K_{vc-j-M} , S_{vc-j-M} and K_{H-M} for Eq. (11). Then, using the assumption of $[\text{OH}^-] \approx [\text{Ca}_{1/2}^+]$ and the general equation of pH, the pH distribution through the profile is also evaluated (Fig. 5). Finally, the CEC_v in the soil profile as a function of Ca^{2+} according to Eq. (7) is calculated (Fig. 6).

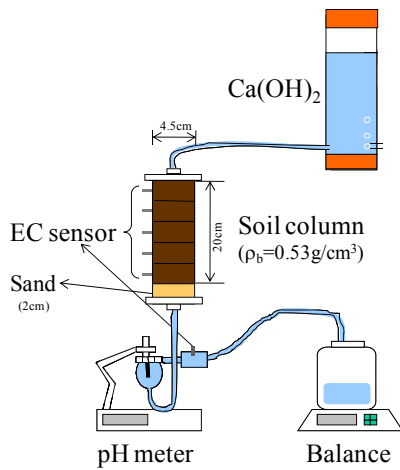


Figure 3. Principle scheme of calcium hydroxide leaching experiment.

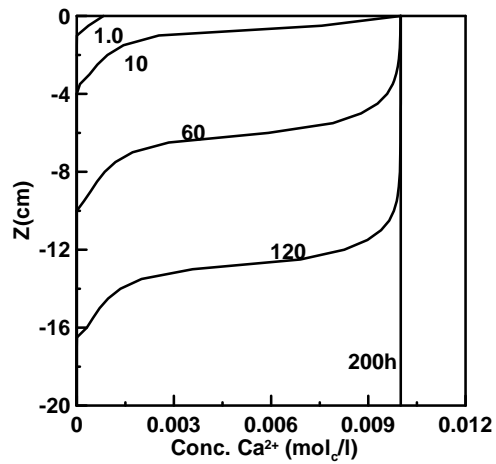


Figure 4. Calculated Ca^{2+} concentration profiles.

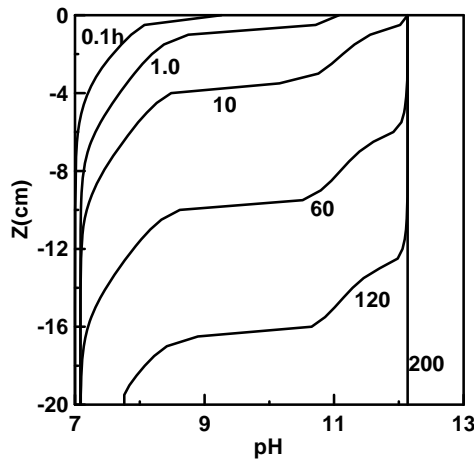


Figure 5. Calculated pH profiles during leaching through the soil profile.

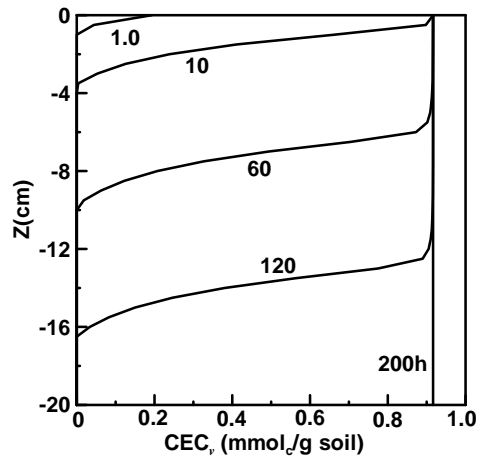


Figure 6. Calculated variable cation exchange capacity through the soil profile.

It takes 160 hours (300 pore volume) Ca^{2+} reaches at the bottom of the column because of high buffering capacity of the volcanic-ash soil (Fig. 4). The calculated pH in the soil column (Fig. 5) is in correspondence with the experimental observations. As the CEC_v is a function of pH and the cation concentration according to Eq. (7), increases in the Ca^{2+} concentration and pH results in the increase in the CEC_v as shown in Fig. 6. With taking into account a suitable buffering capacity based on the variable charge model, HP 1 is a promising tool for quantitative evaluation of the acid or alkaline contaminant transport through well-buffered soils.

REFERENCES

- Appelo, C.A.J. and Postma, D., Geochemistry, groundwater and pollution. 2 edition. Published by: A.A.Balkema Publishers, Leiden, The Netherlands a member of Taylor & Francis Group plc.
- Diederik Jacques and Jirka Šimůnek (2005): User Manual of the Multicomponent Variably-Saturated Flow and Transport Model HP1. Description, Verification, and Examples, Version 1.0. SCK·CEN, Mol, Belgium, Dep. of Environmental Sciences, Univ. of California Riverside, Riverside, USA.
- Okamura, Y. and Wada, K. (1983), Electric charge characteristics of horizons of Ando (B) and Red-Yellow B soils and weathered pumices. *J. Soil Sci.* 34: 87-295
- Parkhurst, D.L. and Appelo, C.A.J. (1999) : The PHREEQC Software Package for Simulating Chemical Reactions and Transport Processes in Natural or Polluted water, Version 2.0. U.S. Department of the Interior Bruce Babbitt, Secretary.
- Šimůnek, J., van Genuchten, M. Th. & Šejna, M. 2005. The HYDRUS-1D software package for simulating the one-dimensional movement of water, heat, and multiple solutes in variably-saturated media. Version 3.0, *HYDRUS Software Series 1*, Department of Environmental Sciences, University of California Riverside, Riverside, CA, 270 pp.
- Wada, K. and Ataka, H. (1958), The ion-uptake mechanism of allophone, *Soil Plant Food* (Tokyo), Vol. 4, 12-18
- Wada, K. (1980), Mineralogical characteristics of andisols: in *Soils with variable charge*, B. K. G. Theng, ed., New Zealand Soc. Soil Sci., Lower Hutt, New Zealand, 87-107.

Development of a Predictive Expression for Soil Water Repellency Curve Based on Soil Organic Carbon Content

A.K. Karunaratna¹⁾, Ken Kawamoto¹⁾, Per Moldrup²⁾, Lis W. de Jonge³⁾ & Toshiko Komatsu¹⁾

1) Graduate School of Science and Engineering, Saitama University, Shimo-okubo, Sakura-ku, Saitama 338-8570, Japan

2) Environmental Engineering Section, Dep. of Biotechnology Chemistry and Env. Engineering, Aalborg University, Sohngaardsholmsvej 57, DK-9000 Aalborg Denmark

3) Department of Agroecology and Environment, University of Aarhus, DK-8830 Tjele Denmark

ABSTRACT: Soil water repellency (WR) is a significant problem worldwide effecting natural and agricultural ecosystems, with important environmental consequences, for which proximate causes are not well understood. Soil organic carbon (SOC) considered being the key factor controlling the soil water repellency. Although few previous studies have examined the relationship between WR and SOC in combination with other soil properties, this study aims to develop a straightforward link between SOC and WR by a comprehensive analysis of different soils. The WR verses water content relationship implied that SOC can increase the degree of WR as well as cause to develop WR over a wide range of soil water content. The trapezoidal area below the WR curve was expressed as a form of sigmoid growth curve where the first derivative of the sigmoid curve gives the water content dependant WR. The proposed sigmoid curve function showed a good fit with observed data, however derived WR curve slightly underestimate the actual water content dependant WR for soils containing high SOC. This suggest that the WR of a soil can be expressed using the single variable of SOC, irrespective of other soil physical and chemical properties.

1 INTRODUCTION

Soil water repellency (WR) is the propensity of soil to keep away from wetting even when free moisture is available. Soil water repellency is a significant problem worldwide effecting natural and agricultural ecosystems, with important environmental consequences, for which proximate causes are not well understood (Wallis and Horne, 1992; Dekker and Ritsema, 1994). The emergence of WR of a soil primarily depends on the soil water content, and the intensity of WR may determine by other factors such as quantity and quality of soil organic carbon (SOC), soil texture and structure (Bisdorn et al., 1993), soil pH, relative humidity (RH) of soil-air interface and wetting history (Dekker and Ritsema, 1994; de Jonge et al., 1999; Kawamoto et al., 2007). However, among these factors, SOC considered to be the key factor controlling the soil WR as hydrophilic organic matter coating on soil particles may lower the surface free energy of soil particles (Wal-lis and Horne, 1992; Roy and McGill, 2002). These organic substances may originated from plant root extrudes, soil biomass extrudes, intermediate or final products of organic matter decomposition and also contamination of soil by external organic hydrophobic substances. The chemical origin of soil WR has been investigated in some studies; some of them have showed a correlation between soil organic carbon content and WR (Mataix-Solera and Doerr, 2004) that has been challenged by the studies on other soils (Horne and McIntosh, 2003) . However, most of those studies tested only few soil types, and WR was expressed by using several variables along with SOC consequently limiting the practical use of those.

The purpose of this study was to link soil WR and SOC content irrespective of other soil properties. Although few previous studies have examined this relationship in combination with other soil properties, this study aim to develop a link between SOC and WR by a comprehensive analysis of soils from different origins, horizons, vegetations, particle size fractions and land

management practices. This work aimed (i) to analyze the relationship between SOC and water content dependant soil water repellency and (ii) to develop a straightforward mathematical relationship between SOC and WR that can use to assess WR of a soil.

2 MATERIALS AND METHODS

2.1 Sampling sites and soil materials

Seven types of soils from two different geographical regions in the world; 5 soils from Denmark and 2 soils from Japan were tested for their water repellency. The sampling locations, sample preparation and WR estimation of Danish soils were described elsewhere (de Jonge et al., 1999). The Japanese soils were sampled from two locations; Fukushima volcanic ash soil from a forested hill site at Fukushima in north-eastern Japan and Aichi Oak forest soils from a forested hill site at Aichi prefecture. Each of Fukushima and Aichi soils were obtained from single soil profiles excavated down to 0.3-0.5 m depth. Each soil profile was divided to 2 to 5 cm thick layers from surface and soil samples were collected from each depth class. The sampled materials were stored in refrigerator at 4°C until used for laboratory tests.

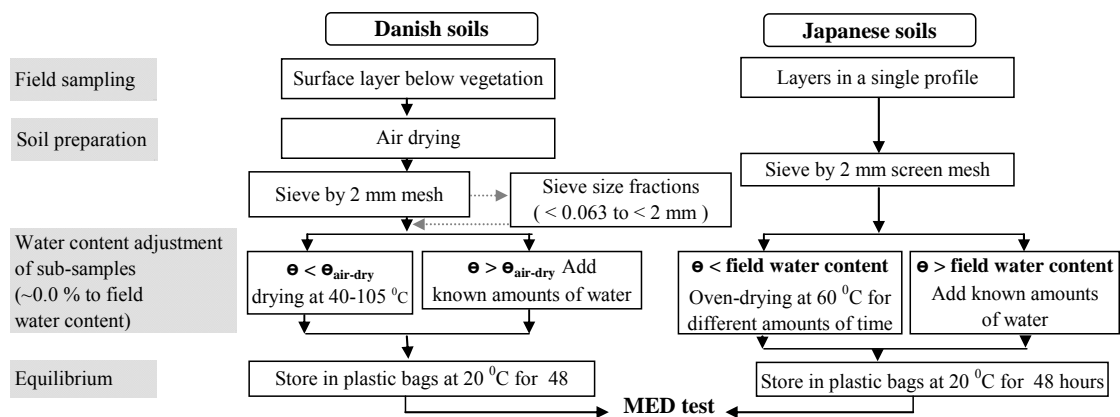


Figure 1. The flow chart of the Molarity of Ethanol Droplet (MED) test including the soil preparation and pretreatment procedures.

2.2 Determination of soil properties and water repellency

The soil texture of each sample was determined at the laboratory. Sampled materials at field water content were sieved through a 2 mm mesh screen and coarser materials as gravel and litter debris were discarded. Sub-samples of sieved soil was dried at air for constant weight and grounded to powder. The SOC and C/N ratio of powdered samples were determined using C-N analyzer (CHN corder MT-5, Yanaco, Kyoto).

Sample preparation procedure for Danish soils and Japanese soils were slightly different, and the detail steps are illustrated in Figure 1. In this study, soil water repellency was assessed by the Molarity of Ethanol Droplet (MED) test (Roy and McGill, 2000). The MED test can be used to estimate the liquid surface tension of an aqueous ethanol droplet that can infiltrate the soil within 5 second. The lower the liquid surface tension (higher the concentration of ethanol) in an added droplet higher the WR of the tested soil samples.

2.3 Description of water repellency parameters

In general, the WR of a soil increase with increasing water content and reached a maximum (de Jonge et al., 1999; Kawamoto et al., 2007). Thereafter, a rapid decrease of WR towards field capacity was observed (Fig. 2a). Based on this WR verses volumetric water content (θ) and WR verses relative water content (Θ) curves (Fig. 2a,b), we defined: WR_{max} - maximum WR; $\theta_{\text{air-dry}}$ (m^3m^{-3}) – the lowest volumetric soil water content obtained by air drying; $\theta_{\text{WR-max}}$ (m^3m^{-3}) - water content at which maximum WR occurs; $\theta_{\text{non-WR}}$ (m^3m^{-3}) - the highest volumetric water con-

tent at which WR disappears; $S_{WR(\Theta)}$ (Nm^{-1}) - the trapezoidal integrated area below the WR versus Θ curve.

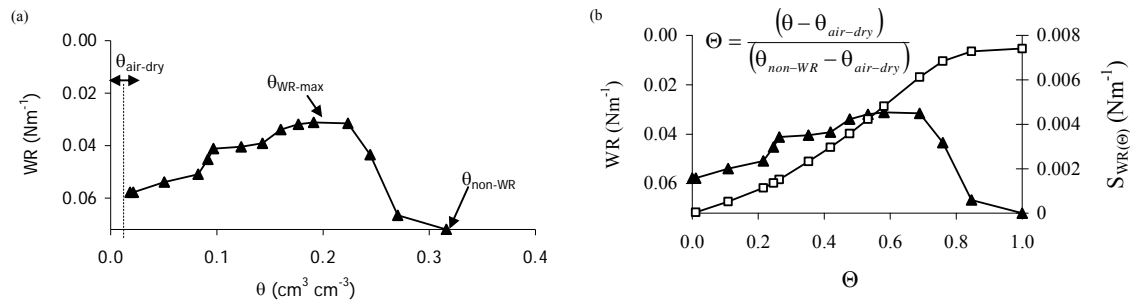


Figure 2. Development of WR versus Θ relationships from WR versus θ curve (a), (b) WR versus Θ curve and $S_{WR(\Theta)}$ versus Θ curve. Note that the WR-axis has been reversed in order to obtain an increase in the curve with increasing WR.

3 RESULTS AND DISCUSSION

3.1 Comparison of soil water repellency behavior

The SOC content of the finest fractions of the Jyndevad soils under grass or barley cover was higher than that of the full sample. The SOC content decreased with depth of soil profile for Japanese soils, as did WR_{max} and $\theta_{\text{non-WR}}$.

Water repellency behavior of three representative soil groups; Aichi, Fukushima and Danish soils are presented in Figure 3. Similar curves were obtained for Jyndevad grass size fractions and Jyndevad barley size fractions (data not shown). All Danish soils showed WR only in dry soils ($\theta = 0.0 \sim 0.2 \text{ m}^3 \text{ m}^{-3}$), except the finer size fractions of Jyndevad soils. Surface soil layers and finer size fractions that contained comparatively higher SOC contents showed water repellency over a wide range of θ , as well as high WR. As shown in Figure 3a and 3b, surface soils with very high SOC contents were water repellent even at $\theta_{\text{air-dry}}$, and WR_{max} value was not apparent. In general, all Danish soils showed low WR, WR_{max} , and $S_{WR(\Theta)}$ compared to Japanese soils (Fig. 3). The decrease of WR with depth was well demonstrated by the $S_{WR(\Theta)}$ versus Θ relationship.

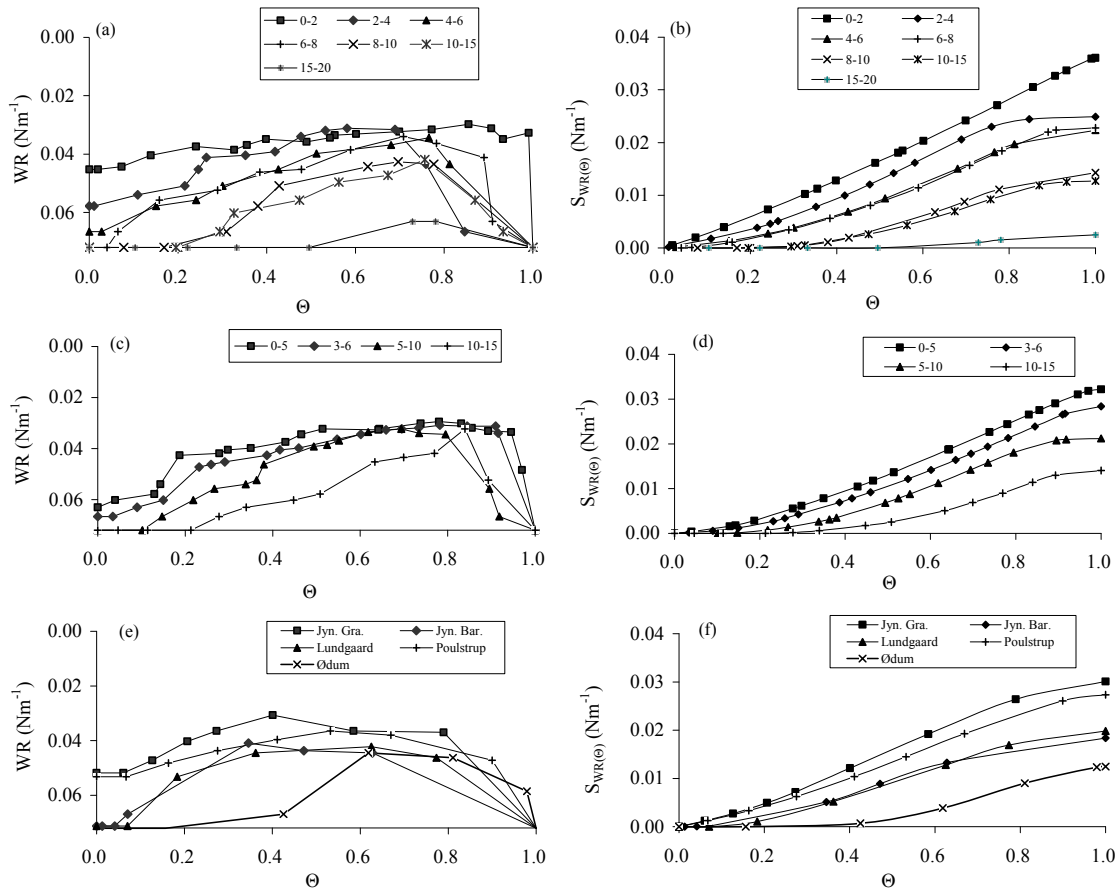


Figure 3. Comparison of water repellency behavior of soils by WR versus Θ and $S_{WR(\Theta)}$ versus Θ curves. (a,b) Aichi, (c,d) Fukushima, and (e,f) Danish soils.

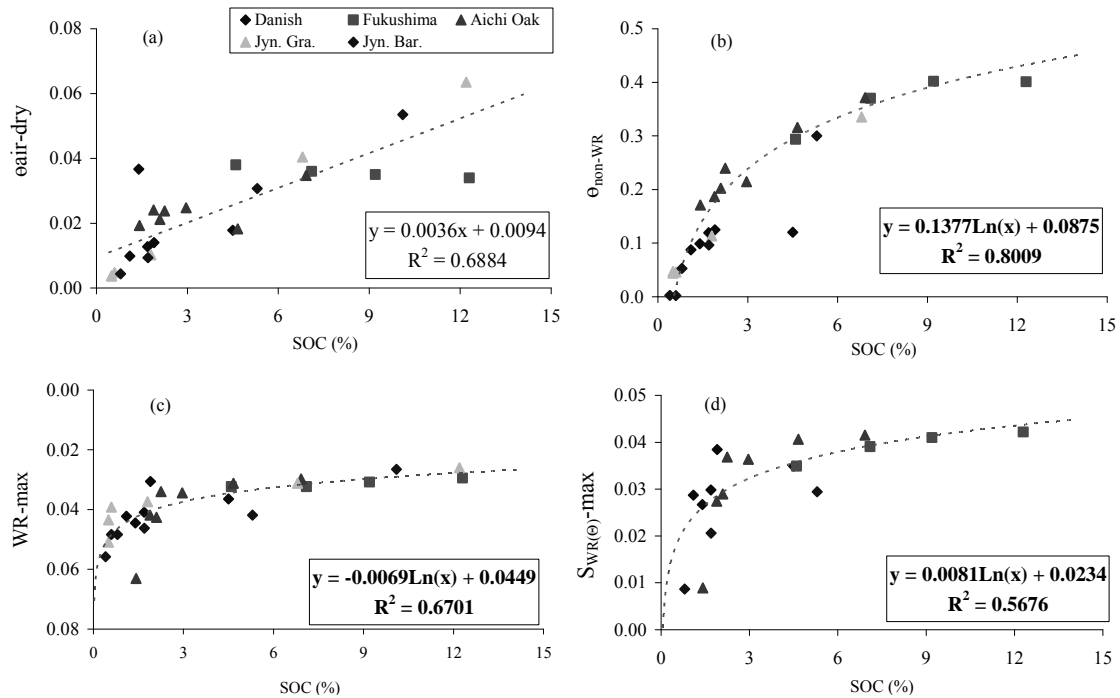


Figure 4. Plot of water repellency parameters versus SOC; (a) $\theta_{\text{air-dry}}$, (b) $\theta_{\text{non-WR}}$, (c) $\theta_{\text{WR-max}}$ and (d) $S_{WR(\Theta)\text{-max}}$.

There was a consistent trend across all data sets, with a positive relationship between water repellency parameters and SOC. Thus, we examined the relationship between SOC and water repellency parameters and presented in Figure 4. In addition, the total water repellency or cumulative $S_{WR(\Theta)}$ value (at $\Theta=1$ of $S_{WR(\Theta)}$ verses Θ curve) was also plotted against SOC (Fig. 4). The $\theta_{\text{air-dry}}$ was increase linearly with increasing SOC (Fig. 4a) whereas the relationship between SOC and $\theta_{\text{non-WR}}$ was a logarithmic curve (Fig. 4b). Accordingly, a log rose of $\theta_{\text{non-WR}}$ value with increasing SOC for soils from 0.5 to 4.0 % of SOC, thereafter a lag increase for higher SOC contents. As shown in Figure 4c, WR_{max} also showed a logarithmic relationship with SOC. However, those relationships along were not able to build a straightforward equation for WR by using SOC.

Therefore, we consider the sigmoid shape of the $S_{WR(\Theta)}$ verses Θ curves and proposed a sigmoid curve relationship based on the Hill function (Giraldo et al., 2002);

$$S_{WR(\Theta)} = \frac{S_{WR(\Theta)-\text{max}}}{(1 + 10^{(\Theta_0 - \Theta)k})} \quad (\text{N m}^{-1}) \quad (1)$$

where $S_{WR(\Theta)-\text{max}}$ is the cumulative $S_{WR(\Theta)}$, Θ_0 is the relative water content at which WR_{max} occurs and k is a curve fitting parameter.

The first derivative of this function gives the relationship between WR and Θ , which can be expressed as;

$$\frac{dS_{WR(\Theta)}}{d\Theta} = \frac{k(S_{WR(\Theta)-\text{max}}) \ln(10) 10^{k(\Theta_0 - \Theta)}}{(10^{k(\Theta_0 - \Theta)} + 1)^2} \quad (\text{N m}^{-1}) \quad (2)$$

All the $S_{WR(\Theta)}$ data were well fitted with the Equation 1, and a representative plot is presented in Figure 5a. The predicted WR values which was derived from Equation 2 were also showed a good agreement. However, predicted curve underestimated the WR of soils which have very high SOC content, but showed a good fit for the soils with low SOC.

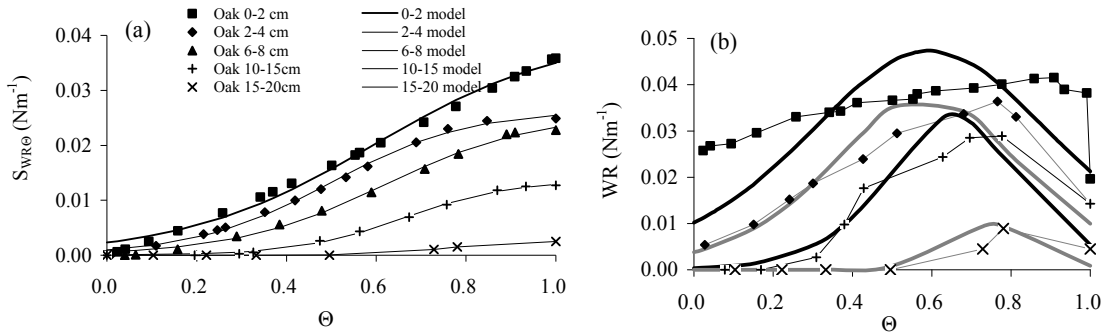


Figure 5. Comparison of observed and predicted WR curves; (a) observed $S_{WR(\Theta)}$ and predicted $S_{WR(\Theta)}$, and (b) observed WR and predicted WR (thick lines are predicted WR curves).

4 CONCLUSIONS

The WR verses relative water content relationship implied that SOC can increase the degree of WR as well as cause to develop WR in soils over a wide range of water content. The SOC content showed positive linear correlation between $\theta_{\text{air-dry}}$, also positive logarithmic correlations between SOC and other WR parameters ($\theta_{\text{non-WR}}$, WR_{max} , and $S_{WR(\Theta)-\text{max}}$. The trapezoidal area below the WR curve was expressed as a form of sigmoid growth curve where the first derivative of the sigmoid curve gives the water content dependant WR. The proposed sigmoid curve function showed a good fit with observed data, however derived WR curve slightly underestimate the ac-

tual water content dependant WR. This suggest that the WR of a soil can be expressed using the single variable of SOC irrespective of other soil physical and chemical properties.

ACKNOWLEDGEMENT

This work is partially supported by the Saitama University Project Grant and a grant from the Japanese Ministry of Education, Science and Culture.

REFERENCES

- Bisdom, E.B.A., Dekker, L.W. & Schoute, J.F.T. 1993. Water repellency of sieve fractions from sandy soils and relationships with organic material and soil structure. *Geoderma* 56:105-118.
- de Jonge, L.W., Jacobsen, O.H. & Moldrup, P., 1999. Soil water repellency: Effects of water content, temperature, and particle size. *Soil Science Society of America Journal*, 63: 437–442.
- Dekker, L.W. & Ritsema, C.J., 1994. How water moves in a water repellent sandy soil. 1. Potential and actual water repellency. *Water Resour. Res.* 30: 2507–2517.
- Giraldo, J. Vivas, N.M., Vila & E., Badia, A. 2002. Assessing the (a)symmetry of concentration-effect curves: empirical versus mechanistic models. *Pharmacology & Therapeutics* 95:21– 45.
- Horne, D.J. & McIntosh, J.C. 2003. Hydrophobic compounds in sands from New Zealand. In: Ritsema, C.J., Dekker, L.W. (Eds.), *Soil Water Repellency. Occurrence, Consequences, and Amelioration*. Elsevier, Wageningen, The Netherlands, 25pp.
- Kawamoto, K., Moldrup, P., Momatsu, T., de Jonge, L.W., & Oda M. 2007. Water repellency of aggregate-size fractions of a volcanic ash soil, *Soil Science Society of America Journal*, 71(5): 1658-1666.
- Mataix-Solera, J., & Doerr, S.H. 2004. Hydrophobicity and aggregate stability in calcareous topsoils from fire-affected pine forests in southeastern Spain. *Geoderma* 118: 77–88.
- Roy, J.L., & McGill, W.B. 2002. Assessing soil water repellency using the molarity of ethanol droplet (MED) test, *Soil Sci.* 167: 83–97.
- Wallis, M.G. & Horne, D.J., 1992. Soil water repellency. *Adv. Soil Sci.* 20: 91–146.

Water and Salt Behavior in Maize Field under repeating boarder irrigation at Gansu province, China.

T. Nishimura¹, Y. Sato², and M. Kato³

1) Graduate School of Agricultural and Life Sciences, University of Tokyo, Tokyo, 113-8657 JAPAN

2) Chemical Grout Co. Ltd. 2-2-5 Toranomom, Tokyo, 105-0001 JAPAN

3) Department of Ecoregion Science, Tokyo University of Agriculture and Technology, Fuchu, Tokyo, 183-8509 JAPAN

ABSTRACT: The use of inappropriate irrigation practices has been causing deterioration of agricultural lands in semi-arid regions. Since sources of fresh water are limited, it is also necessary to raise the efficiency of the irrigation water use in arid and semi-arid regions. Soil survey and continuous soil water monitoring have been conducted at a maize field irrigated with high salt content water in Gansu province, P.R. China. The region has annual precipitation of less than 200 mm and deep ground water is the major source for irrigation. Measurements of soil physical and chemical properties, as well as numerical simulations with HYDRUS-2D have been conducted. Soil hydraulic parameters determined using the multistep outflow method were more similar to those predicted by Rosetta than to those provided by the Soil Catalogue. Numerical simulations represented well water behavior in the field soil with maize when properly measured hydraulic and transport parameters were used. They also suggested that more frequent irrigation can reduce the salt accumulation without reducing water supply to plants.

1 INTRODUCTION

Irrigation has an important role in increasing crop production. Among the total agricultural land, 17% of agricultural land is irrigated, which produces about 40% of total agricultural food production. Simultaneously, salt accumulation due to inadequate amount of irrigation causes approximately 1.5 million hectare of arable land to be unproductive every year. Inappropriate irrigation practices have been deteriorating agricultural lands in semi-arid regions (Oster and Shainberg, 2001). Irrigation with saline water often affects soil physical and chemical characteristics (Tedeschi et al., 2005). As sources of fresh water are limited, it is necessary to increase the irrigation water efficiency in arid and semi-arid regions.

Research work under field conditions is time consuming and costly. In addition, the irrigation cost is higher in arid and semi-arid regions. Numerical simulations can be a cost effective tool to demonstrate the modified irrigation practices (Hassan et al., 2005). HYDRUS (Šimůnek et al., 1999) is becoming a popular and cost effective tool to demonstrate the effects of modified irrigation practices.

However, measurements of soil hydraulic properties are often difficult, laborious, and time consuming. As an alternative to traditional measurements, inverse analysis of experiments conducted under simple initial and boundary conditions can be used as a tool to determine soil hydraulic properties. Also, databases of soil hydraulic properties have been developed. Several pedotransfer functions (PTF), which predict transport parameters from more easily measurable soil parameters, i.e. texture, dry bulk density, and/or particle size distribution were reported (Cosby et al., 1984, Tomasella et al., 2003). A soil catalogue developed using the data about US soils (Cassel and Parrish, 1988) is one of the most common PTFs. In addition to the soil catalogue, Hydrus-2D also implements the Rosetta program (Schaap et al., 1998, 1999) that includes one of the most commonly used PTF developed using neural networks. These PTFs are very convenient since they can predict soil hydraulic parameters from commonly available soils data. However, less is known about the performance of PTFs, especially when applied to soils in the Asian region.

The purpose of this study is to assess soil water behavior in the maize fields under irrigation in northwest China when proper soil hydraulic properties are used. In addition, water saving irrigation practices are evaluated using numerical simulations.

2 MATERIAL AND METHODS

2.1 Field monitoring and soil analysis

The experimental field was located in Wuwei in the Gansu province of P.R. China (N38°10'30.5" and E102°46'47.9"). The field is covered by Yellow loess. Annual precipitation is around 100 to 200 mm, and groundwater is the main source of irrigation water. Electrical conductivity of the irrigation water was 1.71 dSm⁻¹. Experimental field was used for maize cultivation.

Soil samples were collected using a steel cylinder of 5.1-cm diameter and 5-cm length, from layers shown in Table 1. Four probe electrical conductivity (EC) sensors, TDR soil moisture sensors and thermocouples were buried at four different depths at the test field (Table 1). These sensors were connected to the data logger CR10X (Campbell Scientific Ltd., USA) and the data were stored for 6 months.

Particle size distribution by the pipette method, bulk density by gravimetrically, and electrical conductivity by 1:5 soil water ratio method were measured in the laboratory. Calibration of TDR sensors was also conducted. The particle density of soil samples was measured using the pycnometer method, and the saturated hydraulic conductivity of soil samples was measured using the falling head method. Texture and bulk density of different layers are shown in Table 1.

2.2 Determination of soil hydraulic properties and numerical simulation

In this study the HYDRUS-2D software (Šimůnek et al., 1999) was used to evaluate using numerical simulations the impact of irrigation in terms of continuous production. In HYDRUS, the Richards' equation for water movement (1) is employed as the governing equation:

$$\frac{\partial \theta}{\partial t} = \frac{\partial}{\partial x} \left(K(h) \frac{\partial h}{\partial x} \right) + \frac{\partial}{\partial z} \left(K(h) \frac{\partial h}{\partial z} \right) + \frac{\partial K(h)}{\partial z} - S \quad [1]$$

Here, θ is the volumetric water content, t is the time, x and z are positions, and $K(h)$ is the unsaturated hydraulic conductivity.

Soil hydraulic parameters used in numerical simulations were based PTF predictions from measured soil texture and dry bulk density (Table 1) and those obtained by inverse analysis of multistep outflow method (e.g., Eching and Hopmans, 1993). The inverse analysis was conducted by the HYDRUS program. van Genuchten-Mualem equations for soil water retention, $\theta(h)$, and hydraulic conductivity, $K(h)$, functions were assumed (van Genuchten, 1980):

$$S_e(h) = \frac{\theta(h) - \theta_r}{\theta_s - \theta_r} = \frac{1}{(1 + |\alpha h|^n)^m} \quad [2]$$

$$K(h) = K_s S_e^l \left[1 - (1 - S_e^{1/m})^m \right]^2 \quad [3]$$

Here θ_r and θ_s denote the residual and saturated volumetric water contents, respectively; S_e is relative saturation, K_s is the saturated hydraulic conductivity, l is the pore connectivity coefficient, and α , n and m ($=1-1/n$) are empirical coefficients (Table 3) used in the HYDRUS program. Those parameters were optimized to represent cumulative drainage and soil water pressure heads in the soil sample under imposed positive pressures.

Cropping parameters used in the simulation were based on field observation; for example the cropping period for the maize was 6 months. The root water uptake model used in the simulation was given by Feddes et al. (1978).

$$S(h) = a(h)S_p \quad [4]$$

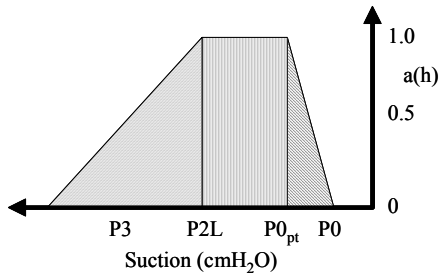


Fig. 1 Water stress response function $a(h)$

where the volume of water removed from the soil due to plant water uptake is represented as S (d^{-1}), $a(h)$ is the water stress response function of the soil water pressure head, and S_p is the potential root water uptake rate derived by modifying the potential transpiration in terms of root zone size. The variable S_p corresponds to the transpiration rate during periods of no water stress when $a(h)=1$. Parameters for the water stress response function are -15, -30, -500, and -24000 (cmH_2O) for P_0 , $P_{0_{pt}}$, P_{2L} , and P_3 , respectively (Fig. 1). Root distribution parameters were assigned according to Vrugt et al. (2001) to represent observed root distribution in the field.

$$\beta(z) = \frac{1}{\lambda} \left[1 - \frac{z}{z_m} \right] e^{-\frac{1}{\lambda} \frac{P_z}{z_m} |z^* - z|} \quad [5]$$

where $\beta(z)$ denotes the spatial root distribution as a function of depth z , z_m is the maximum rooting depth; λ , P_z and z^* (depth of maximum potential uptake) are fitting parameters. The value used for the fitting parameters are 1, 10, 15, respectively.

As the boundary condition, irrigation was the only source of water and was applied according to the schedule shown in Table 2. At the lower boundary of the simulation domain, gravitation was the only driving force for water flow. Water flux at the lower boundary was estimated from changes in TDR sensors at depths of 50 and 80 cm. The evapotranspiration rate was estimated according to Mahmood et al. (2005), and the evapotranspiration rate was divided into evaporation and transpiration rates based on Rosenthal et al. (1977) and Kang et al. (1998). The initial water content for the simulation was based on measured values before planting maize in April 2006.

Table 1. Soil physical properties, and sensors buried in the experimental fields.

Layer (cm)	Fractions (%)			Bulk density g cm^3	Ks cm d^{-1}	Numbers of Sensors	
	Sand	Silt	Clay			TDR	TC
10	77.2	11.9	10.9	1.48	63	2	1
30	80.2	10.4	9.4	1.49	58	2	1
50	63.1	25.4	11.5	1.53	61	2	1
80	-	-	-	-	-	2	1

3 RESULTS AND DISCUSSION

3.1 Estimation of soil hydraulic properties

Fig. 2 shows estimated soil water retention curves for Wuwei yellow loess. Triangle symbols show data measured using the pressure chamber method and the hanging water column. It is clear that the Soil Catalogue can not represent the water retention well and that results provided by Rosetta are better than those by the Soil Catalogue. Results obtained using the multistep outflow-inverse analysis are superior to both PTFs approaches. Hydraulic parameters determined using the multistep outflow-inverse analysis ($\theta_r=0.052$, $\theta_s=0.430$, $\alpha=0.0246$, $n=1.84$, $K_s=58$ cm d^{-1} and $l=0.986$) were used in numerical simulations.

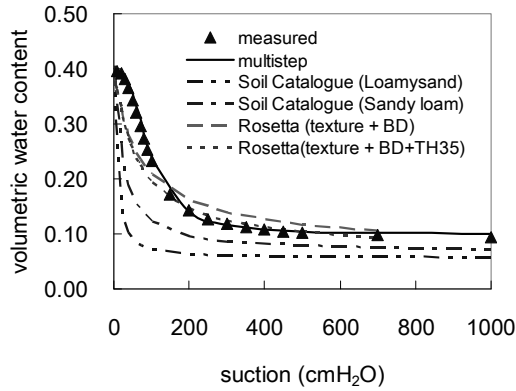


Fig. 2 Estimated water retention curves for Wuwei Yellow loess. (TH35 is θ at 350 cm H₂O instead of 330 cm H₂O)

Table 2 Irrigation schedule (DAP: Days after planting).

No. of irrigation	Case A		Case B	
	DAP (days)	Irrigation depth (mm)	DAP (days)	Irrigation depth (mm)
1	15	180	15	60
2	60	105	70	120
3	80	105	80	60
4	100	105	96	60
5	120	105	109	60
6	140	105	119	90
7	160	105	129	60
8	-	-	139	60
9	-	-	152	60
	Total	810		630

3.2 Water and salt behavior at the field

Fig. 3 shows a comparison between monitored and predicted moisture contents of the soil at depths of 10 and 30 cm. Numerical results can represent actual moisture conditions fairly well.

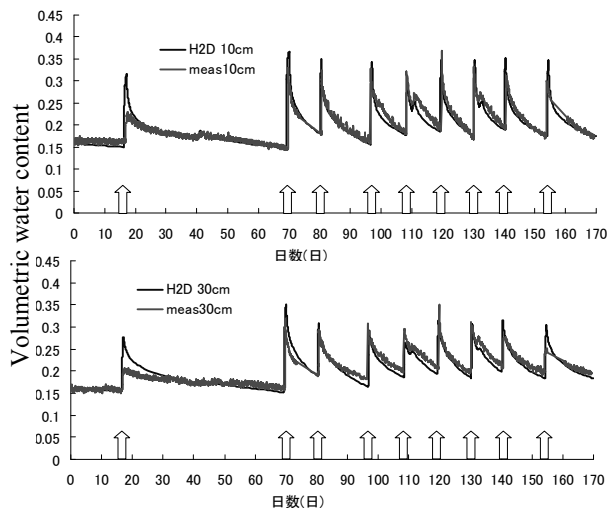


Fig. 3 Comparison of monitored and predicted soil water contents in the maize field (10 cm and 30 cm in depth and arrows denote timing of irrigation).

3.3 Numerical simulation for improved irrigation practice

Results of numerical simulations suggested that HYDRUS-2D with proper soil hydraulic parameters can represent behavior of water in soils well. Thus, a simulation study for subsurface irrigation was attempted for the same climate and soil conditions.

Fig. 4 shows simulated root water uptake and irrigation under boarder irrigation for different irrigation schedules shown in Table 2. Here, Case A is the conventional irrigation scheme a farmer did and Case B is an alternative water saving irrigation schedule. The Case B tends to save water by using more frequent and smaller dose irrigation, which is the difference between cumulative irrigation and root water uptake in these figures. In semi-arid regions many farmers are forced to use ground water with high salt content. For example, pumped water in this study site had electrical conductivity of 0.6 dS m^{-1} which is equivalent to 400-NaCl g m^{-3} of water. Thus, saving irrigation water may reduce the accumulation of salts in the agricultural field.

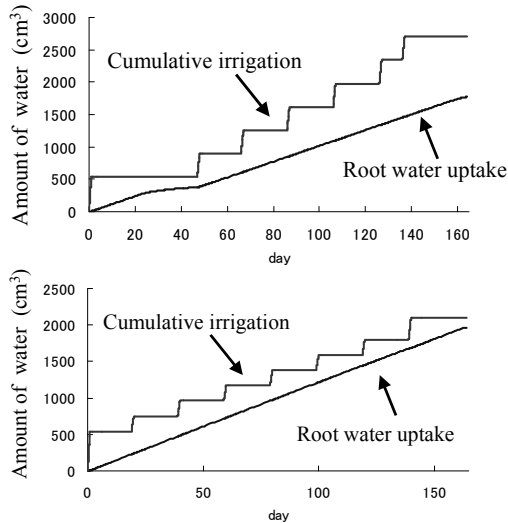


Fig. 4 Simulated cumulative water application and root water uptake of maize under alternative irrigation schedules (Top and bottom are result of the Case A and B, respectively).

4 CONCLUSION

Numerical simulations with properly measured soil hydraulic parameters can represent well the behavior of salt and water in Yellow loess at the maize field in Wuwei. Measured soil hydraulic parameters seem to provide more accurate description of flow and transport processes than pedotransfer functions. Soil hydraulic parameters provided by Rosetta performed better than those from the USDA soil catalogue. A case study on subsurface irrigation suggested that we can enhance efficiency of irrigated water while maintaining proper water conditions for plants.

ACKNOWLEDGEMENT

We appreciate Mr. Yang Cai of his favor to use his field for our monitoring. Also, we appreciate Mr. T. Noguchi, Mr. P. Kumar, Ms. Xiaoduo PAN and Prof. Feng Zhongyun for their help in conducting this study.

REFERENCES

- Carsel, RF. and Parrish, RS 1988. Developing Joint Probability Distributions of Soil Water Retention Characteristics, *Water Resour. Res.* 24(5), p 755-769
- Cosby, B. J., G.M. Hornberger, R.B. Clapp, and T.R. Ginn, 1984. A statistical exploration of the relationships of soil moisture characteristics to the physical properties of soils. *Water Resour. Res.* 20, pp.682-690

- Eching, S.O. and J.W. Hopmans, 1993. Optimization of Hydraulic functions from transient outflow and soil water pressure data, *Soil Sci. Soc. Am. J.* 57(5), pp.1167-1175.
- Feddes, R.A., P. J. Kowalik, and H.Zaradny. 1978. Simulation of field water use and crop yield, John Wiley & Sons, New York, NY.
- Hassan, G., Persaud, N., and Reneau, R.B., 2005. Utility of HYDRUS-2D in modeling profile soil moisture and salinity dynamics under saline water irrigation of soybean. *Soil Sci.* 170 :28- 37.
- Kang Shaozhong, Zongsuo Liang, Wei Hu, and Jianhua Zhang, 1998. Water use efficiency of controlled alternate irrigation on root-divided maize plants, *Agricultural water management*, 38, pp.69-76.
- Mahmood Nachabe, Nirjhar Shah, Mark Ross, and J. Vomacha 2005. Evapotranspiration of two vegetation covers in a shallow water table environment. *Soil Sci. Soc. Am. J.* 69, pp.492-499.
- Oster, J.D., and Shainberg, I. 2001. Soil response to sodicity and salinity: challenges and opportunities. *Australian J. of Soil Res.*, 39: 1219 – 1224.
- Rosenthal, W. D., Kanemasu, E.T., Raney, R. J. and L. R. Stone, 1977. Evaluation of an evapotranspiration model for corn. *Agronomy Journal*, 69, pp.461-464.
- Schapp, M.G., F.J.Leij and M. Th. Van Genuchten, 1998. Neural network analysis for hierarchical prediction of soil water retention and saturated hydraulic conductivity. *Soil Sci. Soc. of Am. J.*, 62:847-855.
- Schaap. M.G., F. J. Leij, and M. Th. van Genuchten, 1999: A bootstrap-neural network approach to predict soil hydraulic parameters. In M. Th. van Genuchten F.J. Leij and L. Wu (eds.), *Proc. Intl. Workshop , Characterization and Measurements of the Hydraulic properties of Unsaturated Porous Medias*, pp.1237-1250, Univ. of California, Riverside, USA.
- Šimůnek, J., M. Šejna, and M. Th. van Genuchten, The HYDRUS-2D software package for simulating two-dimensional movement of water, heat, and multiple solutes in variably saturated media. Version 2.0, *IGWMC - TPS - 53*, International Ground Water Modeling Center, Colorado School of Mines, Golden, Colorado, 251 pp., 1999.
- Tedeschi, A., Aquila, and R. Dell, 2005. Effects of irrigation with saline waters, at different concentrations, on soil physical and chemical characteristics. *Agricultural Water Management*, 77: 308 – 322.
- Tomasella, J., Y. Pachepsky, S. Crestana, and W.J. Rawls, 2003. Comparison of two techniques to develop pedotransfer functions for water retention, *Soil Sci. Soc. Am. J.* 67, pp.1085-1092
- van Genuchten, M. Th. (1980): A closed form equation for predicting the hydraulic conductivity of unsaturated soils, *Soil Sci. Soc. Am. J.* 44 pp.892-898
- Vrugt, J.A., Hopmans, J.W., and Šimůnek, J.2001. Porous media with linearly dimensional root water uptake model, *Soil Sci. Soc. Am. J.* 65, pp.1027-1033.

Modeling of Water and Nitrogen Transport in Tea Fields

Y. Hirono

National Institute of Vegetable and Tea Science, 2769, Kanaya, Shimada, Shizuoka, Japan

S. Nakamura

Swine and Poultry Research Center, Shizuoka Prefectural Research Institute of Animal Industry, 2780 Nishikata, Kikugawa, Shizuoka, Japan

M. Ohta

Tea Research Center, Shizuoka Prefectural Research Institute of Agriculture and Forestry, 1706-11, Kurasawa, Kikugawa, Shizuoka, Japan

ABSTRACT: Simulation models are effective tools for quantitatively comparing environmental loads from agricultural land under the condition of different managements of fertilizer applications. In this study, the water transport and nitrogen transport in tea fields observed by lysimeter experiments and simulated using HYDRUS-1D were compared to evaluate the validity of the model. It was found that the simulated water transport agreed well with observed transport, but the simulated nitrogen transport did not agree with observed transport. Determination of optimal parameters expressing nitrogen transformation in soils remains as one of the key issues for increasing the accuracy of prediction of nitrogen transport in tea fields.

1 INTRODUCTION

In cultivation of tea, large amounts of nitrogen, compared to the amounts used for other crops, have been applied as fertilizer, resulting in an increase in nitrate-nitrogen (NO₃-N) concentrations in surrounding water systems and a high rate of emission of nitrous oxide, one of the major greenhouse gases. In response to these problems, the amounts of nitrogen applied as fertilizer to tea fields has been reduced in the past several years. Various new methods of fertilizer application to improve the efficiency of nitrogen use by tea plants have also been developed in order to achieve a good balance between reduction of environmental loads and preservation of the yield and quality of tea. However, there have been few studies in which environmental loads from tea fields were quantitatively compared under the conditions of different managements of fertilizer application. Since it is thought that the approach using a simulation model is effective to make a quantitative comparison, we used a model to estimate water and nitrogen movement in tea fields and evaluated the validity of the model in this study. The results of this study could help farmers to decide appropriate irrigation and fertilizer application schedules.

2 MATERIALS AND METHODS

2.1 Model description

Modeling of water and nitrogen movement was conducted using a computer simulation model, Version 4.0 of HYDRUS-1D (Šimůnek et al. 2008). Vertical water movement in isotropic soil is described by Richards' equation. This equation is given by

$$\frac{\partial \theta}{\partial t} = \frac{\partial}{\partial z} \left[K(\theta) \frac{\partial h}{\partial z} + K(\theta) \right] - S, \quad (1)$$

where θ is volumetric water content (L³ L⁻³), t is time (T), z is the vertical coordinate (L) (positive upward), h is the pressure head (L), $K(\theta)$ is unsaturated hydraulic conductivity (L T⁻¹), and S is the root water uptake term (L³ L⁻³ T⁻¹). S is computed from

$$S = \alpha(h)b(z)T_p, \quad (2)$$

where $\alpha(h)$ is root-water uptake water stress response function (dimensionless), $b(z)$ is the normalized water uptake distribution (L^{-1}), and T_p is the potential transpiration rate ($L T^{-1}$). The root distribution function, which is needed for the derivation of $b(z)$, was determined from the literature (Aono et al. 1979) and was assumed to be unchanging during the study period. Potential evapotranspiration rates were calculated using the Penman-Monteith equation. Weather data used for this calculation were obtained from AMeDAS of the Japan Meteorological Agency (Kikugawa-Makinohara, Shizuoka) and the weather-monitoring station of National Institute of Vegetable and Tea Science, Shizuoka. The ratio of evaporation to transpiration was 1 to 5, which was determined by the ratio of the soil area covered to that uncovered by the canopy of tea plants. The potential evaporation rate (T_p) was calculated with the assumption that the crop coefficient was 1.0.

Soil hydraulic properties were represented by the model of van Genuchten (1980). The parameters used for this model, including saturated water content (θ_s), residual water content (θ_r), empirical factors (α , n) and saturated hydraulic conductivity (K_s), were predicted using the neural network prediction model available in HYDRUS by giving measured values of clay, silt and sand contents of soil used for lysimeter experiments. The tortuosity parameter (l) was set to 0.5. Basic physical properties and predicted hydraulic properties of the soil are shown in Table 1.

Table 1. Basic physical properties and hydraulic properties of soil.

Particle density ($g\ cm^{-3}$)	Bulk density ($g\ cm^{-3}$)	Clay content (%)	Silt content (%)	Sand content (%)	θ_r ($cm^3\ cm^{-3}$)	θ_s ($cm^3\ cm^{-3}$)	α (cm^{-1})	n (-)	K_s ($cm\ d^{-1}$)
2.7	1.3	32.0	24.5	43.5	0.0778	0.414	0.0195	1.33	6.21

For solute transport, the relationship between adsorbed and soluble NH_4 -N was described by a linear equation. The nitrification process was assumed to occur from the surface to a 0.3 m depth and was considered as a first-order reaction, the rate of which was determined from the literature (Hayatsu & Kosuge 1993). Mineralization and denitrification processes were neglected. Adsorption of nitrate by soil was also neglected. Under these assumptions, the equations governing nitrogen transport are given as

$$\frac{\partial \theta c_1}{\partial t} + \frac{\partial \rho s_1}{\partial t} = \frac{\partial}{\partial z} \left(\theta D_1 \frac{\partial c_1}{\partial z} \right) - \frac{\partial q c_1}{\partial z} - \mu'_{w,1} \theta c_1 - \mu'_{s,1} \rho s_1 - S c_1 \quad (3)$$

$$\frac{\partial \theta c_2}{\partial t} = \frac{\partial}{\partial z} \left(\theta D_2 \frac{\partial c_2}{\partial z} \right) - \frac{\partial q c_2}{\partial z} + \mu'_{w,1} \theta c_1 + \mu'_{s,1} \rho s_1 - S c_2 \quad (4)$$

$$s_1 = K_d c_1 \quad (5)$$

$$\theta D_i = D_L |q| + \theta D_{w,i} \tau, \quad (6)$$

where c_1 and c_2 are the ammonium-nitrogen (NH_4 -N) and NO_3 -N concentrations in solution ($M\ L^{-3}$), respectively, s_1 is the adsorbed NH_4 -N concentration ($M\ M^{-1}$), D_1 and D_2 are the dispersion coefficients ($L^2\ T^{-1}$) of NH_4 -N and NO_3 -N, respectively, $\mu'_{w,1}$ and $\mu'_{s,1}$ are the first-order nitrification rates for liquid and solid phases, respectively, K_d is the empirical factor ($L^3\ M^{-1}$), D_L is the longitudinal dispersivity (L), $|q|$ is the absolute value of the Darcian fluid flux density ($L\ T^{-1}$), $D_{w,i}$ is the molecular diffusion coefficient in free water ($L^2\ T^{-1}$) and τ is a tortuosity factor in liquid phase (-). The parameters used in this study were shown in Table 2.

Table 2. Input parameters for solute transport.

$\mu'_{w,l}$	$\mu'_{s,l}$	K_d	D_L	$D_{w,l}$	$D_{w,2}$
(d ⁻¹)	(d ⁻¹)	(cm ³ g ⁻¹)	(cm)	(cm ² d ⁻¹)	(cm ² d ⁻¹)
0.075	0.075	1.0	10	1.54	1.66

Initial water content was set to be the value at the end of the simulation using the weather data from Apr. 2002 to Mar. 2003. Initial NH₄-N and NO₃-N concentrations were determined by the profile values measured on Mar. 30, 2003 and the concentrations of leachate sampled on Apr. 1, 2003. The upper boundary was represented by atmospheric variable boundary conditions with specified irrigation rates, fertigation rates, precipitation rates, evaporation rates, and NH₄-N and NO₃-N concentrations in the liquid fertilizer. The lower boundary was represented by a seepage boundary condition and a zero concentration gradient.

2.2 Lysimeter experiments

Datasets obtained from lysimeter experiments conducted at the Tea Research Center of the Shizuoka Prefectural Research Institute of Agriculture and Forestry from Apr. 2003 to Mar. 2006 were used for validation of the model. Each lysimeter, with dimensions of 2.0 m in width, 1.5 m in length and 2.0 m in depth, was filled with yellow soil (clay loam) and included five tea plants. Three methods of fertilizer application were compared. One was the conventional method of manually applying fertilizer beside tea plants (CM). The others were fertigation methods of automatically applying liquid fertilizer under the canopy of tea plants (F1 and F2). The fertigation conditions are given in Table 3. Liquid fertilizer was applied by a water spray bar. Nitrogen was applied as ammonium nitrate. In the CM lysimeter, nitrogen was applied as rapeseed meals, fish lees, urea, ammonium sulfate and ammonium nitrate. For each lysimeter, the amount of leachate from the bottom was measured and subsamples were collected from storage tanks and the concentrations of NH₄-N and NO₃-N were quantified using the ion chromatography analysis.

Table 3. Fertigation conditions.

Methods of fertilizer application	Amount of nitrogen applied	Amount of water applied per fertigation	Amount of water applied per year	Interval of fertigation	Nitrogen concentrations of liquid fertilizer
	(kg ha ⁻¹)	(mm)	(mm)	(days)	(mgN L ⁻¹)
CM	540	-	-	-	-
F1	300	5	300	4	100
F2	300	5	60	18	500

3 RESULTS AND DISCUSSION

3.1 Water transport

Observed and simulated cumulative amounts of leachate are shown in Figure 1. Precipitation and irrigation depth are also shown. The largest amount of annual leachate was observed in 2004 due to the highest annual precipitation among the three years. Due to a large amount of rain from Sep. to Nov. in 2004, even the amount of leachate in the lysimeter to which fertilizer was applied by the conventional method reached almost 1000 mm during the period. The annual

precipitation in 2005 was less than usual and the amount of annual leachate in that year was only about half of that in 2004.

A comparison of the observed and calculated amounts of leachate showed that there was good agreement between them for all lysimeters, indicating that the model of water transport in tea fields can predict water transport in tea fields with a high level of accuracy. There was little difference among the calculated cumulative amounts of actual root water uptakes of the three lysimeters, and the amounts of the CM lysimeter were about 596, 664 and 678 in 2003, 2004 and 2005, respectively (data not shown).

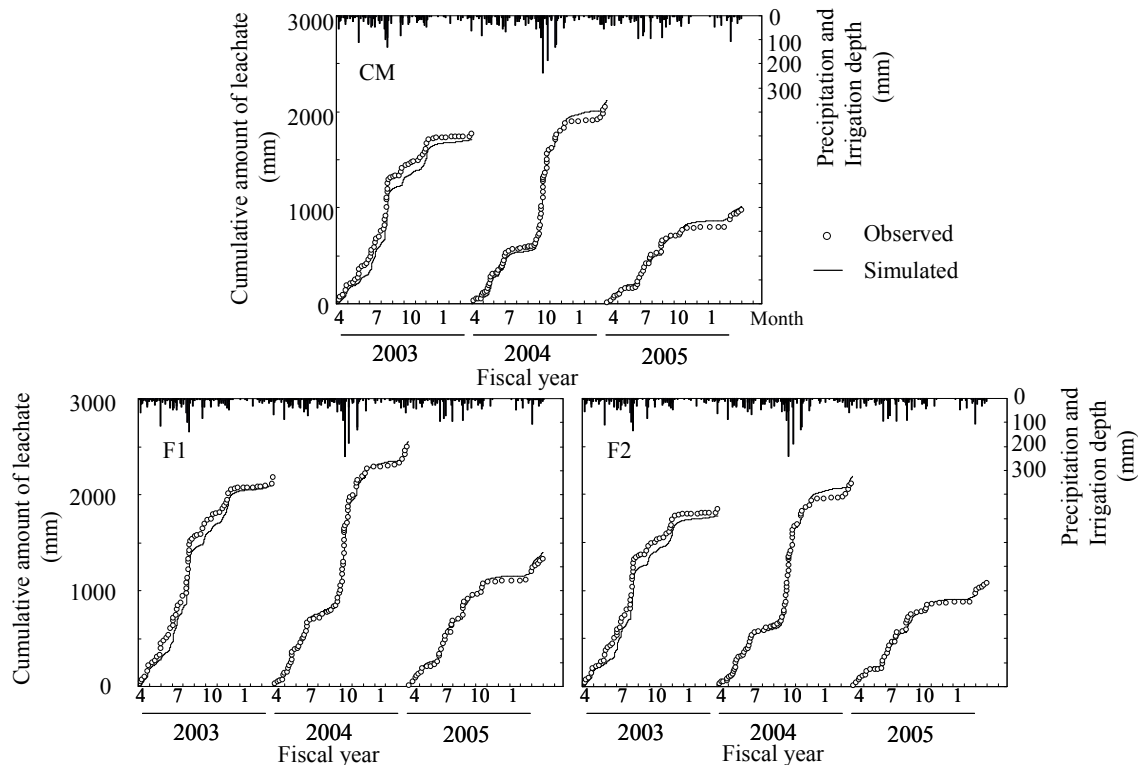


Figure 1. Comparison of the observed and simulated cumulative amounts of leachate from the bottom of each lysimeter.

3.2 Nitrogen transport

Observed and simulated concentrations of $\text{NO}_3\text{-N}$ of leachate of F1 and F2 are shown in Figure 2. The $\text{NO}_3\text{-N}$ concentrations began to increase after heavy rain (around Aug. and Nov. in 2003, Oct. in 2004 and Jul. in 2005). The maximum concentrations of F1 and F2 were observed in Oct. 2004. A comparison of the observed and simulated $\text{NO}_3\text{-N}$ concentrations of leachate showed that, though the simulated concentrations peaked around Oct. 2004 and Jan. 2006 similar to the observed concentrations, the values were significantly overestimated throughout the study period. Conversely, $\text{NH}_4\text{-N}$ concentrations were underestimated (data not shown). One possible reason for these errors is the unsuitableness of given nitrification rates. Smaller nitrification rates should be given to fit observed data. Another possible reason is the neglect of some processes such as mineralization, denitrification and adsorption of $\text{NO}_3\text{-N}$. These processes might play important roles in nitrogen transport in tea fields.

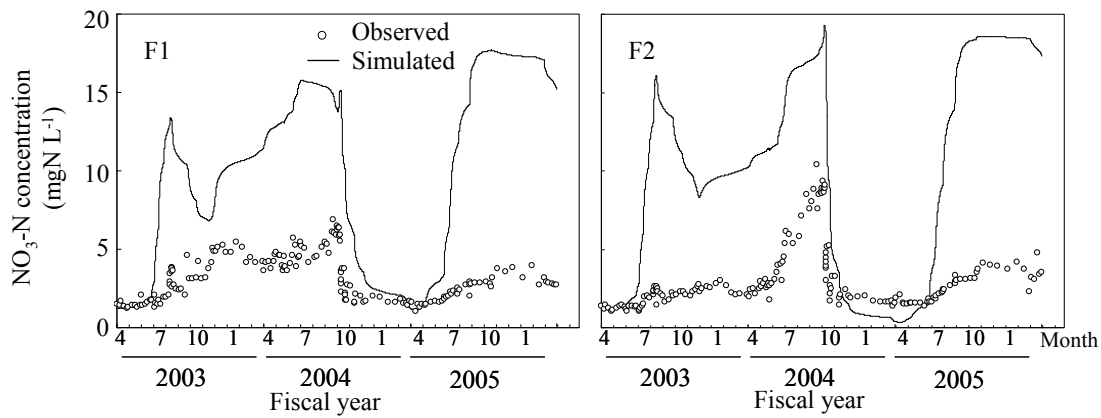


Figure 2. Comparison of the observed and simulated $\text{NO}_3\text{-N}$ concentrations of leachate from the bottom of each lysimeter.

4 CONCLUSIONS

The results of the lysimeter experiments and simulation of water transport in tea fields were compared. The cumulative amounts of simulated leachate agreed well with observed values. For solute transport, the simulated $\text{NO}_3\text{-N}$ concentrations of leachate were greatly overestimated. The results indicate that the model used in this study is useful tool for the proposal of optimal water management for tea cultivation but not of fertilizer application management. Further studies on the determination of optimal parameters are needed to achieve our goal of establishing appropriate irrigation and fertilizer application schedules.

REFERENCES

- Aono, H., Yanase, Y., & Tanaka, S. 1979. Development and distribution of tea roots in tea field and influence of cultural condition on tea roots. *Tea Research Journal* 56: 10-29 (in Japanese with English summary).
- Hyatsu, M. & Kosuge, N. 1993. Autotrophic nitrification in acid tea soils. *Soil Sci. Plant Nutr.* 39: 209-217.
- Šimůnek, J., Šejna, M. & van Genuchten, M. Th. 2008. The HYDRUS-1D Software Package for Simulating One-Dimensional Movement of Water, Heat, and Multiple Solutes in Variable Saturated Media. Version 4.0.
- van Genuchten, M. Th. 1980. A closed-form equation for predicting the hydraulic conductivity of unsaturated soils. *Soil Sci. Soc. Am. J.* 44: 892-898.

Simulation of Soil Water Movement in a Water Harvesting System with Sand Ditches

T. Saito & H. Yasuda

Arid Land Research Center, Tottori University, 1390 Hamasaka, Tottori 680-0001, Japan

H. Fujimaki

Graduate School of Life and Environmental Sciences, University of Tsukuba, Tsukuba, Ibaraki 305-8572, Japan

ABSTRACT: A new method of water harvesting system with ditches filled with highly permeable materials that has potential to reduce soil water evaporation has been proposed. Laboratory experiments were carried out using a soil tank with dielectric sensors and various fillers for the ditch to evaluate the water storage ability of this system. The soil water movement in the system was simulated using HYDRUS-2D, and the results were compared with the measured results. The simulated water content distributions and cumulative water influxes were relatively in good agreement with the measured results in the infiltration process. The estimated evaporation rates did not agree well with the measured rates especially at the late stage in the evaporation process when the atmospheric boundary conditions were applied to the model. This may be due to excluding the calculation scheme of vapor flux in the model.

1 INTRODUCTION

Rain water harvesting systems are traditional agricultural ways to collect and recharge runoff water into soils by such means as ditches and dams. They are essential for sustainable agriculture and afforestation without depending on irrigation systems in arid and semi-arid regions. In general, the most important point in evaluating the effect of water harvesting is determined how much water is collected and recharged into the soil. However, a large amount of water is lost from the soil and collected water surface due to high evaporation conditions in arid environments. As a measure for this problem, a new method of water harvesting that has potential to reduce soil water evaporation has been proposed by means of ditches filled with highly permeable materials (Saito et al. 2000; Abu-Zreig et al. 2000). In this method, a ditch is dug and then filled with highly permeable materials (e.g. sand) as a device to collect runoff water. It can be expected that runoff water infiltrates promptly into the ditch, and the infiltrated water then seeps to the adjacent soil through the side and bottom of the ditch due to the high matric potential gradient between the material in the ditch and adjacent soil. In addition, this method can reduce the amount of evaporation from the soil surface since the infiltrated water is stored deeper in the soil profile. Considering its distribution shape of the soil water, this method would be suitable for applying to trees. This filled ditch, called “sand ditch”, is simple and cost-effective, therefore it can be applied to large fields along contour lines.

The effectiveness of sand ditches has been confirmed through laboratory and field experiments. Abu-Zreig et al. (2000) reported that sand ditches increased water storage and infiltration depth in an olive field in Jordan. Saito et al. (2006) carried out laboratory experiments using various fillers for the ditches to evaluate their water storage ability and to examine suitable fillers. In addition to such experimental approaches, numerical modeling of the system is important to generalize the results. Simulation of the system may provide optimal designing of the ditch and filler based on the regional environmental conditions through numerical experiments. The objective of this study, therefore, was to model the water harvesting system with sand ditches. The soil water movement in the system was simulated using HYDRUS-2D (Šimůnek, et al., 2005), and the results were compared with the measured results from laboratory experiments.

2 MATERIALS AND METHODS

2.1 Experimental soil and filler in the ditch

A homogeneous and dry experimental soil was made by mixing silica sand with 10% by weight of Kibushi clay. Five types of large porous and highly permeable materials were employed as the filler in the ditch namely: sand mixed with 5% clay, sand, gravel, chopped plastic pipes and rice chaff. The ditches filled with the above fillers are rafter to as clay-ditch (CD), sand-ditch (SD), gravel-ditch (GD), pipe-ditch (PD) and rice chaff- ditch (RD), respectively. Some physical properties of the experimental soil and fillers are listed in Table 1. In addition to five types of the ditch treatments, non-ditch (ND) treatment was also performed as a control.

2.2 Experimental setup and procedure

Figure 1 shows the schematic diagram of the experimental apparatus. The experimental soil was carefully placed in an acrylic test soil tank (inside dimension: 89 × 48 × 15 cm). The inside walls of the soil tank were previously treated by experimental soil with bonding adhesive to prevent fingering and preferential flow of water along the wall. A ditch was dug out (41 × 9 × 15cm) at the side of the tank as shown in Fig.1, and filled with highly permeable materials. Dielectric soil moisture sensors (ThetaProbe ML2x: Delta-T Devices Ltd, Cambridge, UK) were set up at 26 points along the side of the soil tank. All of the equipments were placed on weighing machines to measure evaporation rate.

Table 1. Physical properties of the experimental soil and fillers

Soil and filler in the ditch	Bulk density	Saturated hydraulic conductivity	Saturated volumetric water content
	Mg m ⁻³	cm s ⁻¹	m ³ m ⁻³
Experimental soil	1.81	9.78×10 ⁻⁵	0.288
Sand mixed with 5% clay (CD)	1.69	1.30×10 ⁻³	0.326
Sand (SD)	1.67	1.05×10 ⁻¹	0.396
Gravel (GD)	1.30	6.35	0.495
Chopped plastic pipes (PD)	0.28	12.9	0.734
Rice chaff (RD)	0.12	1.29	0.840

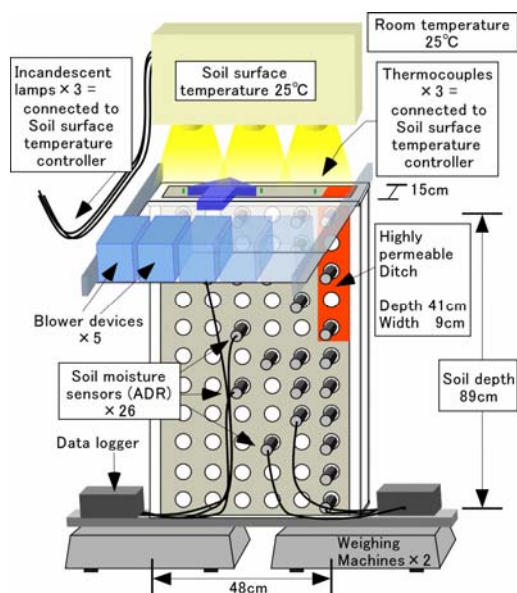


Figure 1. Schematic diagram of the experimental apparatus.

After the equipments were set up, assumed runoff water was uniformly poured over the soil surface using an irrigation device. Depth of the poured water was 40 mm per unit area. The poured water was ponded on the soil surface until infiltration was completed. The ponding time of each ditch treatment was measured as an index to evaluate the promotion of infiltration by the ditch. This ponding term is referred to as “infiltration process” in this paper. Following the completion of the infiltration, the soil tank was uncovered to allow evaporation. The soil water was evaporated under constant meteorological conditions during 7 days (168 h); this term is referred to as “evaporation process”. Soil surface temperature was automatically regulated at 25°C by temperature control devices, which were connected thermocouples and incandescent lamps. Room temperature was also kept at 25°C. Wind velocity was kept constant by five blower devices.

2.3 Simulation of soil water movement

The HYDRUS-2D software package (Šimůnek et al., 2005) was used to simulate the soil water movement in both infiltration and evaporation processes. The modified van Genuchten model (Vogel & Cislérova, 1988) was employed as the soil hydraulic model to adjust the air-entry value of the experimental soil since the soil was clayey. The soil hydraulic parameters given to the model were basically determined by referring the values in Table 1 and retention curves for each soil and filler. However, in order to stabilize the calculations, some parameter values such as the hydraulic conductivities of the fillers were adjusted within the range that had little influence on the water movement.

The simulations were separately performed for the infiltration and evaporation processes. In the calculation of the infiltration process, we applied the time variable pressure condition corresponding to the measured ponding depth as the upper boundary condition for each treatment. The final time of the calculation was also set at the measured ponding time. The simulation of the evaporation process was started after finishing the calculation of the infiltration process. The simulated water content distributions at the end of the infiltration process were imported as the initial water content conditions of the evaporation process. Two types of upper boundary conditions were applied for the evaporation process: (i) time variable flux condition corresponding to the measured evaporation rate and (ii) atmospheric boundary condition. In this paper, we show the simulated results for ND, CD, SD and GD in the infiltration process, and for ND and SD in the evaporation process.

3 RESULTS AND DISCUSSION

3.1 Experimental results

The experimental results were described and discussed in detail by Saito et. al (2006). All of the with-ditch treatments promoted the infiltration of the pored water and reduced the cumulative evaporation compared to ND (non-ditch) treatment (Figure 2). The tendency can be seen that the large pore fillers have high water storage ability.

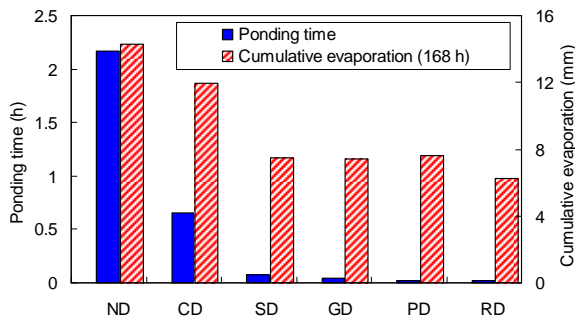


Figure 2. Comparison of the ponding time in the infiltration process and cumulative evaporation at the end of evaporation process.

3.2 Simulated results

Figures 3 and 4 show the distributions of volumetric water content at the ends of the infiltration and evaporation processes, respectively. The simulated distributions were in relatively good agreement with the measured distributions in the infiltration process. The simulated water content was a little higher than the measured water content in each ditch; this was probably because the actual field-saturated water content was lower than the saturated water content used in the calculation (Table 1). The calculated cumulative water influxes were also in relatively good agreement with the amount of the poured water.

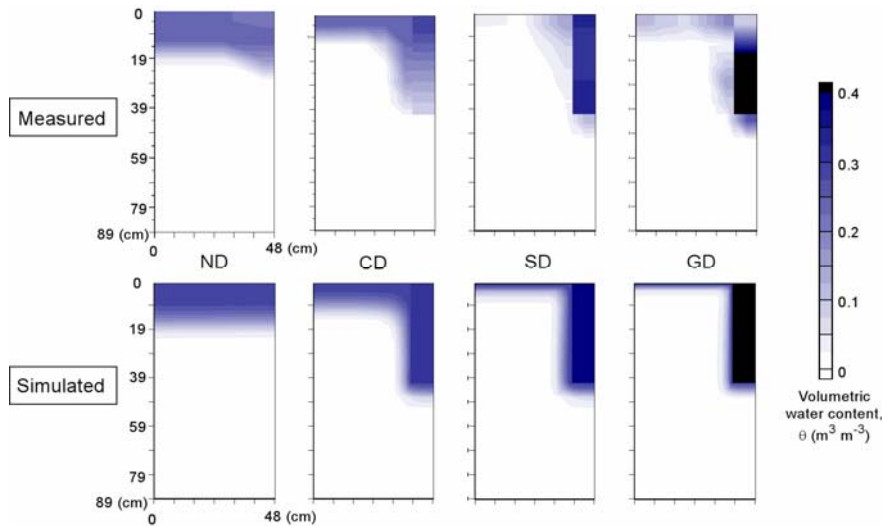


Figure 3. Distributions of volumetric water content at the end of the infiltration process: ND = non-ditch, CD = clay-ditch, SD = sand-ditch and GD = gravel-ditch.

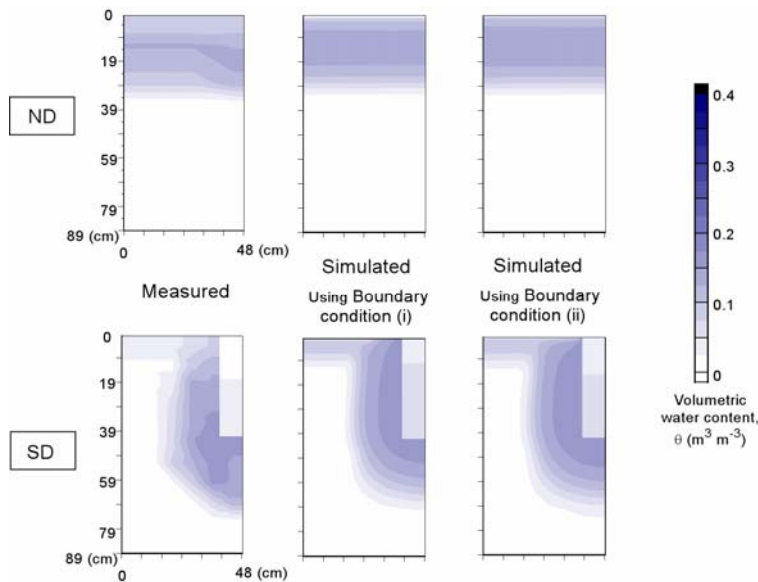


Figure 4. Distributions of volumetric water content at the end of the evaporation process (168 h): ND = non-ditch and SD = sand-ditch. The boundary condition (i) is the time variable flux condition corresponding to the measured evaporation rate. The boundary condition (ii) is the atmospheric boundary condition.

In the evaporation process, the simulated distributions were in moderate agreement with the measured distribution (Figure 4). The near-surface soil water content (0 – 10 cm) was overestimated in all of the simulated results. At the end of the evaporation process (168 h), the cumulative evaporation values calculated under the boundary conditions (i) were approximately equal to the measured values in both ND and SD, in contrast, the calculated values under the boundary conditions (ii) were 77 and 231 % of the measured values in ND and SD, respectively.

The variations of the estimated evaporation rates under the boundary conditions (ii) with time are presented in Figure 5. The estimated rates were in relatively good agreement with the measured rates at the first stage of evaporation ($h < 12$) in both ND and SD. However, the evaporation rate of ND was underestimated at the second ($12 < h < 36$) and third stages ($h > 36$), and the rate of SD was underestimated at the second stage and was overestimated at the third stage. These estimation errors at the late stages may be caused by excluding the calculation scheme of vapor flux in the model. Further improvement of the model will contribute to the accurate estimation of water content distribution and evaporation rate. Seeking optimal hydraulic parameter values and h_{critA} value also seems to be important for better calculation.

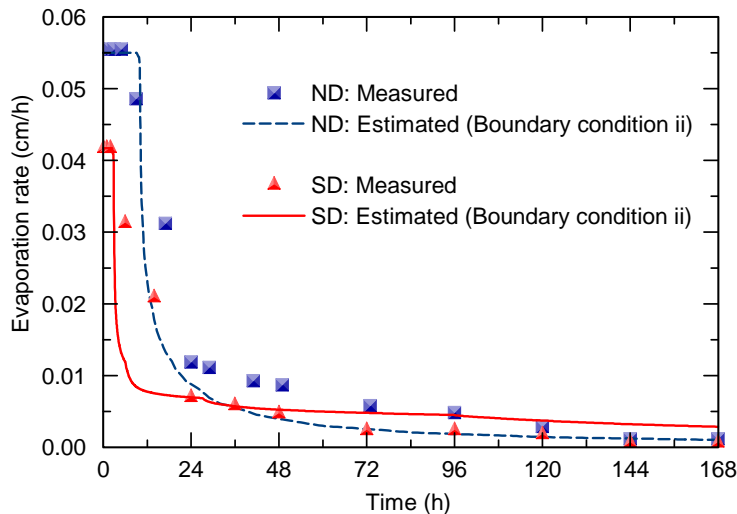


Figure 5. Variations of the measured and estimated evaporation rates with time. The plots are the measured evaporation rate that corresponds to the time variable flux used for the boundary condition (i). The lines are the estimated evaporation rate by the model under boundary condition (ii).

REFERENCES

- Abu-Zreig, M., Attom, M. & Hamasha, N. 2000. Rainfall harvesting using sand ditches in Jordan. *Agric. Water Manage.* 46:183–192.
- Saito, T., Abe, Y., Yasuda, H. & Yamada, K. 2000. Effect of water harvesting considering evaporation control in arid areas. *The XIV memorial CIGR world congress 2000*, pp.1143–1147.
- Saito, T., Maehara, K., Yasuda, H. & Abe, Y. 2006. Experimental study of water harvesting by means of a ditch filled with highly permeable material. *J. Arid Land Studies* 15: 379–382.
- Šimůnek, J., Šejna, M. & van Genuchten, M. Th. 2005. The HYDRUS-2D software package for simulating the two-dimensional movement of water, heat, and multiple solutes in variably saturated media. Version 2.0. Int. Ground Water Model. Ctr. TPS-53. Colorado School of Mines, Golden.
- Vogel, T. & Cislérova, M. 1988. On the reliability of unsaturated hydraulic conductivity calculated from the moisture retention curve. *Transp. Porous Media* 3:1–15.

The Third HYDRUS Workshop

Edited by Hirotaka Saito, Masaru Sakai, Nobuo Toride, and Jirka Šimůnek

Tokyo University of Agriculture & Technology

Department of Ecoregion Science

Fuchu Tokyo

Workshop proceedings

Full papers are also available at the address <http://www.pc-progress.cz/>

152 pages

First Printing

2008

ISBN: 978-4-9901192-5-6